



TECHNISCHE
UNIVERSITÄT
WIEN
Vienna | Austria

DISSERTATION

Experimental and Computational Studies on Combustion of Surrogate and Alternative Fuel Components at Atmospheric and Elevated Pressures

submitted in partial satisfaction of the requirements for the degree
Doctor technicae (Dr. techn.)

by

Martin Hunyadi-Gall

Registration Number: 0625332

to the

Faculty of Mechanical and Industrial Engineering
of TU Wien

Advisor: Ao.Univ.-Prof.i.R. Dipl.-Ing. Dr.techn. Ernst Pucher
TU Wien

Institute of Powertrains and Automotive Technology
Getreidemarkt 9, 1060 Vienna, Austria

Reviewer: Prof. Dr. Kalyanasundaram Seshadri

University of California San Diego

Jacobs School of Engineering

Department of Mechanical and Aerospace Engineering

9500 Gilman Drive, La Jolla, CA 92093, USA

Univ.Prof. Dipl.-Ing. Dr.techn. Franz Winter

TU Wien

Institute of Chemical, Environmental

and Bioscience Engineering

Getreidemarkt 9, 1060 Vienna, Austria



TECHNISCHE
UNIVERSITÄT
WIEN
Vienna | Austria

DISSERTATION

Experimental and Computational Studies on Combustion of Surrogate and Alternative Fuel Components at Atmospheric and Elevated Pressures

ausgeführt zum Zwecke der Erlangung des akademischen Grades
Doktor der technischen Wissenschaften (Dr. techn.)

eingereicht von

Martin Hunyadi-Gall

Matrikelnummer: 0625332

an der

Fakultät für Maschinenwesen und Betriebswissenschaften
der Technischen Universität Wien

Betreuer: Ao.Univ.-Prof.i.R. Dipl.-Ing. Dr.techn. Ernst Pucher
Technische Universität Wien
Institut für Fahrzeugantriebe und Automobiltechnik
Getreidemarkt 9, 1060 Wien, Österreich

Gutachter: Prof. Dr. Kalyanasundaram Seshadri
University of California San Diego
Jacobs School of Engineering
Department of Mechanical and Aerospace Engineering
9500 Gilman Drive, La Jolla, CA 92093, USA

Univ.Prof. Dipl.-Ing. Dr.techn. Franz Winter
Technische Universität Wien
Institut für Verfahrenstechnik, Umwelttechnik
und technische Biowissenschaften
Getreidemarkt 9, 1060 Wien, Österreich

I confirm that going to press of this thesis needs the confirmation of the examination committee.

Affidavit

I declare in lieu of oath that I wrote this thesis and performed the associated research myself, using only literature cited in this volume. If text passages from sources are used literally, they are marked as such.

I confirm that this work is original and has not been submitted elsewhere for any examination, nor is it currently under consideration for a thesis elsewhere.

I acknowledge that the submitted work will be checked electronically-technically using suitable and state-of-the-art means (plagiarism detection software). On the one hand, this ensures that the submitted work was prepared according to the high-quality standards within the applicable rules to ensure good scientific practice “Code of Conduct” at the TU Wien. On the other hand, a comparison with other student theses avoids violations of my personal copyright.

Bad Vöslau, May 2023

(Signature Author)

Acknowledgements

First and foremost, I would like to thank my advisor and mentor here in Austria, Prof. Dr. Ernst Pucher of TU Wien, for his encouragement, trust, and constant support in not just professional, but also personal matters, especially during demanding and challenging times, of which there has been a fair share. His engagement as an advisor and supervisor extends far beyond the academic level, whereby he inspires and influences the lives of many students, including mine, by encouraging them to gather as much professional and life experience as possible when opportunities present themselves. Equally, I would like to express my deepest gratitude to my supervisor and mentor in California, Prof. Dr. Kalyanasundaram Seshadri of UC San Diego, for his invitation to manage and work in his and Prof. Dr. Forman A. Williams' Combustion Laboratory at the Department of Mechanical and Aerospace Engineering. What started out with a lot of paperwork developed into a wonderful relationship, now spanning across half the globe. Therefore, I would like to thank him for the great discussions, honest feedback, patience, and support whether on or off campus. The opportunity these two mentors opened up for me led to more profound experiences over the course of this dissertation than I could count or ever even dared to imagine. It contributed to my professional and personal growth like no other phase in my life and thereby culminated in a debt that could never be paid by worldly means. Therefore, I can only offer my sincerest "Thank you".

Furthermore, I want to thank the amazing and seasoned staff of the Department of Mechanical and Aerospace Engineering at UCSD I had the pleasure to get to know and work with for their support and help in all the organizational matters that come with lab and campus life. Their knowledge and expertise facilitated the initial phase while settling in and the following day to day work throughout the years significantly. I want to express the same gratitude to the professors and academic staff of MAE for all the

ACKNOWLEDGEMENTS

fruitful discussions, advice, and the help they were all providing so generously. I also want to thank all the visiting scholars and students I got to work with and mentor for their enthusiastic engagement, help in the lab, and the opportunity to further develop my personal skill set on not just an academic level. In that regard, I also want to express my deepest gratitude to all the amazing teachers and friends of Aoinagi Ken Shu Kai at UCSD who are the shining embodiment of what is truly relevant in every aspect of life. They helped to develop and shape my path and character in more wonderful ways than I could ever imagine when I started this journey.

My gratitude and love also goes to my family and friends, new and old in both my homes, for their support, visits, and for simply being there. You are always with me wherever I go, providing the potential to recharge and gain fresh energy. This acknowledgement would not be complete without thanking my partner, Marianne, for letting me go, taking me back, and all her loving support and strength during the adventurous times in between on this endeavour by being my constant... always together alone. I also want to thank my mom, Anna, for being the spirited caretaker and educator that she is, her constant and unconditional support, patience, and guidance. I would like to thank my dad, Martin, for raising me in the spirit of fixing things instead of tossing or turning them over, for empowering me to dare to be hands-on when necessary, and for showing me the importance of balance between intellectual and physical skills.

Abstract

Experimental and computational investigations are carried out with the goal to expand the body of knowledge of combustion science and engineering. The dissertation's focus is set on combustion at elevated pressures and encompasses measurements and numerical calculations of fundamental limit phenomena and critical conditions. Development of the methodology and computational framework, as well as the expansion of capabilities of the experimental setup are documented herein. Results of preliminary and additional studies at atmospheric pressure are given and discussed to complement the key investigations where necessary, and to test the developed computational methods and models for their reliability and efficiency.

The experimental device used for the investigations and modeled for the simulations is the counterflow burner in various configuration for gaseous and liquid fuels. The measurements were taken at UC San Diego's Combustion Laboratory where a modular burner for experiments at atmospheric pressure as well as the unique High Pressure Combustion Experimental Facility (HPCEF) for investigations of combustion processes and flames at elevated pressures are housed. At atmospheric pressure, extinction and autoignition experiments to measure extinction strain rates and autoignition temperatures of gaseous, prevaporized liquid and pools of condensed fuels were conducted, while at the HPCEF, exclusively condensed liquid fuels were studied to determine autoignition temperatures under varying boundary conditions at pressures from 5 bar up to 25 bar. The tested fuels for the investigations were the gaseous alternative fuel components dimethyl ether (DME) and propane, and the liquid primary reference fuel (PRF) and surrogate components n-heptane, n-decane, and n-dodecane. Graphical representations of the experimental data and numerical calculations including the imposed boundary conditions are given in the respective chapters, while the individual data points of the measurements together with their standard errors are given in tabulated form in the appendix for reference.

ABSTRACT

For the computations and simulations of this thesis, the open source software toolkit Cantera was used. While its solver, capable of handling thermodynamic, chemical kinetic, and transport phenomena to numerically solve chemically reacting flow problems and simulate flames, was left unmodified, the basic implementation and model of the counterflow configuration was adapted and vastly expanded to fit the needs of the investigations presented in this thesis. Eventually, a Python module interfacing with Cantera named “UCSDComLab” was developed to facilitate and streamline the computations and numerical processes by implementing several objects and functions to model, simulate, and evaluate experiments conducted in the course of this dissertation. To provide the required property and reaction data for all the relevant species in the simulated systems and processes, various complete, reduced, and specialized versions of the San Diego and PoliMi Mechanisms were used.

Kurzfassung

Mit dem Ziel den Wissensstand der Verbrennungswissenschaft und -technik zu erweitern, werden im Zuge dieser Dissertation experimentelle und rechnerische Untersuchungen ausgeführt. Der Fokus der Betrachtungen liegt auf der Verbrennung bei erhöhten Drücken und beinhaltet Messungen und numerische Berechnungen fundamentaler Grenzphänomene der Flammbarkeit und kritischer Bedingungen. Die Entwicklung sowohl der experimentellen als auch der computergestützten Methodologie werden zusammen mit der Erweiterung der Kapazitäten der experimentellen Anlage hierin protokolliert. Ergebnisse vorangehender und zusätzlicher Untersuchungen bei atmosphärischem Druck werden angeführt und diskutiert, um im Bedarfsfall die Betrachtungen im Hauptaugenmerk zu ergänzen und die entwickelten rechnerischen Methoden und Modelle auf ihre Zuverlässigkeit und Effizienz zu prüfen.

Die experimentelle Anlage, welche während der Untersuchungen angewendet und für die Simulationen modelliert wird, ist der Gegenstrombrenner in verschiedenen Konfigurationen für gasförmige und flüssige Brennstoffe. Die Messungen wurden in UC San Diego's Verbrennungslabor unternommen, in welchem sowohl ein modulares Brennersystem für Experimente bei atmosphärischem Druck als auch die einzigartige High Pressure Combustion Experimental Facility (HPCEF) zur Untersuchung von Verbrennungsprozessen und Flammen bei erhöhten Drücken zur Verfügung stehen. Bei atmosphärischem Druck wurden Auslöschungs- und Selbstzündungsexperimente zur Ermittlung der Auslöschungsströmungsgeschwindigkeiten und Selbstentzündungstemperaturen bei gasförmigen, vorverdampft flüssigen und angestaut kondensierten Brennstoffen durchgeführt, während am HPCEF ausschließlich kondensiert flüssige Brennstoffe untersucht wurden, um deren Selbstentzündungstemperaturen unter variierenden Randbedingungen bei Drücken von 5 bar bis zu 25 bar zu bestimmen. Die während der Versuche untersuchten Brennstoffe sind die gasförmigen Alternativkraftstoff-

komponenten Dimethyl Ether (DME) und Propan und die flüssigen Referenzkraftstoffe und Surrogatkomponenten n-Heptan, n-Decan, and n-Dodecan. Graphische Darstellungen der experimentellen Daten und numerischen Berechnungen, zusammen mit den vorherrschenden Randbedingungen, befinden sich in den jeweiligen Kapiteln, während die individuellen Datenpunkte der Messungen, inklusive ihrer dazugehörigen Standardfehler, zur Referenz in tabellarischer Form im Anhang angeführt sind.

Für die Berechnungen und computergestützten Simulationen dieser Arbeit kam das open source Software Toolkit Cantera zum Einsatz. Während sein Löser, welcher in der Lage ist thermodynamische, chemische und transporttechnische Phänomene zu lösen, um Strömungsprobleme mit chemischen Reaktionen und Flammen zu simulieren, unverändert verwendet wurde, wurden die Basisimplementierung und das Modell der Gegenstromkonfiguration angepasst und signifikant erweitert, um den Anforderungen der Untersuchungen dieser Arbeit gerecht zu werden. Als Resultat entstand ein Python Modul namens "UCSDComLab", welches durch die Implementierung zahlreicher Objekte und Funktionen zur Modellierung, Simulation und Evaluierung der Experimente, die im Zuge dieser Dissertation durchgeführt wurden, eine Schnittstelle zu Cantera bietet, um die Berechnungen und numerischen Prozesse zu erleichtern und zu beschleunigen. Für die Bereitstellung der benötigten physikalischen und reaktionskinetischen Parameter der auftretenden Stoffe, welche zur Simulation der Systeme und Prozesse notwendig sind, wurden verschiedene vollständige, vereinfachte und spezialisierte Versionen des San Diego und des PoliMi Mechanismus eingesetzt.

Contents

List of Symbols and Abbreviations	ix
List of Figures	xiii
List of Tables	xxi
List of Code Listings	xxiii
1 Introduction	1
2 Fundamentals	3
2.1 Combustion of Hydrocarbons	3
2.1.1 Thermodynamics	3
2.1.2 Thermodynamic and Thermochemical Property Data	12
2.1.3 Chemical Kinetics	14
2.2 Thermocouple Measurements	18
2.3 Tested Fuels and Chemicals	20
3 Apparatus	23
3.1 Counterflow Burner	23
3.1.1 Gaseous Configuration	24
3.1.2 Liquid Pool Configuration	25
3.1.3 Strain Rate Formulation	26
3.1.4 Limit Phenomena and Critical Conditions	28
3.2 Atmospheric Counterflow Setup	30
3.2.1 Gas Supply	30
3.2.2 Flow Control	31
3.2.3 Burner Top	32
3.2.4 Burner Bottom	34
3.2.5 Data Acquisition (DAQ)	39
3.2.6 Control Software	40
3.2.7 Flow Calibration	42
4 Combustion at Elevated Pressures	45
4.1 High Pressure Combustion Experimental Facility (HPCEF)	45
4.1.1 Counterflow Burner Assembly	48
4.1.2 Facility Control and Data Acquisition	48
4.1.3 Pressure Chamber	50

4.1.4	Separator	51
4.1.5	Modifications	52
4.2	Nitrogen Supply System	63
4.3	Experimental Procedures	66
4.4	Computational Considerations	68
4.4.1	Chemical Kinetic Mechanisms	70
4.4.2	Simulation Module	72
4.4.3	Modeling and Code Development	74
5	Investigations, Results, and Discussion	79
5.1	Atmospheric Pressure	79
5.1.1	Experimental and Computational Investigation on Critical Conditions of Extinction of Laminar, Non-Premixed Dimethyl Ether Flames . .	79
5.1.2	Experimental and Computational Investigation of Extinction and Autoignition of Propane and n-Heptane in Non-Premixed Flows . .	89
5.1.3	Experimental and Computational Investigation of Extinction and Autoignition of Prevaporized Primary Reference Fuels in Non- Premixed Flows	106
5.2	Elevated Pressures	111
5.2.1	Experimental and Computational Investigation of Autoignition of Condensed Primary Reference Fuels in Non-Premixed Flows	111
5.3	Liquid Pool and the Crossover	125
5.3.1	Fuel Level Prior to Ignition	126
5.3.2	Elevated Strain Rates	130
5.3.3	Simulation of the Crossover	131
5.3.4	Helium as an Inert	136
6	Conclusion and Future Work	139
A	Code Listings	143
B	Apparatus	151
C	Experiments	163
D	Experimental Data	167
	Bibliography	173

List of Symbols and Abbreviations

Latin Symbols

a	coefficient (polynomial)	1
a_i	strain rate	1/s
a_{ij}	number of atoms	1
A	area	m ²
A	frequency factor (Arrhenius)	variable
c_p	isobaric heat capacity	kJ/(mol K), J/(kg K)
C	concentration	mol/m ³ , kg/m ³
D	diameter	m
D_i	diffusion coefficient	m ² /s
E_k	activation energy	kJ/mol
g	molar Gibbs free energy	kJ/mol
G	Gibbs free energy	kJ
ΔG	change of Gibbs free energy	kJ/mol
h	molar enthalpy	kJ/mol
H	enthalpy	kJ
h_L	latent heat of vaporization	J/kg
ΔH_r	enthalpy of reaction	kJ/mol
ΔH_f	enthalpy of formation	kJ/mol
h_w	heat transfer rate coefficient	W/(m ² K)
j	diffusive mass flux	mol/(s m ²), kg/(s m ²)
k	thermal conductivity	W/(m K)
k_k	reaction rate constant	variable
K_C	equilibrium constant (constant concentration)	variable
K_P	equilibrium constant (constant pressure)	1
L	separation distance	mm
L_{ch}	characteristic length	m
m	mass	kg
\dot{m}	mass flow rate	kg/s, kg/(s m ²)
M	chemical symbol	text
n	number of moles	mol
n	temperature exponent (Arrhenius)	1
p, P	pressure	Pa, bar
p_i	partial pressure	Pa, bar

Latin Symbols (continued)

q	exponent (polynomial)	1
Q	heat	kJ/mol, J/kg
r	radius, radial component	m
r_k	specific reaction rate	mol/(s m ³), mol/(s m ²), mol/(s kg)
R_i	rate of change of species amount	mol/(s m ³), mol/(s m ²), mol/(s kg)
s	molar entropy	kJ/(mol K)
S	entropy	kJ/K
t	time	s
T	temperature	K, °C
u	molar internal energy	kJ/mol
u, v, w	velocity (components)	m/s
U	internal energy	kJ
V	volume	m ³
V_i	velocity	m/s
W	molecular weight	g/mol
x, y, z	spatial coordinates	m
X	mole fraction	1
Y	mass fraction	1
Z	mixture fraction	1
Z_j	local mass fraction	1

Greek Symbols

α	heat transfer rate coefficient	W/(m ² K)
β	volumetric thermal expansion coefficient	1/K
ε	emissivity	1
λ	thermal conductivity	W/(m K)
Λ	pressure eigenvalue	N/m ⁴
μ	dynamic viscosity	N s/m ²
ν	stoichiometric coefficient/ratio	1
ρ	density	kg/m ³
ϕ	equivalence ratio	1
$\dot{\omega}$	molar production rate	mol/(s m ³)
Ω	coupling function	1

Subscripts and Superscripts

'	reactant
"	product
°	standard state
0	initial, at boundary
1	fuel stream/side boundary
2	oxidizer stream/side boundary
Air	air
b	mixture (burned)
B	boiling point
Cur	curtain
f	forward, flow
F	fuel
g	gas, gaseous
He	helium
In	inert
i	species, stream, index
j	element, atom
k	reaction
l	liquid
N ₂	nitrogen
m	mean
O ₂	oxygen
Ox	oxidizer
r	reverse, reaction
ref	reference
st	stoichiometric
Sur	surroundings
tc	thermocouple
u	mixture (unburned)

Constants

g	constant of gravity	9.806 65 m/s ²
R	universal gas constant	8.314 459 8 J/(mol K)
σ	Stefan-Boltzmann constant	5.670 367 $\times 10^{-8}$ W/(m ² K ⁴)

Characteristic Numbers

Da	Damköhler (first)	$\frac{r_k L_{ch}}{V_i C_0}, \frac{t_f}{t_r}$	$\frac{\text{reaction rate}}{\text{flow rate}}, \frac{\text{flow time}}{\text{chemical time}}$
Fr	Froude	$\frac{V_i^2}{g L_{ch}}$	$\frac{\text{inertia force}}{\text{gravity force}}$
Gr	Grashof	$\frac{\rho^2 g L_{ch}^3 \beta \Delta T}{\mu^2}$	$\frac{(\text{inertia force})(\text{buoyant force})}{(\text{viscous force})^2}$
Le	Lewis	$\frac{\lambda}{\rho c_p D_i}$	$\frac{\text{thermal diffusivity}}{\text{mass diffusivity}}$
Nu	Nusselt (heat transfer)	$\frac{\alpha L_{ch}}{\lambda}$	$\frac{\text{heat transfer}}{\text{heat conductivity}}$
Pr	Prandtl (heat transfer)	$\frac{\mu c_p}{\lambda}$	$\frac{\text{momentum diffusivity}}{\text{thermal diffusivity}}$
Re	Reynolds	$\frac{\rho V_i L_{ch}}{\mu}$	$\frac{\text{inertia force}}{\text{viscous force}}$
Ri	Richardson	$\frac{g L_{ch} \Delta \rho}{\rho V_i^2}$	$\frac{\text{buoyant force}}{\text{turbulent force}}$

Abbreviations

AI	autoignition (experiment)
CAD	computer aided design
DAQ	data acquisition
DME	dimethyl ether
EX	extinction (experiment)
GN2	gaseous nitrogen
HPCEF	High Pressure Combustion Experimental Facility
LN2	liquid nitrogen
LPG	liquefied petroleum gas
P&ID	pipng and instrumentation diagram
PAH	polycyclic aromatic hydrocarbon
PRF	primary reference fuel
SDS	safety data sheet
SE	standard error
SOP	standard operating procedure
STP	standard temperature pressure
VI	Virtual Instrument

List of Figures

2.1	Progression of an exothermic chemical reaction.	11
3.1	Gaseous counterflow burner configuration.	25
3.2	Liquid pool counterflow burner configuration.	26
3.3	S curve of reaction temperature over inverse of the characteristic flow time showing combustion limits, and critical conditions of autoignition and flame extinction.	29
3.4	Atmospheric counterflow setup in its gaseous fuel configuration for determining autoignition temperatures.	31
3.5	Rendering and section view of the counterflow burner for determining autoignition temperatures of gaseous and prevaporized fuels.	33
3.6	Rendering and section view of the counterflow burner for determining extinction strain rates of gaseous and prevaporized fuels.	35
3.7	Atmospheric counterflow setup in its gaseous configuration for determining autoignition temperatures of prevaporized fuels.	36
3.8	Rendering and section view of the counterflow burner for determining autoignition temperatures of liquid fuels.	38
3.9	Atmospheric counterflow setup in its liquid pool configuration for determining autoignition temperatures of condensed fuels.	39
3.10	The main VI's user interface used to control the atmospheric counterflow setup in its gaseous configuration during an ongoing experiment, recording a typical autoignition event of a prevaporized fuel in LabVIEW.	41
3.11	The main VI's user interface used to configure the virtual representation of the atmospheric counterflow setup in LabVIEW where each port represents a mass flow controller in the physical installation.	43
3.12	VI used to calibrate each mass flow controller by comparing the setpoint to the actual flow rate measured by a calibrated drum type gas meter, and adjusting the controller's maximum flow rate.	43
4.1	High Pressure Combustion Experimental Facility at UC San Diego's Combustion Laboratory.	46
4.2	Rendering and section view of the counterflow burner used in the High Pressure Combustion Experimental Facility for determining autoignition temperatures of liquid fuels at elevated pressures.	47
4.3	Screenshots of the HPCEF's two workstation screens during an ongoing autoignition experiment showing the main VI (top) and the received camera feed to monitor the reaction zone and liquid level in the fuel cup (bottom).	49

4.4	Flow control stand with the high pressure set of mass flow controllers in parallel on top of the low pressure set in its idle state.	53
4.5	Pressure chamber hull showing one viewport covered up with a round stainless steel plate and another one with a sight glass installed.	55
4.6	HPCEF's separator removed from the counterflow burner assembly before modifications and ultrasonic level sensors were implemented.	56
4.7	Pressure chamber's top plate bearing a pressure relief valve, burst disc assembly, ball valve for venting, pressure gauge and eyes for connecting to the electric hoist.	58
4.8	Low and high back pressure valves together with their controllers and online sensors in the HPCEF's exhaust and venting system set for operation at high pressure.	59
4.9	Calibrated pressure signal in blue and setpoint in red over time demonstrating the stability of the pressure in the chamber even at high flow rates.	61
4.10	The system's responses to setpoint step changes and impulses with the final PID tuning settings for the new back pressure valve at high flow rates.	61
4.11	Simplified piping and instrumentation diagram of the newly designed nitrogen supply system for the HPCEF.	65
4.12	Two different stills each of the reaction zone during an experiment at 22 bar with the flush at 100% (top) and 90% (bottom) showing the relevant areas where reactant gas is noticeably breaking away and streaming into the chamber instead of the suction gap.	67
5.1	Counterflow burner in gaseous configuration (left) and stabilized, non-premixed dimethyl ether flame (right) during an experiment to determine the extinction strain rate.	81
5.2	Experimental data of the measured strain rate of extinction of a non-premixed DME flame at atmospheric pressure and for various stoichiometric mixture fractions maintaining a constant adiabatic flame temperature of 2000 K. (Appendix, Table D.1)	83
5.3	The computational results from Cantera used in conjunction with the UCSDComLab-Module and the San Diego Mechanism compared against the experimental data obtained through measurements on the real physical device. (Appendix, Table D.1)	85
5.4	Comparing computational results from Cantera used in conjunction with the UCSDComLab-Module and the San Diego Mechanism for the same set of boundary conditions, but different refinement criteria settings and resulting final solution grids.	86

5.5	Computationally generated temperature profiles of the reaction zone inside the counterflow burner at $Z_{st} = 0.7$ for tight (top) and loose (bottom) refinement criteria, indicating the position of the DME flame where the maximum is.	87
5.6	Computationally generated temperature profiles of the reaction zone inside the counterflow burner at $Z_{st} = 0.4$ for tight (top) and loose (bottom) refinement criteria, indicating the position of the DME flame where the maximum is.	87
5.7	Counterflow burner in gaseous configuration (left) and stabilized, non-premixed propane flame (right) during an experiment to determine the extinction strain rate.	92
5.8	Counterflow burner in gaseous configuration with autoignition top (left) and non-premixed propane flame (right) established after reaching autoignition temperature.	92
5.9	Experimental data obtained through measurements plotted with standard errors and compared against computational results from Cantera used in conjunction with the UCSDComLab-Module and different mechanisms. (Appendix, Table D.2)	94
5.10	Experimental data from measurements plotted with standard errors and compared against computational results with various mechanisms. The fuel mass fraction is varied while the oxygen mass fraction is kept constant. (Appendix, Table D.3)	95
5.11	Experimental data from measurements plotted with standard errors and compared against computational results with various mechanisms. The oxygen mass fraction is varied while the fuel mass fraction is kept constant at 0.21. (Appendix, Table D.4)	96
5.12	Experimental data from measurements plotted with standard errors and compared against computational results with various mechanisms. The oxygen mass fraction is varied while the fuel mass fraction is kept constant at 0.4. (Appendix, Table D.5)	97
5.13	Experimental data from measurements plotted with standard errors and compared against computational results with various mechanisms. The oxygen mass fraction is varied while the fuel mass fraction is kept constant at 0.6. (Appendix, Table D.6)	97
5.14	Summary of the experimental and computational results from the autoignition experiments with propane for different fuel mass fractions while varying the oxygen mass fraction. (Appendix, Tables D.4, D.5, and D.6)	98

5.15	Experimental setup employing the counterflow burner in its gaseous configuration for determining autoignition temperatures of prevaporized fuels. . .	99
5.16	High-speed camera set up to observe flame events during an experiment. .	100
5.17	Extinction event recorded with the high-speed camera. The fuel is prevaporized n-heptane at 533 K.	101
5.18	Autoignition event recorded with the high-speed camera. The fuel is prevaporized n-heptane at 533 K.	101
5.19	Experimental data obtained through measurements plotted with standard errors and computational results generated with Cantera using the UCSDComLab-Module at stream temperatures of $T_1 = 533$ K and $T_2 = 298.15$ K. (Appendix, Table D.7)	102
5.20	Experimental data obtained through measurements plotted with standard errors and computational results generated with Cantera using the UCSDComLab-Module at a fuel stream temperature of $T_1 = 533$ K and a strain rate of $a_2 = 550$ 1/s. (Appendix, Table D.8)	104
5.21	Experimental data obtained through measurements plotted with standard errors and computational results generated with Cantera using the UCSDComLab-Module at a fuel stream temperature of $T_1 = 533$ K and a strain rate of $a_2 = 550$ 1/s. (Appendix, Table D.9)	104
5.22	Computational results generated with Cantera using the UCSDComLab-Module showing a noticeable discontinuity at $Y_F = 0.4$ when utilizing the San Diego Heptane Mechanism. The data points mark individual numerical results and the lines represent second order polynomial curve fits of the respective points.	105
5.23	Experimental data obtained through measurements plotted with standard errors and computational results generated with Cantera using the UCSDComLab-Module at stream temperatures of $T_1 = 533$ K and $T_2 = 298.15$ K for various primary reference fuels. The oxygen mass fraction was 0.23. (Appendix, Tables D.7, D.10, and D.13)	108
5.24	Experimental data obtained through measurements plotted with standard errors and computational results generated with Cantera using the UCSDComLab-Module at a fuel stream temperature of $T_1 = 533$ K and a strain rate of $a_2 = 550$ 1/s for various primary reference fuels. The oxygen mass fraction was 0.23. (Appendix, Tables D.8, D.11, and D.14)	109

5.25	Experimental data obtained through measurements plotted with standard errors and computational results generated with Cantera using the UCSDComLab-Module at a fuel stream temperature of $T_1 = 533$ K and a strain rate of $a_2 = 550$ 1/s for various primary reference fuels. The fuel mass fraction was 0.4. (Appendix, Tables D.9, D.12, and D.15)	109
5.26	Screenshots of high-speed recordings from the HPCEF showing n-heptane flames at 5 bar (top) and 11 bar (bottom).	114
5.27	Computational results for n-heptane, n-decane, and n-dodecane at elevated pressures generated with Cantera in conjunction with various versions of the PoliMi Mechanism and under identical boundary conditions.	117
5.28	Computational results for n-heptane, n-decane, and n-dodecane at elevated pressures presented in Figure 5.27, but curve fitted with second order polynomials.	117
5.29	Experimental data obtained through measurements plotted with standard errors and computational results for n-heptane at a strain rate of 150 1/s and an oxygen mass fraction of 0.15. (Appendix, Tables D.16 and D.17) . .	118
5.30	Experimental data obtained through measurements plotted with standard errors and computational results for n-decane at a strain rate of 150 1/s and an oxygen mass fraction of 0.15. (Appendix, Tables D.20 and D.21)	121
5.31	Experimental data obtained through measurements plotted with standard errors and computational results for n-dodecane at a strain rate of 150 1/s and an oxygen mass fraction of 0.15. (Appendix, Tables D.24 and D.25) . .	121
5.32	Experimental and computational results for n-heptane, n-decane, and n-dodecane at a strain rate of 150 1/s and an oxygen mass fraction of 0.15 up to 13 bar. (Appendix, Tables D.16, D.20, and D.24)	123
5.33	Experimental and computational results for n-heptane, n-decane, and n-dodecane at a strain rate of 150 1/s and an oxygen mass fraction of 0.15 up to 25 bar. (Appendix, Tables D.16, D.17, D.20, D.21, D.24, and D.25) .	124
5.34	Experimental setup employing the counterflow burner in its liquid pool configuration for determining autoignition temperatures of condensed fuels.	125
5.35	Counterflow burner in liquid pool configuration with autoignition top (left) and the reaction zone of the assembly showing the cup for condensed fuels and the needle to facilitate the monitoring of the liquid pool level (right). .	126
5.36	Flames after autoignition above the liquid pool surface of n-dodecane at regular/full (top), high/overflowing (middle), and low (bottom) cup levels.	127

5.37	Autoignition events of n-dodecane at regular/full (top), high/overflowing (middle), and low (bottom) cup levels leading to the respective flames shown in Figure 5.36.	127
5.38	Measured autoignition temperatures including standard error bars for n-decane and n-dodecane at various liquid levels in the fuel cup immediately prior to ignition.	128
5.39	Autoignition temperatures obtained through measurements plotted with standard errors and computational results generated with Cantera using the UCSComLab-Module for condensed n-heptane and n-decane at atmospheric pressure and an oxygen mass fraction of 0.23 in the oxidizer. (Appendix, Tables D.26 and D.27)	130
5.40	Computational results from Cantera with the UCSComLab-Module implementing an experimental and purely empirical liquid pool model (dynamic LP) compared to simulations based on the classic model (static LP).	133
5.41	Experimentally measured autoignition temperatures for condensed n-heptane and n-decane at elevated pressures up to 13 bar and various strain rates. The oxygen mass fraction was 0.15. (Appendix, Tables D.16, D.18, D.19, D.20, D.22, and D.23)	134
5.42	Computational predictions for autoignition temperatures of condensed n-heptane and n-decane at elevated pressures up to 18 bar, an oxygen mass fraction of 0.15, and various strain rates generated with Cantera, the UCSComLab-Module with the experimental liquid pool model implementation, and reduced versions of the PoliMi Mechanism.	135
5.43	Flames of n-decane after autoignition with nitrogen (top) and helium (bottom) as an inert in the oxidizer stream at slightly different boundary conditions.	136
5.44	Autoignition temperature measurements including standard errors of condensed n-decane at atmospheric pressure with respectively nitrogen and helium as an inert in the oxidizer. The strain rate was 450 1/s and the oxygen mole fraction 0.21.	137
5.45	Flames of n-decane after autoignition with helium as an inert in the oxidizer stream at strain rates of 450 1/s (top) and 1400 1/s (bottom).	138
B.1	High Pressure Combustion Experimental Facility - Workstation.	151
B.2	High Pressure Combustion Experimental Facility - Apparatus.	151
B.3	High Pressure Combustion Experimental Facility - Workstation during experimentation with high-speed camera recording.	152
B.4	High Pressure Combustion Experimental Facility - Chamber closed for experimentation (left) and opened for maintenance (right).	152

B.5	High Pressure Combustion Experimental Facility - View of the bottom plate during pressure testing, with droplets of water forming on fittings showing leakage.	154
B.6	High Pressure Combustion Experimental Facility - Residual water on o-ring sealed surface after pressure testing with water.	154
B.7	High Pressure Combustion Experimental Facility - Water from the chamber pushed into workstation units through connected wiring during pressure testing.	155
B.8	High Pressure Combustion Experimental Facility - Water leaking from electrical wiring during pressure testing due to inadequate fittings on the bottom plate.	155
B.9	Nitrogen Supply System - Cylinder carts carrying a manifold of pressurized gas cylinders providing gaseous nitrogen for experiments and pressurization to the HPCEF.	158
B.10	Nitrogen Supply System - Cylinder carts carrying a manifold of pressurized gas cylinders providing various gases to the HPCEF.	158
B.11	Nitrogen Supply System - Portable tank on stand (right), vaporizer and control station assembly (center), and high pressure cylinder pack (left). . .	159
B.12	Nitrogen Supply System - Back view of the system showing the cryogenic pump together with its actuating motor (left) and moving the tank for refilling (right).	159
B.13	Atmospheric Counterflow Setup.	160
B.14	Atmospheric Counterflow Setup - Workstation and gas flow control.	160
B.15	Atmospheric Counterflow Setup - Mass flow controllers, MFC controller units, and gas flow control switch and plug boards.	161
B.16	Atmospheric Counterflow Setup - Gas flow control quick connect board. . .	161
C.1	View of the fuel duct during an ongoing autoignition experiment with inserted thermocouple and the oxidizer stream at around 1100 K.	163
C.2	View of the oxidizer duct during an ongoing autoignition experiment with inserted thermocouple and the oxidizer stream at around 1100 K.	163
C.3	Established n-heptane flame after the autoignition event at 5 bar.	164
C.4	N-heptane flame at 22 bar before (upper left) and after autoignition showing the preceding curtain ignition typically occurring at elevated pressures. . .	164
C.5	Established n-heptane flame after the autoignition event at 13 bar.	165
C.6	Screenshots of a high-speed recording at 13 bar showing the autoignition event which led to the flame depicted in Figure C.5.	165
C.7	Autoignition event of condensed n-heptane at atmospheric pressure.	166

List of Tables

2.1	Liquid fuel components and chemicals used in the experiments, and their relevant physical and chemical property data [6]	20
2.2	Gaseous fuel components and chemicals used in the experiments, and their relevant physical and chemical property data [116]	21
2.3	Gaseous oxidizer and inerts used in the experiments, and their relevant physical and chemical property data [116]	21
4.1	Chemical kinetic mechanisms used with Cantera for computational investigations	70
4.2	Chemical kinetic mechanisms used with Cantera for computational investigations (continued)	71
5.1	Fuel (Y_1) and oxidizer (Y_2) mass fractions at the boundary for various values of stoichiometric mixture fraction (Z_{st}) at constant adiabatic flame temperature $T_{st} = 2000$ K	83
D.1	Mean values and standard errors (SE) plotted in Figures 5.2 and 5.3	167
D.2	Mean values and standard errors (SE) plotted in Figure 5.9	167
D.3	Mean values and standard errors (SE) plotted in Figure 5.10	167
D.4	Mean values and standard errors (SE) plotted in Figure 5.11 ($Y_F = 0.21$)	167
D.5	Mean values and standard errors (SE) plotted in Figure 5.12 ($Y_F = 0.4$)	168
D.6	Mean values and standard errors (SE) plotted in Figure 5.13 ($Y_F = 0.6$)	168
D.7	Mean values and standard errors (SE) plotted in Figures 5.19 and 5.23	168
D.8	Mean values and standard errors (SE) plotted in Figures 5.20 and 5.24	168
D.9	Mean values and standard errors (SE) plotted in Figures 5.21 and 5.25	168
D.10	Mean values and standard errors (SE) plotted in Figure 5.23	169
D.11	Mean values and standard errors (SE) plotted in Figure 5.24	169
D.12	Mean values and standard errors (SE) plotted in Figure 5.25	169
D.13	Mean values and standard errors (SE) plotted in Figure 5.23	169
D.14	Mean values and standard errors (SE) plotted in Figure 5.24	170
D.15	Mean values and standard errors (SE) plotted in Figure 5.25	170
D.16	Mean values and standard errors (SE) plotted in Figures 5.29, 5.32, 5.33, and 5.41 ($a_2 = 150$ 1/s)	170
D.17	Mean values and standard errors (SE) plotted in Figures 5.29 and 5.33 ($a_2 = 150$ 1/s, $P > 13$ bar)	170
D.18	Mean values and standard errors (SE) plotted in Figure 5.41 ($a_2 = 130$ 1/s)	170
D.19	Mean values and standard errors (SE) plotted in Figure 5.41 ($a_2 = 100$ 1/s)	171

D.20 Mean values and standard errors (SE) plotted in Figures 5.30, 5.32, 5.33, and 5.41 ($a_2 = 150$ 1/s)	171
D.21 Mean values and standard errors (SE) plotted in Figures 5.30 and 5.33 ($a_2 = 150$ 1/s, $P > 13$ bar)	171
D.22 Mean values and standard errors (SE) plotted in Figure 5.41 ($a_2 = 130$ 1/s)	171
D.23 Mean values and standard errors (SE) plotted in Figure 5.41 ($a_2 = 100$ 1/s)	171
D.24 Mean values and standard errors (SE) plotted in Figures 5.31, 5.32, and 5.33 ($a_2 = 150$ 1/s)	172
D.25 Mean values and standard errors (SE) plotted in Figures 5.31 and 5.33 ($a_2 = 150$ 1/s, $P > 13$ bar)	172
D.26 Mean values and standard errors (SE) plotted in Figure 5.39	172
D.27 Mean values and standard errors (SE) plotted in Figure 5.39	172

List of Code Listings

4.1	Structure of the UCSDComLab-Module - ucsdcomlab.py (excerpt)	73
4.2	Code segment to switch infinitely fast chemistry on and off according to the type of experiment while setting the initial guess before simulation - ucsdcomlab.py (excerpt)	75
4.3	Calculation of the relevant parameters for the gaseous inlets of the counterflow burner model - ucsdcomlab.py (excerpt)	76
4.4	Calculation of the relevant parameters for the liquid pool configuration of the counterflow burner model - ucsdcomlab.py (excerpt)	78
A.1	Calculations from the counterflow setup control software's main VI to compute all relevant fluid flow parameters implemented as a function in MATLAB - calcFlows.m	143
A.2	Working example of a Python script to simulate an autoignition experiment utilizing the module "UCSDComLab" - ucsdcomlab.exp.py	148
A.3	Working example of a Python script to simulate an autoignition experiment utilizing the module "UCSDComLab" by means of different methods - ucsdcomlab.expai.py	148
A.4	Working example of a Python script to simulate an autoignition experiment in liquid pool configuration utilizing the module "UCSDComLab" - ucsdcomlab.explp.py	150
B.1	Comparison of high pressure 2-way solenoid valves for automatically draining the residual liquid components from the HPCEF - SeparatorDrainValves.m	153
B.2	Calculations for estimating the minimum nitrogen demand and comparison of the approximated time for experimentation on the HPCEF using gaseous and liquid nitrogen supply systems in Mathcad - N2 Supply.xmcd	156

1 Introduction

Combustion and harnessing the power, heat, and light of fire was arguably one of the first technological endeavours of mankind to set out for. Over millennia, well before any analytical approach and the advent of modern science, its practical applications were ranging from basic survival needs over religious and ceremonial purposes to, like many other technologies throughout history, the other end of the spectrum, warfare. Gradually, the curiosity, sparked by combustion's shining physical manifestation of fluidlike structures in form of flames and their seemingly magical attributes, developed into a vastly complex and interdisciplinary science with profound applications and implications for today's society and economy. Combustion, being the primary process in power generation and transportation today, is still not only fascinating to users, scientists, and engineers, but also shapes the environment and our planet's future. Even though, grand efforts are undertaken to substitute this exothermic chemical reaction in certain areas to mitigate its negative effects, combustion will continue to remain in the toolbox of mankind for the foreseeable future, as it constitutes one of its most important, versatile, and powerful discoveries that enabled and shaped the technological development of our civilization like no other.

From a scientific point of view, combustion is a highly complex and interdisciplinary field encompassing thermodynamics, chemical kinetics, and fluid mechanics. These fundamental areas are tightly interwoven and need to be understood in depth, not just individually, but also when interacting. Adding the layer of engineering and application to the discipline, to make technological use of the process, further expands its complexity and explains why combustion still offers so many different opportunities for research. Even though it is the oldest technology of mankind and its application is spread out across history and not just our planet, but even beyond its atmospheric border, the fundamental processes of combustion are still not fully understood. In engineering and science, the understanding

of fundamental principles is just as good as the predictions they can make, based on the knowledge at that time. Even today, constantly new observations in relatively simple setups and well established experiments are made that require adaptation of the accepted body of knowledge of combustion science to account for the newly observed phenomena.

One aspect of that body of knowledge is combustion at elevated pressures. Most modern technologically applied combustion processes, particularly in transportation, happen in a mildly to severely pressurized environment, mostly to increase efficiency. While there are numerous experimental studies under elevated pressures in basic flow reactors and batch operated devices like shock tubes, investigations implying the counterflow configuration at pressures above atmosphere are rare. That scarcity is the motivation and driving force behind this dissertation which aims to expand the experimental and computational body of knowledge of combustion science at elevated pressures. Preliminary and supplementary studies at atmospheric pressure, as well as measurement and numerical results for the gaseous alternative fuel components dimethyl ether (DME) and propane, and the primary reference fuel (PRF) and surrogate components n-heptane, n-decane, and n-dodecane complement this thesis. The experimental device used for the investigations is the counterflow burner which, aside from perfectly mirroring the complexity of this scientific field, is capable of capturing the interaction between combustion's major areas: thermodynamics, chemical kinetics, and fluid mechanics.

2 Fundamentals

2.1 Combustion of Hydrocarbons

Combustion is a special form of a highly complex exothermic chemical reaction which involves a fuel in its solid, liquid, or gaseous state providing the necessary hydrocarbons, and a gaseous oxidizer serving as a source of oxygen. Regardless of the physical state of the reactants, eventually the combustion reaction itself takes place in a gaseous phase resulting in various products, most prominently carbon dioxide and water, heat, and also light. Like other chemical reactions, the overall course and outcome of the conversion process is not only governed by its chemical aspects, but also by physical parameters like temperature and residence time which lead to numerous ways of influencing the process path. Considering the practical applications and the mechanical engineering involved to make technological use of this conversion process, combustion combines advanced principles from thermodynamics, chemical kinetics, and fluid mechanics into a multidisciplinary and highly interrelated field.

The influence of these three major scientific fields has led to varying nomenclature and use of symbols, and sometimes even differing definitions throughout the literature. For the sake of clarification and consistency, the most important fundamental definitions for this thesis are given in the following chapters.

2.1.1 Thermodynamics

The nomenclature and indices herein follow [131] and [77] for the most part while considerable differences are adapted for consistency. The upcoming definitions in the following paragraphs are found and further explained in greater detail in [131], [24], [45], and [77].

Mole and Mass Fractions

Looking at combustion phenomena as a continuous conversion process of multiple components, the use of mole and mass fractions proved to be a convenient way of describing concentrations throughout a system. The mole fraction X_i and the mass fraction Y_i of species i are defined as

$$X_i = \frac{n_i}{n} \quad i = 1, 2, \dots, N_{\text{species}} \quad (2.1)$$

$$Y_i = \frac{m_i}{m} \quad i = 1, 2, \dots, N_{\text{species}} \quad (2.2)$$

$$n = \sum_{i=1}^N n_i \quad [\text{mol}] \quad (2.3)$$

$$m = \sum_{i=1}^N m_i \quad [\text{kg}] \quad (2.4)$$

with n_i being the number of moles of species i , n the total number of moles, m_i the mass of all molecules of species i and m the total mass of the mixture. The mean molecular weight W and W_i , the molecular weight of species i , given by

$$W = \frac{m}{n} \quad (2.5)$$

$$W_i = \frac{m_i}{n_i} \quad (2.6)$$

respectively, allow for the conversion between mole and mass fractions of the same species.

$$Y_i = \frac{W_i}{W} X_i \quad (2.7)$$

Due to the conservation of elements throughout the combustion process it can be particularly helpful to further define Z_j , the local mass fraction of an element j , as

$$Z_j = \frac{m_j}{m} \quad (2.8)$$

where m_j , the mass of all atoms of element j in the system, together with a_{ij} , the number of atoms of element j in one molecule of species i and W_j , the molecular weight of element j , is

$$m_j = \sum_{i=1}^N \frac{a_{ij}W_j}{W_i}m_i \quad j = 1, 2, \dots, N_{elements}. \quad (2.9)$$

Mixture Fraction

Mole and mass fractions are practical for describing concentrations in homogeneous systems of multiple components. For combustion processes, involving at least two components, fuel and oxidizer, and typically a third species like nitrogen as an inert, a variable that can capture the concentration distribution in a system with a single representation is more effective than describing its state with multiple fractions throughout the system. Therefore, the mixture fraction Z is introduced. It is a very powerful tool, frequently used for non-premixed combustion, and can be defined in multiple ways.

In this thesis, all systems and experiments consist of two non-premixed streams, also called sides, containing a certain fraction of either fuel or oxidizer at its boundaries. The stream containing the fuel (F) is designated by the subscript 1, and the stream carrying the oxidizer (Ox) is designated by the subscript 2. Both streams are separately mixed with inerts (In), forming individual mass fractions of fuel (Y_F) and oxidizer (Y_{Ox}) respectively in their initial state at the boundary (subscript 0), the fuel stream not containing any oxidizer and the oxidizer stream not containing any fuel before entering the system.

Introducing the fuel-oxidizer coupling function Ω , the mixture fraction for a single-step reaction can be defined as [24,131]

$$Z = \frac{\Omega - \Omega_{Ox,0}}{\Omega_{F,0} - \Omega_{Ox,0}} \quad (2.10)$$

$$0 \leq Z \leq 1. \quad (2.11)$$

For general chemistry with complex multi-step mechanisms it is more practical to use a species elements based approach. For that, Ω can be replaced by Z_j , the local mass fraction of element j , to give

$$Z = \frac{Z_j - Z_{j,Ox,0}}{Z_{j,F,0} - Z_{j,Ox,0}}. \quad (2.12)$$

Together with this relation, providing the mass fractions of the fuel and oxidizer streams at the boundary, $Y_{F,0} = Y_1$ and $Y_{Ox,0} = Y_2$, and the local mass fraction Z , the entire species element distribution of the system can be described because of the relations between Equations (2.8), (2.9), and (2.2).

$$Z_j = \frac{m_j}{m} = \sum_{i=1}^N \frac{a_{ij} W_j}{W_i} Y_i \quad (2.13)$$

Note that defining the mixture fraction in this manner results in Z reaching unity in the fuel stream and a value of 0 in the oxidizer stream. A fact that can also be rewritten in terms of mass fractions of the unburned mixture inside the system, designated by the subscript u , before any chemical reactions take place.

$$Y_{F,u} = Y_1 Z \quad (2.14)$$

$$Y_{Ox,u} = Y_2 (1 - Z) \quad (2.15)$$

Stoichiometric Mixture Fraction

In general, a chemical reaction equation can be written in the form [77]

$$\sum_{i=1}^N \nu_i' M_i = \sum_{i=1}^N \nu_i'' M_i \quad (2.16)$$

where ν_i' denotes the stoichiometric coefficient of the reactant species i , ν_i'' the stoichiometric coefficient of the product species i , and where M_i represents the chemical symbol of species i . The overall net stoichiometric coefficient ν_i is calculated by

$$\nu_i = \nu_i'' - \nu_i' \quad i = 1, 2, \dots, N_{\text{species}}. \quad (2.17)$$

The reaction equation defines the stoichiometry, which describes the molar conversion relations between the participating species. According to the stoichiometry, the conversion of n_1 moles of species 1 to n_i moles of any other species i are in relation to each other through their respective stoichiometric coefficients. In differential form this can be written as

$$\frac{dn_i}{\nu_i} = \frac{dn_1}{\nu_1} \quad i = 2, 3, \dots, N_{\text{species}}. \quad (2.18)$$

Together with Equation (2.6), basing the equation on the total mass by dividing with m , and using Equation (2.2), a relation between the mass fractions for species 1 and any other species i in the reaction can be derived

$$\frac{dm_i}{\nu_i W_i} = \frac{dm_1}{\nu_1 W_1} \quad i = 2, 3, \dots, N_{\text{species}} \quad (2.19)$$

$$\frac{dY_i}{\nu_i W_i} = \frac{dY_1}{\nu_1 W_1} \quad i = 2, 3, \dots, N_{\text{species}}. \quad (2.20)$$

Equation (2.20) can now be integrated between the unburned mixture and a later state for the fuel F and the oxidizer Ox to result in a coupling function for the mass fractions of the fuel and the oxidizer

$$\frac{Y_{Ox} - Y_{Ox,u}}{\nu'_{Ox} W_{Ox}} = \frac{Y_F - Y_{F,u}}{\nu'_F W_F}. \quad (2.21)$$

Stoichiometry dictates that, for a fuel-oxidizer mixture to be stoichiometric (subscript st), the ratio of moles of unburned fuel and oxidizer in a mixture equals the ratio of their respective stoichiometric coefficients. An equivalent statement holds true for the ratio of the mass fractions of the unburned fuel and oxidizer, and leads to the definition of the stoichiometric mass ratio ν

$$\left. \frac{n_{Ox,u}}{n_{F,u}} \right|_{st} = \frac{\nu'_{Ox}}{\nu'_F} \quad (2.22)$$

$$\left. \frac{Y_{Ox,u}}{Y_{F,u}} \right|_{st} = \frac{\nu'_{Ox} W_{Ox}}{\nu'_F W_F} = \nu. \quad (2.23)$$

Using this definition of the stoichiometric mass ratio ν in Equation (2.21), the coupling function can be rewritten as

$$\nu Y_F - Y_{Ox} = \nu Y_{F,u} - Y_{Ox,u}. \quad (2.24)$$

In this later form, the two Equations (2.14) and (2.15) can be introduced to replace the mass fractions of unburned mixture in the system. After solving for Z , another definition for the local mass fraction, relating the fuel and oxidizer mass fractions can be derived. In this form, the equation is based on the species rather than the species elements.

$$Z = \frac{\nu Y_F - Y_{Ox} + Y_2}{\nu Y_1 + Y_2} \quad (2.25)$$

According to Equation (2.23), the statement $\nu Y_F = Y_{Ox}$ needs to be true for a stoichiometric mixture. Introducing this condition into the last given equation for the mixture fraction, finally leads to the stoichiometric mixture fraction Z_{st}

$$Z_{st} = \frac{Y_2}{\nu Y_1 + Y_2} \quad (2.26)$$

Combustion processes are not always stoichiometric. Equations (2.25) and (2.26) can be used to determine the mass fraction of leftover or burned mixture (subscript b) either for the fuel or the oxidizer in the system after combustion is complete, depending on which side was completely consumed during the process. If there was more fuel in the system than required for stoichiometric combustion, the mixture is called fuel rich ($Z > Z_{st}$), and if it was less, it is called fuel lean ($Z < Z_{st}$). As soon as one of the reactants is depleted in the system, the combustion process stops and leaves a burned mixture containing unburned fuel or oxidizer.

$$Y_{F,b} = Y_1 \frac{Z - Z_{st}}{1 - Z_{st}} \quad Z \geq Z_{st} \quad (2.27)$$

$$Y_{Ox,b} = Y_2 \left(1 - \frac{Z}{Z_{st}} \right) \quad Z \leq Z_{st} \quad (2.28)$$

Another frequently used form of the mixture fraction is ϕ , the so called equivalence ratio. It is the ratio of the fuel to oxidizer ratios of a given mixture to that of its corresponding stoichiometric mixture. Together with Equations (2.23), (2.14), (2.15), and a rearranged form of (2.26), ϕ can be rewritten in terms of the mixture fraction.

$$\phi = \frac{\frac{Y_{F,u}}{Y_{Ox,u}}}{\frac{Y_{F,u}}{Y_{Ox,u}} \Big|_{st}} = \frac{Z}{1 - Z} \frac{1 - Z_{st}}{Z_{st}} \quad (2.29)$$

Reaction Heat and Activation Energy

Every chemical reaction is a process in which energy stored in the bonds between the atoms of the participating molecules is converted. The conversion process can eventually either release, or consume heat, which can be measured by an outside observer. That net heat difference is called the heat or enthalpy of reaction ΔH_r , and can be calculated for any reaction with the aid of the relation [24]

$$\Delta H_r^\circ = \sum_i^N \nu_i'' \Delta H_{f,i}^\circ - \sum_i^N \nu_i' \Delta H_{f,i}^\circ \quad [\text{kJ/mol}] \quad (2.30)$$

if the heats of formation ΔH_f for each product (superscript $''$) and reactant (superscript $'$) are known. The heat of formation is essentially another reaction heat, derived from the heat released or consumed during formation of a substance from its constituent elements at a certain reference state. The superscript $^\circ$ signifies that the heat of formation was determined at standard state, which most often refers to 298.15 K and atmospheric pressure.

Using Equation (2.30) helps to make predictions about the heat released through chemical reaction if the conversion process eventually takes place. But in order to be able to make estimations about the initiation of the reaction, or to predict if a certain reaction is even able to progress, different principles have to get introduced. According to collision theory, for a chemical reaction to take place, not only do the reacting components have to physically meet, they also have to collide with an energy that is high enough to activate the process. The minimally required energy to start a chemical reaction is called the activation energy E_k , and is visually depicted together with the reaction heat ΔH_r in Figure 2.1 [45]. The curve marks the course of potential energy throughout a chemical reaction where the reactants on the left side of the energy transfer barrier convert to the products on the right hand side. Since the potential energy level of the products is lower than that of the reactants, heat is released during the conversion, and the process is called exothermic. If the level

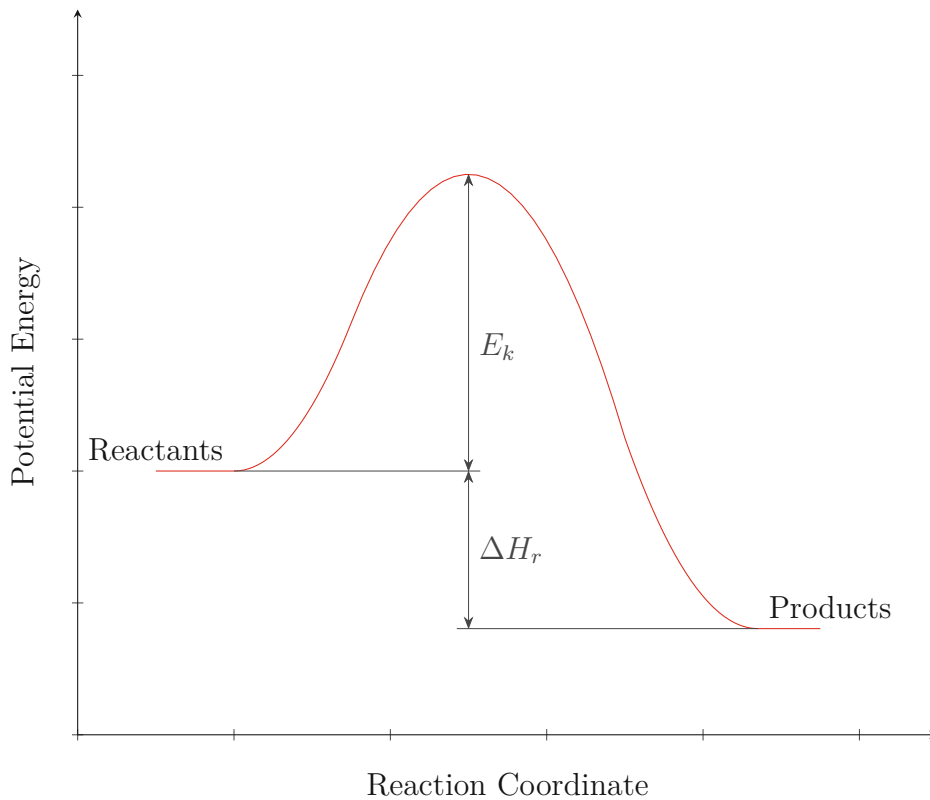


Figure 2.1: Progression of an exothermic chemical reaction.

of the products was higher, it would be called endothermic. Either way, enough energy, namely at least the activation energy E_k , has to be supplied to the process to surpass the intermediate state of maximum potential energy, and convert the reactants to the products.

Thermodynamic Equilibrium and Gibbs free energy

The states before and after the conversion can be described as local minima of potential energy and signify equilibrium states of the process where maximum entropy at constant volume and energy is reached. With the introduction of the Gibbs free energy G [24,131]

$$G = H - TS \quad [\text{kJ}] \quad (2.31)$$

$$H = U + PV \quad [\text{kJ}] \quad (2.32)$$

where U is the internal energy, H the enthalpy of a system of volume V at pressure P , and S its entropy, the equilibrium state at constant temperature and pressure T, P of a chemical system is reached when the Gibbs free energy is not changing anymore.

$$(dG)_{T,P} = 0 \quad (2.33)$$

At that point, the net composition of the reacting system is not changing either, even if multiple forward and reverse reactions are still taking place.

2.1.2 Thermodynamic and Thermochemical Property Data

For numerical calculations involving the dynamic equilibrium of reactions, it is essential to have data for basic thermodynamic and thermochemical properties of the participating species available. The data is available in the literature in tabular form, usually given at temperature intervals where the property at the required temperature can be interpolated [21], the most prominent source being the NIST-JANAF Thermochemical Tables [69]. It can also be directly collected from related databases like the NIST Chemistry WebBook [68] which relies on the same calculations as the JANAF Thermochemical Tables. This approach is only useful if the requirement for data is limited. For computational calculations, it is far more efficient to have a polynomial representation of the required properties available to calculate them as it becomes necessary.

The polynomial representations are parametrizations of the thermodynamic and thermochemical properties, and help in describing their temperature dependence in computational calculations. The thermodynamic properties are either parametrized individually [28,132],

or based on the isobaric heat capacity c_p which is then related to the enthalpy h , and entropy s at the temperature T by [21]

$$h_T^\circ = h_{T_{ref}}^\circ + \int_{T_{ref}}^T \dot{c}_p \, dT \quad [\text{kJ/mol}] \quad (2.34)$$

$$s_T^\circ = s_{T_{ref}}^\circ + \int_{T_{ref}}^T \frac{\dot{c}_p}{T} \, dT \quad [\text{kJ}/(\text{mol K})] \quad (2.35)$$

where T_{ref} denotes the reference temperature, and superscript $^\circ$ the standard state of 1 atm pressure. For thermochemical considerations, $h_{T_{ref}}^\circ$ in Equation (2.34) is commonly replaced by $\Delta H_{f,T_{ref}}^\circ$ to define the absolute enthalpy h_T° . The definition of the Gibbs free energy, Equation (2.31), is also relevant in this context, and can be applied in its molar form to calculate relevant thermodynamic and thermochemical data with the aid of Equations (2.34) and (2.35).

The most frequently used polynomial representations are the NASA Polynomials. They represent the heat capacity, enthalpy, and entropy individually by using the universal gas constant R to result in the following dimensionless forms [28,57].

$$\frac{\dot{c}_p}{R} = \sum_i^N a_i T^{q_i} \quad (2.36)$$

$$\frac{h_T^\circ}{RT} = \frac{a_{N+1}}{T} + \frac{\int \dot{c}_p \, dT}{RT} \quad (2.37)$$

$$\frac{s_T^\circ}{R} = a_{N+2} + \int \frac{\dot{c}_p}{RT} \, dT \quad (2.38)$$

Coefficients for individual substances can be found for different temperature ranges in various databases. To calculate the required properties at a certain temperature T , the following equations can be evaluated after introducing the coefficients for the species and temperature range in question [27]. As shown here, usually seven or nine coefficients are given, known as the NASA 7 Coefficients Polynomial Parametrization or NASA7,

$$\frac{\overset{\circ}{c}_p}{R} = a_1 + a_2T + a_3T^2 + a_4T^3 + a_5T^4 \quad (2.39)$$

$$\frac{h_T^\circ}{RT} = a_1 + \frac{a_2}{2}T + \frac{a_3}{3}T^2 + \frac{a_4}{4}T^3 + \frac{a_5}{5}T^4 + \frac{a_6}{T} \quad (2.40)$$

$$\frac{\overset{\circ}{s}_T}{R} = a_1 \ln T + a_2T + \frac{a_3}{2}T^2 + \frac{a_4}{3}T^3 + \frac{a_5}{4}T^4 + a_7 \quad (2.41)$$

and its new updated version NASA9 utilizing nine coefficients [26,56].

$$\frac{\overset{\circ}{c}_p}{R} = a_1T^{-2} + a_2T^{-1} + a_3 + a_4T + a_5T^2 + a_6T^3 + a_7T^4 \quad (2.42)$$

$$\frac{h_T^\circ}{RT} = -a_1T^{-2} + a_2T^{-1} \ln T + a_3 + a_4\frac{T}{2} + a_5\frac{T^2}{3} + a_6\frac{T^3}{4} + a_7\frac{T^4}{5} + \frac{a_8}{T} \quad (2.43)$$

$$\frac{\overset{\circ}{s}_T}{R} = -a_1\frac{T^{-2}}{2} - a_2T^{-1} + a_3 \ln T + a_4T + a_5\frac{T^2}{2} + a_6\frac{T^3}{3} + a_7\frac{T^4}{4} + a_9 \quad (2.44)$$

2.1.3 Chemical Kinetics

Equation (2.16) shown earlier denotes a general chemical reaction in form of a balance between the reactants on the left side, and the products on the right side. Due to the fact that in a real mixture the conversion process can occur both ways simultaneously, and not only from left to right, chemical reaction equations use arrows pointing in both directions

to signify the establishment of a dynamic equilibrium. An example of a dynamic chemical equilibrium reaction, here called k , can then be written as [45]



The symbols above and below the equilibrium arrows are the forward (k_f , k_k) and reverse (k_r , k_{-k}) rate constants of reaction k , and indicate that the forward and reverse reactions may not progress at the same speed, thus leading to a final, but still dynamic, and asymmetrical equilibrium state.

Reaction Rates

The approximation of infinitely fast chemistry is often used to simplify problems, but in reality different reactions progress at different finite speeds. In combustion, this fact becomes very dominant because of the complexity of reaction systems where a manifold of species and reactions compete with each other. To quantify the progression of the conversion described by a chemical reaction equation the specific reaction rate r_k for any reaction k can be defined as [45]

$$r_k = \frac{dn_i}{dt} \frac{1}{V} \frac{1}{\nu_i} \quad [\text{mol}/(\text{s m}^3)]. \quad (2.46)$$

Here, the specific reaction rate is based on the reaction volume V . In the context of other applications, a definition based on different parameters like reacting surface A or mass of catalyst m might be useful. Further defining R_i , the rate of change of the amount of species i in a fixed volume as

$$R_i = \frac{dC_i}{dt} = \frac{dn_i}{dt} \frac{1}{V} \quad [\text{mol}/(\text{s m}^3)], \quad (2.47)$$

allows for a more general expression of the reaction kinetics in complex systems, where more than one equilibrium reaction is taking place simultaneously, by accounting for all the reactions involving species i .

$$R_i = \sum_k^N \nu_{ik} r_k \quad (2.48)$$

Ultimately, the net specific reaction rate is described as a function of the rate constants, the concentrations of the participating compounds, and their stoichiometric coefficients, and is called the reaction's rate equation or rate law. The relation is usually non trivial, and for complex reactions, has to be determined empirically by assuming an expression for r_k , according to the type of reaction and its order, and then verifying that assumption with measurements of the concentrations in an experiment. For well known reactions, these rate laws can be found in the literature, and are usually a form of power law.

$$r_k = f(k_k, k_{-k}, C_i, \dots) = k_k ([M_i]^{\nu_i} [M_{i+1}]^{\nu_{i+1}} \dots)' - k_{-k} ([M_i]^{\nu_i} [M_{i+1}]^{\nu_{i+1}} \dots)'' \quad (2.49)$$

Reaction Rate Constants

In general, chemical reactions are strongly dependent on temperature. To capture that phenomenon in the system-describing equations, reaction rate constants mirror the dependence in the form of the Arrhenius equation, even if their name suggests that they are constant. For gas-phase chemistry, usually an extended form is used for added flexibility, and to account for the fact that the expression before the exponential term is not a constant either [45,127].

$$k_k = AT^n \exp\left(-\frac{E_k}{RT}\right) \quad (2.50)$$

In this extended form, the coefficient A is a constant, and called the frequency factor. The exponent n is the temperature exponent, E_k the activation energy, and R the universal

gas constant. Note that this description of reaction rate constants makes the previous expressions containing k_k temperature dependent.

Chemical Equilibrium and the Law of Mass Action

As described in Section 2.1.1, for a chemical system to reach its equilibrium state it is necessary for the change of Gibbs free energy to be zero which furthermore implies that its composition reaches a steady state, its so-called equilibrium composition. Applying that concept to Equation (2.49) results in the net reaction rate becoming zero as well, and the concentrations of the species in the system appear constant which leads to the definition of the equilibrium constant K_C [45,127].

$$r_k = 0 = k_k([M_i]^{\nu_i}[M_{i+1}]^{\nu_{i+1}}\dots)' - k_{-k}([M_i]^{\nu_i}[M_{i+1}]^{\nu_{i+1}}\dots)''$$

$$\frac{k_k}{k_{-k}} = \frac{([M_i]^{\nu_i}[M_{i+1}]^{\nu_{i+1}}\dots)''}{([M_i]^{\nu_i}[M_{i+1}]^{\nu_{i+1}}\dots)'} = \frac{\text{constant}}{\text{constant}} = K_C \quad (2.51)$$

Under the assumption of an ideal gas where, other than during the reaction, intermolecular interactions are neglected, the following relation for the change of Gibbs free energy ΔG of a reaction can be derived [24,45]

$$-\Delta G = RT \ln \left(\frac{\{(p_i/p_{ref})^{\nu_i}(p_{i+1}/p_{ref})^{\nu_{i+1}}\dots\}''}{\{(p_i/p_{ref})^{\nu_i}(p_{i+1}/p_{ref})^{\nu_{i+1}}\dots\}'} \right) \quad (2.52)$$

where p_i represents the partial pressure of species i in the mixture, and p_{ref} a reference pressure. If standard state is chosen as the reference, p_{ref} is 1 atm, and the superscript $^\circ$ is used, leading to

$$-\Delta G^\circ = RT \ln \left(\frac{(p_i^{\nu_i} p_{i+1}^{\nu_{i+1}} \dots)''}{(p_i^{\nu_i} p_{i+1}^{\nu_{i+1}} \dots)'} \right). \quad (2.53)$$

The expression in the natural logarithm is used to define K_P , the equilibrium constant at constant pressure. Note that K_P is only dependent on the temperature, and is not a function of total pressure.

$$K_P = \frac{(p_i^{\nu_i} p_{i+1}^{\nu_{i+1}} \cdots)''}{(p_i^{\nu_i} p_{i+1}^{\nu_{i+1}} \cdots)'} \quad (2.54)$$

$$K_P = \exp\left(-\frac{\Delta G^\circ}{RT}\right) \quad (2.55)$$

In more general terms, K_P describes the law of mass action which with the aid of ν_i , the net stoichiometric coefficient of species i described in Equation (2.17), can be formulated as

$$K_P = \prod_{i=1}^N \left(\frac{p_i}{p_{ref}}\right)^{\nu_i}. \quad (2.56)$$

K_P is also called the dimensionless or thermodynamic equilibrium constant, and relates to K_C , sometimes called the chemical equilibrium constant, through

$$K_C = K_P \left(\frac{p_{ref}}{RT}\right)^{\sum \nu_i}. \quad (2.57)$$

2.2 Thermocouple Measurements

The measurements of the temperature inside the reaction zone of the combustion process and at its boundaries were taken with the aid of thermocouples. Due to the potentially high temperatures above 1000 K, the measured temperatures need to be corrected for radiative heat loss from the used thermocouple. From the numerous propositions for the approximation of the heat loss correction, a cylindrical correlation for the Nusselt

number Nu at low Reynolds numbers Re was chosen, based on Collis and Williams [8]. In a range of $0.02 < Re < 44$, the correlation for Nu is then assumed to be [109]

$$Nu_{cyl} = (0.24 + 0.56Re_{cyl}^{0.45}) \left(\frac{T_m}{T_\infty} \right)^{0.17} \quad (2.58)$$

where T_m denotes the film temperature which is defined as the mean of the thermocouple temperature and T_∞ , the temperature of the stream. The latter term can furthermore be approximated as unity, and if the fluid is assumed to be air, the heat transfer rate coefficient h_w between the gas and the thermocouple can be calculated according to the definition of the Nusselt number.

$$h_w = \frac{Nu_{cyl} k_{Air}}{L_{ch}} \quad [\text{W}/(\text{m}^2 \text{K})] \quad (2.59)$$

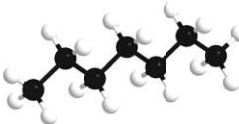
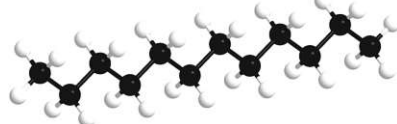
For the calculations herein, the characteristic length L_{ch} is assumed to be the thermocouple wire diameter, and k_{Air} designates the thermal conductivity of air. For measurements under steady state conditions, the energy balance on the thermocouple can be reduced to a convective-radiative balance which, after some rearranging, eventually yields the actual temperature of the gas T_g to be [109]

$$T_g = T_{tc} + \frac{\varepsilon_{tc} \sigma (T_{tc}^4 - T_{Sur}^4)}{h_w} \quad (2.60)$$

with T_{tc} as the temperature of the thermocouple, ε_{tc} its emissivity, σ being the Stefan-Boltzmann constant, and T_{Sur} the temperature of the surrounding environment and equipment.

2.3 Tested Fuels and Chemicals

The tested fuels and chemicals used in the experiments are listed in this section together with their relevant property data to serve as a reference. The values shown here are also implemented in the underlying software that is used to control the experimental devices and to calculate the desired streams of volume and mass flow. The property data for the liquid chemicals was acquired through Chemwatch [6], either from their proprietary compiled safety data sheets (SDS) or the respective chemical manufacturer's SDS within the database. The data for the gaseous compounds was obtained from the mass flow controller manufacturer Teledyne Hastings Instruments [116], and implies a standard temperature pressure (STP) of 25 °C and 1 atm for the gas density. Table 2.1 lists the physical and

Name		Molecular	Boiling	Density
Chemical Formula	Ball-and-Stick Model	Weight	Point	
CAS Number		[g/mol]	[°C]	[kg/m ³]
n-Heptane C ₇ H ₁₆ 142-82-5		100.2	98.4	684 ^a
n-Decane C ₁₀ H ₂₂ 124-18-5		142.28	174.1	730 ^b
n-Dodecane C ₁₂ H ₂₆ 112-40-3		170.34	216.1	753 ^a
Isobutanol C ₄ H ₉ OH 78-83-1		74.2	108.0	802 ^a

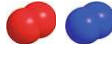
^a at 20 °C ^b at 25 °C

Table 2.1: Liquid fuel components and chemicals used in the experiments, and their relevant physical and chemical property data [6]

Name		Molecular	Density*
Chemical Formula	Ball-and-Stick Model	Weight	[g/L]
CAS Number		[g/mol]	
Propane		44.097	1.802
C ₃ H ₈			
74-98-6			
Dimethyl Ether		46.069	1.883
C ₂ H ₆ O			
115-10-6			

* at standard temperature pressure of 25 °C and 1 atm

Table 2.2: Gaseous fuel components and chemicals used in the experiments, and their relevant physical and chemical property data [116]

Name		Molecular	Density*
Chemical Formula	Space-Filling Model	Weight	[g/L]
CAS Number		[g/mol]	
Air		28.9	1.185
0.21 O ₂ + 0.79 N ₂			
132259-10-0			
Oxygen		31.998	1.308
O ₂			
7782-44-7			
Nitrogen		28.013	1.145
N ₂			
7727-37-9			
Helium		4.003	0.164
He			
7440-59-7			

* at standard temperature pressure of 25 °C and 1 atm

Table 2.3: Gaseous oxidizer and inerts used in the experiments, and their relevant physical and chemical property data [116]

chemical properties of the used liquid fuels and chemicals. Depending on the source, the density at room temperature is either given at 20 °C or 25 °C. Tables 2.2 and 2.3 list the physical and chemical properties of the gaseous fuels, oxidizers, and inerts.

The main focus of this thesis is set on the primary reference fuel (PRF) component n-heptane and the pure research chemicals n-decane and n-dodecane. These single-component fuels are commonly used in combustion research to produce surrogates that help emulate certain properties of interest of real fuels like gasoline, diesel, kerosene, or jet fuels. The pure surrogate components n-heptane, n-decane, and n-dodecane were tested under atmospheric and elevated pressures. Isobutanol was used to study its role as an inhibitor of the low-temperature chemistry involved when mixed with n-heptane and n-decane in different ratios at atmospheric pressure.

3 Apparatus

3.1 Counterflow Burner

The outcome and reaction path of a combustion process can widely vary depending on the mode in which the reactants are brought in contact with each other. To study the influence of the manifold of chemical and transport parameters relevant in combustion, several model burners were developed to focus on certain aspects of the process and their interactions, one of which is the counterflow burner.

As its name suggests, two streams are set opposed to each other to form a flow field between them in which combustion can take place. The streams are directed by axisymmetric ducts, and plug flow boundary conditions are assumed. Also, if the injection velocity of one of the streams is high enough buoyancy effects can be neglected. While premixed experiments are possible if required, the streams are usually non-premixed at the boundary, with one side carrying the fuel, and the other one the oxidizer. The mixing of fuel and oxidizer happens inside the flow field in the mixing layer and is governed by diffusion which, compared to the fast chemistry of combustion, is slow, and thereby the limiting step in the overall process. The resulting diffusion flame in the mixing layer owes its name to this circumstance.

Inside the flow field where the two streams meet, a stagnation plane is formed where the axial velocities of both streams become zero, and mixing between them occurs. Under arbitrary conditions, the mixing would be a highly complex, three dimensional problem to solve, but due to the counterflow configuration and its stagnation flow conditions, it is possible to reduce the transport problem to one spatial dimension. Thanks to boundary layer approximations, eventually, profiles of temperature and composition inside the flow

field become functions of the axial coordinate only, making the chemical and transport phenomena taking place more manageable solely through the boundary conditions.

The experiments carried out for this thesis made use of two major configurations of the counterflow burner. The gaseous configuration consisting of two similar axisymmetric ducts for gaseous reactants, and the liquid pool configuration made up of one duct for a gaseous oxidizer and an axisymmetric pool for condensed fuels replacing the second duct.

3.1.1 Gaseous Configuration

The gaseous counterflow configuration is shown in Figure 3.1 in form of a rendering of the CAD model of one of the actual devices used in the experiments. The counterflow burner is divided into three major segments: the top part which is the oxidizer side (boundary conditions are designated by the subscript 2), the lower part which is the fuel side (boundary conditions are designated by the subscript 1), and the segment between them which holds the flow field and the reaction zone where combustion takes place. The flow field is divided by the stagnation plane, and above it the flame is formed after ignition.

The ducts are depicted in yellowish material around the vertical center line of Figure 3.1, and both are holding three fine-wire meshed screens each, to assure plug flow boundary conditions when the streams enter the reaction zone. The distance between the ducts is an essential parameter in the experiments and is denoted as the separation distance L . Around each duct, another annular duct is placed which carries an inert, generally nitrogen, to shield the reaction zone from the surrounding environment. Due to their purpose, these streams are called the curtains. The curtain streams do not actively participate in the combustion reactions inside the reaction zone, but, as experience shows, play a vital role in stabilizing the resulting flame.

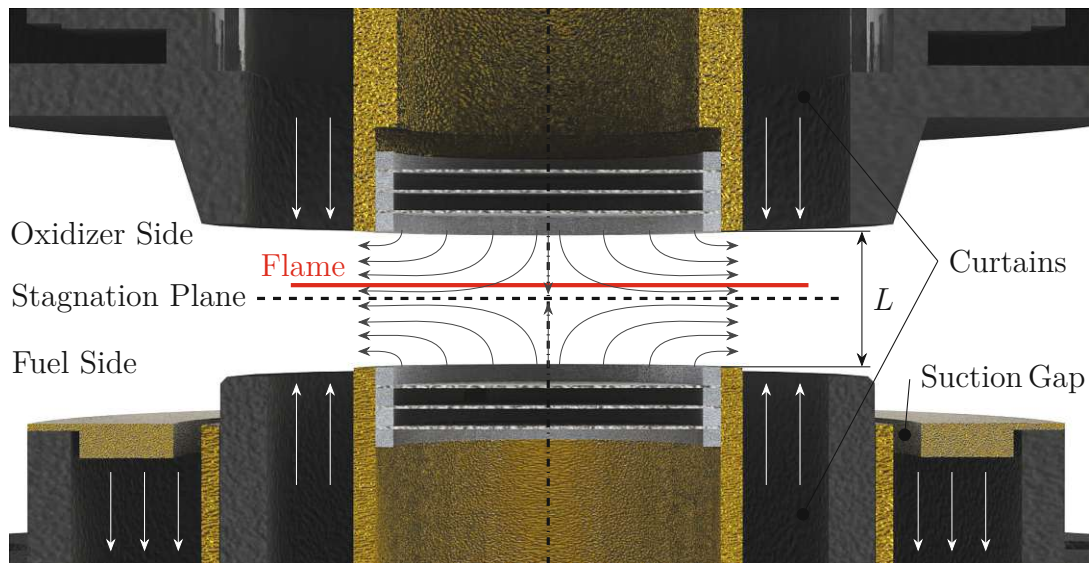


Figure 3.1: Gaseous counterflow burner configuration.

After the combustion reaction, the gases are guided into the exhaust system of the burner through the suction gap which is an annular area around the fuel side curtain. The connection to the building ventilation system is established here, and is basically a line at a lower than environmental pressure level to provide enough suction to draw the gases exiting the reaction zone away from it. It also houses the cooling sprays which distribute water-mist via nozzles into the product gas stream to cool it down after the reaction, and to prevent possible further propagation of the flame into the system.

3.1.2 Liquid Pool Configuration

In the liquid pool counterflow configuration as shown in Figure 3.2, while the oxidizer side is similar to the gaseous configuration, the duct of the lower part is replaced with a cup to hold a liquid fuel. The fuel is fed into the cup externally through a line shown on the bottom of the cup to replenish evaporating reactant, and to keep a constant level of fuel in the cup. The off-center object on the left side inside the cup is a needle which aids in visually determining the actual level and surface of the fuel inside the cup.

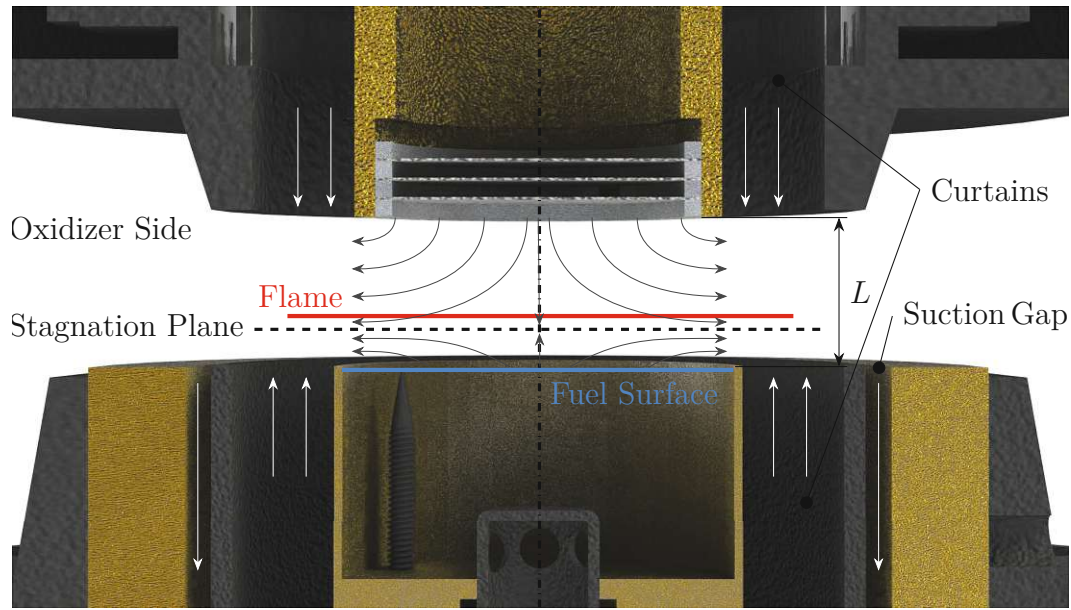


Figure 3.2: Liquid pool counterflow burner configuration.

Other than the cup, the fuel side bares the same functionality as in the gaseous configuration. As the evaporation of the condensed fuel is not directly controlled during experimentation, neither is the position of the stagnation plane or the flame, resulting in a potentially varying, but still one dimensional flow field between the duct and the liquid pool. Here, the separation distance L is measured between the duct and the fuel surface which is supposed to be at the brim of the cup.

3.1.3 Strain Rate Formulation

The residence time of reactants in the reaction zone, and especially in its mixing layer, is an essential parameter to determine whether the species have enough time to interact with each other physically. Burners with enforced flows utilize some form of variation of the injection velocity to manipulate the residence and flow time of the participating components. Traditionally, counterflow burners were imposed with symmetrical injection velocity boundary conditions which are strongly temperature dependent. To avoid the

temperature dependence, and to rid the boundary conditions of the requirement of equal injection, Seshadri and Williams [104] derived the strain rate formulation for laminar flow between the two ducts of a counterflow burner [32,65,98].

$$a_2 = \frac{2|V_2|}{L} \left(1 + \frac{|V_1|\sqrt{\rho_1}}{|V_2|\sqrt{\rho_2}} \right) \quad [1/\text{s}] \quad (3.1)$$

$$a_1 = a_2 \sqrt{\frac{\rho_2}{\rho_1}} \quad [1/\text{s}] \quad (3.2)$$

The strain rate a_i represents the reciprocal of the characteristic flow time, with ρ_i denoting the density, and V_i the injection velocity of the respective stream at the boundary. The separation distance L is applied in axial direction as shown in Figures 3.1 and 3.2 between the two stream outlets, designating the height of the reaction zone.

From an engineering perspective, it is desired to place the stagnation plane in the center of the flow field between the two ducts to provide enough space for the laminar diffusion flame to form. Since the $|V_i|\sqrt{\rho_i}$ terms in Equation (3.1) represent the square root of the respective stream's momentum, the momentum balance $V_2^2\rho_2 = V_1^2\rho_1$ can be applied, resulting in the strain rate formulation for the gaseous counterflow configuration with a centrally balanced stagnation plane to become

$$\text{Gaseous:} \quad a_2 = \frac{4|V_2|}{L}. \quad (3.3)$$

For practical considerations of the liquid pool configuration, the injection velocity on the fuel side can be approximated as zero since the Reynolds number is negligible compared

to that of the oxidizer side, leading to the strain rate formulation for the liquid pool counterflow configuration to be [101]

$$\text{Liquid Pool: } a_2 = \frac{2|V_2|}{L}. \quad (3.4)$$

Notice, that by prescribing the strain rate instead of the injection velocity directly as the boundary condition, the residence and flow time become temperature independent and stay constant even if the temperature of the streams at the boundary is changed.

3.1.4 Limit Phenomena and Critical Conditions

Temperature and residence time represent two significant physical limits of the combustion process, in the sense that a flame can only reach a certain maximum temperature, and can only be maintained above a certain minimum residence time of its reactants. Those limits are shown visually in Figure 3.3 in form of the so called S curve which is characteristic for the counterflow configuration [19,48].

In the S curve, the maximum reaction temperature is plotted against a form of representation of the residence time, subdividing the curve into three sections or branches, to describe the combustion limits of a mixture in a flow field. To signify the application of the counterflow configuration, in Figure 3.3 the strain rate is used as a representation of the flow time. For a more general purpose, the Damköhler number Da could be used which would invert the given axis.

The upper branch of the S curve signifies the existence of a flame and an actively ongoing combustion process, while the lower one depicts the reactants at their initial temperature in the mixing layer. The middle section describes an unstable state and the transition

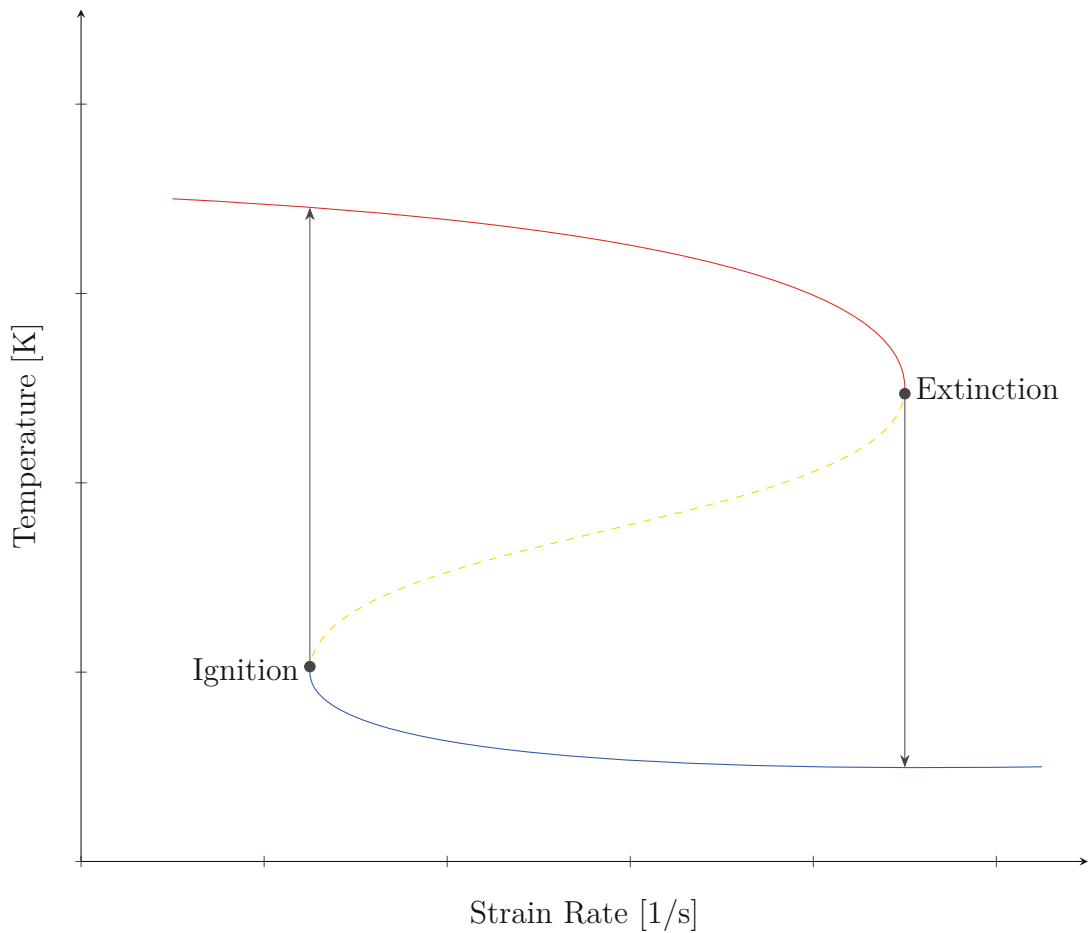


Figure 3.3: S curve of reaction temperature over inverse of the characteristic flow time showing combustion limits, and critical conditions of autoignition and flame extinction.

from one branch to the other which cannot be maintained experimentally. Moving along the lower branch, points of steady strain rate can be found at which the reactants are mixing and starting to interact, but ignition has not happened yet. At a certain critical point, when the strain rate is low enough or the residence time long enough, the mixture ignites to form a flame, and its state jumps to the upper branch. Along this section of the curve, the flame temperature is depicted for various strain rates while a flame is maintained in the mixing layer. If the strain rate is increased up to another critical point, and the residence time becomes too short for the reactants to interact, the flame gets extinct, and the state of the mixing layer is returned to the lower branch.

3.2 Atmospheric Counterflow Setup

The experiments for this thesis were carried out on two different setups. One operating at atmospheric pressure without any shield from the surrounding environment, and another one where the burner is placed inside a chamber which can be pressurized for experimentation at variable elevated pressure levels. The atmospheric counterflow setup is built in a modular fashion, meaning that the burner and other parts of the setup can be exchanged and modified as required by the experiments at hand. By changing the top part of the burner, either autoignition temperatures or extinction strain rates can be experimentally obtained, and by exchanging the bottom part, fuels in either gaseous or liquid form can be tested. Furthermore, in its gaseous configuration a vaporizer can be placed in the feed line on the fuel side to analyze the properties of prevaporized liquid fuels.

The basic configuration of the atmospheric counterflow setup is in its gaseous mode and is shown in Figure 3.4. Over the years, numerous experiments and publications featured the setup housed in UC San Diego's Combustion Laboratory in its gaseous and various modified configuration due to its reliability and reproducibility of experimental results [3,20,29,33–35,50,64,94,96–99,107,108]. Because of the modular nature of the setup, the workings and operations of the different configurations are very similar requiring only minimal downtime and work when switching between various types of experiments.

3.2.1 Gas Supply

As shown in Figure 3.4, the setup is made up of the gas supply system and a set of mass flow controllers on the left, the counterflow burner in the middle, and the controlling and data evaluating devices on the right. The gas supply system consists of a manifold of standard pressurized gas cylinders which contain the reactant and inert gases and a set of

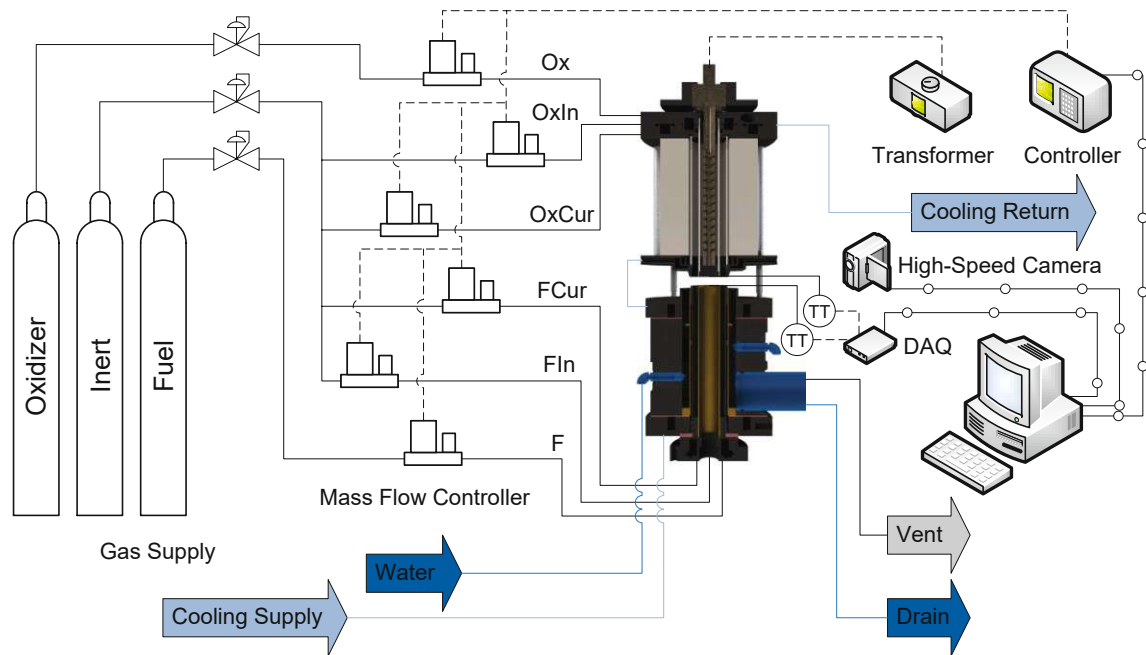


Figure 3.4: Atmospheric counterflow setup in its gaseous fuel configuration for determining autoignition temperatures.

connected pressure regulators to match the required upstream pressure of the mass flow controllers. In the atmospheric setup, the oxidizer can either be supplied from gas cylinders as depicted in the schematics, or it can also be directly fed into the mass flow controllers from the building's shop-air supply replacing the oxidizer cylinder altogether. Since the mode of supply used can potentially have an effect on the experimental results, it is noted for each set of experiments which form of oxidizer supply was used.

3.2.2 Flow Control

There are more mass flow controllers available than required for the counterflow setup so that the required flow of the respective experiment can always be matched with the optimal flow range of operation of the mass flow controllers [117,118]. Each mass flow controller has a specific range of operation for certain gases. If the flow rate is too low, the mass flow controller might not open for gas to flow at all, or if the flow rate is too high,

the controller is unable to provide enough gas to the system, altering the experimental conditions. Therefore, each mass flow controller can be set individually into each line to satisfy the respective experiment's requirements, and to provide an adequate and steady flow of gas. Each device is operated individually through a designated controller which is connected to and controlled by a computer [119]. The controlling device not only serves as an interface between the mass flow controllers and the computer, but is also used for measuring and monitoring the actual flows of each line in real-time, thus providing a vital part of the experimental setup and its safety.

3.2.3 Burner Top

Coming from the supplying devices set in place upstream, the fluids are directly fed into the main apparatus of the setup, the counterflow burner. It is made up of two major parts, top and bottom, which determine its functionality, the type of experiment, and the physical state of the tested fuel at room temperature the burner can handle. By switching between two different tops, it is possible to experimentally measure either a fuel's autoignition temperature, or its extinction strain rate for a specific set of conditions.

Autoignition

When the autoignition temperature of a fuel under certain conditions is of interest, the autoignition top is used. It guides a mixture of oxidizer and inert gas to the reaction zone of the apparatus, and houses an electric heating element inside its duct which is used to heat up the gases on the oxidizer side before their reaction [39]. Figure 3.5 shows a rendering of the autoignition top placed on the bottom part used for the testing of gaseous and prevaporized fuels, and a section view of the fully assembled counterflow burner together with annotations of some of its most significant components.

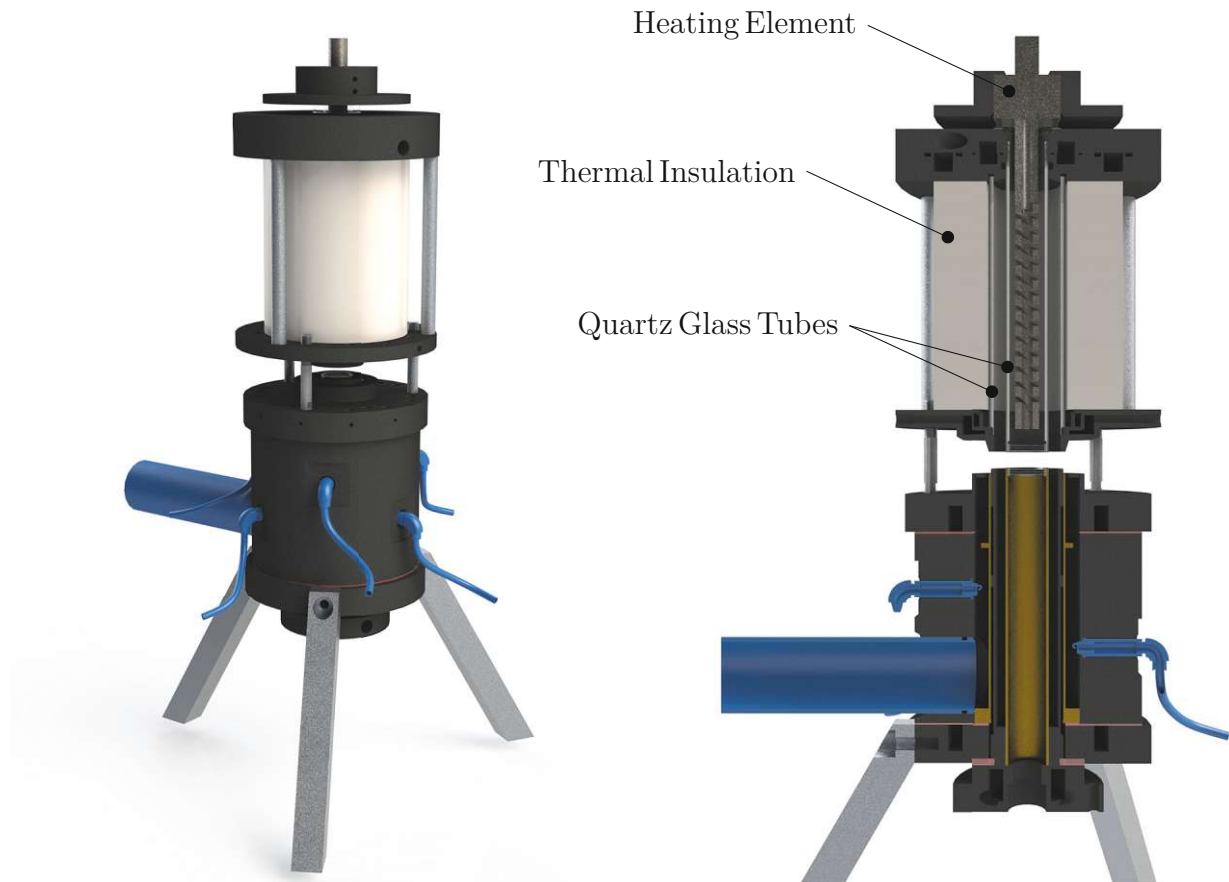


Figure 3.5: Rendering and section view of the counterflow burner for determining auto-ignition temperatures of gaseous and prevaporized fuels.

The main part of the top is the duct together with its surrounding and containing components. Because of the potentially high temperatures required to thermally ignite fuels without a spark, the duct is a custom designed tube made of quartz glass. Around the duct, another glass cylinder is set to form an annular outlet which is used to deliver the inert curtain flow. Inside the duct, a heating element is placed which is built from silicon carbide and powered with alternating current to heat up the oxidizer stream to the desired temperature. The heating element is connected to a variable transformer which is used to manually set the power input to the heating element, thereby regulating the temperature of the oxidizer stream.

The duct assembly is covered with thermal insulation material to assure effective heating of the oxidizer stream, and to protect the rest of the top from the emitted heat. The upper and lower components of the top holding the glass tubes in place are cooled with deionized water to prevent expansion of the material and cross transfer of gases, and to maintain proper sealing at all critical interfaces.

Extinction

The extinction top is used when critical strain rates need to be determined experimentally at which a flame cannot be further maintained and extinguishes. Since the strain rate of the injected gas is regulated with the mass flow controllers, and no heating, insulation, or cooling of the oxidizer side are required for this type of experiment, the top only serves as a guide for the stream which makes the design of the extinction top not as complex as the autoignition top's. A rendering, and a section view of the fully assembled counterflow burner used for the testing of gaseous and prevaporized fuels utilizing the extinction top is shown in Figure 3.6.

3.2.4 Burner Bottom

The physical state of the tested fuel at room temperature determines the required bottom part and configuration of the counterflow burner. One burner bottom is used for fuels that are either gaseous or form a liquid at room temperature, but are vaporized and kept above their boiling point before being injected into the reaction zone. This type is shown in Figures 3.5 and 3.6. The other type of burner bottom is directly fed with fuel in its condensed state forming a liquid pool, and is depicted in Figure 3.8 under upcoming Paragraph "Liquid Fuels" in this Section.

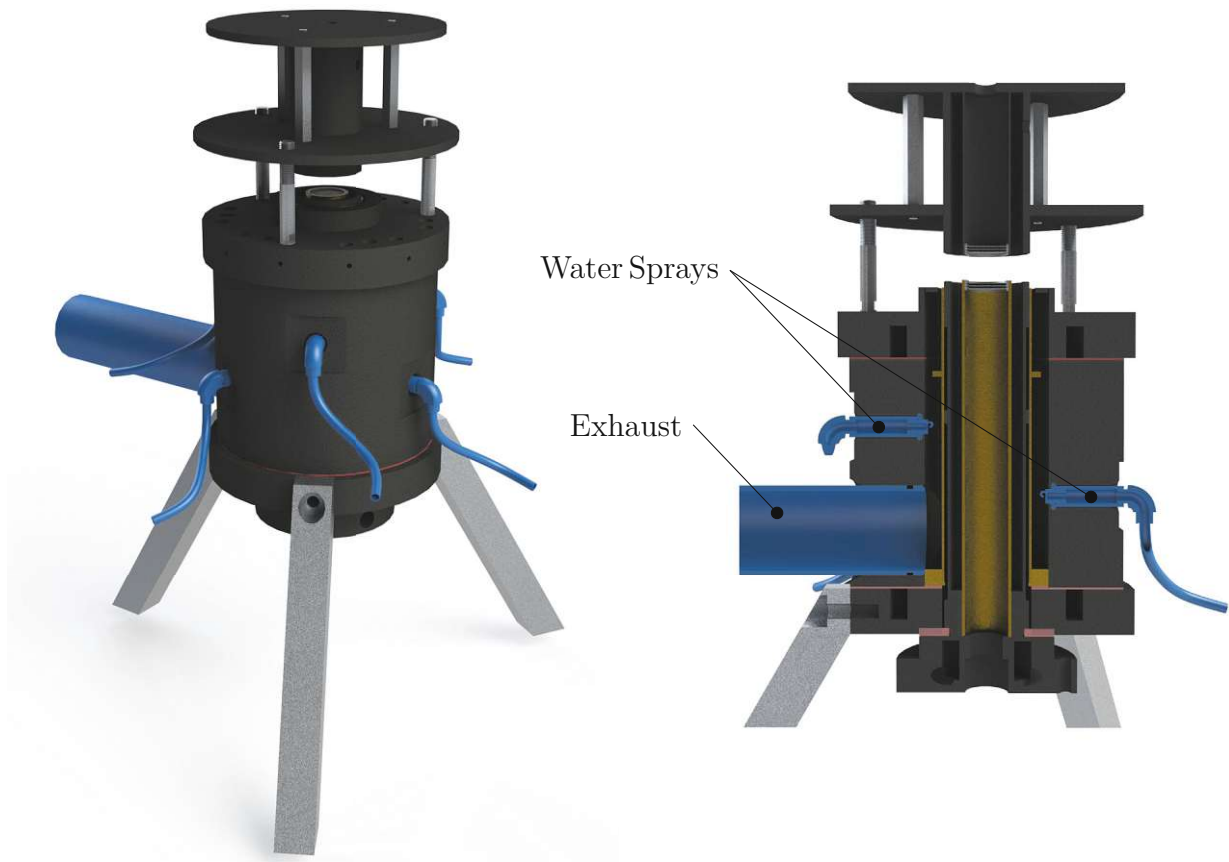


Figure 3.6: Rendering and section view of the counterflow burner for determining extinction strain rates of gaseous and prevaporized fuels.

Both types of bottom parts not only contain the fuel inlet, but also house the exhaust system of the counterflow burner which withdraws the unburned and product gases from the reaction zone, and directs them to the ventilation system. The exhaust system starts at the suction gap, an annular intake slot around the inert curtain flow outlet, leading the gases after their reaction through the burner and into the exhaust pipe. The system houses a set of water-mist sprays to cool the stream passing through, and to prevent possible propagation of the flame into the burner. The exhaust also serves as a separator to split the stream's components into liquids, guiding them to the drain, and gases flowing to the vent.

The fuel is contained in a high precision syringe pump which is used to feed the liquid into the vaporizer [121,122]. Inside the device, the fuel is dispersed through a cooled nozzle, evaporated by the heated environment, and carried to the burner by the gaseous inert. Like the mass flow controllers, the syringe pump is controlled through the computer which allows for an inline mixing of fuel vapor and inert to gain the exact mass fraction on the fuel side required by the experiment. The power output from the vaporizer is set manually via a variable transformer, and the temperatures at inlet and outlet are monitored with the aid of thermocouples in the process pathway. In addition to the manual adjustment of the temperature on the fuel side and the vaporizer, the line leading to the counterflow burner is kept at a constant temperature setpoint through its own designated controller and heat supply system.

Liquid Fuels

The latest expansion of the atmospheric counterflow burner at UC San Diego's Combustion Laboratory is the addition of a burner bottom to handle and examine liquid fuels in their condensed form [30,64,99,101]. To achieve that, the gas duct is replaced with a cup to hold fuels that are liquid at room temperature. The cup is filled with the aid of the syringe pump which again is controlled by the computer. In this configuration, not only the burner bottom is cooled with deionized cooling water, but also the cup, to keep the fresh liquid fuel at constant temperature before its evaporation by the heated oxidizer stream from the autoignition top. A rendering and its respective section view of the atmospheric counterflow burner for determining autoignition temperatures of condensed liquid fuels is shown in Figure 3.8.

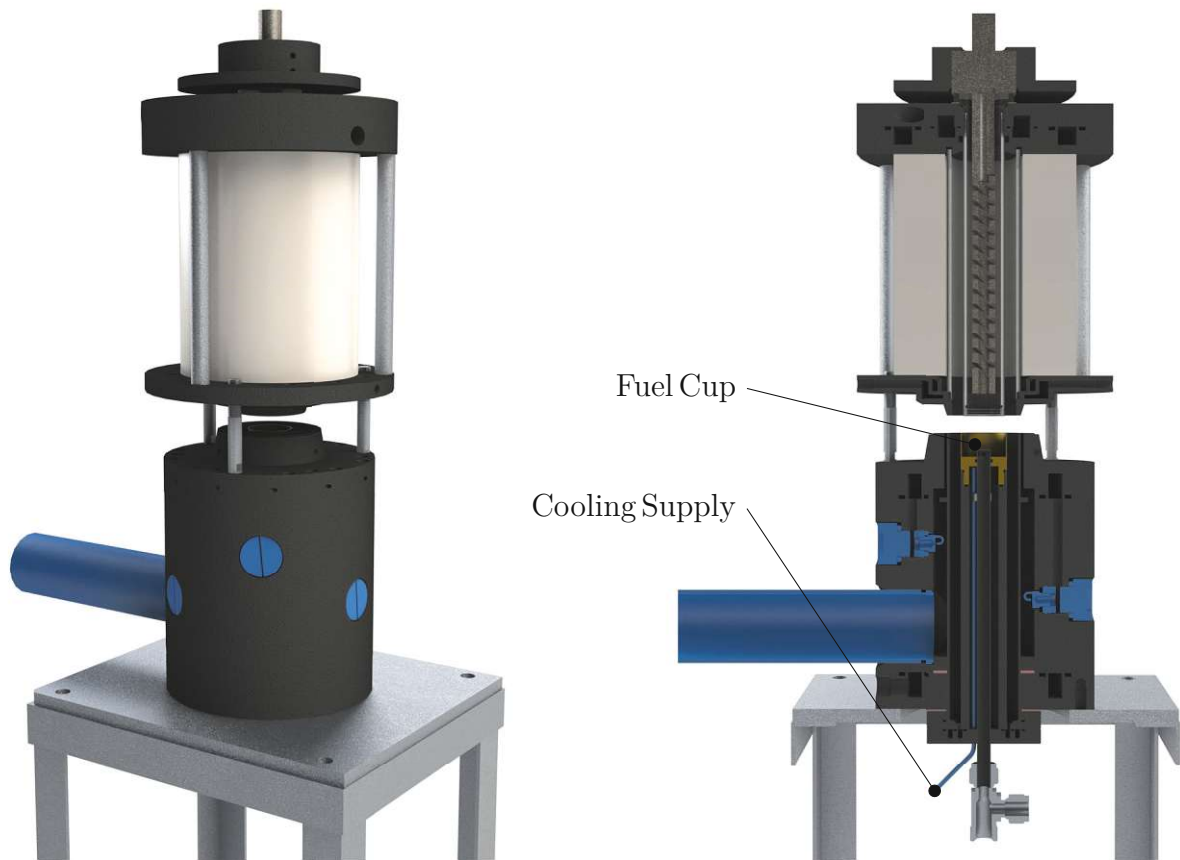


Figure 3.8: Rendering and section view of the counterflow burner for determining auto-ignition temperatures of liquid fuels.

For the combustion reaction to take place, the fuel needs to evaporate first, and form fume that eventually enters the reaction zone. Because of the evaporation, the level of liquid in the fuel cup is constantly dropping, and needs to be replenished. Therefore, a needle is placed inside the cup with its tip aligned with the cup's brim. Thanks to the needle it is possible to monitor the liquid level visually, and set the syringe pump to constantly refill the cup at a steady flow rate of fuel from its reservoir to maintain a constant level.

Due to the nature of the liquid level handling, the cup might get overfilled, resulting in fuel overflowing into the curtain duct of the burner bottom. For that reason, a separate line is set in the duct guiding the inert curtain flow which allows for overflowed fuel from the cup to be withdrawn from the burner. The excessive fuel is stored in an external

container during experimentation, and can be emptied manually. A diagram of the complete atmospheric counterflow setup in its liquid pool configuration for handling liquid fuels in their condensed form is shown in Figure 3.9.

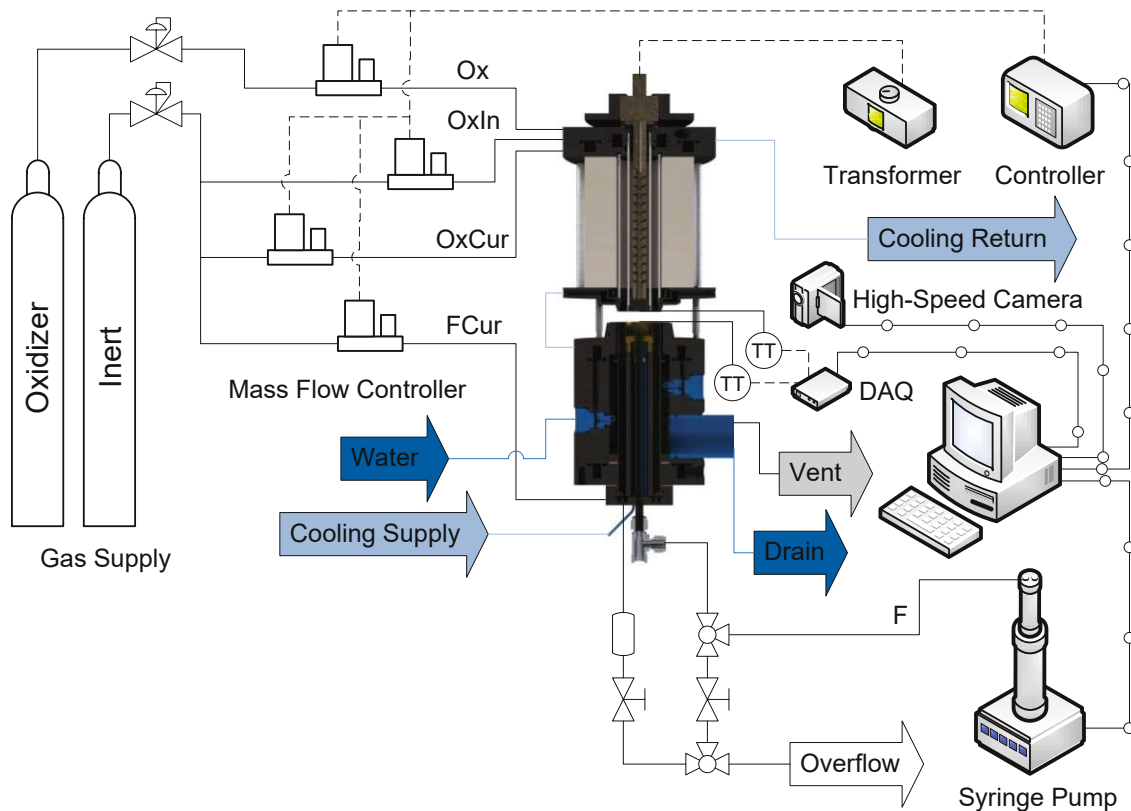


Figure 3.9: Atmospheric counterflow setup in its liquid pool configuration for determining autoignition temperatures of condensed fuels.

3.2.5 Data Acquisition (DAQ)

The two main parameters that are to be determined through experiments with the counterflow burner setup are the extinction strain rate and the autoignition temperature. To measure the strain rate indirectly, the mass flow controllers and syringe pump are used by providing a volume flow setpoint calculated by the computer used to operate

the experimental setup. To obtain accurate flows from the mass flow controllers, proper calibration for the imposed gas and conditions in the laboratory are required.

To measure and record the relevant temperatures in the counterflow setup, different types of thermocouples with wire diameters varying between 0.001 and 0.005 in are used. All the probes are connected to a computer through an analog-to-digital converter featuring cold junction compensation required when using thermocouples for measuring temperatures [59]. The main sensor for measuring autoignition temperatures is a type R thermocouple made of a combination of platinum with 13% rhodium, and pure platinum wires that can be used for measuring gas temperatures of up to 1768 °C [71,72].

For the purpose of visually recording and analysing the events taking place in the reaction zone of the counterflow burner, a high-speed camera capable of capturing color images at up to 5200 frames per second is set up [79]. A video is continuously recorded on the device during experimentation, and a limited time frame of that recording, which is determined by the camera settings, can be saved to the controlling computer after a user specified trigger event. The high-speed camera is used to evaluate certain events and conditions during ongoing experiments, and also to analyse the recorded events offline after the experiments have been carried out.

3.2.6 Control Software

Once the hardware for the atmospheric counterflow setup is installed and configured, the entire set of reactant streams can be operated through a computer, requiring only few manual user interactions with the physical device, like ignition and temperature regulation, during experimentation. The workstation is running the software LabVIEW to control the setup's hardware and to acquire data, utilizing a Virtual Instrument (VI)

that was created in UC San Diego's Combustion Laboratory specifically for the atmospheric counterflow setup and its hardware [44]. The respective manufacturer's drivers and proprietary VIs were implemented into the main VI for optimal use of the existing hardware's capabilities [58,119,122]. The main VI's user interface during an ongoing experiment, recording a typical autoignition event of a prevaporized fuel, is shown in Figure 3.10.

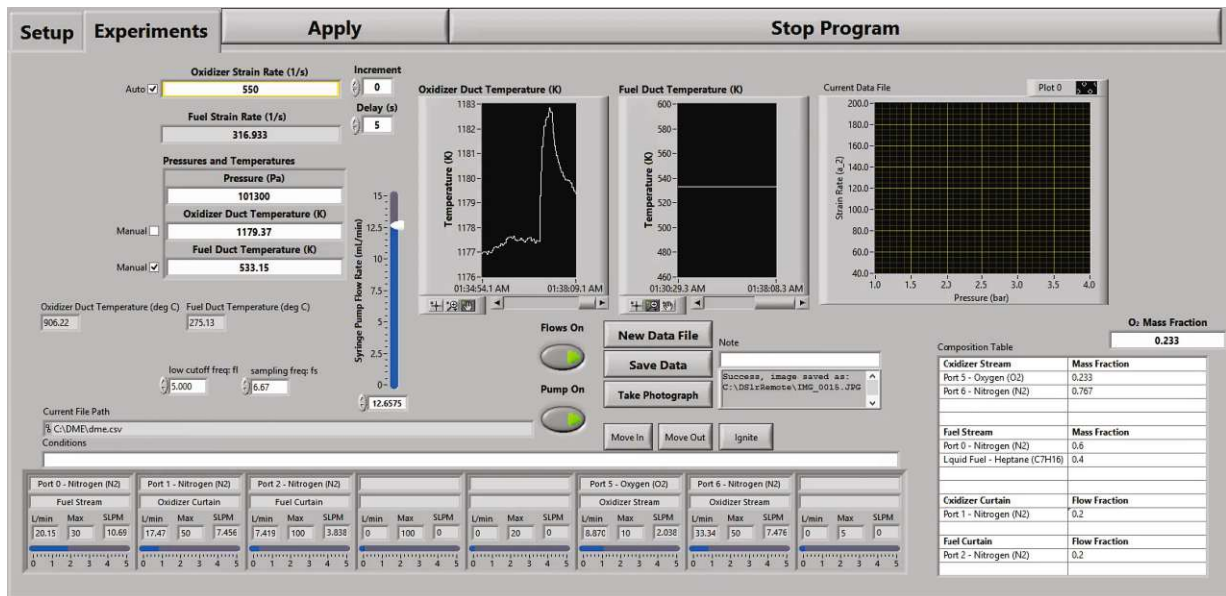


Figure 3.10: The main VI's user interface used to control the atmospheric counterflow setup in its gaseous configuration during an ongoing experiment, recording a typical autoignition event of a prevaporized fuel in LabVIEW.

The VI allows for the manipulation of the flow rate and composition of each stream by providing the oxidizer strain rate and the mass fractions on the fuel and oxidizer side. Given these input parameters together with the burner geometry stored in the VI, and optional duct temperature readings or settings for both sides, the volumetric flow rates for each mass flow controller and the syringe pump are calculated, and sent to their controllers as current setpoints upon user request. The exact underlying calculations done by the main VI to compute all relevant flow parameters for the entire setup can be viewed in Listing A.1 in Appendix A where the complete calculation procedure for the fluid components according to the calibration settings is implemented as a function in MATLAB [55].

It is worth noting that the VI does not receive and process any feedback from the controlling hardware, but only from the data acquiring devices, thus requiring the user to monitor the correct flow rates on the physical controllers to make sure the set experimental conditions are transmitted correctly and met. While the VI is running, temperature data from the thermocouples is continuously received, recorded and plotted for the user's convenience, and can be saved upon request. To counteract temporary hardware failure, or if it is desired to avoid even minimal fluctuation in the temperature reading, which is occurring due to the nature of the measurement with thermocouples and the processing of the data, an option is provided to manually override the thermocouple readings with temperature settings on both sides individually. When this option is active, a constant signal is assumed for the calculations of the flow rates of the respective side.

3.2.7 Flow Calibration

Before the VI is able to accurately calculate the flow rates for all connected devices, two prerequisites have to be met. The virtual configuration of the VI has to be properly configured to mirror the actual installation, and the mass flow controllers have to be calibrated for the gases and conditions imposed by the experiment. Both tasks are achieved from within the main VI in LabVIEW shown in Figure 3.11 which is depicting an example configuration of an autoignition experiment for testing a prevaporized fuel. Each port in the configuration is representing a mass flow controller in the physical setup, and each device requires separate calibration.

Since during experimentation the flow rates are regulated and measured through the mass flow controllers, and the tested gases, required ranges, and experimental conditions might change between sets of experiments, it is required to calibrate each mass flow controller to achieve the highest possible level of accuracy. Proper calibration is achieved by adjusting

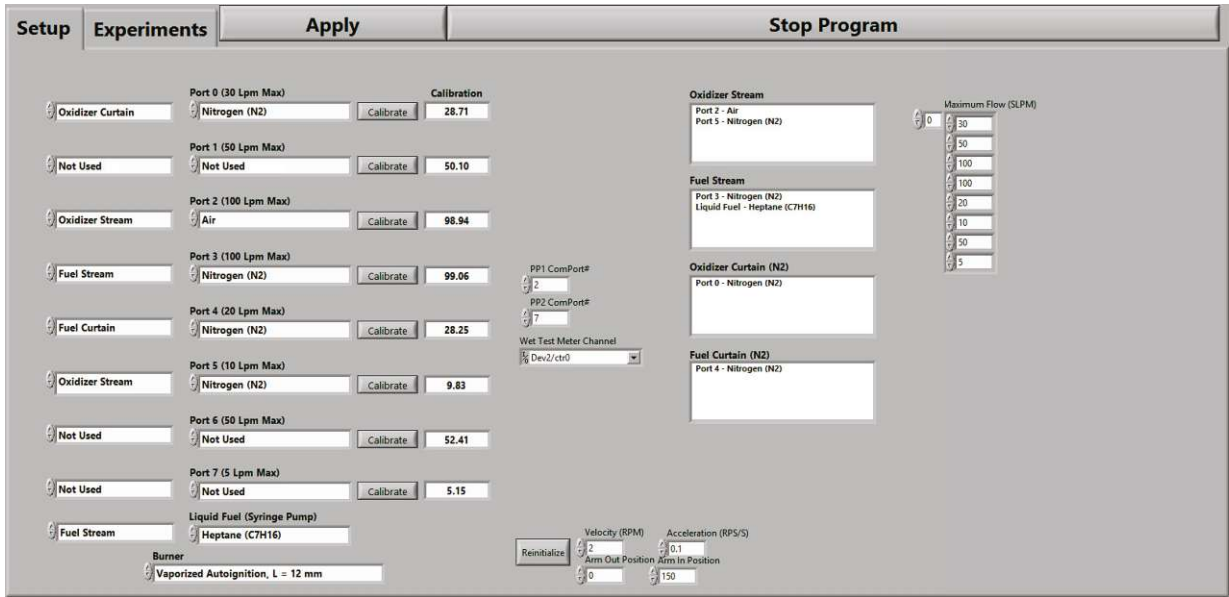


Figure 3.11: The main VI's user interface used to configure the virtual representation of the atmospheric counterflow setup in LabVIEW where each port represents a mass flow controller in the physical installation.

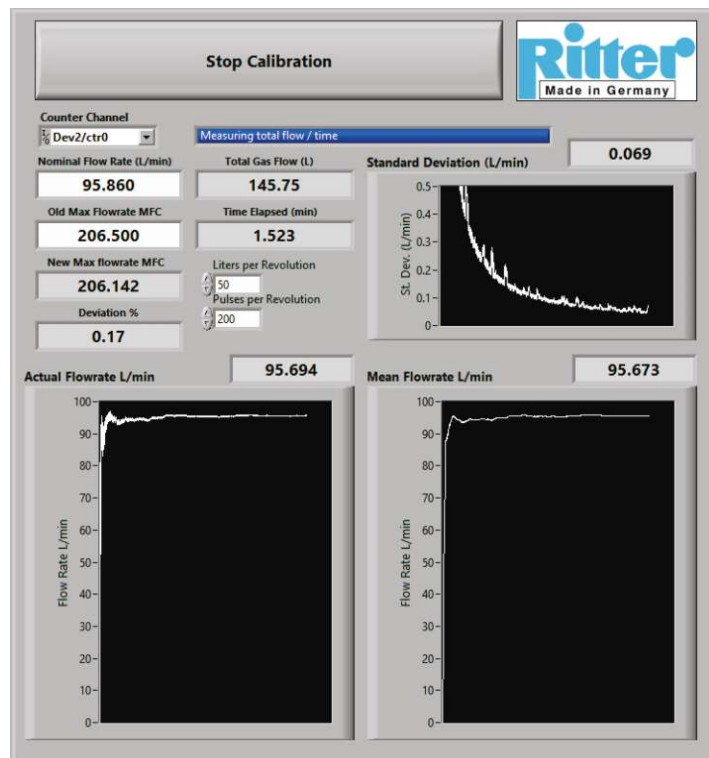


Figure 3.12: VI used to calibrate each mass flow controller by comparing the setpoint to the actual flow rate measured by a calibrated drum type gas meter, and adjusting the controller's maximum flow rate.

each mass flow controller's range and maximum possible flow rate when a certain gas is regulated. Therefore, a factory calibrated drum type gas meter is used to measure the actual flow rate provided by a mass flow controller at a certain setpoint [90,91]. The measured value is then compared to the setpoint and the deviation indicates how to adjust the mass flow controller's calibration. After a few iterations, sufficiently accurate readings can be obtained. During calibration, the gas meter is connected to the computer through its very own digital interface module, and allows for real-time data acquisition and evaluation in LabVIEW. A designated VI, seen in Figure 3.12 during an iteration, is used to execute the calibration procedure every time the experimental conditions change.

4 Combustion at Elevated Pressures

4.1 High Pressure Combustion Experimental Facility (HPCEF)

The High Pressure Combustion Experimental Facility (HPCEF) at UC San Diego was custom designed and set up by members of the Department of Mechanical and Aerospace Engineering's Combustion Laboratory to provide a worldwide unique workspace where experiments on open flames above atmospheric pressures could be conducted. Their idea was to build a pressurizable chamber that can house a variety of burner devices to analyze the structure and properties of open flames, particularly in the counterflowing configuration. The High Pressure Facility's pressure chamber in its original design was a 40 in tall closed cylinder with a diameter of 16 in and a wall thickness of 3/8 in, housing a counterflow burner in its gaseous configuration and equipment for experiments on critical conditions of extinction, and the measurement of temperature profiles at pressure levels up to 25 bar [62,63,67]. Over the years, several modifications by multiple generations of engineers and scientists were made to expand the capabilities of the facility. Major developments were the design and implementation of a burner bottom to handle liquid fuels in their condensed form [22,23], and later, the expansion of the facility with the addition and integration of a burner top and the necessary equipment to conduct experiments to determine the autoignition temperatures of liquid fuels at elevated pressures [51–53].

The most recent upgrades for the HPCEF were implemented in the course of this thesis, and involved the expansion of the working pressure range of the facility's experimental apparatus up to 60 bar, and the evaluation of the impact of these newly imposed conditions on autoignition experiments conducted at the facility. So far, flame properties data on extinction gathered on the HPCEF was published in a range of up to 20 bar while data sets of autoignition ranged only up to 6 bar. The reason for the difference in pressure

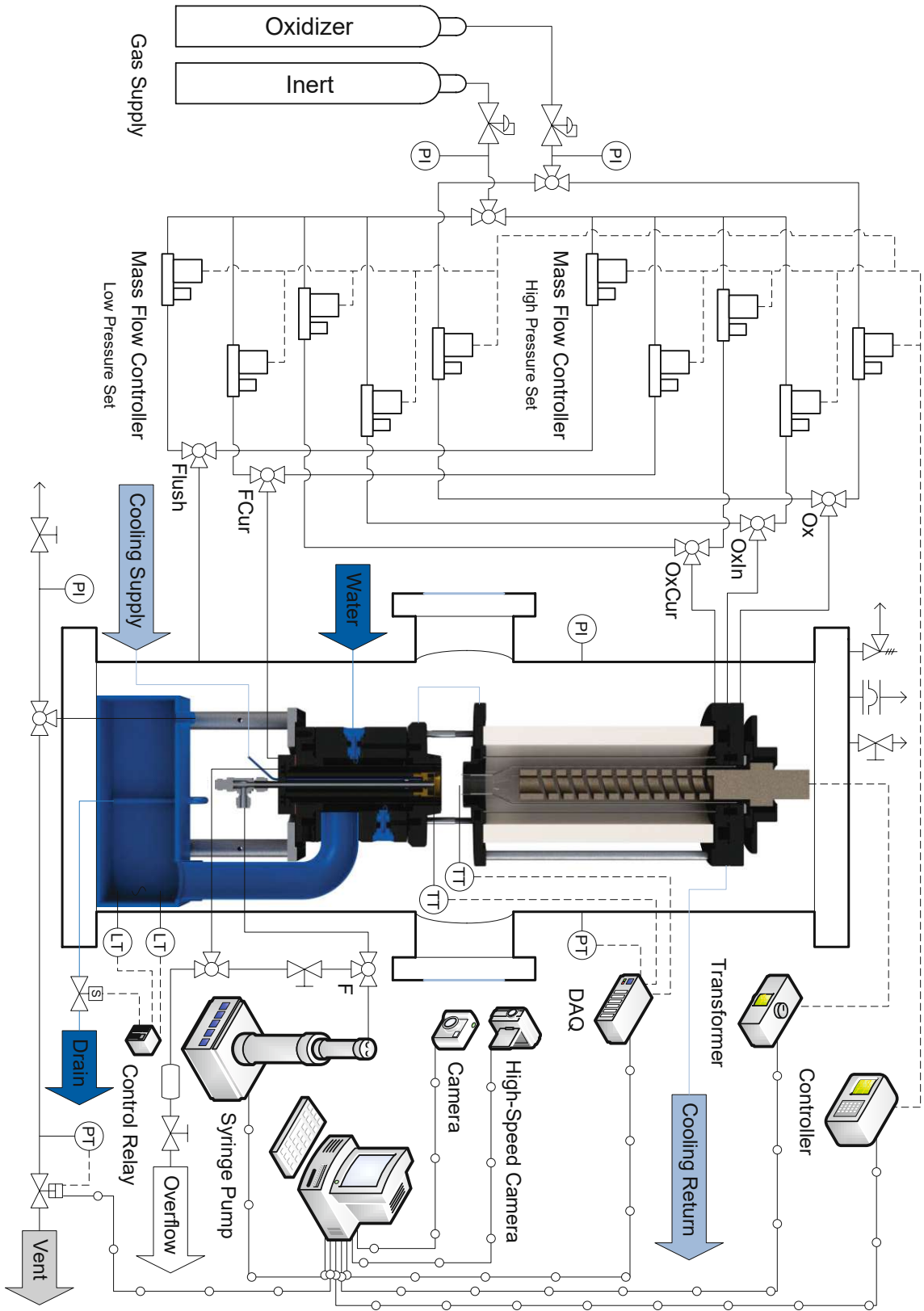


Figure 4.1: High Pressure Combustion Experimental Facility at UC San Diego's Combustion Laboratory.

range is the significantly more complex nature of the experimental setup and the additional technical challenges that come with it to generate consistent data, namely the heated oxidizer stream required to ignite the pool of liquid fuel, and the management of the gaseous streams while maintaining a constant pressure level and steady flow field in the reaction zone. The schematic in Figure 4.1 is showing the High Pressure Combustion Experimental Facility with all of its relevant components and streams in its modified and most recent setup deployed for this thesis. The renderings in Figure 4.2 depict the facility's counterflow burner assembly in its liquid pool configuration without its enclosing chamber. Photographs showing the HPCEF and the main apparatus in various states are included in Appendix B for further reference.

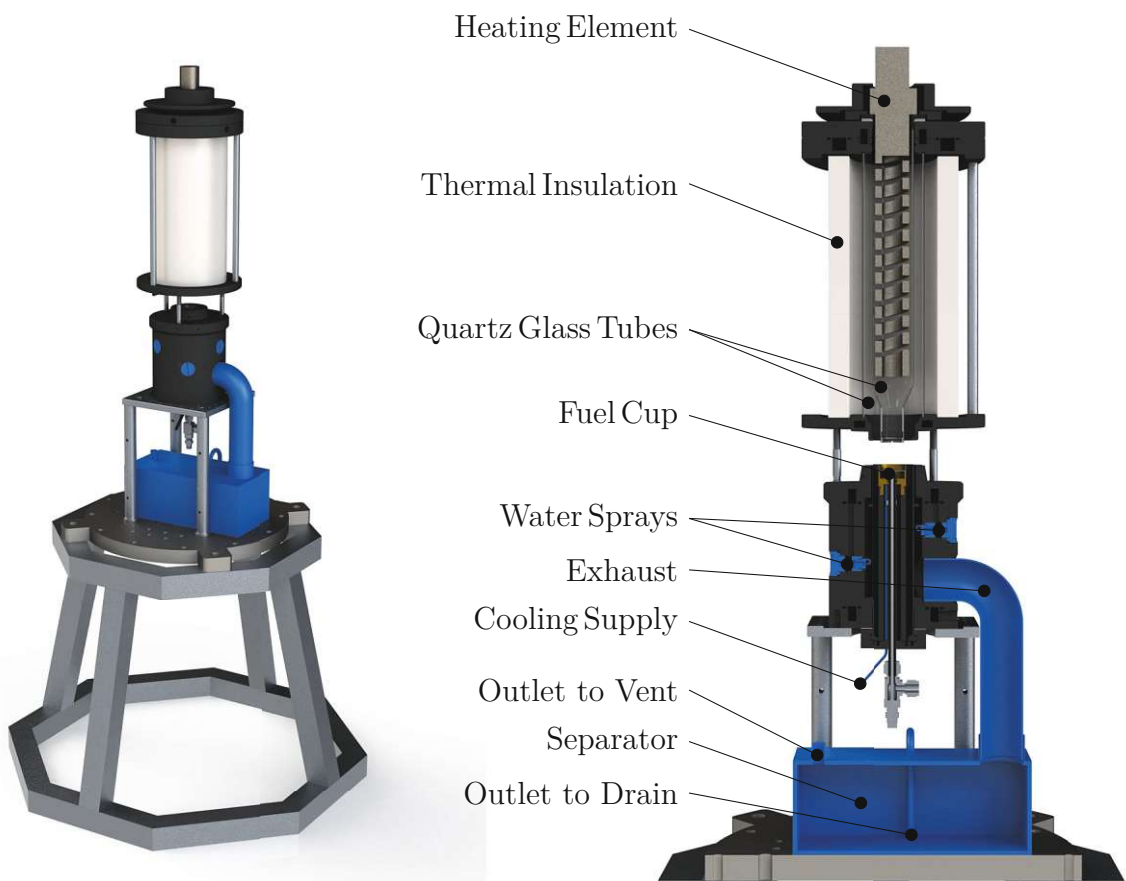


Figure 4.2: Rendering and section view of the counterflow burner used in the High Pressure Combustion Experimental Facility for determining autoignition temperatures of liquid fuels at elevated pressures.

4.1.1 Counterflow Burner Assembly

In many aspects, the HPCEF is similar to the atmospheric setup described in the preceding sections, and the major differences and additional equipment will be pointed out in the upcoming sections. The experimental device, the counterflow burner in its liquid pool configuration assembled with the autoignition top, is shown in the form of a rendering and its section view in Figure 4.2 together with annotations of its components. With the exception of a few minor refinements, the burner is of the same basic design as in the atmospheric setup described in Sections 3.2.3 and 3.2.4, but with a significantly larger heating element and resulting power output capacity for heating up the oxidizer stream [39]. Corresponding to the heating element, a larger variable transformer is required, which, compared to the atmospheric setup, was modified and equipped with a stepper motor and respective controller to gain the ability to operate the device via the controlling workstation from a distance, as indicated in the schematic of the HPCEF in Figure 4.1. Also the mass flow controllers [118], the drum type gas meter to calibrate the gaseous streams [90,92], and the syringe pump to feed the liquid fuel cup [120,122], are larger and have a higher capacity to cope with the more demanding experimental conditions and requirements at elevated pressures, but are of the same make and operated similarly as in the atmospheric setup.

4.1.2 Facility Control and Data Acquisition

The entire installation can be operated and monitored centrally from the workstation, and only requires manual user interaction during start up and shut down procedures. The reaction zone can be monitored during experimentation with the aid of a camera, and its live stream can be viewed at the workstation as well. Figure 4.3 shows screenshots of the HPCEF's two workstation screens during an ongoing autoignition experiment picturing the main VI on the upper screen, and the received camera live feed to monitor the reaction

4.1 HIGH PRESSURE COMBUSTION EXPERIMENTAL FACILITY (HPCEF)

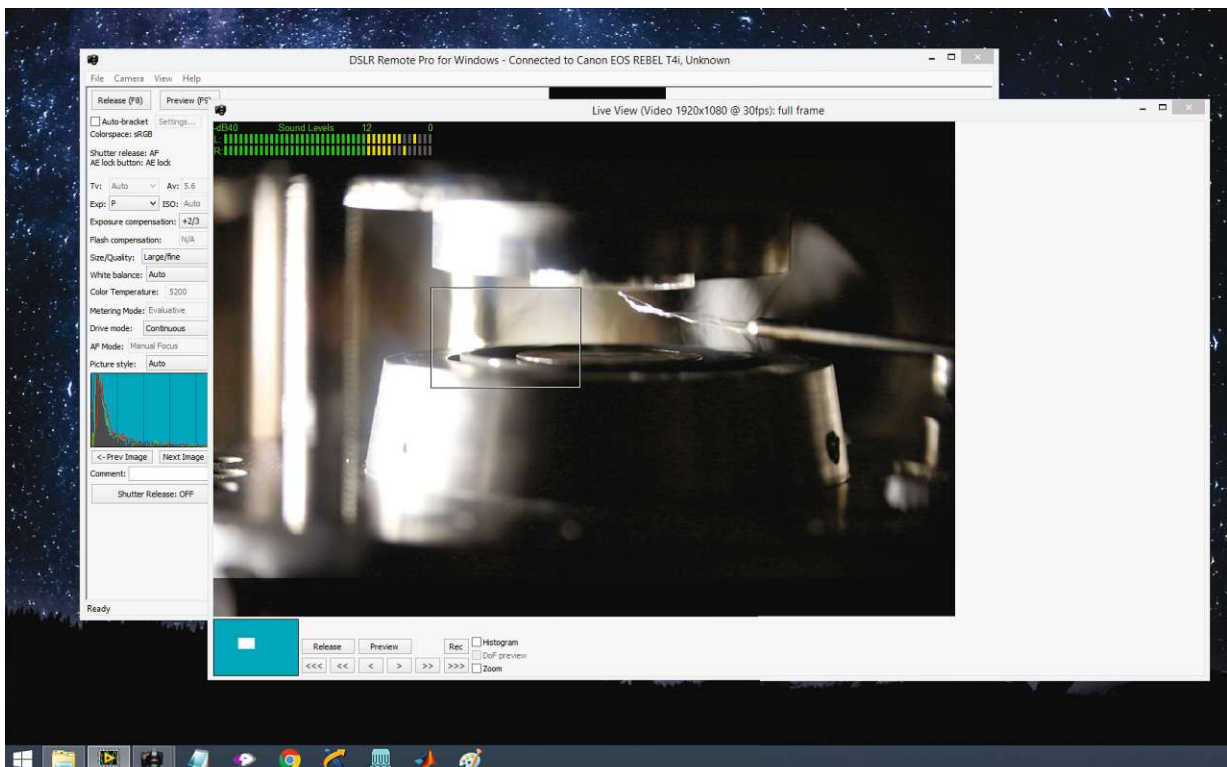
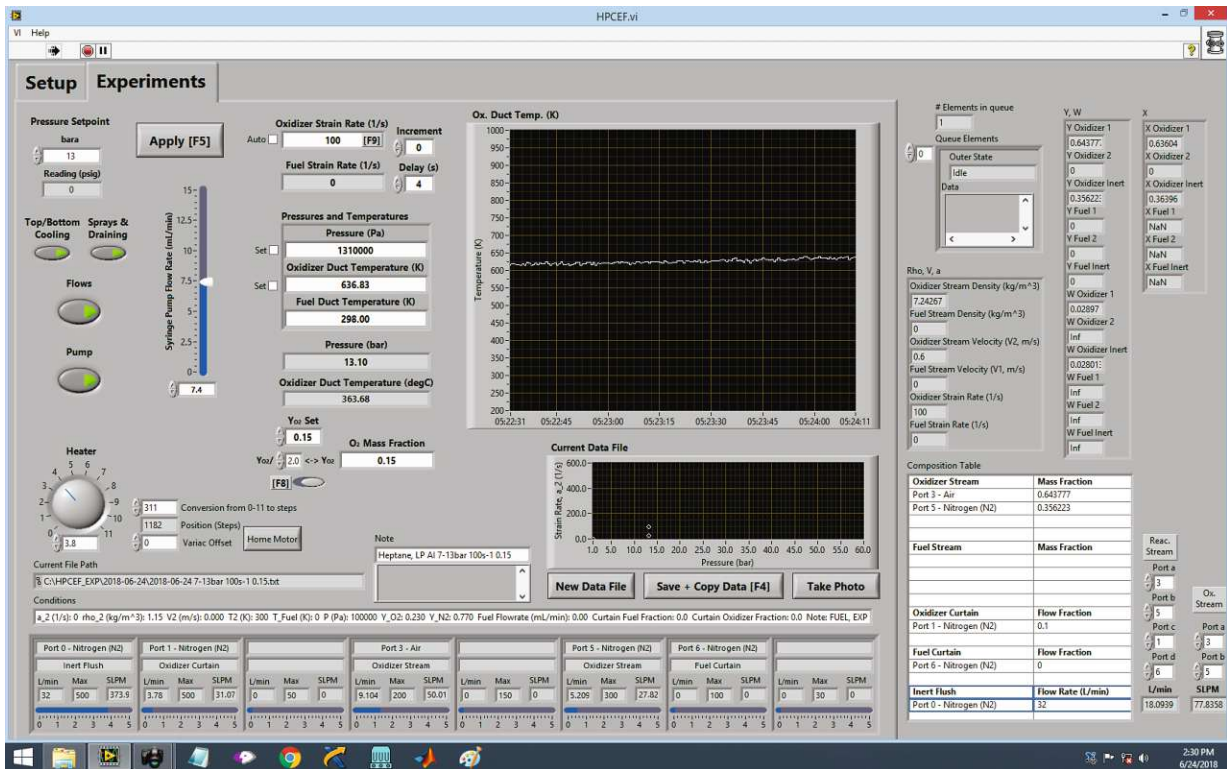


Figure 4.3: Screenshots of the HPCEF's two workstation screens during an ongoing autoignition experiment showing the main VI (top) and the received camera feed to monitor the reaction zone and liquid level in the fuel cup (bottom).

zone and liquid level in the fuel cup on the lower screen. In addition to that, a third terminal is available, and designated solely to display and trigger the saving of the feed from the high-speed camera [79].

As observable from the upper screenshot in Figure 4.3, the main VI for controlling the HPCEF has a few different features than the atmospheric setup VI, to accommodate the operation of the additional equipment, namely the power input to the heating element, and the setting of the pressure in the system. Since the controller for the mass flow controllers [119], and the thermocouples in place for measuring temperatures are the same as in the atmospheric setup [71,72], the remaining differences in the VI are either solely cosmetic to display the information from the new data sources, or were added for increased safety of the operator and the apparatus. To gather all the relevant data during experimentation, in addition to the analog-to-digital converter for reading the signals from the thermocouples [59], a modular data acquisition system is set up to measure and process the data received from pressure sensors throughout the facility [61].

4.1.3 Pressure Chamber

As indicated by the schematic in Figure 4.1, the counterflow burner assembly is enclosed in a pressurizable chamber which constitutes the main apparatus of the HPCEF. The custom designed structure has a cylindrical stainless steel hull with four openings on its side serving as viewports for visual access to the enclosed device during experimentation, and two plates covering its top and bottom bases. The viewports bear fused silica windows which can be individually exchanged with stainless steel plates if optical access is not required from certain sides. To provide enough light for the installed cameras to monitor ongoing experiments, a high luminous direct current light source is set up and shone through one of the viewports. During the expansion of the facility for autoignition experiments, the chamber had to be

extended in height with an addition ring to fit the taller burner top part inside. The closing plate on the bottom has numerous openings with fitted pipes for guiding all the process streams in and out of the chamber, while the one on top carries essential safety equipment like a pressure relief valve and burst disc, and eyes to connect to a hoist installed on the facility. The hull and the plates are held together by bolts, and the bottom plate is attached to an aluminum stand. By releasing the bolts between the hull and the bottom plate, it is possible to lift the chamber off its base with an electrical hoist to gain access to the assembly placed inside, necessary when changing equipment and for maintenance.

To pressurize the chamber, a designated stream of compressed inert gas, called the flush, fed through one of the mass flow controllers is used while the pressure inside the chamber is regulated by a computer controlled and pneumatically actuated back pressure valve [123–125], installed and connected to the buildings ventilation system to extract the gaseous products from the system. The liquid fluid components are released and drained through a high pressure solenoid valve [75], automatically operated by a designated programmable digital relay [18]. Since the high pressure in the system is posing a potentially severe safety risk, several layers of protection are implemented in the system, and the chamber specifically. As the final measure and layer of protection, in case all other prior layers fail and a sudden release of pressurized gas from the chamber occurs, the pressure vessel is surrounded with clear shatter and high-impact resistant polycarbonate panels protecting the operator and surrounding equipment.

4.1.4 Separator

Another significant part of the assembly, specific to the HPCEF, is the separator in the exhaust line after the counterflow burner seen in Figure 4.2. As the assembly is placed in a closed environment, but gases from the mass flow controllers and water for the cooling

sprays from a high pressure pump are continuously fed into the system, the fluids need to be properly withdrawn from the chamber while simultaneously maintaining a steady level of pressure. The separator is responsible for separating the gaseous and liquid components of the exhaust stream from the burner, and for guiding them to the appropriate outlets.

The separator, which is essentially an aluminum box with several openings, receives the exhaust stream through one inlet, and evacuates the gaseous components through an outlet on the top leading to the back pressure valve assembly [123–125], and eventually to the ventilation system. The remaining liquid components are pushed out of the chamber by the built up pressure contained in the system through a snorkel placed inside the separator. While the gases are removed continuously due to the nature of the pressure regulation in the HPCEF, the draining of the liquids is automatically triggered by the water level in the separator. To achieve that, two level sensors [73] are installed in the separator and connected to a programmable digital relay [18] which triggers a high pressure solenoid valve [75] to open every time the liquid level reaches its upper limit, and to close when it hits the lower limit again.

4.1.5 Modifications

During an initial testing phase, and before any experiments were conducted, several parts of the High Pressure Combustion Experimental Facility were upgraded, modified, and then tested to safely operate at a higher pressure level. After the modifications made in the course of this thesis, the highest potential working pressure of the HPCEF was raised to 60 bar and the chamber was pressure tested with water up to 30 bar. In accordance with the implementation of equipment with higher capacity and ranges required to increase the maximum potential pressure in the system, significant changes to safety related equipment had to be made to accommodate the more demanding conditions imposable by the newly

integrated devices. Some minor improvements of noncritical parts of the device were also implemented in the process by exchanging and complementing components with newly designed and 3D printed parts and supports.

Flow Control

In the original setup, the mass flow controllers were capable of delivering gases in a range of up to almost 26 bar. Controllers of higher capacity were already available on the facility, but neither integrated nor usable in the system. On top of the original mass flow controllers, a second set was permanently installed in parallel and fitted on a custom built structure. As the controllers work most reliably and accurately in the middle of their respective downstream pressure range, the flow control stand was designed to allow for switching between the two sets of mass flow controllers by manipulating two sets of 3-way ball valves installed



Figure 4.4: Flow control stand with the high pressure set of mass flow controllers in parallel on top of the low pressure set in its idle state.

up and down stream of the mass flow controllers. That way, the appropriate set can be chosen for experimental conditions above or below 25 bar without the need to change the physical setup. Proper configuration of the mass flow controller power supply and control unit is still required and needs to be done upon every pressure level switch to ensure correct flow rates. The picture in Figure 4.4 shows the flow control stand with the high pressure set mounted above the previously existing low pressure set.

Additionally, high pressure filters and gauges with markings indicating the required upstream high and low pressure levels were installed inline before each mass flow controller for their protection, and to ensure that the upstream pressure from the gas supply system is regulated down appropriately, since the mass flow controllers can only operate properly if the upstream pressure falls within their range. After the installation had been finished, the existing labeling was updated and additional transferable stream and line labeling was added for increased safety, to make it easier to identify each relevant stream in case of an emergency.

Viewports

Before the modifications for this thesis were implemented, the pressure chamber's four viewports were bearing fused silica windows of 10 in diameter, which were pressure tested up to 45 atm for safety [63]. To withstand higher pressure levels, special design quartz sight glasses mounted on adapter plates to fit the viewports were manufactured and available, but neither installed nor tested on the HPCEF. Three of the windows covering the viewports were replaced with the new sight glasses, while the fourth was exchanged for a simple stainless steel plate due to the lack of requirement for another viewport. The picture in Figure 4.5 shows the chamber with one viewport covered with a round plate on the left, and a second one with a sight glass installed on the right.



Figure 4.5: Pressure chamber hull showing one viewport covered up with a round stainless steel plate and another one with a sight glass installed.

Because of the different design and the curvature of the quartz glass on the inside, the sight glasses show a considerable demagnifying effect compared to their simple round predecessors. Especially near the edges of the glass if the line of sight is not perpendicular to the glass's outer surface, the view from the inside of the chamber can get distorted which can potentially make monitoring of the liquid pool level in the cup difficult if the camera is not adjusted carefully. Additional challenges arise when further light sensitive equipment or optical devices, like the high-speed camera, are required in the setup.

Separator

Figure 4.6 shows a picture of the separator while it was removed from the assembly to accommodate new level sensors capable of bearing high pressure. The large opening on its top is the inlet and the two disconnected fittings are the outlets for gaseous and liquid matter. The two blue components with the attached wires mounted on the side of the

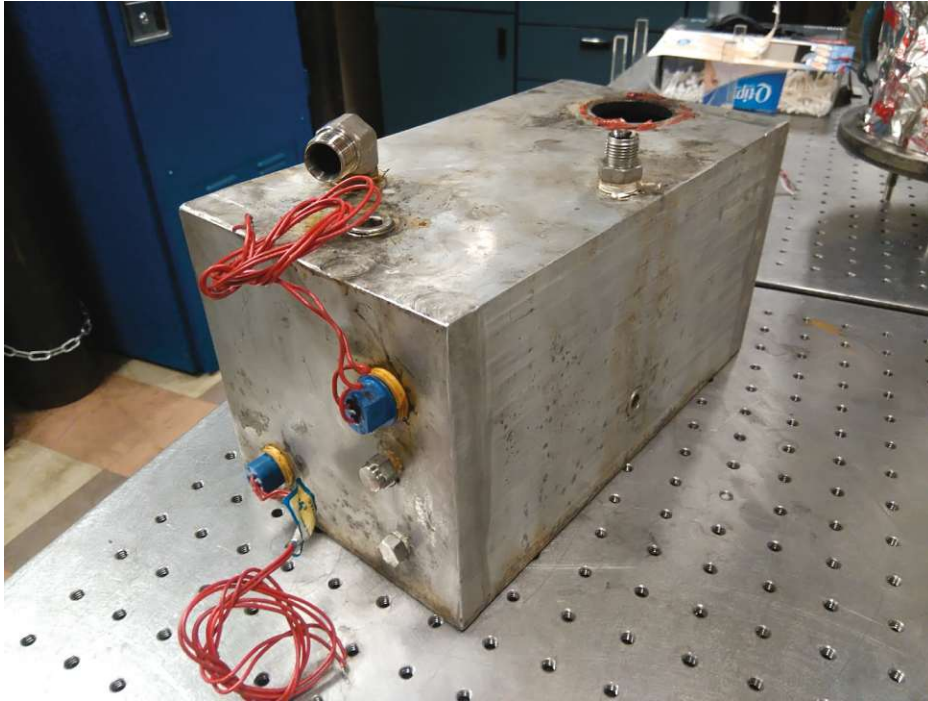


Figure 4.6: HPCEF’s separator removed from the counterflow burner assembly before modifications and ultrasonic level sensors were implemented.

separator are floating swing arm liquid level switches which are not designed to withstand high pressure environments for a prolonged time period. To avoid regular replacement of the switches, they were replaced with ultrasonic level sensors [73]. Due to the increased size of the switches and space restrictions around the separator, the openings for the sensors required repositioning to another side.

To drain the liquids from the separator, an automatically operated solenoid valve triggered by the level sensors is placed outside the chamber. The valve needed to be replaced as well to withstand higher pressure levels above 25 bar. To avoid flooding of the chamber with water from the cooling sprays, which are the main source of water in the system, a valve was chosen from the available ones on the facility and potential candidates, that ensures fast emptying of the separator at all possible experimental pressure levels [75]. The considerations and conditions for the choice of an appropriate valve are given in Listing B.1 in Appendix B.

During the testing and experimental phase it was observed that due to the electrically noisy environment on the HPCEF, the drain valve was frequently triggered erroneously and failed to properly open or close which led to either flooding of the chamber and the vent, or uncontrollable pressure drop and fluctuation. To avoid these undesirable situations, a manual override switch to operate the solenoid valve was installed at the workstation to grant the operator the option to intervene, should the valve fail.

Liquid Fuel Overflow

Liquid fuel that is overflowing from the cup is collected in the curtain area of the burner and withdrawn through a designated line into a container. Accumulating fuel in the curtain area is not desirable because of the potential propagation of formed fumes back towards the reaction zone. The collecting container used to be placed inside the chamber, but the piping and bottom plate connections were modified to place the overflow container outside the chamber to increase accessibility and simplify maintenance. A double-ended high pressure stainless steel 500 ml sample cylinder with quick connect fittings was installed on the bottom plate, to make it possible to remove the overflowed fuel from the system even during ongoing experiments and while the chamber is pressurized [113].

Safety Equipment

Safety related equipment installed on the HPCEF was upgraded and reset in accordance with the pressure rating of the previously modified components. The 2 in burst disc housed in its assembly installed on the top plate of the chamber, seen as the device in the middle of the picture in Figure 4.7, was replaced with a disc made to order with a higher rating [74]. The safety pressure relief valve, left of the burst disc assembly in Figure 4.7, was disassembled to replace the spring in its closing mechanism with a more rigid one [114,115]. After the



Figure 4.7: Pressure chamber's top plate bearing a pressure relief valve, burst disc assembly, ball valve for venting, pressure gauge and eyes for connecting to the electric hoist.

modification, the relief pressure setting of the valve was verified on a custom build test stand, and then mounted back on the chamber's top plate. To ensure proper venting when filling, and to avoid evacuation when emptying the chamber during the safety pressure tests with water, a manual ball valve was installed on the top plate at the highest point of the chamber. For completely emptying the system during the water test, or in case the chamber gets flooded with water from the sprays, another manual ball valve was set at the system's lowest point in the exhaust line outside the protective panels right before the back pressure valve. This valve is used to protect the back pressure valve from unwanted liquids, and also serves as a last measure to manually release pressurized gas from the chamber if needed or in case of emergency.

As the pressurized lines and devices feeding fluids into the apparatus are placed at the HPCEF's workstation, shatter and high-impact resistant polycarbonate shields were set up by the pressure bearing parts to protect the operator in case of failure. Furthermore, the

high voltage electrical connectors on the facility were replaced according to code to comply with safety regulations, and also the electrical wiring and equipment inside the chamber on the burner assembly received additional insulation and was tested for proper grounding.

Pressure Regulation

The back pressure valve responsible for regulating the pressure in the system also required attention. To cover a higher range, a new valve needed to be set into place. Because of the tighter operating pressure range of the old valve, and its resulting comparably faster response time, the decision was made to modify the exhaust and venting system to fit both back pressure valves in parallel and make them selectable through a switch. In the picture in Figure 4.8, both valves with their respective controllers on top and online pressure sensors in the foreground can be seen, set for operation at high pressure [123–125].

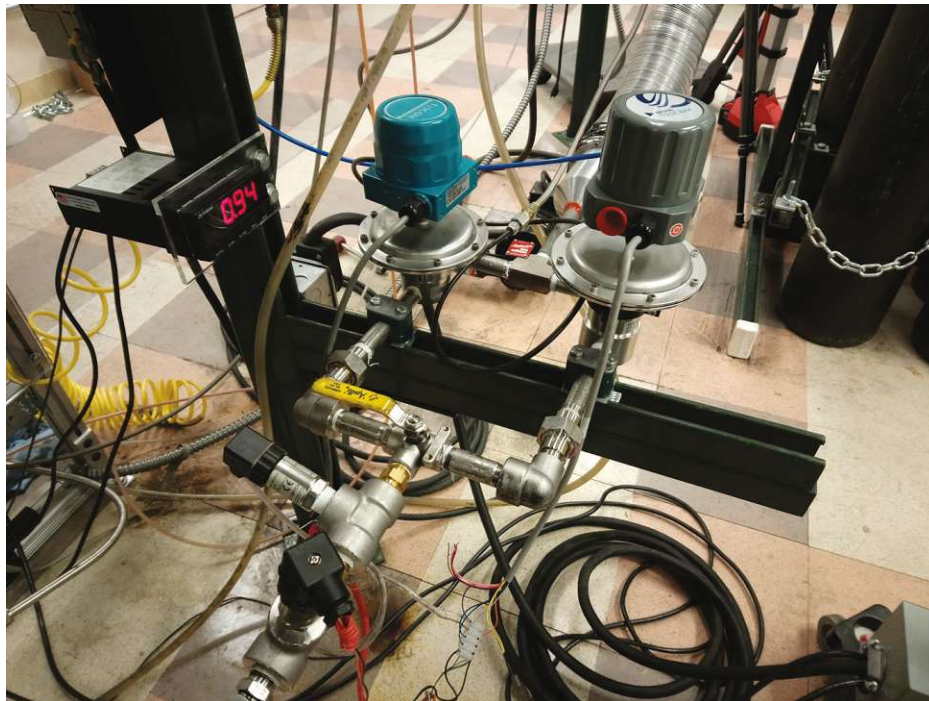


Figure 4.8: Low and high back pressure valves together with their controllers and online sensors in the HPCEF's exhaust and venting system set for operation at high pressure.

The calibration of the new pressure sensor and the tuning of the PID controller were done on site with the calibrated high precision pressure gauge mounted on the chamber's top plate, and a combination of the HPCEF's main VI and proprietary software provided by the back pressure valve's manufacturer. The configuration was based on the old valve's settings and improved mainly through trial and error during the imposition of typical flow rates and elevated pressures on the system. The new settings were tested for stability until no significant fluctuation in the steady state chamber pressure was noticeable, and the signal's overshooting, ringing, and rise time were under control when forcing responses to setpoint step changes and impulses as seen in the graphs in Figures 4.9 and 4.10.

As expected, due to the difference in pressure range, and since higher pressure levels require overall higher flow rates from the mass flow controllers, the new back pressure valve controller requires more aggressive settings to regulate optimally while simultaneously allowing more overshooting and slightly longer settling times. Especially at lower levels, these effects are more significant than with the old back pressure valve because of its optimization for higher pressure levels. Therefore, it is advised to use the old valve and low pressure set of mass flow controllers for experimental pressures below 25 bar, and only operate the high pressure set when required by the experimental conditions.

Control Software

Clutter and obsolete elements from previous modifications were removed, and a few helpful information displays were added to significantly improve readability of the user interface during experimentation. In general, only relevant data and options were left to remain on the interface for the ability to operate faster and safer. In terms of configuration, options were added to dynamically switch between the two back pressure valves and their respective configurations.

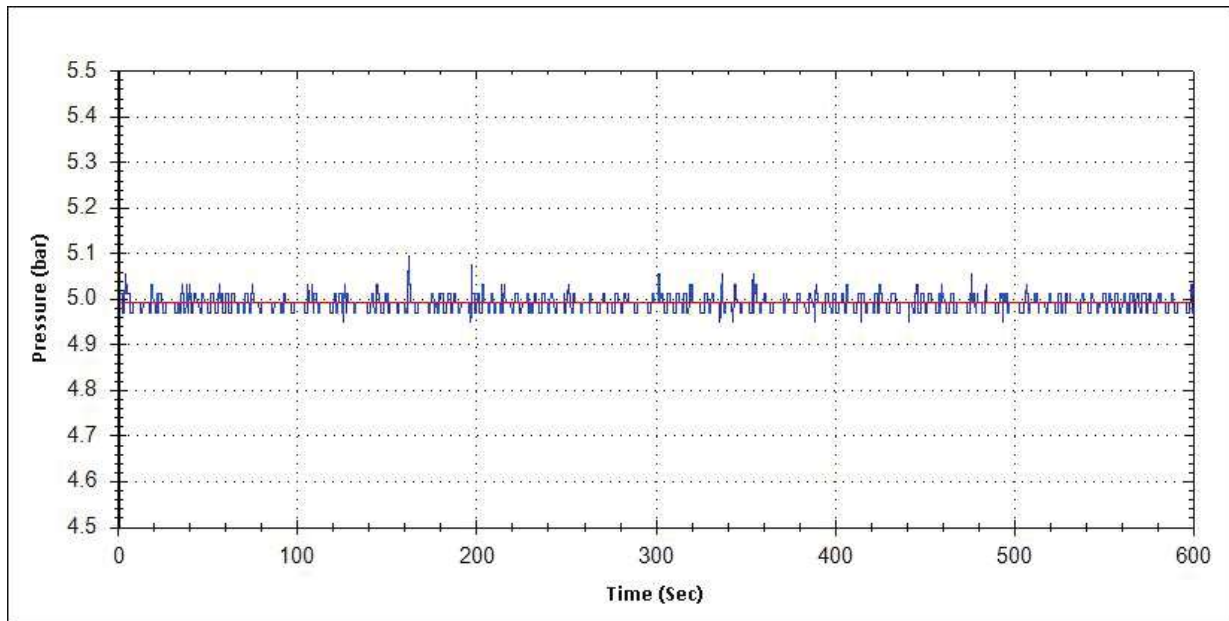


Figure 4.9: Calibrated pressure signal in blue and setpoint in red over time demonstrating the stability of the pressure in the chamber even at high flow rates.

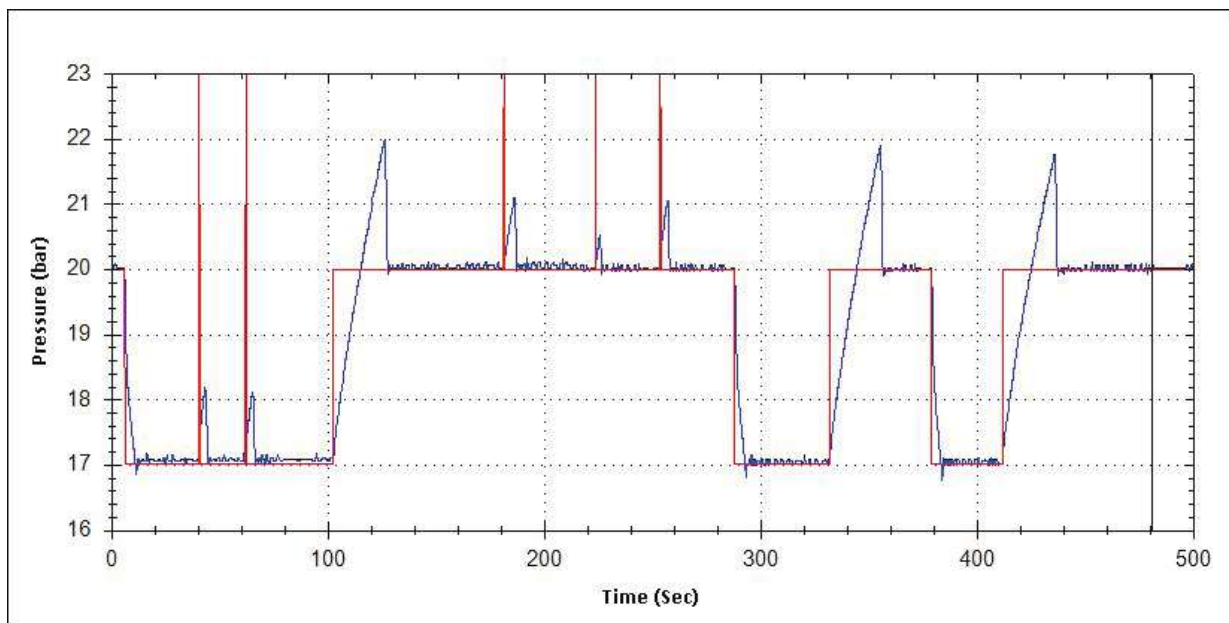


Figure 4.10: The system's responses to setpoint step changes and impulses with the final PID tuning settings for the new back pressure valve at high flow rates.

To improve safety on the software side of the facility, several conditional user interactions, required before triggering specific high risk events, were added to the VI to enforce proper procedures during start up and shut down. For instance, the heating process can only be started once the user confirms proper cooling of the device and functioning of the separator. Another safety relevant feature was added by providing a configurable selection switch to instantly toggle between two states of oxygen mass fraction in the oxidizer stream by the click of a single button when the flame needs to be extinguished or the oxygen supply to the system needs to be reduced quickly.

Pressure Testing

As the final phase and after the modifications has been done, the setup was pressure tested with water during two individual sessions. The equipment sensitive to water was removed from the chamber, and all the inlet and outlet pipes were plugged up and temporarily sealed. The system was first entirely filled through a single line with deionized water which afterwards was steadily compressed with the syringe pump to build up pressure in the water-filled chamber. During the first round, the pressure inside the system barely reached 20 bar because it was losing pressure too quickly for the pump to keep up at its maximum flow rate. Several minor, but noticeable leaks were patched, and a second session was conducted where the system reached 30 bar and was then left to rest. After about one hour, the system lost almost 10 bar in pressure, and the water was drained from the chamber to conclude the testing phase.

After the second round, several points prone to leakage in the system were identified. The most significant spots were found to be on the bottom plate, specifically at almost each of its fitted openings. First of all because the NPT threaded and taped fittings are incapable of providing enough sealing at elevated pressures, and more significantly due

to the special compression seal fittings bearing various types of wires. Even the properly sealed special fittings leaked fluid due to their fitted insulated leadwires which allowed for fluid flow between the insulation and the wire they were enclosing. It was found that this way a significant amount of water from the chamber was pushed into the electrical equipment at the workstation within an hour of continuous pressure load, and pouring from the insulated wires coming from the chamber. That poses no major safety risk during experimentation because the chamber is pressurized with inert gas, but makes a significant contribution to the overall leakage.

The second source was identified to be the sealed surfaces bearing o-rings. After small amounts of water had been observed leaking from those interfaces, the chamber and its viewports were disassembled and checked for water. In the grease on and around the o-rings, spots and streaks of water were clearly visible. The identified leaks can be compensated up to a certain point by adjusting the flow rate of the flush used to pressurize the system, but the stream is limited by the maximum flow rate of its respective mass flow controller, and also increases the demand on the inert gas supply system which can be significant at elevated pressures. For further reference, photographs of the bottom plate and the sealed surfaces during and after the pressure test can be found in Appendix B.

4.2 Nitrogen Supply System

When it comes to experimentation at elevated pressures, the gas supply system is of utmost importance. Not only does it deliver the required reactant gases to the reaction zone, it also feeds the flush stream with nitrogen to pressurize the chamber. The two key factors that determine the overall consumption and available amount of nitrogen, and thus the time frame for experiments, are the flow rate of the reactant streams and the pressure inside the chamber. As the counterflow burner requires continuous streams of reactants

during experimentation while the pressure simultaneously has to be kept constant, the flush used to set the pressure in the chamber also has to continuously flow through the system. Thereby, the flush depends on the other streams fed into the chamber. Furthermore, since the nitrogen for the flush is supplied from pressurized gas cylinders which are delivered at a certain pressure level, the time available for experiments is limited by the experimental conditions, specifically the pressure inside the chamber, because once the pressure in the cylinders drops below the experimental conditions, it cannot be kept up in the system due to the required continuous flow of the flush.

To expand the time frame for experiments at elevated pressures, it was necessary to set up a nitrogen supply system of greater capacity which ideally is capable of delivering its full available load at a constant pressure level without being dependent on the experimental conditions. As the first step and temporary solution while the final nitrogen supply system was designed and installed, multiple carts carrying manifolds of gas cylinders bundled together to packs of six were made to order [129]. With those, the number of previously ten available cylinders for nitrogen was expanded to twenty five. Even if the run time at elevated pressure was more than doubled, the system was highly labor and cost intensive because all the cylinders had to be exchanged manually after each experiment, and it was also inefficient due to the high amount of residual gaseous nitrogen (GN₂) when the cylinders were required to be exchanged.

Therefore, a new nitrogen supply system was designed utilizing a portable 1500 L tank for liquid nitrogen (LN₂) [80]. Due to geographical restrictions in the surroundings of the laboratory and space limitations, the system was installed inside the laboratory with the possibility to remove the portable tank from the system for refilling when the liquid nitrogen is depleted. The piping and instrumentation diagram (P&ID) in Figure 4.11 shows the system including its main devices and safety equipment. A cryogenic pump is withdrawing liquid nitrogen from the tank and feeding it into a vaporizer to pressurize a pack of sixteen

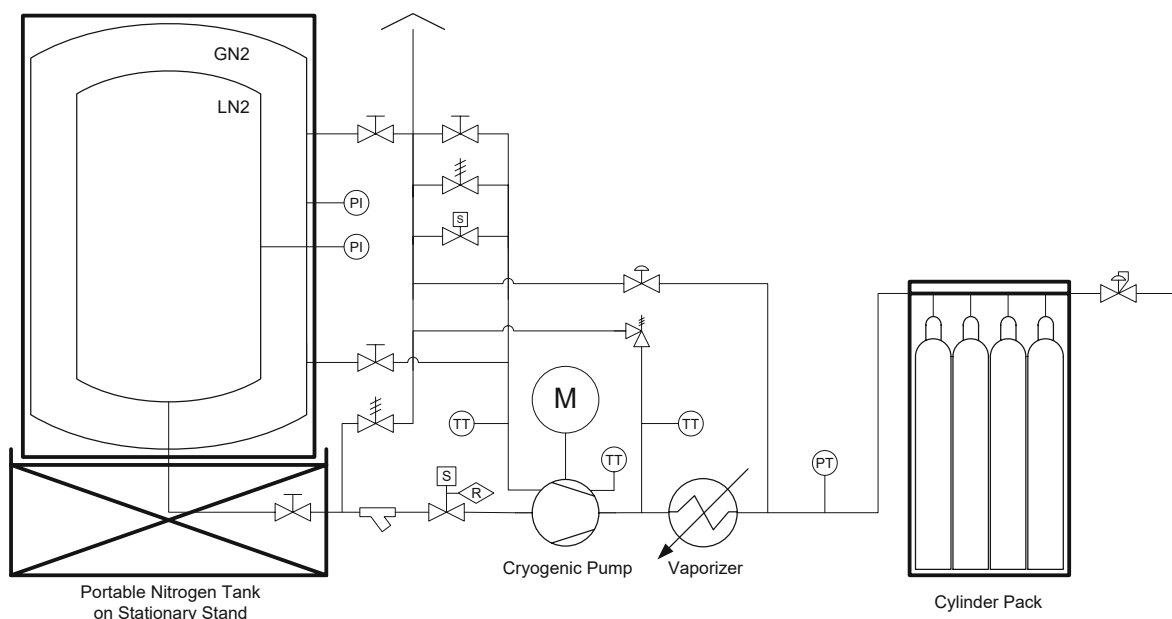


Figure 4.11: Simplified piping and instrumentation diagram of the newly designed nitrogen supply system for the HPCEF.

cylinders. From the pack, gaseous nitrogen can be withdrawn at a constant pressure level while the system can be operated to work on demand or continuously. Furthermore, in this configuration it is possible to empty out the tank with almost no residual nitrogen being wasted, and the refilling is a one-step procedure where the entire tank assembly is removed from its stand and taken outside of the laboratory with a forklift.

The new nitrogen supply is a highly effective system which minimizes the manual workload and downtime for preparing the HPCEF for experimentation and also provides enough gas to run experiments at elevated pressure over an extended time period including warm up and cool down procedures. The considerations and estimation of the run time for various experimental conditions with gaseous and liquid nitrogen are given in Listing B.2 together with photographs of the temporary cylinder cart and the final liquid nitrogen supply solutions in Appendix B.

4.3 Experimental Procedures

Due to the complex nature of the HPCEF's main device and the numerous critical safety risks involved, proper operation, start up and shut down procedures are vital for the operator's safety. For that reason, and to avoid errors during start ups which might require to abort an experiment prematurely, or lead to erroneous results, standard operating procedures (SOP) for each type of experiment were developed and evaluated. The two major factors during start up being the steady heating up of the oxidizer stream and the pressurization of the chamber with the inert flush stream makes them the focus of the SOPs.

Since the counterflow burner requires multiple continuous streams of reactants that are fed into the chamber while simultaneously the flush is used to maintain an overall constant pressure level, all the gaseous matter, the product and residual gases as well as the inert used for pressurization, need to be withdrawn from the vessel continuously. As the gaseous components in the chamber are already partially mixed and the accumulated matter is withdrawn through the same outlet leading to the back pressure valve and vent, the only option available to regulate the composition of the environment inside the chamber and to avoid accumulation of unwanted reactant gases and fumes, especially oxidizer and fuel, is through the flow rate of the flush.

At the atmospheric counterflow setup, the suction from the ventilation system is responsible for removing the gases from the reaction zone and guiding them to the vent. At the HPCEF, that task is achieved through the flush which not only pushes all the gases out of the system and towards the vent, but also plays a major role in stabilizing the flow field in the reaction zone and eventually the flame. That means that leakage from the chamber at any point other than the outlet to the vent needs to be compensated with a higher flow rate of the flush to avoid accumulation of reactant gases. When the stream pressurizing the chamber is set too low, gases from the reaction zone start breaking away which, due to the

difference in density, can clearly be observed when occurring as shown in Figure 4.12. Gas breaking away from the reaction zone and streaming into the chamber during an ongoing experiment is shown in the lower two stills in the figure and the relevant areas are marked in red. The reactant gases and fumes stream into the chamber which furthermore leads to a rise in temperature inside the pressurized vessel and also allows for vapor to deposit on the glass of the view ports, fogging the sight and making proper observation of the reaction zone impossible. On the other hand, when the flush is set too high, the flow field in the reaction zone and the resulting flame become very unstable and volatile.

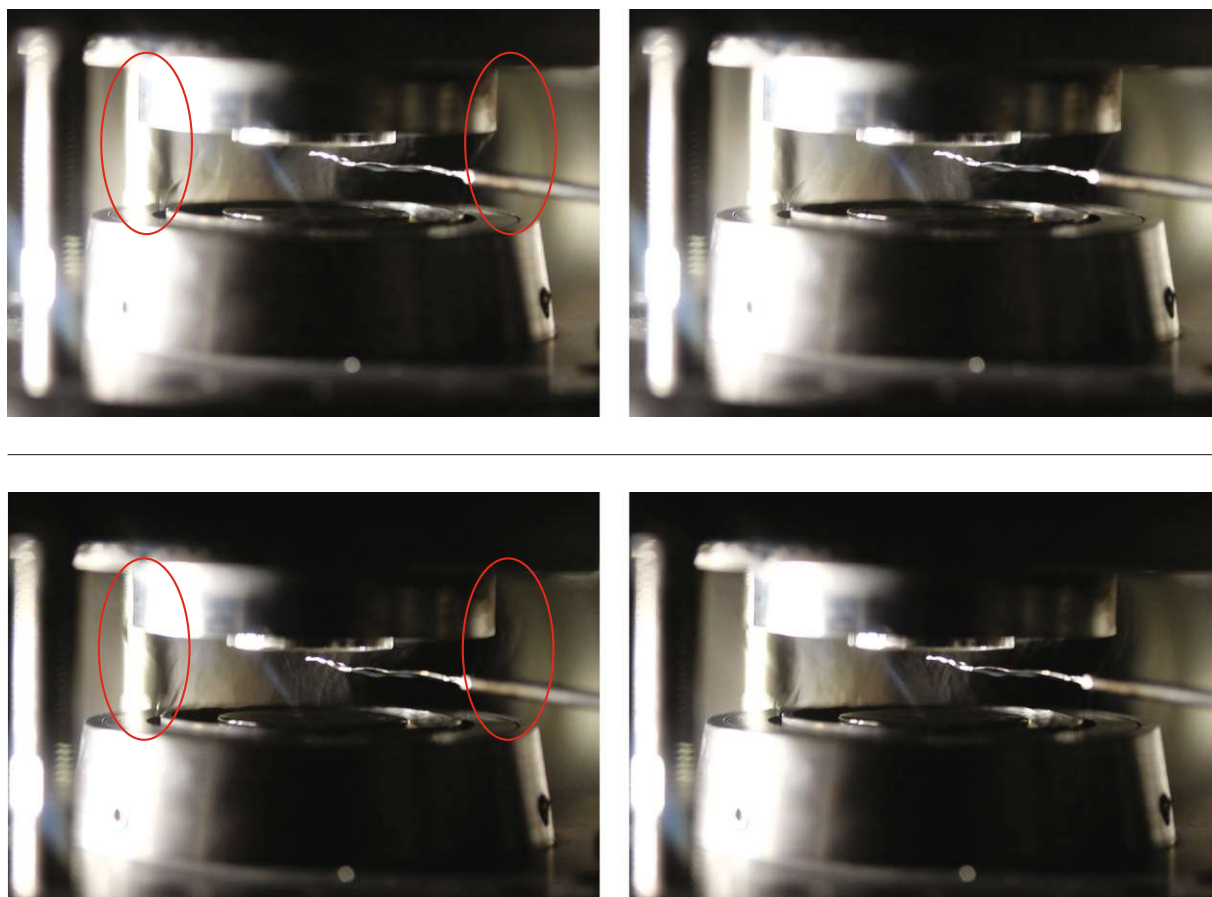


Figure 4.12: Two different stills each of the reaction zone during an experiment at 22 bar with the flush at 100 % (top) and 90 % (bottom) showing the relevant areas where reactant gas is noticeably breaking away and streaming into the chamber instead of the suction gap.

Through extensive testing and experimentation, it was found that for proper operation the flow rate of the flush has to be set to roughly double the rate of all the other streams entering the chamber combined. For that reason, a display showing the combined flow rate of all the streams feeding the counterflow burner was implemented into the VI, to allow the operator to properly adjust the flush throughout each experiment to avoid any other stream than the flush from accumulating in the chamber.

In addition to the inert flush, the heating of the oxidizer stream during start up and shut down needs to be carefully considered to ensure safety and a long equipment lifetime. From the safety point of view ideally, oxidizer should only stream into the chamber during an actual experiment, but as the silicon carbide heating element in the system requires continuous flow and an oxidizing environment when operated to avoid glass formation, local overheating, thermal stress, and eventually breaking, the oxidizer stream has to be turned on and carrying oxygen during start up and shut down. Furthermore, the load on the heating element needs to be increased gradually until the desired temperature of the oxidizer stream is reached to avoid arching between the element and surrounding equipment. After several test runs under various conditions it was confirmed that, to safely reach a temperature of 900 K at a low oxygen mass fraction of 0.075 in the oxidizer stream, heating should require at least 30 min to keep the formation of any depositions on the heating element under control and to avoid equipment failure.

4.4 Computational Considerations

Due to the accessibility and transparency of its underlying code and its flexibility, the open source software toolkit Cantera was chosen for the numerical and computational considerations of this thesis [25]. Cantera is capable of handling chemical kinetic, thermodynamic, and transport phenomena and numerically solving chemically reacting

flow problems to simulate flames. To model laminar flames stabilized in an axisymmetric stagnation flow such as in the counterflow configuration, Cantera uses a similarity solution to first reduce the governing equations to a one dimensional problem, and then generates solutions along the stagnation streamline in the center of the flow field for continuity, momentum, energy, and species [5]. Assuming a tangential velocity w of zero, steady state conditions, and ideal gas behaviour where

$$p = \rho RT \sum_i \frac{Y_i}{W_i} \quad (4.1)$$

holds true, while designating u as the axial velocity and $V_r = v/r$ as the scaled radial velocity, the governing equations in cylindrical coordinate form become [43,110]

Continuity:

$$\frac{\partial \rho u}{\partial z} + 2\rho V_r = 0 \quad (4.2)$$

Momentum (radial):

$$\rho u \frac{\partial V_r}{\partial z} + \rho V_r^2 = -\Lambda + \frac{\partial}{\partial z} \left(\mu \frac{\partial V_r}{\partial z} \right) \quad (4.3)$$

Energy:

$$\rho c_p u \frac{\partial T}{\partial z} = \frac{\partial}{\partial z} \left(\lambda \frac{\partial T}{\partial z} \right) - \sum_i j_i c_{p,i} \frac{\partial T}{\partial z} - \sum_i h_i W_i \dot{\omega}_i \quad (4.4)$$

Species:

$$\rho u \frac{\partial Y_i}{\partial z} = -\frac{\partial j_i}{\partial z} + W_i \dot{\omega}_i \quad (4.5)$$

where $\Lambda = \frac{1}{r} \frac{\partial p}{\partial r} = \text{constant}$ is the pressure eigenvalue, $j_i = \rho Y_i V_i$ the diffusive mass flux, and $\dot{\omega}_i$ the molar production rate of species i which is equivalent to R_i , the rate of change of species i in a fixed volume, described under Paragraph “Reaction Rates” in Section 2.1.3. Note that temperature and composition inside the reaction zone of the counterflow burner only change along the axial, but not the radial direction.

4.4.1 Chemical Kinetic Mechanisms

To solve the governing equations, it is necessary to provide Cantera with the property and reaction data for all the relevant species in the system in addition to the boundary conditions imposed by the respective experiment. Chemical kinetics data for sets of reactions is provided in form of mechanisms which also hold thermodynamic and transport data for their containing species. Given the mechanism files, boundary conditions, and governing equations, Cantera can simulate steady states of laminar flames and solve for the composition inside the reaction zone of the counterflow configuration.

For this thesis, the complete and specialized forms of the San Diego Mechanism from UC San Diego's Combustion Research Group were used due to their compact nature and resulting efficiency [9]. For the sake of comparison, or when certain surrogate fuel components not contained in the San Diego Mechanism were of interest, various forms of the PoliMi Mechanism from Politecnico di Milano's CRECK Modeling Group were used [11].

Mechanism Specification Version	Notes	Species Reactions	Species of Interest	References
San Diego Complete 2018-11	Nitrogen, JP10, DME, Heptane not included; based on Complete Version 2016-12-14	58 270	Propane	[9,82]
San Diego DME 2015-07-31	based on Complete Version 2018-11	62 282	Dimethyl Ether	[9,83]
San Diego Heptane 2015-03-01	based on Complete Version 2018-11	65 303	n-Heptane	[9,81,84] [31,46]

Table 4.1: Chemical kinetic mechanisms used with Cantera for computational investigations

Mechanism Specification Version	Notes	Species Reactions	Species of Interest	References
PoliMi C1-C3 1412	high temperature chemistry only	84 1698	Propane	[11,86]
PoliMi C1-C3 1412	high + low temperature chemistry	107 2642	Propane	[11,86]
PoliMi n-Heptane 1410	high + low temperature chemistry	106 1791	n-Heptane	[11,111] [89,112]
PoliMi n-Decane 1906	high + low temperature chemistry; kindly provided by CRECK Modeling Group	122 2747	n-Decane	[11]
PoliMi n-Dodecane 1410	high + low temperature chemistry	130 2399	n-Dodecane	[11,111] [89,112]
PoliMi Gasoline 1410	high + low temperature chemistry	156 3465	n-Heptane	[11,111] [89,112]
PoliMi Diesel 1410	high + low temperature chemistry	201 4417	n-Decane n-Dodecane	[11,111] [89,112]
PoliMi PRF + PAH 1412	high + low temperature chemistry; species and reaction of CSOLID removed based on PRF + PAH Version 1412;	299 11789	n-Heptane n-Decane n-Dodecane	[11,17,76] [3,93]
PoliMi Real Fuels 1412	high + low temperature chemistry; species and reaction of CSOLID removed	351 13263	n-Heptane n-Decane n-Dodecane	[11,34,88] [13,14,85]

Table 4.2: Chemical kinetic mechanisms used with Cantera for computational investigations (continued)

The specific mechanisms used for each experimental case are listed in Tables 4.1 and 4.2 together with their properties and respective bibliographical references which give further information on the containing reactions.

4.4.2 Simulation Module

Cantera's model of one dimensional counterflow diffusion flames assumes infinitely fast chemistry to generate and set an initial guess before a problem is solved. That means that if the boundary conditions defined by temperature, pressure, composition, and inlet velocity of the reactant streams allow for the existence of a flame in the reaction zone, Cantera will start the simulation in an ignited steady state and generate temperature and composition profiles along the central streamline accordingly. This behaviour is desired in the case of modeling extinction experiments and when determining the critical conditions for the existence of a flame are in the focus. But when it comes to autoignition experiments, the assumption of infinitely fast chemistry must be rejected to be able to capture the moment of ignition under given conditions.

To represent the experimental configurations and conditions of UC San Diego's Combustion Laboratory as accurately as possible and to facilitate and automate the generation of numerical solutions for the models of the various counterflow burners in place, Cantera's solver and Python implementation were used and its existing model for one dimensional counterflow diffusion flames was modified. For that purpose, a Python module named "UCSDComLab" was developed in the course of this thesis, which, by integrating Cantera as a solver, offers several objects and functions to model, simulate, and evaluate experiments conducted by the Combustion Research Group. During development, the SciPy toolkit in conjunction with a variety of other scientific data evaluation packages available for Python were implemented to interface with the module [36,41,70,126]. To

evaluate the required species properties for pure fluids outside the Cantera environment, or to generate data which is not directly deductible from the chemical kinetic mechanism files, the open source thermophysical property library CoolProp and its corresponding wrapper were used [2,10]. The structure of the Python module together with brief comments on the purpose of each object and method in its most recent version at date of writing are shown in Listing 4.1.

Listing 4.1: Structure of the UCSDCoMlab-Module - ucsdcomlab.py (excerpt)

```

1 # UCSDCoMlab Module: Counterflow and Experiment Class (Python 3.6.2)
2 # by Martin Hunyadi-Gall <mhunyadigall@ucsd.edu>

138 class Parameters(object):
139     """ Simulation Parameters ... """ ...

233 class Counterflow(cantera.CounterflowDiffusionFlame):
234     """ UCSD Combustion Lab Counterflow Setup Model ... """ ...

653 class Experiment(Parameters):
654     """ UCSD Combustion Lab Experiment ... """ ...

1537 class Result(object):
1538     """ ucsdcomlab.Result Object from ucsdcomlab.solve() """ ...

1586 class Log2Files(object):
1587     """ Log ucsdcomlab.Result Object Data to TXT, PDF, and MAT Files and write Cantera's
        ↪ XML and CSV Files """ ...

1799 class Log2File(object):
1800     """ Log complete Screen Output to LOG File """ ...

1820 def solve(*args,**kwargs):
1821     """ Create and solve ucsdcomlab.Counterflow Object using Cantera """ ...

1920 def fitFile(*args,**kwargs):
1921     """ Curve-fit Data in FIT File with ucsdcomlab.fitArrays() """ ...

1937 def fitArrays(*args,**kwargs):
1938     """ Curve-fit Data in Arrays and export Data to PDF and MAT Files """ ...

2020 def senFile(*args,**kwargs):
2021     """ Read and plot Sensitivity Analysis Data """ ...

```

To utilize the module, simple Python commands and scripts can be used to virtually set up a counterflow experiment by imposing the desired boundary conditions and then run a single experiment or simulate sets with varying conditions as shown in the following Code Listing of example command lines:

```
Exp = ucSDcomlab.Experiment(*param)
Res = Exp.run(loglevel=1)
Res = Exp.sim(mode=3,loglevel=1)
```

By passing the experimental parameters as arguments during the creation of a new instance of the UCSDComLab-Class “Experiment”, the object “Exp” is generated. It contains an object of the UCSDComLab-Class “Counterflow” which is representing the extended model of the counterflow burner and is based on Cantera’s model “CounterflowDiffusionFlame”. Depending on the provided parameters, the created Experiment-Object can then be either directly simulated or automatically iterated over given sets of conditions in different modes and with various options for solving method, data logging, and output generation. Both methods produce a Result-Object “Res” which can be used to display, manipulate, and post-process the acquired data. The numerical solving of the problem is done with the aid of Cantera by calling the Experiment-Object’s respective function “run” or “sim” depending whether a single set of experimental conditions is provided or one parameter is varied during the experiment. After the simulation with either method, the module can be used to process and store the resulting data in various formats to make it available for other software packages and facilitate evaluation. Full working examples of scripts used to simulate autoignition experiments at atmospheric and elevated pressures utilizing the module “UCSDComLab” are given in Listings A.2, A.3, and A.4 in Appendix A.

4.4.3 Modeling and Code Development

The first stage of the modeling and code development process consisted of the modification of Cantera’s counterflow model to allow the simulation of autoignition experiments and the implementation of a model representing the liquid pool configuration. During the second stage, the focus was the automation, processing, and presentation of solutions for extinction and autoignition experiments. In the course of development, Cantera’s model

was adapted and expanded to accept the exact same boundary conditions that are relevant for the experiments carried out by UC San Diego’s Combustion Laboratory to facilitate the usability of the module and the evaluation of the results. In general, the module was designed to seamlessly interface with Cantera without the need of having any knowledge about its internal workings, so that the operator is only required to provide information about the real physical experiment. For that reason, extensive error handling and several methods for analyzing convergence problems specific to the counterflow configuration were implemented while simultaneously maintaining readability of the code through comments, in case it becomes necessary to adapt the module for specific circumstances.

Autoignition Experiments

After correspondence with Cantera’s lead developer and looking into various methods of switching infinitely fast chemistry on and off during the computation of the initial guess, the simplest and most efficient way with minimal impact on the existing code was found to be the implementation of a single if-condition in Cantera’s function used to set the initial guess as shown in Listing 4.2.

Listing 4.2: Code segment to switch infinitely fast chemistry on and off according to the type of experiment while setting the initial guess before simulation - `ucsdcomlab.py` (excerpt)

```

567     """ ##### check Experiment Type ##### """
568     if self.exp == list(self.dctExp.keys())[1]:      # dctExp = {'AI':12,'EX':10}
569         self.gas.equilibrate('HP')
570     """ ##### if Extinction ##### """

```

The code in line 568 checks if the experiment is of the type “Extinction” (EX). If the outcome is positive, Cantera’s default behaviour is triggered and an initial guess with an ignited flame inside the reaction zone is generated if the given boundary conditions permit so. In case of an autoignition experiment (AI), line 569 is skipped and the initial guess is still set according to the boundary conditions, but without infinitely fast chemistry. This works

because Cantera uses its function “equilibrate” during the computation of the initial guess to calculate the gas mixture’s equilibrium state in the system adiabatically and at constant pressure (‘HP’). Omitting the “equilibrate(‘HP’)” statement, defaults Cantera’s behaviour back to calculating the mixture’s equilibrium at constant temperature and pressure (‘TP’) which virtually prevents the ignition before the start of the simulation and allows for the computation of numerical solutions for autoignition experiments.

Gaseous Inlets

To allow the module to work with the exact same parameters relevant for the real physical experiment, and since the inlets of Cantera’s counterflow model require the reactant streams to be provided in terms of mass flow, the strain rate formulation according to Seshadri and Williams [104] was implemented. Listing 4.3 shows how the oxidizer and fuel streams are initiated according to the boundary conditions. Afterwards, first the injection velocities and then their mass flow rates are calculated, differentiating whether the counterflow burner is in its gaseous or liquid pool configuration.

Listing 4.3: Calculation of the relevant parameters for the gaseous inlets of the counterflow burner model - ucsdcomlab.py (excerpt)

```

370 Ox = cantera.Solution(mechanism)           # create Oxidizer Stream Object
371 F = cantera.Solution(mechanism)           # create Fuel Stream Object
372 TinOx = TOxGas                             # Ox Inlet Temperature [K]
373 TinF = TFVap                               # F Inlet Temperature [K]
374 compYOx = 'O2:'+str(YO2)+'', N2:'+str(1-YO2) # Ox Composition [-]
375 compYF = Fuel+':'+str(YF)+'', N2:'+str(1-YF) # F Composition [-]
376 Ox.TPY = TinOx,P,compYOx                   # set Ox State
377 F.TPY = TinF,P,compYF                       # set F State
378
379 # calculate Mass Flow Rates: config = 2 (Gaseous/Vaporized) | 1 (Liquid Pool)
380 V2 = a2 * L / (2 * config)                   # Ox Injection Velocity [m/s]
381 V1 = sqrt(Ox.density * V2**2 / F.density)     # F Injection Velocity [m/s]
382
383 mdotOx = V2 * Ox.density                       # Ox Mass Flow Rate [kg/m^2 s]
384 mdotF = V1 * F.density                         # F Mass Flow Rate [kg/m^2 s]

```

Liquid Pool Configuration

Cantera's basic counterflow model requires both inlets to be positive and virtually flow or otherwise no mixing of the two streams will occur, thus generating a trivial solution. Therefore, the mass flow originating from the evaporation of the liquid fuel needs to be modeled for computational considerations of the liquid pool configuration. Assuming that the mass flow from fuel evaporation \dot{m} matches the burning rate on the oxidizer side, the formulation of the balance conditions at the liquid-gas interface on the gaseous side of the liquid pool configuration is [30,64,78]

$$\dot{m}Y_i + j_i = 0 \quad i \neq F \quad (4.6)$$

$$\dot{m}(1 - Y_F) - j_F = 0 \quad (4.7)$$

$$\lambda \frac{dT}{dz} - \dot{m}h_L = 0 \quad (4.8)$$

$$T = T_{F,B} \quad (4.9)$$

where λ denotes the thermal conductivity of the gas mixture, h_L the latent heat of vaporization of the liquid, and the surface temperature is presumed to be at the fuel's boiling point $T_{F,B}$.

Implementation of these equations to complement the existing governing equations in the model, so that the evaporation rate \dot{m} is calculated during the numerical processing and becomes part of the solution, would drastically increase computation time. Therefore, instead of altering the governing equations to match the liquid pool configuration case, the mass flow originating from fuel evaporation is approximated based on boundary layer

theory and empirical evaluation. That way, the approximated mass flow rate can directly be used on the existing model's gaseous fuel side inlet, facilitating the computations considerably while maintaining the accuracy of the position of the flame as observed during experimentation. Listing 4.4 is showing the code segments implementing the boundary layer approximation [95].

Listing 4.4: Calculation of the relevant parameters for the liquid pool configuration of the counterflow burner model - ucsdcomlab.py (excerpt)

```

407 # Fuel Parameters
408 TFB = coolprop('T','P',P,'Q',0,Fuel) # Boiling Point [K]
409 TFC = coolprop('TCRIT',Fuel) # Critical Temperature [K]
410 PFC = coolprop('PCRIT',Fuel) # Critical Pressure [Pa]
411 vFC = 1/coolprop('RHOCRIT',Fuel) # Critical Specific Volume [m^3/kg]
412 hVap = coolprop('H','P',P,'Q',1,Fuel) # Specific Enthalpy of Vapor at
      ↪ Boiling Point [J/kg]
413 hLiq = coolprop('H','P',P,'Q',0,Fuel) # Specific Enthalpy of Liquid at
      ↪ Boiling Point [J/kg]
414 hFL = hVap - hLiq # Latent Heat of Vaporization [J/kg]
415 kF = coolprop('L','P',P,'T|gas',TFB,Fuel) # Thermal Conductivity at
      ↪ Boiling Point [W/m K]

427 # Oxidizer Parameters
428 # ... approximated as Air
429 rhoOx = coolprop('D','P',P,'T',TOx,'Air') # Density [kg/m^3]
430 muOx = coolprop('V','P',P,'T',TOx,'Air') # Viscosity [Pa s]
431 ReOx = VOx * L * rhoOx / muOx # Reynolds Number [-]
432
433 # Liquid Pool Parameters
434 TFL = TFL # Liquid Fuel Temperature [K]
435 TFSur = TFB # Pool Surface Temperature [K]
436 TFVap = TFSur # Fuel Vapor Temperature [K]

446 charL = factorLP * L # Characteristic Length [m]
447 dy = charL * ReOx**(-1/1.5) # Boundary Layer Thickness [m]
448 dT = TOx - TFSur # Temperature Difference [K]
449
450 mdotF = kF/hFL * dT/dy # Fuel Evaporation Rate [kg/m^2 s]

```

At first, all the required parameters of the fuel and oxidizer, approximated to be air, are gathered. Then, the boundary layer thickness is estimated in line 447 utilizing an adapted approximation of a laminar plate boundary layer and an empirically determined factor. Eventually, in line 450 the fuel evaporation rate is calculated through an energy balance similar to the one in Equation (4.8) by replacing the differentials with differences, or more specifically, the change of temperature over the boundary layer.

5 Investigations, Results, and Discussion

5.1 Atmospheric Pressure

The following sections describe the investigations at atmospheric pressure, carried out by using various configurations of the counterflow burner setup described in Section 3.2, and discuss their results. Each experimental setup and its respective boundary conditions are given, together with detailed information and notes on the experimental procedures. The exact numerical values of the experimental data gathered herein are summarized in tabulated form in Appendix D for reference.

5.1.1 Experimental and Computational Investigation on Critical Conditions of Extinction of Laminar, Non-Premixed Dimethyl Ether Flames

Dimethyl ether (DME), also known as methoxymethane, is a colorless gas at room temperature with a boiling point of $-24.8\text{ }^{\circ}\text{C}$ [6]. Its properties allow it to be liquefied under mild conditions for the purpose of storage, similar to the behaviour and handling of propane. Of the chemicals and components examined in this thesis, DME is the component most influenced by low-temperature chemistry during combustion [1,15,16,128]. Today, the simplest possible ether, DME, has low-temperature applications in laboratories, is a precursor for synthesis reactions, a compound in freezing agents, and can be used as an alternative fuel in modified diesel engines.

Previous investigations by UC San Diego's Combustion Research Group examined the influence of the stoichiometric mixture fraction on the limit conditions of extinction of DME flames [37,54]. Based on their results and findings, and to test the new counterflow model and solver module, the existing experimental data was reevaluated after some technical

changes to the atmospheric counterflow setup had been implemented. Additional data points were gathered to properly determine and narrow down the standard error, and a computational analysis employing the new UCSDComLab-Module, Cantera, and the San Diego Mechanism were carried out.

Experimental Setup and Boundary Conditions

The setup used to carry out the experimental investigations was the basic gaseous configuration of the atmospheric counterflow burner with the extinction top in place, described in Section 3.2 and shown in Figures 3.4 and 3.6 in the same section. Due to the highly reactive nature of DME and its incompatibility with certain materials used in the mass flow controllers, their diaphragms needed to be exchanged to ensure accurate and safe operations. Also, careful attention was paid to the actual volume flow delivered by the mass flow controllers during operation because it was observed, that after prolonged periods of experimentation with high DME demand, the actual flow would drop gradually due to the lack of capacity to regulate the evaporation of DME to match or surpass the volume flow demand imposed by the experimental conditions.

During the experiments, both, the oxidizer (subscript 2) and fuel stream (subscript 1), were delivered at the system boundary at constant temperature $T_1 = T_2 = 298\text{ K}$, and atmospheric pressure $P = 1\text{ atm} \hat{=} 1.013\text{ bar}$. Since extinction experiments were carried out, the research group's standard separation distance of $L = 10\text{ mm}$ between the two outlet ducts was applied. During experimentation, the boundary conditions were established before the mixture in the reaction zone of the counterflow burner was ignited manually. With the stabilized flame, the strain rate was steadily increased by smaller and smaller increments during each run, until the extinction of the flame was noticed. The same experiments were carried out multiple times throughout different days where the strain rate

values of the oxidizer stream at the inlet, a_2 , were recorded as the extinction strain rates for each set of boundary conditions. Figure 5.1 is showing the counterflow burner used for the experiments, and a stabilized flame while determining the extinction strain rate.

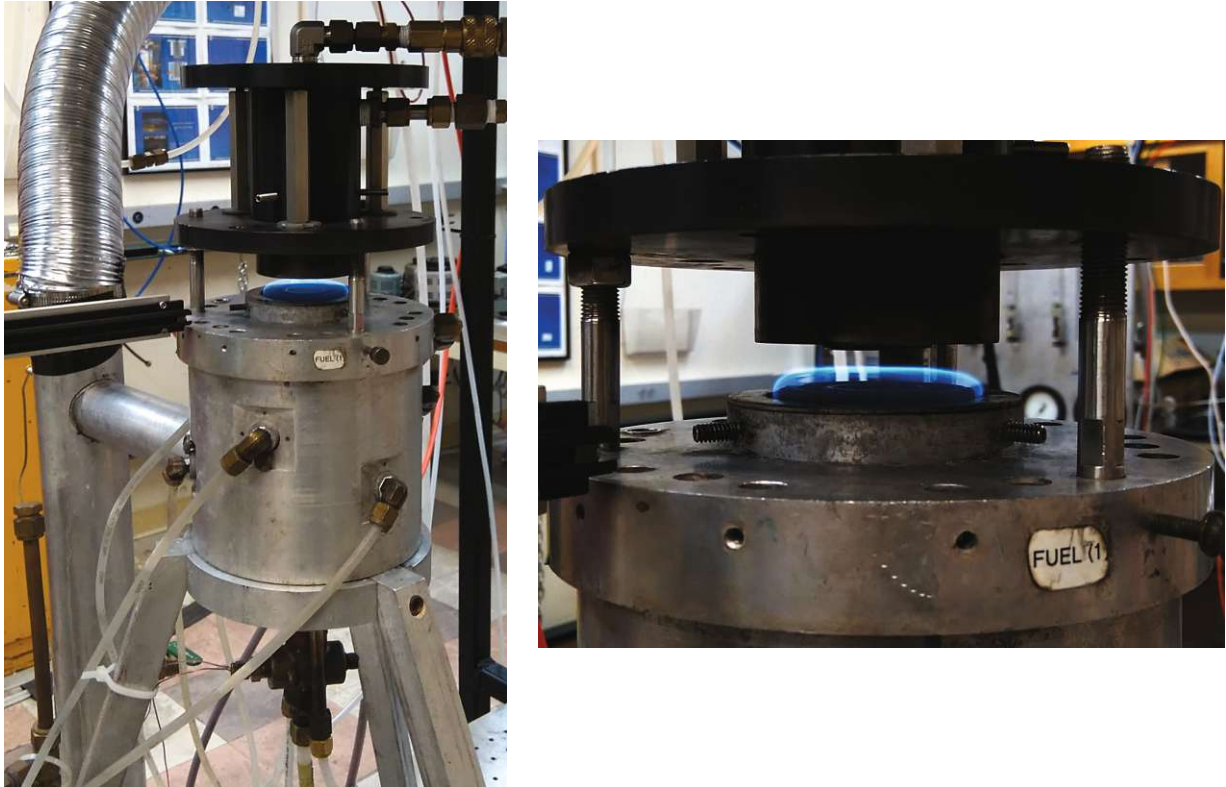


Figure 5.1: Counterflow burner in gaseous configuration (left) and stabilized, non-premixed dimethyl ether flame (right) during an experiment to determine the extinction strain rate.

The experiments were carried out for various compositions of the oxidizer and the fuel stream, with fixed mass fractions at the boundary for each set. The oxidizer stream was described by the mass fraction, $Y_2 = Y_{Ox, boundary}$, and was made up of oxygen as the oxidizer, and nitrogen as an inert, while the fuel stream consisted of varying mass fractions, $Y_1 = Y_{F, boundary}$, of DME as the fuel, and nitrogen. Experimental data was gathered for various values of the stoichiometric mixture fraction, Z_{st} , while the adiabatic flame temperature, T_{st} , was kept constant at 2000 K. The oxidizer and fuel mass fractions for each set of boundary conditions were calculated upfront by applying asymptotic analysis [66,100,103,105,106], and assuming a Lewis number, Le , of 1 for all

species, except DME, which was chosen to be 1.5. Eventually, the following relations between Y_1 , Y_2 , Z_{st} , and T_{st} for steady, axisymmetric, laminar flow inside the counterflow burner were derived [37,54]

$$T_{st} = T_2 + (T_1 - T_2)Z_{st} + \nu Q_{DME} Z_{st} \frac{1 - Z_{st}}{c_p W_{N_2}} \quad (5.1)$$

$$Z_{DME} = \frac{1}{2} \operatorname{erfc} \left[\sqrt{Le_{DME}} \operatorname{erfc}^{-1}(2Z) \right] \quad (5.2)$$

$$\frac{dZ}{dZ_{DME}} = \sqrt{Le_{DME}} \exp \left\{ (1 - Le_{DME}) \left[\operatorname{erfc}^{-1}(2Z) \right]^2 \right\}^{-1} \quad (5.3)$$

$$Y_1 = \nu \frac{W_{DME}}{W_{N_2}} (1 - Z_{DME,st}) \left(\frac{dZ}{dZ_{DME}} \right)_{st} \quad (5.4)$$

$$Y_2 = 3\nu Z_{st} \frac{W_{O_2}}{W_{N_2}} \quad (5.5)$$

where Q_{DME} , the heat released per mole of DME consumed or heating value, was assumed to be 1328 kJ/mol, c_p was considered to be 1300 J/(kg K), and ν was introduced as a notational convenience during the derivation of the given relations, representing the stoichiometry of the overall reaction of DME with oxygen. Table 5.1 lists the boundary conditions as a result of the evaluation of Equations (5.1) - (5.5) for all values of Z_{st} at which experimental data was gathered, imposing an adiabatic flame temperature of 2000 K.

Experimental and Computational Results

The experimental data gathered through measurements by the method described earlier is summarized in Figure 5.2. The strain rate at which the flame inside the reaction zone of the counterflow burner could no longer be maintained and extinguished is plotted for

Z_{st}	Y_1	Y_2
0.134	1.000	0.185
0.160	0.795	0.190
0.190	0.635	0.198
0.220	0.526	0.205
0.314	0.335	0.233
0.400	0.247	0.267
0.500	0.188	0.320
0.600	0.150	0.400
0.700	0.125	0.533
0.800	0.106	0.800

Table 5.1: Fuel (Y_1) and oxidizer (Y_2) mass fractions at the boundary for various values of stoichiometric mixture fraction (Z_{st}) at constant adiabatic flame temperature $T_{st} = 2000$ K

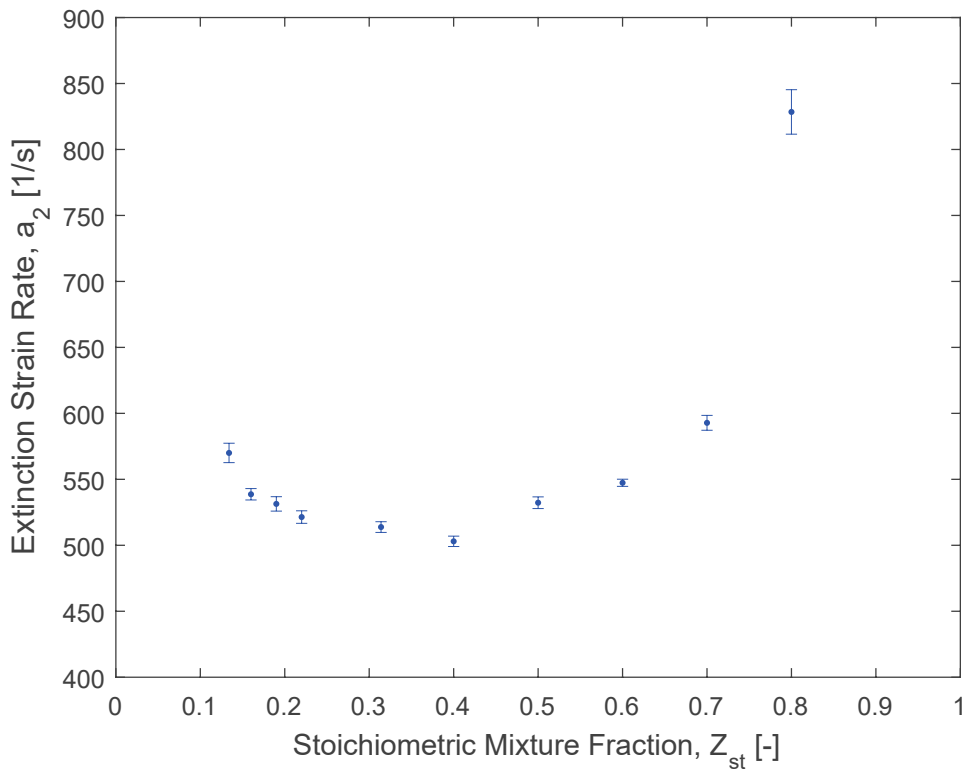


Figure 5.2: Experimental data of the measured strain rate of extinction of a non-premixed DME flame at atmospheric pressure and for various stoichiometric mixture fractions maintaining a constant adiabatic flame temperature of 2000 K. (Appendix, Table D.1)

various values of the stoichiometric mixture fraction, for all of which the adiabatic flame temperature was calculated to be 2000 K. The mean values of all the meaningful data points gathered are given together with their respective standard errors. The issues that arose during experimentation at relatively low and high stoichiometric mixture fractions are evidently reflected in the measurements and the calculated errors. Nevertheless, it is clear, that with increasing stoichiometric mixture fraction, at first, the extinction strain rate slightly drops and at roughly $Z_{st} = 0.4$ starts to rise again. Below the value of 0.16 and, even more significantly, beyond 0.7 it becomes more and more difficult to produce consistent data since the experiment becomes more sensitive to slight changes arising from the equipment and environment, for example surroundings, equipment, and reactant gas temperatures and particularly instabilities in the supply of DME or from the mass flow controllers during the, notably non-synchronous, adaptation of each stream to the next higher level of the strain rate.

The resulting flames generated during the experiments were simulated under the very same conditions using Cantera, the models and functions from the UCSDComLab-Module, and the San Diego Mechanism. The computational results, represented by a solid line, are compared to the gathered experimental data points in the graph in Figure 5.3. During the numerical calculations, convergence issues under conditions of relatively low and high stoichiometric mixture fractions, similar to the instabilities during the measurements on the physical experiment were encountered, and were thereby omitted from consideration for the generation of the final simulation results.

As shown in Figure 5.3, the computations using the San Diego Mechanism match the experiments, and especially the trend of the data, well. However, to generate meaningful computational results, the initial grid and also its refinement criteria, internally used by the solver during calculations, need to be considered and carefully chosen. Throughout the computational investigations for this thesis, it was consistently observed that Cantera, its

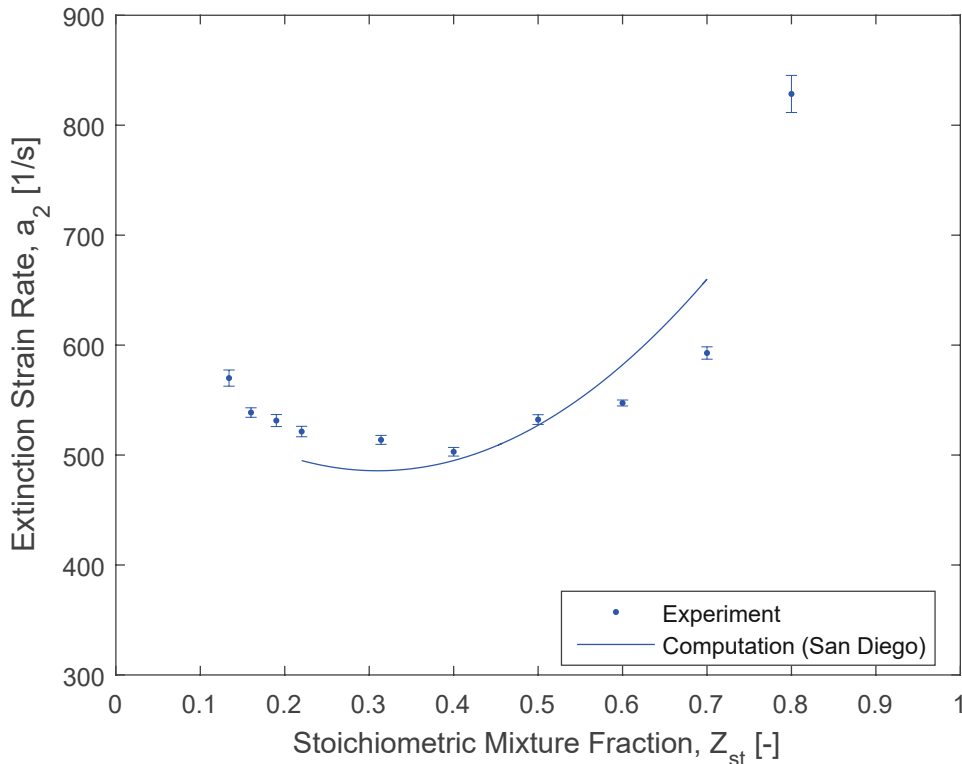


Figure 5.3: The computational results from Cantera used in conjunction with the UCSDComLab-Module and the San Diego Mechanism compared against the experimental data obtained through measurements on the real physical device. (Appendix, Table D.1)

methods, the underlying models, and by extension also the UCSDComLab-Module can be highly sensitive to the solution grid when certain mechanisms are used, particularly so when low-temperature chemistry is involved. This can be demonstrated for DME flames in conjunction with the San Diego Mechanism by adapting the initial grid and changing how Cantera’s solver refines the grid from one iteration to another until a final solution for all parameters is generated. Herein, the term “tight” is used for criteria with little tolerance that aim for a finer grid and resulting resolution inside the domain where the solver is operating, while “loose” signifies a high tolerance resulting in a coarse final grid. The graph in Figure 5.4 shows how significantly results, all of which are otherwise using the same boundary conditions and mechanism, can differ for various solution grids and refinement criteria.

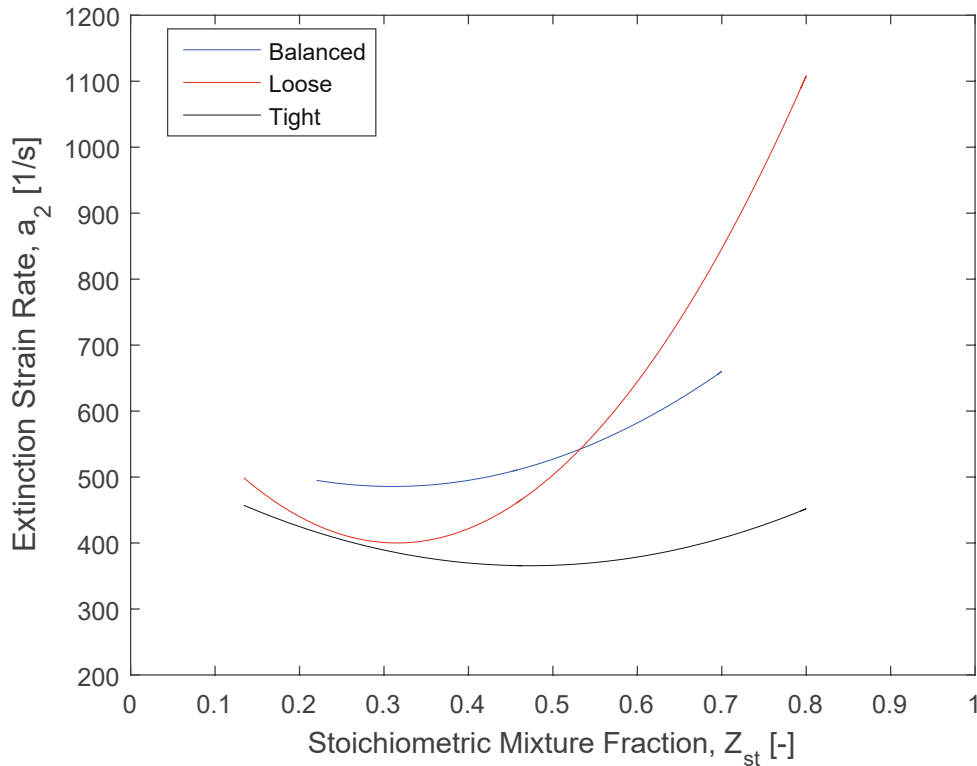


Figure 5.4: Comparing computational results from Cantera used in conjunction with the UCSDComLab-Module and the San Diego Mechanism for the same set of boundary conditions, but different refinement criteria settings and resulting final solution grids.

To visualize the differences in the final solution grid, which is automatically generated during the simulation process by Cantera and is based on the initial grid and its refinement criteria, two graphs, each at individual conditions, are given in Figures 5.5 and 5.6. They show the temperature profiles of the reaction zone inside the counterflow burner right before extinction of the DME flame, with the fuel stream inlet on the far left and the oxidizer stream inlet on the far right side. These graphs of the temperature profiles are automatically generated by the UCSDComLab-Module during the computations and prove to be a helpful tool in validating computational results on the way to a final solution. If required, and as Cantera calculates the parameters during the computations, the graphs can also include profiles for velocity, local strain rate, pressure, density, and every species concentration involved.

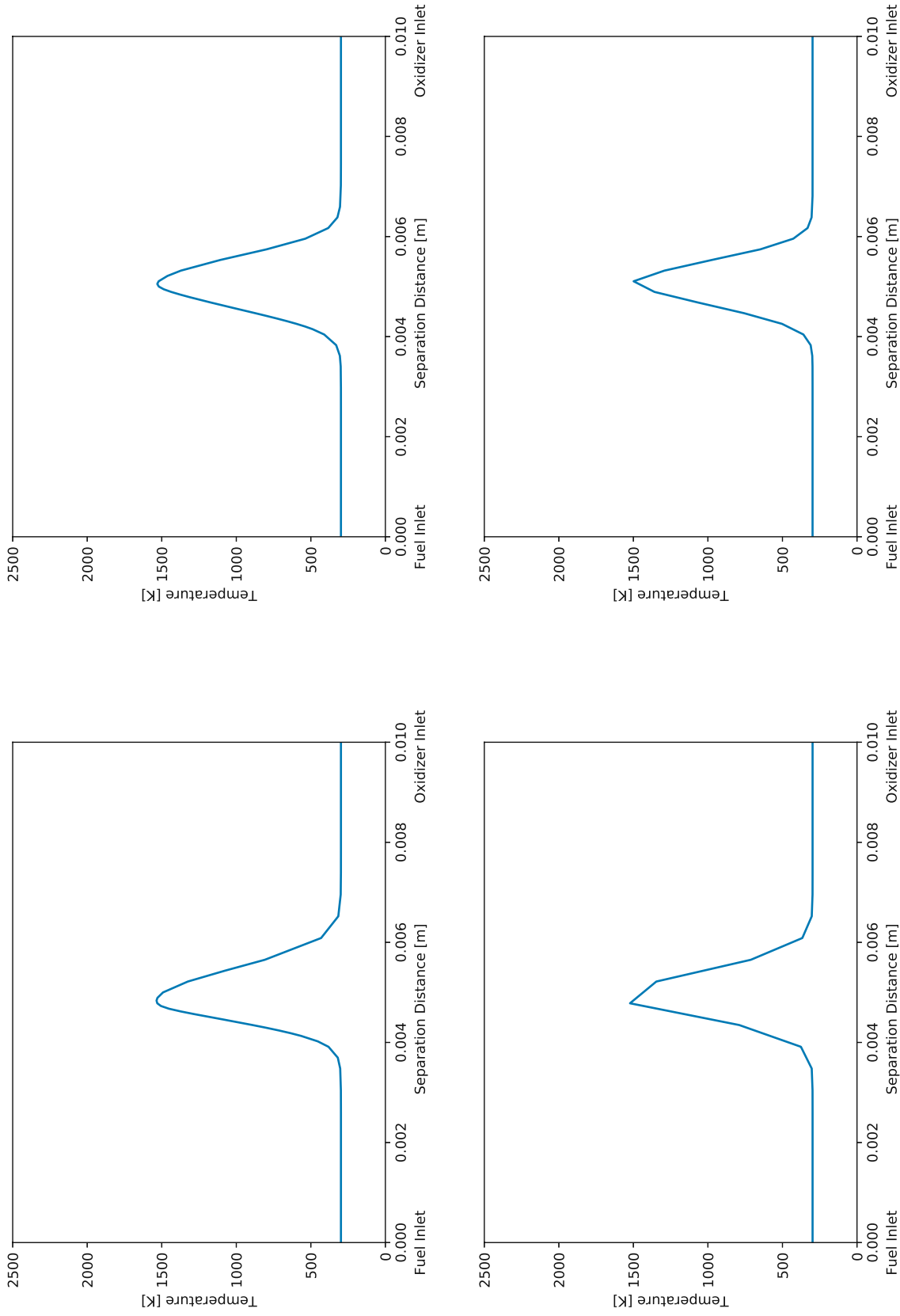


Figure 5.5: Computationally generated temperature profiles of the reaction zone inside the counterflow burner at $Z_{st} = 0.7$ for tight (top) and loose (bottom) refinement criteria, indicating the position of the DME flame where the maximum is.

Figure 5.6: Computationally generated temperature profiles of the reaction zone inside the counterflow burner at $Z_{st} = 0.4$ for tight (top) and loose (bottom) refinement criteria, indicating the position of the DME flame where the maximum is.

Both figures demonstrate that tighter settings, shown respectively in the top graphs, produce grids, and ultimately profiles, of finer resolution, while in general, they predict lower extinction strain rates than with loose criteria. It is noticeable in Figure 5.4, that at $Z_{st} = 0.7$ the difference in simulated extinction strain rate is about 500 1/s, while at $Z_{st} = 0.4$ it is below 50 1/s. At the same time, looking closer at the width of the virtual flames in Figures 5.5 and 5.6, it can be seen that at $Z_{st} = 0.4$ the flame before extinction simulated with loose settings, shown in the bottom graph, is slightly more narrow than its tight settings counterpart on top, although the difference in strain rate between top and bottom is only 50 1/s. On the other hand, comparing the graphs in Figure 5.5 at $Z_{st} = 0.7$ reveal that the flame thickness is roughly the same for both settings, even though their underlying strain rates differ by 500 1/s, a factor of ten compared to the difference at $Z_{st} = 0.4$.

The difference in flame thickness, as well as the variation in extinction strain rate by refinement criteria, can be attributed to the combination of the resulting solution grid and the local slopes of the profiles at the grid's individual points inside the domain where Cantera's solver is operating. Whether tight or loose settings are used, there is always a chance for convergence issues if the slope at a certain point along one of the parameter profiles is too steep. That happens partially due to the nature of the counterflow setup and its model, but also because of the imposition of certain boundary conditions. When strain rates at the boundaries are high, for instance, the mixing layer and domain of the flame become more narrow and thus more difficult for the solver to operate on. Under most circumstances, Cantera even warns the user about the individual layers being too thin and to consider different conditions for better results.

Issues arise because the mixing layer inside the reaction zone of the counterflow burner can be, by design, very thin, leaving the profiles inside the simulation domain constant for most of their segments between two grid points, but bearing very steep inclination and declinations over short distances. For that reason, it is essential to choose a proper initial

grid and refinement criteria for each set of boundary conditions, so that more grid points are evaluated only where they are required and not where no changes are to be expected. That means taking more points in and around the mixing layer into consideration instead of those near the inlets. As seen in Figures 5.3 and 5.4, by testing for and eventually using varying “balanced” settings that capture the profiles at relevant points during individual simulations, it is possible to generate reliable and meaningful computational results while simultaneously avoiding convergence issues.

5.1.2 Experimental and Computational Investigation of Extinction and Auto-ignition of Propane and n-Heptane in Non-Premixed Flows

As DME, propane is a colorless gas at room temperature and atmospheric pressure. Its boiling point of $-42.1\text{ }^{\circ}\text{C}$ allows for its liquefaction under relatively mild conditions, thereby making the alkane a member of the group of liquefied petroleum gases (LPG) [6]. It is a common fuel used for transportation as well as various industrial and domestic applications. Because of its low emission characteristics during combustion, it is considered a clean fuel.

Several experimental measurements in various configurations with and without flow were previously conducted to examine the mechanisms involved in propane’s combustion, and to elucidate the influence of changes in boundary conditions on critical conditions. From a chemical point of view, even though it is known that propane does exhibit low-temperature chemistry, it was demonstrated in previous experiments that it is generally not significant when tested in the counterflow configuration because of the low residence time of the reactants resulting from elevated strain rates [12,35,60,96].

Unlike propane, n-heptane is a liquid at room temperature and therefore requires external vaporization before investigation in the counterflow burner in its gaseous configuration. Its main application today is its use as a solvent in chemical laboratories and commercial products. Furthermore, n-heptane makes up a significant part of gasoline, thus making it an important component of surrogate fuels. In its pure form and together with iso-octane, it is used in test engines as a primary reference fuel (PRF) and surrogate component for octane ratings.

The seven carbon alkane, n-heptane, was also thoroughly tested in configurations with and without flow to provide insights into the underlying combustion system [4,7,87,130]. Previous experiments in the liquid pool configuration suggest the presence of significant low-temperature chemistry, which, as with propane, is expected to be negligible in the counterflow configuration when prevaporized due to low residence time. Smaller alkanes, like propane, play a significant role in the combustion of high molecular weight hydrocarbons, such as n-heptane, as they are an important component formed in a subsystem of the overall combustion, thus establishing a close relation between the two chemical groups and their kinetic mechanisms [3,30,42,49,52,53,97,98,101,102].

The measurements herein, employing the counterflow configuration which is a powerful tool to highlight the interaction of chemistry and flow during combustion, are taken to investigate the influence of variations of fuel and oxygen concentrations on the critical conditions of extinction and autoignition of propane and n-heptane [38,40,47,48,48,104,131]. The results are also compared with computations generated with Cantera and the new UCSDComLab-Module, using the San Diego, and various versions of the PoliMi Mechanism. Furthermore, the extent of the influence to be expected from the low-temperature chemistry on the experiments is examined with the aid of different mechanism files containing or omitting low-temperature chemistry respectively.

Setup and Boundary Conditions for Experiments with Propane

The setup employed during the experimental investigations was the basic gaseous configuration of the atmospheric counterflow burner, with either the extinction or auto-ignition top in place. The apparatus is described in Section 3.2 and schematically depicted in Figures 3.4, 3.5, and 3.6 in the same section. No extra mechanism was used to regulate the evaporation of propane which made it a requirement for the operator to constantly check if the mass flow controller setpoints and prescribed boundary conditions were met by the actual flow rates.

During the experiment to determine the extinction strain rate, the fuel mass fraction, Y_F , in the fuel stream, made up of propane and nitrogen, was kept constant at a value of 0.6. The extinction strain rate, a_2 , was then recorded for various oxygen mass fractions in a range between 0.195 and 0.233. The oxidizer stream was made up of a mixture of oxygen and nitrogen and, as the fuel stream, mixed inline and delivered to the counterflow burner at room temperature of 298.15 K to match the required boundary conditions. Each set of experiments for individual oxygen mass fractions was repeated several times, starting with a stabilized flame at a strain rate below extinction and gradually increasing the strain rate by smaller and smaller increments until the extinction event was observed. The setup and a stabilized flame during an ongoing experiment is shown in Figure 5.7.

For the autoignition experiments, the oxygen mass fraction, Y_{O_2} , and the strain rate, a_2 , were kept constant at 0.23 and 400 1/s respectively for fuel mass fractions between 0.3 and 0.6. Additionally, sets at constant fuel mass fractions of 0.21, 0.4, and 0.6 were conducted, varying the oxygen mass fraction in a range between 0.07 and 0.23 for each set. All experiments were repeated several times to reach an acceptable level of standard error. The boundary conditions were kept constant, except for the temperature of the oxidizer stream, T_2 , which was slowly increased and measured with the aid of a thermocouple



Figure 5.7: Counterflow burner in gaseous configuration (left) and stabilized, non-premixed propane flame (right) during an experiment to determine the extinction strain rate.



Figure 5.8: Counterflow burner in gaseous configuration with autoignition top (left) and non-premixed propane flame (right) established after reaching autoignition temperature.

placed close to the oxidizer duct. The stream temperature was regulated manually by the operator through the output of a transformer powering the heating element in the duct of the autoignition top. To compensate for the change in temperature and resulting volume flow, the measured temperature was also used to automatically calculate and update the mass flow controller setpoints accordingly, maintaining constant boundary conditions throughout the experiments. The temperature of the oxidizer stream was gradually increased until autoignition was observed and subsequently recorded. The setup and a stabilized flame after the autoignition event has taken place is shown in Figure 5.8. Photographs of the heated reaction zone during a live autoignition experiment are added in Appendix C.

Experimental and Computational Results for Extinction of Propane

The results from the extinction experiments with propane are given in Figure 5.9. Included in the figure are the numerical results from the simulations with Cantera used in conjunction with the UCSDComLab-Module. The Complete San Diego Mechanism and the C1-C3 PoliMi Mechanism with and without low-temperature chemistry were used. No major difficulties were experienced throughout the experiments with propane, and as indicated by the narrow error bars, the measurements proved to be highly consistent and reproducible even on different days and after required maintenance activities, adjustments, and resets on the experimental setup and devices. As seen in Figure 5.9, the strain rate at extinction increases with increasing oxygen mass fraction on the oxidizer side when the fuel mass fraction is kept constant at a value of 0.6. The predictions from the simulations with both mechanisms, San Diego as well as PoliMi, agree very well with the experimental results, although San Diego consistently yields slightly lower values, while PoliMi tends to over-predict the extinction strain rate. The deviation between the two mechanisms also increases with the oxygen mass fraction, giving the San Diego Mechanism an advantage at higher oxygen mass fractions.

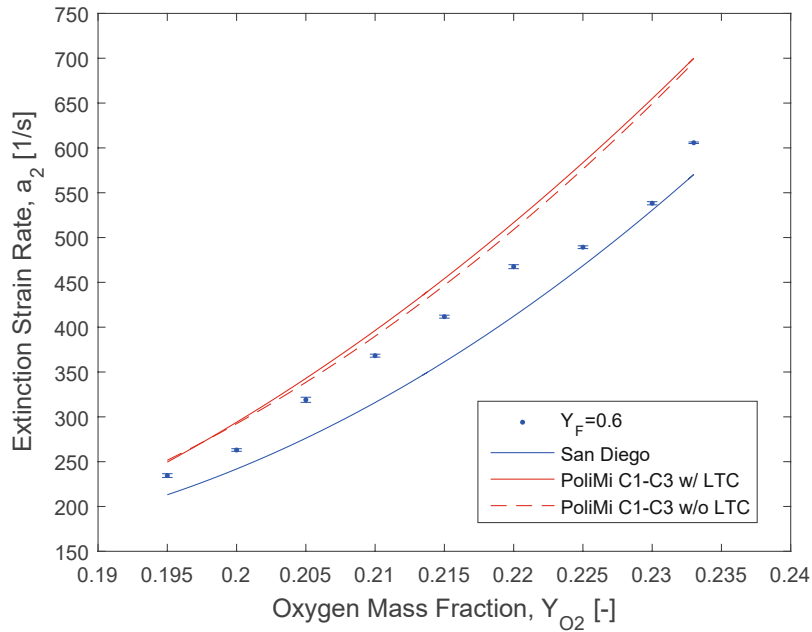


Figure 5.9: Experimental data obtained through measurements plotted with standard errors and compared against computational results from Cantera used in conjunction with the UCSDComLab-Module and different mechanisms. (Appendix, Table D.2)

Comparing the computational results achieved with the aid of the PoliMi Mechanism with and without low-temperature chemistry reactions included, it can be seen that, as expected, low-temperature chemistry does not play a significant role in the counterflowing configuration at high strain rates. Both simulations with Cantera, using the mechanism with low-temperature chemistry included and high-temperature chemistry only, yield almost the same results, confirming the assumption that high strain rates potentially inhibit low-temperature chemistry.

Experimental and Computational Results for Autoignition of Propane

In Figure 5.10, the experimental and computational results of the autoignition behaviour of propane are given. The oxygen mass fraction, Y_{O_2} , and strain rate, a_2 , were kept at constant values of 0.23 and 400 1/s respectively, while the fuel mass fraction was

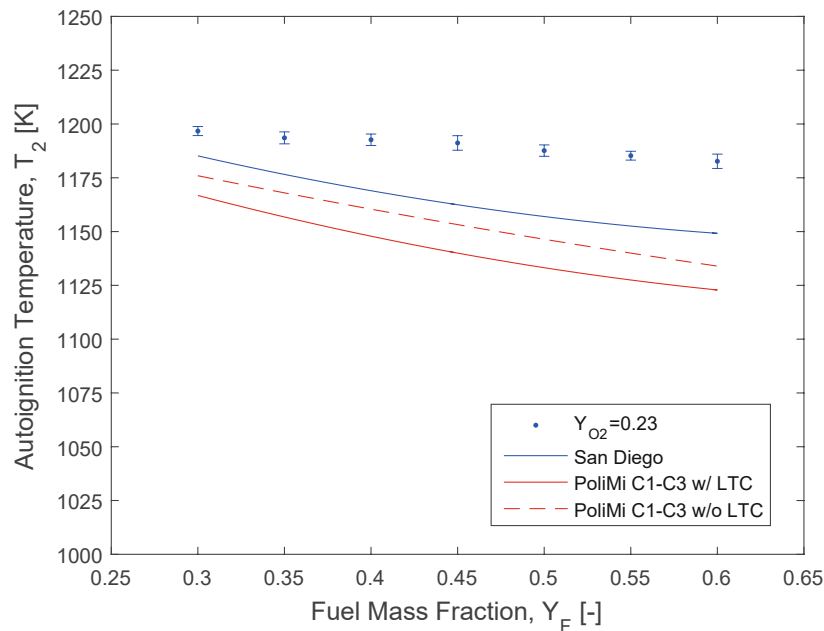


Figure 5.10: Experimental data from measurements plotted with standard errors and compared against computational results with various mechanisms. The fuel mass fraction is varied while the oxygen mass fraction is kept constant. (Appendix, Table D.3)

varied in a range between 0.3 and 0.6. Also included in the plot in addition to the experimental data are the simulations done by Cantera, the UCSDComLab-Module, and employing various mechanisms. Similar to the extinction experiments, the San Diego and C1-C3 PoliMi Mechanism with and without low-temperature chemistry were used. Again, as reflected by the relatively narrow error bars, no major difficulties were experienced during experimentation. Even if the procedure and maintenance required are significantly more complex compared to the extinction experiments due to the different and more sophisticated burner top, results stayed consistent throughout several days of experimentation and after downtime of the device for maintenance and repairs. The experimental data as well as the simulations agree very well and consistently show a minor dependency of the autoignition temperature with changing fuel mass fractions at an oxygen mass fraction of 0.23. As expected, the difference in using mechanisms with and without low-temperature included do not affect the numerical results significantly. With increasing fuel mass fractions, the

temperatures at which autoignition occurs only decrease slightly for both, measurements and simulations. Even if this trend is consistent throughout the data, it is more prominent in the numerical calculations with both mechanisms, resulting in a higher deviation between experimental measurements and simulations at increased fuel mass fractions. This observation led to the decision to investigate the deviation for varying the oxygen mass fraction during various sets of experiments while keeping the fuel mass fraction at a constant level.

The following Figures 5.11, 5.12, and 5.13 show the experimental and numerical results for propane when the fuel mass fraction was kept constant at 0.21, 0.4, and 0.6 respectively. The oxygen mass fraction was varied in a range between 0.07 and 0.23 during each set of experiments. As with previous simulations for propane, the San Diego and C1-C3 PoliMi Mechanism with and without low-temperature chemistry were used, and consistently show no significance of low-temperature chemistry in propane's combustion in the counterflow configuration with elevated strain rates.

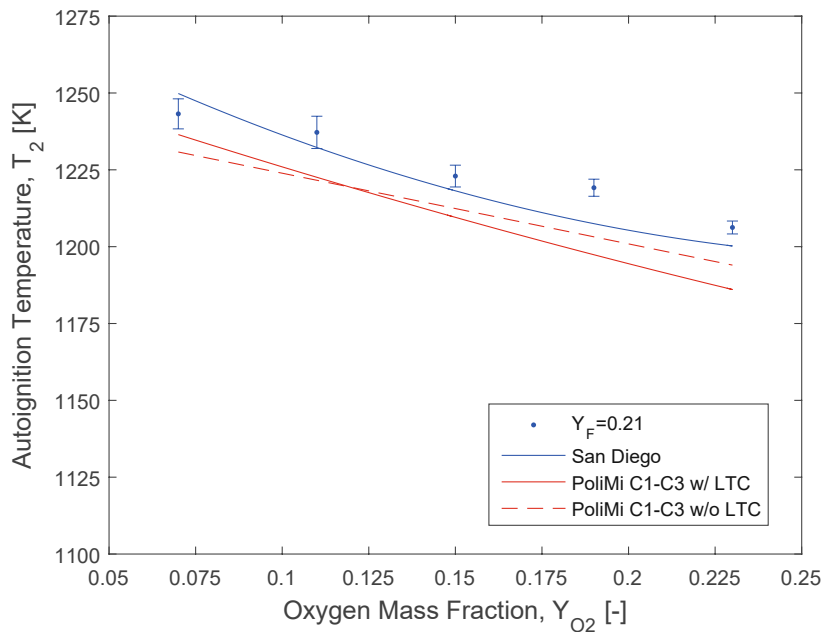


Figure 5.11: Experimental data from measurements plotted with standard errors and compared against computational results with various mechanisms. The oxygen mass fraction is varied while the fuel mass fraction is kept constant at 0.21. (Appendix, Table D.4)

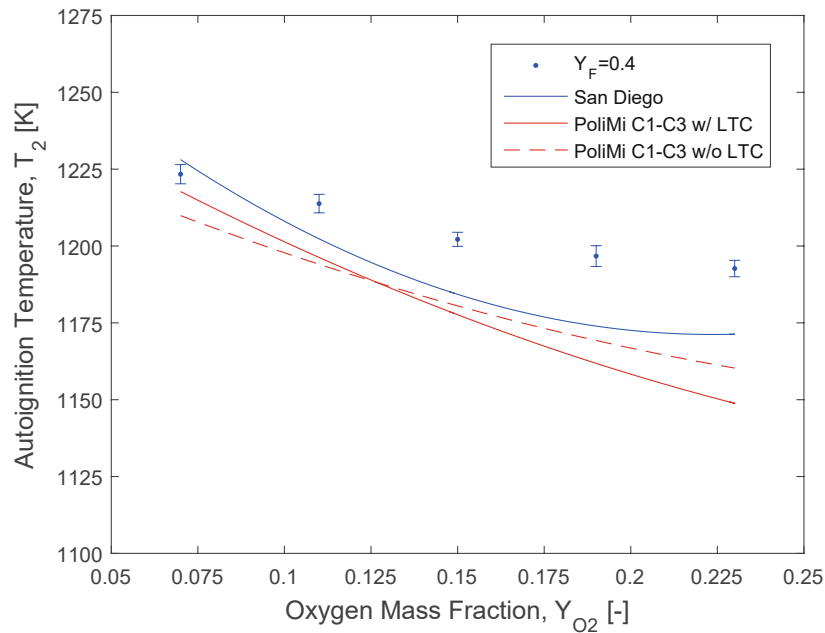


Figure 5.12: Experimental data from measurements plotted with standard errors and compared against computational results with various mechanisms. The oxygen mass fraction is varied while the fuel mass fraction is kept constant at 0.4. (Appendix, Table D.5)

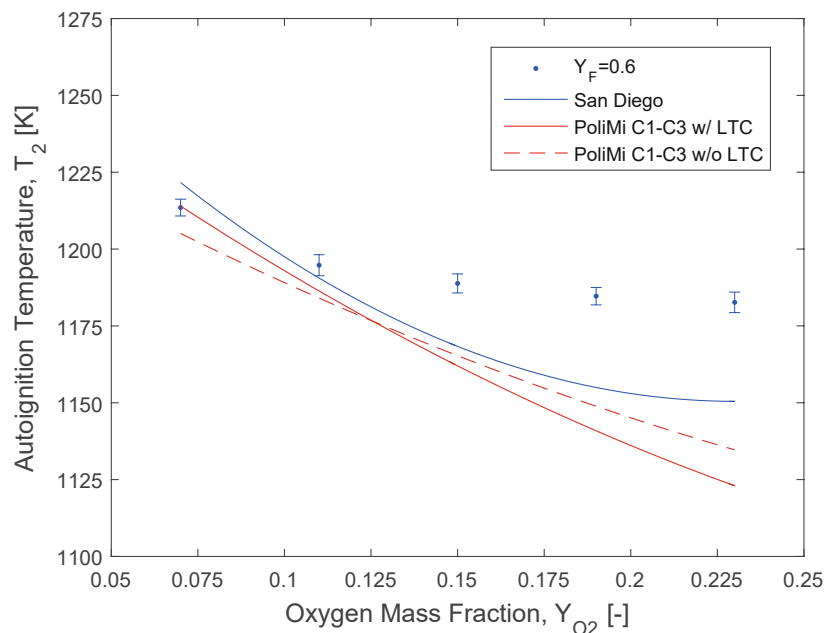


Figure 5.13: Experimental data from measurements plotted with standard errors and compared against computational results with various mechanisms. The oxygen mass fraction is varied while the fuel mass fraction is kept constant at 0.6. (Appendix, Table D.6)

The measurements show that with increasing oxygen mass fraction the autoignition temperature decreases slightly for each level of fuel mass fraction tested and that the temperatures also decrease the higher the fuel mass fraction is set. Nevertheless, while the numerical results match the measured experimental data almost perfectly at low oxygen mass fractions, their deviation from the measurements increases together with the oxygen mass fraction. Furthermore, it can be seen that with higher levels of fuel in the reacting stream the deviation and gap between experimental and numerical results increases as well. While overall both mechanisms tend to underestimate the autoignition temperature at elevated oxygen mass fractions, showing the closest agreement at low fuel mass fractions, San Diego yields numerical results slightly closer to the measurements even at higher oxygen mass fractions. The complete set of results for propane's autoignition behaviour over the oxygen mass fraction for the various fuel levels tested is summarized in Figure 5.14.

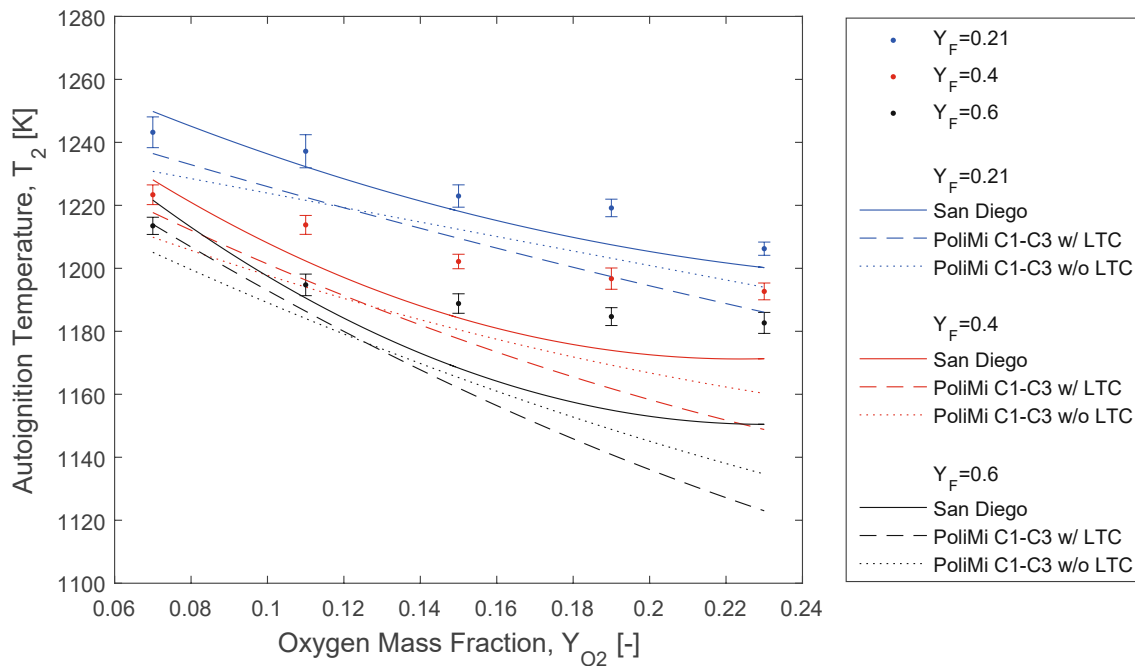


Figure 5.14: Summary of the experimental and computational results from the autoignition experiments with propane for different fuel mass fractions while varying the oxygen mass fraction. (Appendix, Tables D.4, D.5, and D.6)

Setup and Boundary Conditions for Experiments with n-Heptane

As n-heptane is in liquid form at room temperature, the experiments involved the apparatus and setup for prevaporized fuels described in Figure 3.7 in Section 3.2 which is depicted together with labels for each of its major components in Figure 5.15. The burner top was switched and the thermocouple omitted according to the type of experiment conducted. The vaporizer was continuously fed with the liquid fuel from the syringe pump according to the boundary conditions. After testing various vaporization temperatures, it was settled to keep a constant temperature of 533 K at the duct on the fuel side. The temperature was monitored with the aid of a thermocouple placed inside the fuel duct close to its exit and was maintained throughout both, extinction and autoignition experiments.

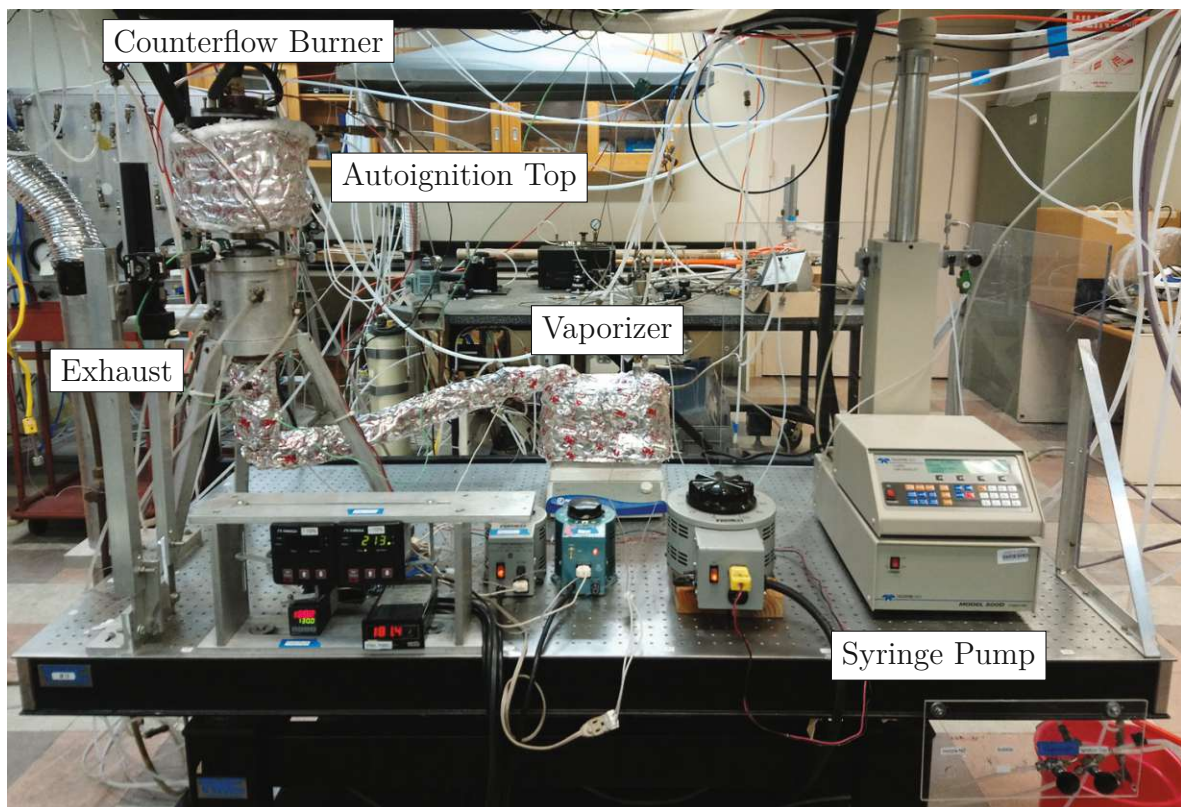


Figure 5.15: Experimental setup employing the counterflow burner in its gaseous configuration for determining autoignition temperatures of prevaporized fuels.

In addition to the basic apparatus, a high-speed camera was set up to observe extinction and autoignition events. The camera was a useful tool to regularly check if ignition occurs in the center of the mixing layer. Central ignition is an essential indicator if the imposed boundary conditions are met and if the flow field inside the reaction zone corresponds with the underlying model of the experiment. The high-speed camera, recording during an autoignition experiment, is shown in Figure 5.16. Sequences of images of extinction and autoignition events are given in Figures 5.17 and 5.18 respectively. It can be seen that, unlike autoignition which targets the center of what subsequently forms the flame, extinction happens, as expected, uniformly throughout the flame sheet.

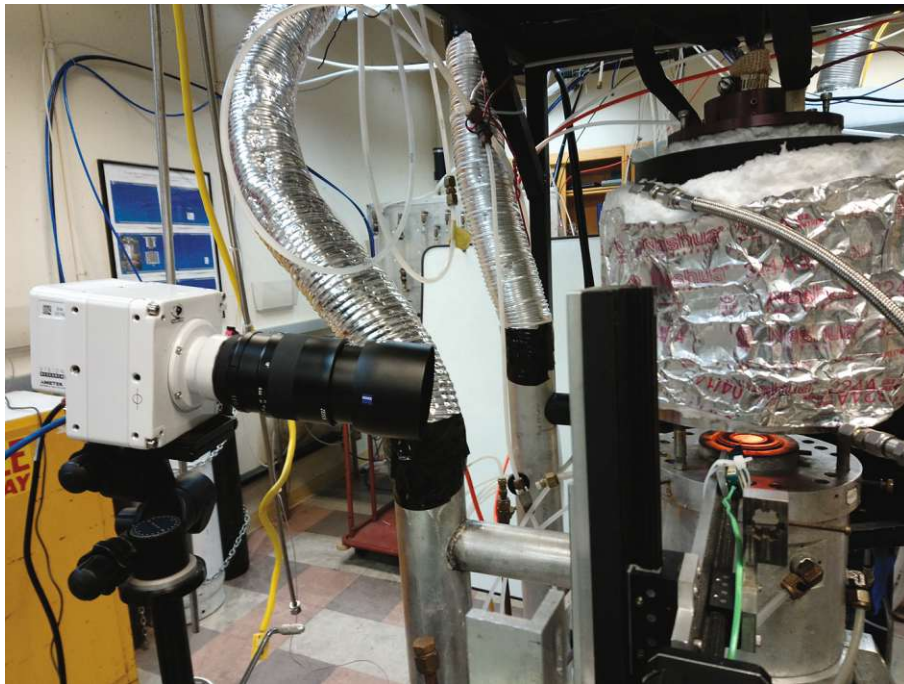


Figure 5.16: High-speed camera set up to observe flame events during an experiment.

The oxidizer during the experiments was either air with an oxygen mass fraction, Y_{O_2} , of 0.23, or a mixture of oxygen and nitrogen to fit the required boundary conditions of the experiment. The stream was delivered at room temperature of 298.15 K during the extinction experiments. The fuel mass fraction, Y_F , was set to 0.4 during experiments when the oxygen mass fraction was varied and the stream was made up of prevaporized



Figure 5.17: Extinction event recorded with the high-speed camera. The fuel is prevaporized n-heptane at 533 K.



Figure 5.18: Autoignition event recorded with the high-speed camera. The fuel is prevaporized n-heptane at 533 K.

n-heptane and nitrogen, mixed inline in the vaporizer. Its temperature was constantly kept at 533 K during both types of experiments. During the autoignition experiments, the strain rate, a_2 , was kept at a constant value of 550 1/s while the volume flows were automatically compensated for the change in temperature by the control software and mass flow controllers.

Experimental and Computational Results for n-Heptane

The plot in Figure 5.19 shows the results of the extinction experiments with n-heptane. The data points were obtained through measurements on the physical device while the lines represent the computational results. Here, the oxygen mass fraction was kept constant while the strain rate of extinction was determined for various values of the fuel mass fraction.

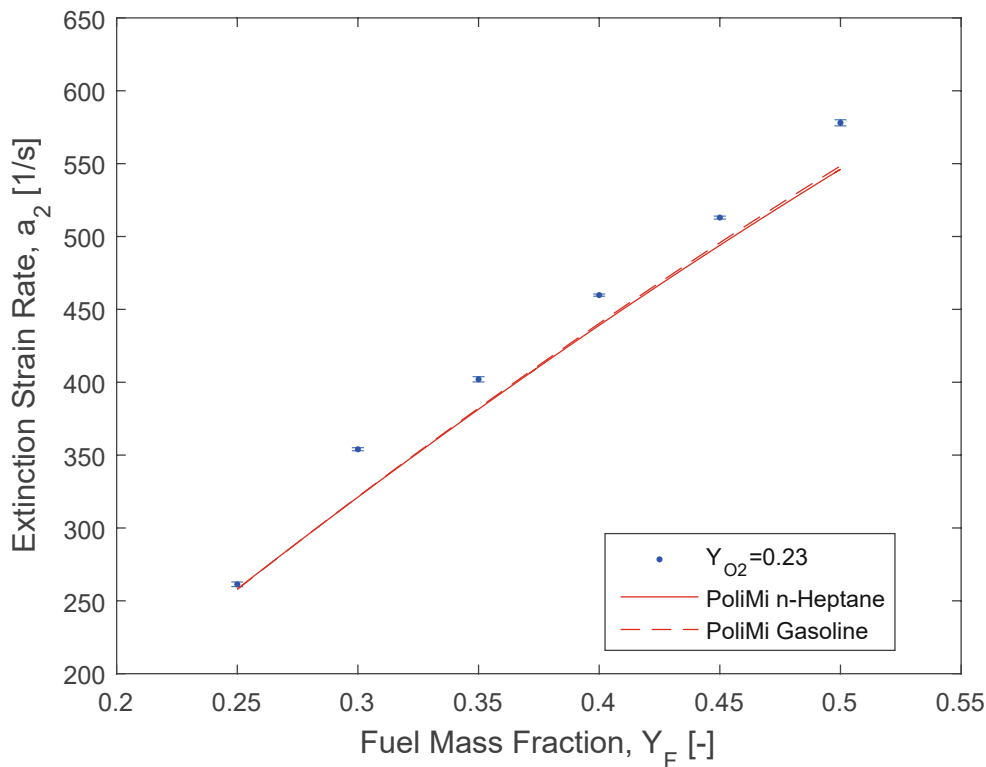


Figure 5.19: Experimental data obtained through measurements plotted with standard errors and computational results generated with Cantera using the UCSDComLab-Module at stream temperatures of $T_1 = 533$ K and $T_2 = 298.15$ K. (Appendix, Table D.7)

The results were highly reproducible, resulting in overall low standard errors at vaporization temperatures of 533 K. No difficulties were experienced during the investigations and the temperatures in the vaporizer system were stable throughout experimentation. The plot does not include numerical results involving the San Diego Heptane Mechanism due to convergence issues during the computations and because subsequently no steady state solutions could be reached under the given boundary conditions. The PoliMi n-Heptane Mechanism was a reduced mechanism and included high- and low-temperature chemistry. It was tested against the PoliMi Gasoline Mechanism to check if the reduced mechanism with its significantly lower number of species and reactions, and resulting increased computation speed, yields the same results as more extensive versions of the mechanism [11].

Overall, the measurements agree very well with the computations. As expected, the extinction strain rate steadily increases together with the fuel mass fraction. Unlike the experiments with propane where the PoliMi Mechanism consistently predicts higher strain rates, for n-heptane the results lie slightly beneath the measurements. Furthermore, it can be seen that there is essentially no difference between the numerical results obtained with the PoliMi n-Heptane and the PoliMi Gasoline Mechanisms which gives the reduced mechanism an advantage due to its significantly shorter computation time. Similar tests were made for the numerical calculations for autoignition temperatures leading to the same outcome. Therefore, further result plots only include the computations with PoliMi's reduced mechanism.

The results from the autoignition experiments with prevaporized n-heptane are summarized in Figures 5.20 and 5.21. First, the fuel mass fraction was varied at constant levels of oxygen, and then the oxygen mass fraction was adapted for a fixed value of the fuel mass fraction. In both cases the autoignition temperature was measured while maintaining a constant strain rate of 550 1/s. Notice that the apparent difference in standard error is solely a result of the scales of the autoignition temperature axis.

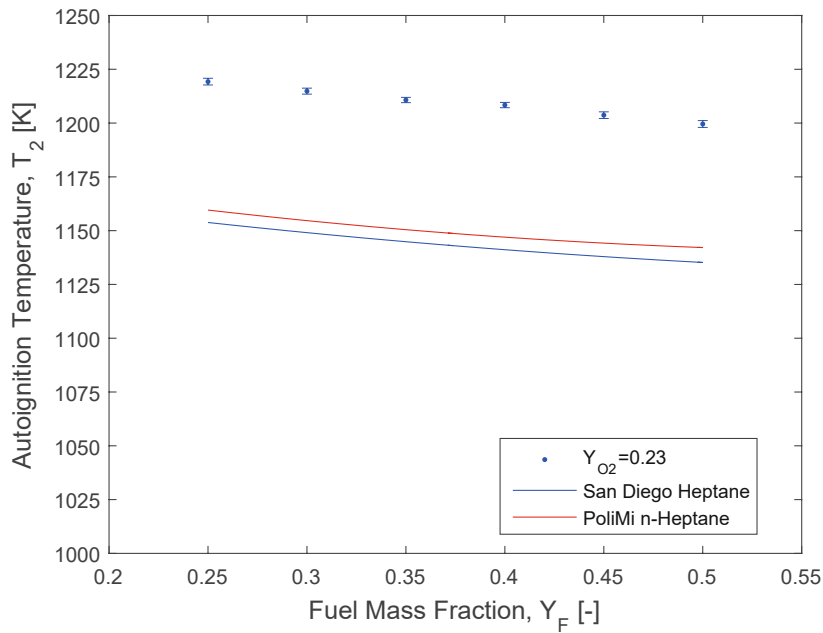


Figure 5.20: Experimental data obtained through measurements plotted with standard errors and computational results generated with Cantera using the UCSDComLab-Module at a fuel stream temperature of $T_1 = 533$ K and a strain rate of $a_2 = 550$ 1/s. (Appendix, Table D.8)

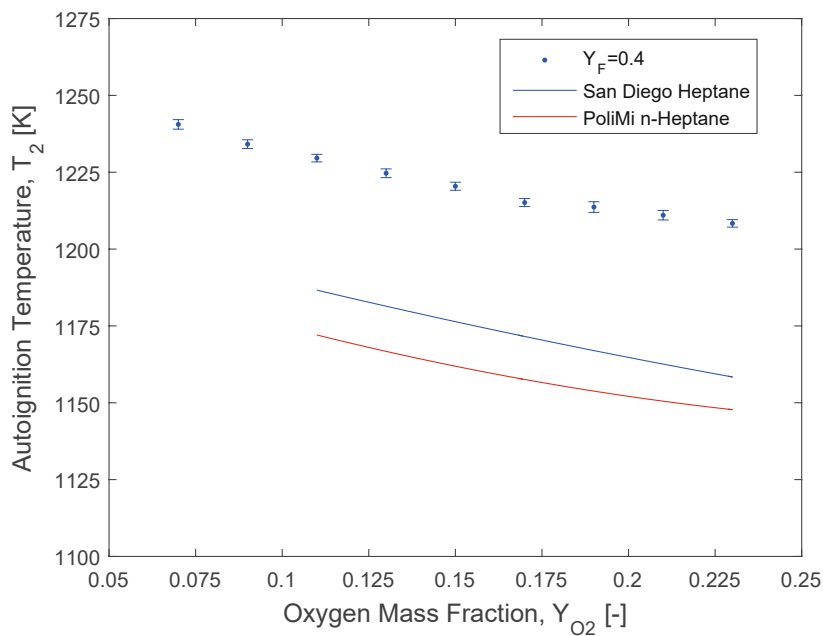


Figure 5.21: Experimental data obtained through measurements plotted with standard errors and computational results generated with Cantera using the UCSDComLab-Module at a fuel stream temperature of $T_1 = 533$ K and a strain rate of $a_2 = 550$ 1/s. (Appendix, Table D.9)

Similar to the extinction experiments, no difficulties were experienced and standard errors are low. Both curves show the same trend that the autoignition temperature slowly decreases when the oxygen or fuel mass fraction are increased. The changes of 19 K and 33 K respectively over the tested ranges are not significant, but considering the low standard errors, they are measurable. Both mechanisms, San Diego Heptane and PoliMi n-Heptane, generate similar results, predicting consistently lower values for the autoignition temperature than measured in the experiments. At low oxygen mass fractions, Cantera and its solver ran into convergence issues and were unable to generate consistent and meaningful predictions. Therefore, results below $Y_{O_2} = 0.13$ are omitted in Figure 5.21.

It is noticeable that in Figure 5.21 the simulation curve of the San Diego Heptane Mechanism suddenly lies above the one of the PoliMi n-Heptane Mechanism. Numerical investigations revealed that the usage of the San Diego Heptane Mechanism results in a

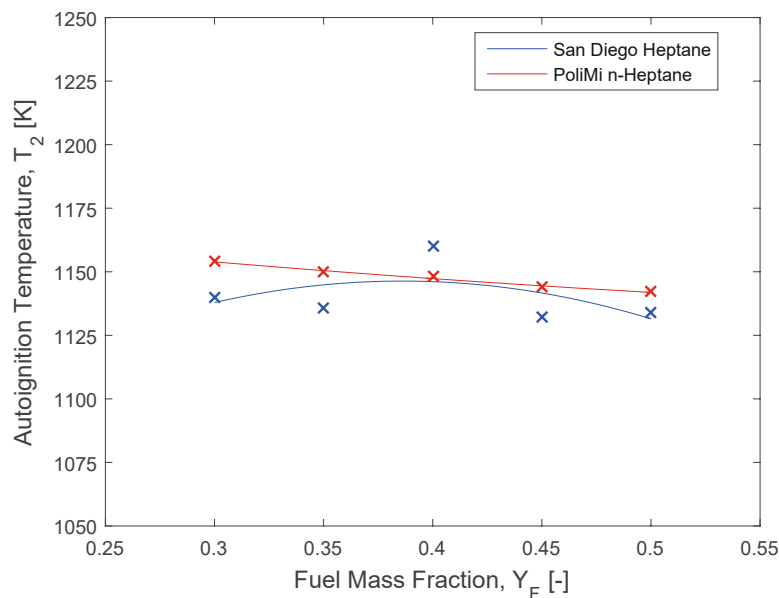


Figure 5.22: Computational results generated with Cantera using the UCSDComLab-Module showing a noticeable discontinuity at $Y_F = 0.4$ when utilizing the San Diego Heptane Mechanism. The data points mark individual numerical results and the lines represent second order polynomial curve fits of the respective points.

discontinuity at fuel mass fractions of 0.4 which were exactly one of the boundary conditions during the experiments with varied oxygen mass fractions. Looking at individual data points from the numerical calculations with Cantera, as seen in Figure 5.22, the discontinuity can be seen. For the curve in Figure 5.20, the discontinuity is not significant due to its highly specific location, and is balanced out by numerical results in the vicinity of that critical boundary condition. But for simulations with the exact value of 0.4, results are all shifted throughout the entire oxygen mass fraction range.

Note that usually all the presented autoignition data obtained through measurements is corrected for heat loss in an environment at room temperature. As the fuel side is at an elevated temperature level during experiments with prevaporized fuels, it was tested how significant the difference for the correction might become under these modified circumstances. The calculations showed that even if the burner was placed in an environment at the given vaporization temperature, the deviation would only be a few Kelvin less in heat loss, and therefore insignificant.

5.1.3 Experimental and Computational Investigation of Extinction and Auto-ignition of Prevaporized Primary Reference Fuels in Non-Premixed Flows

During the investigations involving prevaporized n-heptane described in the previous section, other primary reference fuels, namely the diesel surrogate components n-decane and n-dodecane, were examined under the same conditions. The apparatus, setup, and boundary conditions were identical to the ones described in Section 5.1.2. Also the data and results for n-heptane plotted in this section are the same as previously presented, but are included in the result plots for the sake of completeness and to summarize the data at atmospheric pressure for the prevaporized primary reference fuels gathered for this thesis.

Since the San Diego Mechanism did not include the reactions for the combustion of n-decane and n-dodecane at the time of writing, only reduced versions of the PoliMi Mechanism were used during the computations involving the two diesel surrogate components [9]. The reduced mechanism for n-decane was kindly provided by the CRECK Modeling Group upon request and is currently not publicly available online. Similar to the numerical calculations with the various versions used for the n-heptane computations, the mechanisms were again checked against the higher level PoliMi Diesel Mechanism which contains a significantly higher number of reactions, to validate if similar results were generated [11]. Due to the positive outcome of the validation, only the results originating from the reduced versions of the PoliMi Mechanism are included here.

Experimental and Computational Results

The results of the extinction experiments for prevaporized primary reference fuels are presented in Figure 5.23. The extinction strain rate, a_2 , was recorded for various fuel mass fractions, Y_F , while the oxygen mass fraction, Y_{O_2} , was kept at 0.23. The vaporization temperature was 533 K and the oxidizer side was at room temperature of 298.15 K. Due to convergence issues during the numerical calculations with Cantera when the San Diego Heptane Mechanism was used, no solution could be generated. Therefore, only results for the various reduced PoliMi Mechanisms are plotted. Standard errors are as low as expected and the overall trend of the measurements is captured very well by the computational results, meaning that the extinction strain rate steadily increases with the fuel mass fraction for every surrogate component tested. Also, it can be seen that with increased molecular weight of the fuel components, the limit condition of extinction is lowered consistently. The numerical results for n-decane agree perfectly at lower values of the fuel mass fractions and deviate towards over-predicting the extinction strain rates at

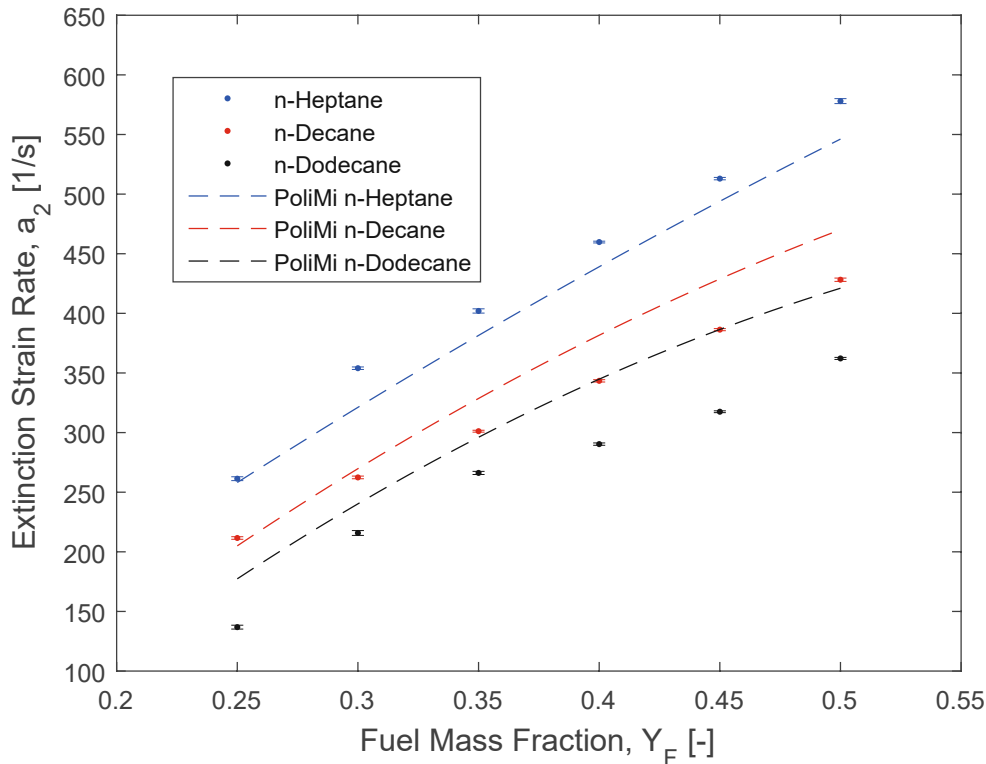


Figure 5.23: Experimental data obtained through measurements plotted with standard errors and computational results generated with Cantera using the UCSDComLab-Module at stream temperatures of $T_1 = 533$ K and $T_2 = 298.15$ K for various primary reference fuels. The oxygen mass fraction was 0.23. (Appendix, Tables D.7, D.10, and D.13)

higher values of Y_F . The computations for n-dodecane on the other hand predict higher limits of extinction over the entire tested range.

The autoignition results are given in Figures 5.24 and 5.25. In both cases, the temperature on the fuel side and the oxidizer strain rate were maintained at 533 K and 550 1/s respectively. At first, the fuel mass fraction was varied at an oxygen mass fraction of 0.23, and then the influence of the oxygen mass fraction at fixed values of $Y_F = 0.4$ was investigated. Computational results below $Y_{O_2} = 0.13$ were omitted in Figure 5.25 because of convergence issues and subsequent inconsistencies in the numerical results.

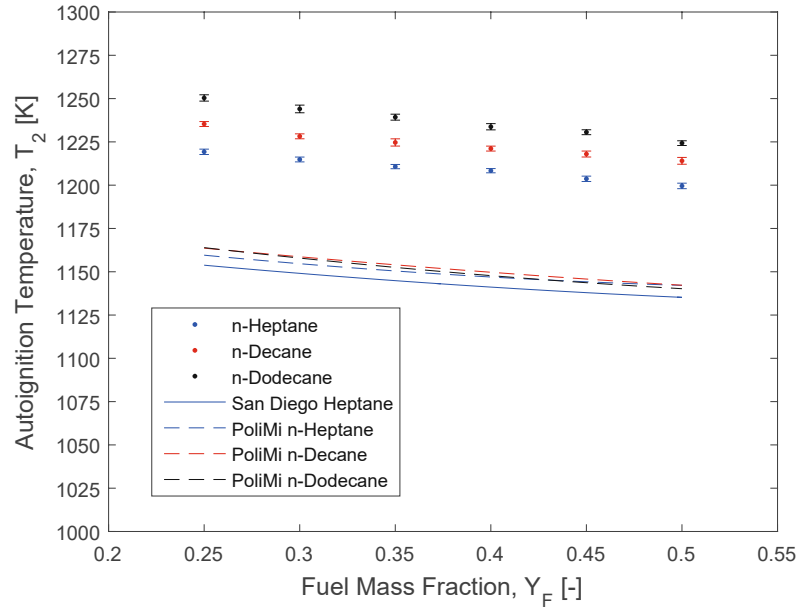


Figure 5.24: Experimental data obtained through measurements plotted with standard errors and computational results generated with Cantera using the UCSDComLab-Module at a fuel stream temperature of $T_1 = 533$ K and a strain rate of $a_2 = 550$ 1/s for various primary reference fuels. The oxygen mass fraction was 0.23. (Appendix, Tables D.8, D.11, and D.14)

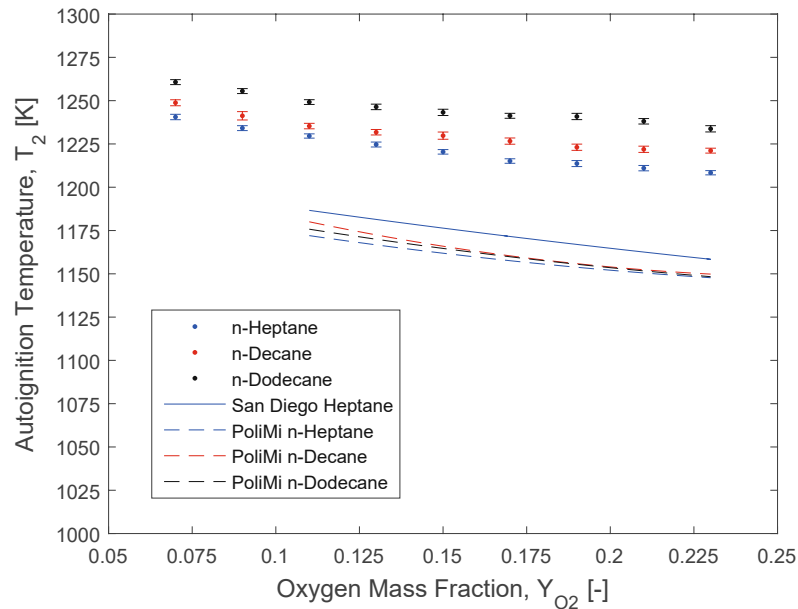


Figure 5.25: Experimental data obtained through measurements plotted with standard errors and computational results generated with Cantera using the UCSDComLab-Module at a fuel stream temperature of $T_1 = 533$ K and a strain rate of $a_2 = 550$ 1/s for various primary reference fuels. The fuel mass fraction was 0.4. (Appendix, Tables D.9, D.12, and D.15)

It is immediately noticeable that for both, the measurements and the computations, the results of the three different surrogate components are very close together. Particularly the numerical calculations involving the PoliMi Mechanism yield practically the same results for all fuels, making it difficult to distinguish each individual line. Especially at higher values of the oxygen and fuel mass fractions the results become essentially congruent. The change in position of the San Diego Heptane Mechanism relative to PoliMi was investigated and explained in the previous section on the n-heptane experiments, but overall, all mechanisms under-predict the autoignition temperatures over the entire range in both sets. The general trend, however, is captured accurately in every numerical solution. The magnitude of the deviation of the computations lies between 60 to 90 K below the measurements. That might be an indicator that the mechanisms require refinement of the reactions and their respective parameters involving the tested primary reference fuels. Considering the better agreement between the computations and the measurements from the experiments with propane given in Section 5.1.2, the issue probably does not arise solely from the combustion of the lower molecular weight components. Further experimental as well as numerical investigations are required to identify the critical species and reactions.

5.2 Elevated Pressures

This section summarizes the experimental and computational investigations carried out at the High Pressure Combustion Experimental Facility (HPCEF) introduced and described in Section 4.1. The respective boundary conditions for each set of experiments and relevant observations are given. Results for the combustion at elevated pressures and their representing plots are discussed herein while exact numerical values of the experimental data gathered during the investigations are tabulated and included for reference in Appendix D.

5.2.1 Experimental and Computational Investigation of Autoignition of Condensed Primary Reference Fuels in Non-Premixed Flows

The HPCEF facilitates a custom designed pressure chamber that can hold a counterflow burner assembly to be operated in a pressurized environment. Similar to the experimental device used for the experiments at atmospheric pressure, the one in the HPCEF is modular and was used in its gaseous and liquid pool configuration for extinction, autoignition, as well as other system relevant experiments in several preceding works [22,23,51–53,62,63,67]. For this thesis, the burner was in its configuration for liquid fuels to test for autoignition temperatures. As extensive and significant changes were made to the system prior to the experiments for this thesis, a thorough baseline test was conducted to compare the results with previous works before any new data was gathered.

Experimental Setup and Boundary Conditions

The exact setup of the HPCEF and the burner are described in great detail in Section 4.1. All modifications implemented prior to the experiments for this thesis that were not present in previous works involving the HPCEF are given in Section 4.1.5. The modifications to the

facility included parts that require a minimum absolute pressure of 5 bar inside the chamber to operate properly and safely over the entire pressure range that was desired for the facility. Therefore, the boundary conditions had to be maintained at at least 5 bar working pressure during the conducted experiments. Photographs of the entire facility and the used counterflow burner after the implementation of the modifications are given in Appendix B.

The main parameter to be varied throughout sets of experiments was usually the absolute pressure inside the chamber. Experiments were carried out for the pure primary reference fuels n-heptane, n-decane, and n-dodecane in their condensed form, and since autoignition temperatures were determined, the separation distance between the liquid surface and the oxidizer duct outlet was 12 mm. The investigations included strain rates in a range between 100 and 150 1/s. Below, no proper flame structure could be achieved, and above, first, the capacity of the mass flow controllers was not sufficient to provide an adequate flush stream, and second, the device geometry in combination with certain equipment pieces in place did not allow for proper ventilation of the reactant gases which could have resulted in unsafe states of the system. Furthermore, out of the bounds of the given strain rate range, autoignition results were highly inconsistent and not satisfyingly reproducible. The same inconsistencies due to the limitations of the flush, which are described in Section 4.3, were observed within the experimental strain rate range at pressures above 13 bar, becoming significant at about 15 bar.

For safety reasons, premixed air and pure nitrogen were used as an oxidizer instead of mixing pure oxygen and nitrogen inline. Due to the characteristics of the system, specifically the mass flow controllers, the oxygen mass fraction in the oxidizer stream was always kept below that of air for the experiments, usually at 0.15. The fuel side was always made up of pure fuel and was evaporated in the process by the heat carried by the oxidizer stream, while the fuel level was carefully observed and manually regulated with the aid of a syringe pump. The flush, responsible for building and maintaining the pressure inside

the chamber, as well as pushing out reactant gases from the system, was manually set in accordance with the pressure level of the experiment and the findings from the setup phase described in Section 4.3. Unlike with the atmospheric setup, where their influence on the flow field is minor and a fairly consistent setting can be used, the curtain flows had to be carefully considered for the HPCEF to maintain a proper flow field inside the reaction zone. That required preliminary testing for each set of experiments and varied strongly with the pressure level and the flow rate of the flush.

Observations from Experiments at Elevated Pressures

With increasing pressure, the flush stream and its influence on the flow field and results, specifically its flow rate, becomes more and more significant. Its settings have massive impact on a host of parameters, process and safety related, which influence the outcome of an experiment. Due to the geometry and combination of certain equipment parts, minor leakage from the chamber, and buoyancy as well as the increased amount of heated gas fed into the system at elevated pressures, the flush needs to be carefully considered and adequately set for the entire duration of an experiment. The upper limit of the flush, considering the pressure range investigated for this thesis, is currently the size and capacity of the mass flow controllers. The lower limit is determined by the boundary conditions of the given experiment, which mainly are the pressure in the chamber and the resulting overall flow rate of gases going into the system. After extensive testing, it was found that at an oxidizer strain rate of 150 1/s, in the current configuration of the HPCEF, the maximum pressure for which the flush can be set adequately to stabilize the pressure inside the chamber as well as the flow field properly without any gas breaking away from the reaction zone, is 13 bar. Above that threshold, reactant gases can be observed streaming away from the reaction zone and into the chamber, heating up the entire system and accumulating inside it, leading to several undesirable effects. The phenomena are described

and illustrated in Section 4.3. Furthermore, at about 15 bar, the autoignition data start to become inconsistent and difficulties to generate meaningful results within reasonable bounds arise. That circumstance can be seen in the standard errors of the autoignition temperatures in Appendix D for pressures higher than 13 bar.

Figure 5.26 shows two n-heptane flames, at 5 and 11 bar respectively, established after autoignition. The differences in flame structure and underlying flow field are clearly visible, and are a result of the combination of the oxidizer stream and the flush parameters. The flow field, and with it the flame structure, can be influenced to a certain extent by the flush stream, which is not actively taking part in the reaction otherwise. Thereby, regulating the flush adequately to stabilize the flow field between the liquid pool and the oxidizer duct, especially at elevated pressures, is quintessential for achieving meaningful and reproducible results. Additional n-heptane flames at various pressures are given in Appendix C.

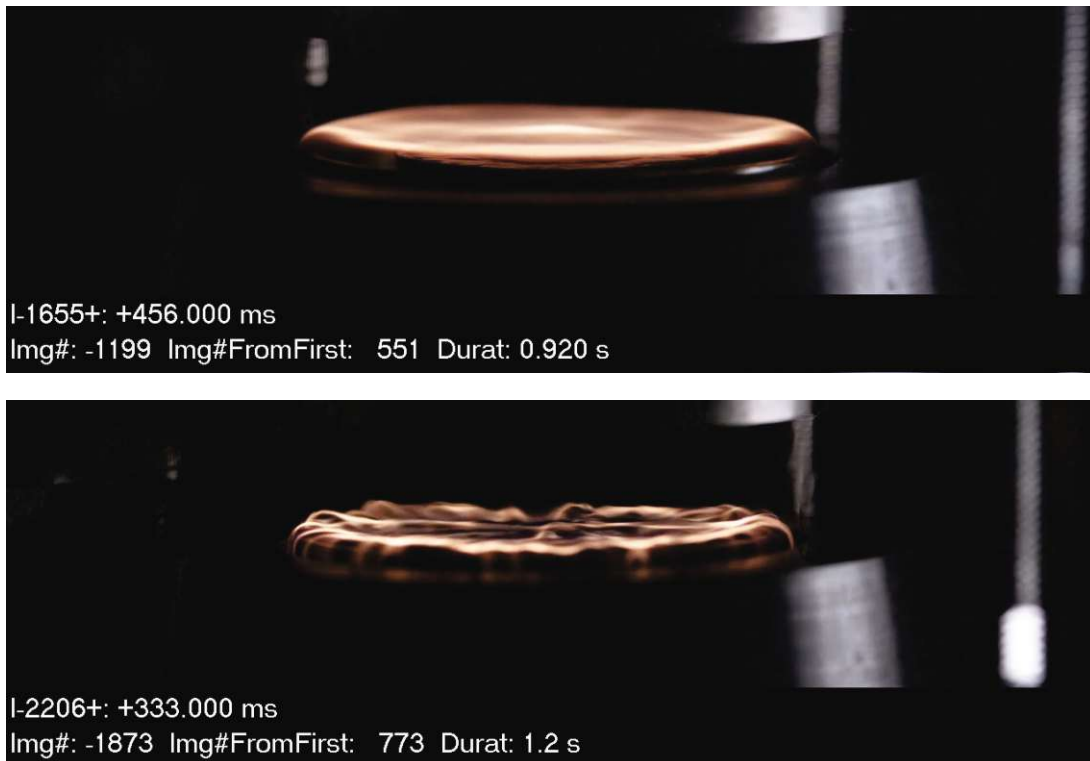


Figure 5.26: Screenshots of high-speed recordings from the HPCEF showing n-heptane flames at 5 bar (top) and 11 bar (bottom).

Another effect observed at elevated pressures, which is not seen at the atmospheric setup, is the ignition and flame formation in the curtain area around the liquid pool. Fuel is overflowing from the cup into the curtain stream and can also potentially condense before being withdrawn from the reaction zone through the suction gap. Therefore, fuel can accumulate in the curtain area which is then transported back towards the reaction zone through the curtain stream. At elevated pressures, this often leads to ignition and a stabilized flame in the curtain area, while the actual ignition event above the liquid pool has not occurred yet and still no flame is formed in the reaction zone. Nevertheless, it was found that whether premature curtain ignition is occurring or not, eventually the same autoignition temperature is measured when the mixture above the pool ignites. Curtain ignition can, however, obscure the view of the liquid pool, making it difficult to properly observe the actual ignition event.

Oscillation and vibration of the liquid pool is another phenomenon observed at the HPCEF. It is partially due the piston pump used for feeding water into the system, but is, for the most part, actually an optical illusion caused by density gradients and buoyancy of the heated gases. When the oxidizer stream is not heated, even at high flow rates and pressures, the visual impression of the vibration is reduced to a minimum. Nevertheless, it is recommended to replace the current single piston pump with a double acting pump to completely eliminate vibration from the system.

Furthermore, it is important to mention that at pressures above 13 bar, the cylindrical correlation for the Nusselt number used to correct the measured autoignition temperatures for heat loss, tends to fail to stay inside validity bounds because of too high Reynolds numbers. As described in Section 2.2, for the approximation of the heat loss correction, a cylindrical correlation for the Nusselt number was chosen, which in turn is only valid for Reynolds numbers in a range between 0.02 and 44. Even though in some cases that range is superseded, the same correlation and correction is used for all the measured temperatures.

Computations of Experiments at Elevated Pressures

In addition to the numerical calculations with Cantera using the UCSDComLab-Module, PoliMi's CRECK Modeling Group kindly provided computing power and simulation results using their in-house software suit OpenSmoke in conjunction with their PoliMi Mechanism in its full detailed version [11]. The simulations with Cantera were all done utilizing reduced and specialized versions of the PoliMi Mechanism to minimize computation time. For numerical calculations involving n-heptane, also the San Diego Heptane Mechanism was used. To verify that the specialized mechanisms for the investigated PRFs adequately approximate the higher level versions of the PoliMi Mechanism which cover significantly more species and reactions, all reduced versions were tested under the same boundary conditions. Figure 5.27 is showing computational results for n-heptane, n-decane, and n-dodecane comparing PoliMi's specialized mechanisms for each species, Gasoline, Diesel, and Real Fuel Mechanisms.

The very similar results from the various mechanisms used on each PRF suggest that the reduced PoliMi Mechanisms are interchangeable for the purposes of this thesis. Slight deviations among the different mechanisms are only noticeable at the upper end of the investigated pressure range, and are not considered significant. Therefore, only the reduced and specialized mechanisms for n-heptane, n-decane, and n-dodecane are used for the simulations of the HPCEF for this thesis. Computation time is greatly improved due to the reduced number of species and reactions considered in the mechanisms. Furthermore, instead of second order polynomials, as shown in Figure 5.28 and used for the simulations at atmospheric pressure, fourth order polynomials are used to fit the computational results at elevated pressures. Fourth order polynomials were found to give closer fits for the progression suggested by the numerical results and also mirror certain phenomena observed in the experimental data gathered during the investigations.

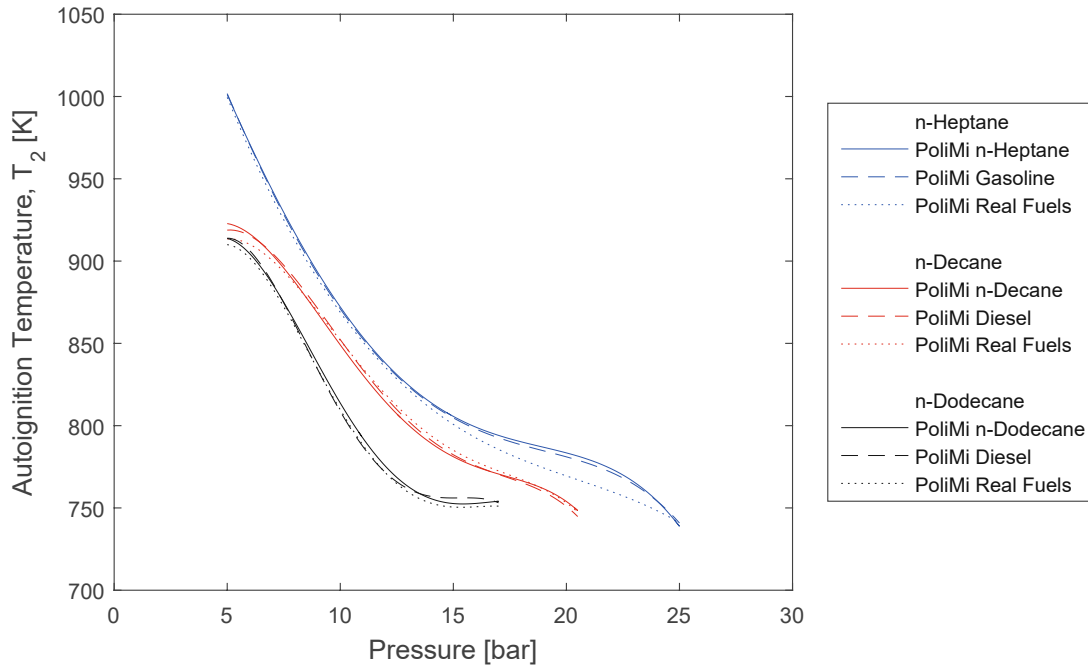


Figure 5.27: Computational results for n-heptane, n-decane, and n-dodecane at elevated pressures generated with Cantera in conjunction with various versions of the PoliMi Mechanism and under identical boundary conditions.

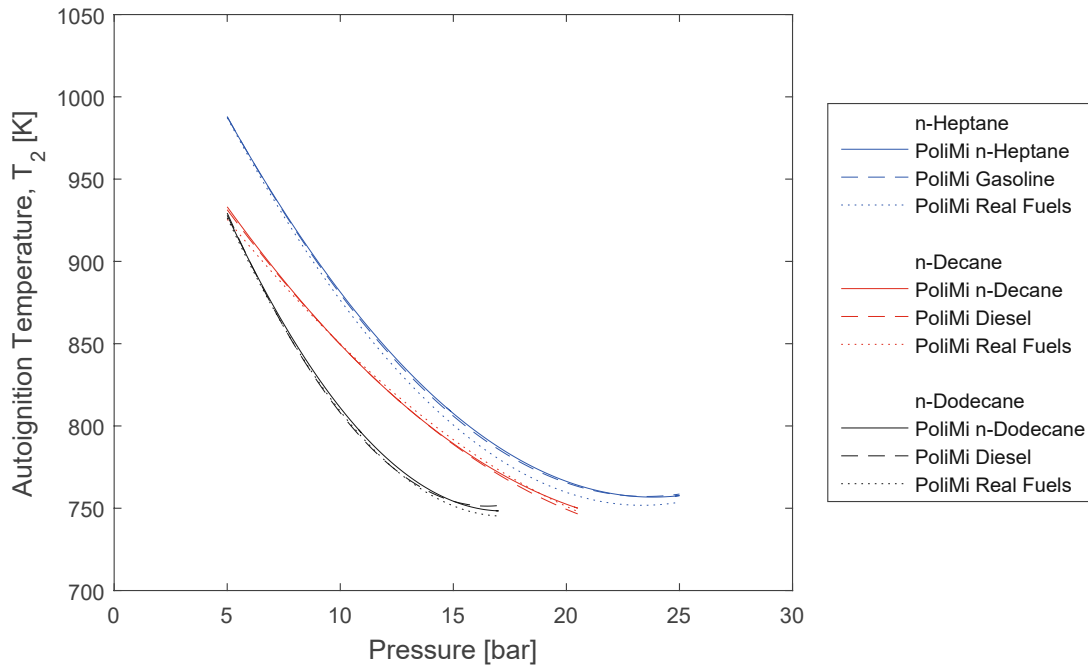


Figure 5.28: Computational results for n-heptane, n-decane, and n-dodecane at elevated pressures presented in Figure 5.27, but curve fitted with second order polynomials.

Experimental and Computational Results for n-Heptane

The experimental and computational results from determining the autoignition temperatures of n-heptane at elevated pressures, including the standard errors for the measured data, are given in Figure 5.29. The strain rate during these experiments was 150 1/s and the oxygen mass fraction 0.15. Cantera in conjunction with the UCSDComLab-Module and also the software suit OpenSmoke were used for the numerical calculations. While Cantera utilized reduced and specialized mechanisms, the simulations with OpenSmoke were based on the complete version of the PoliMi Mechanism.

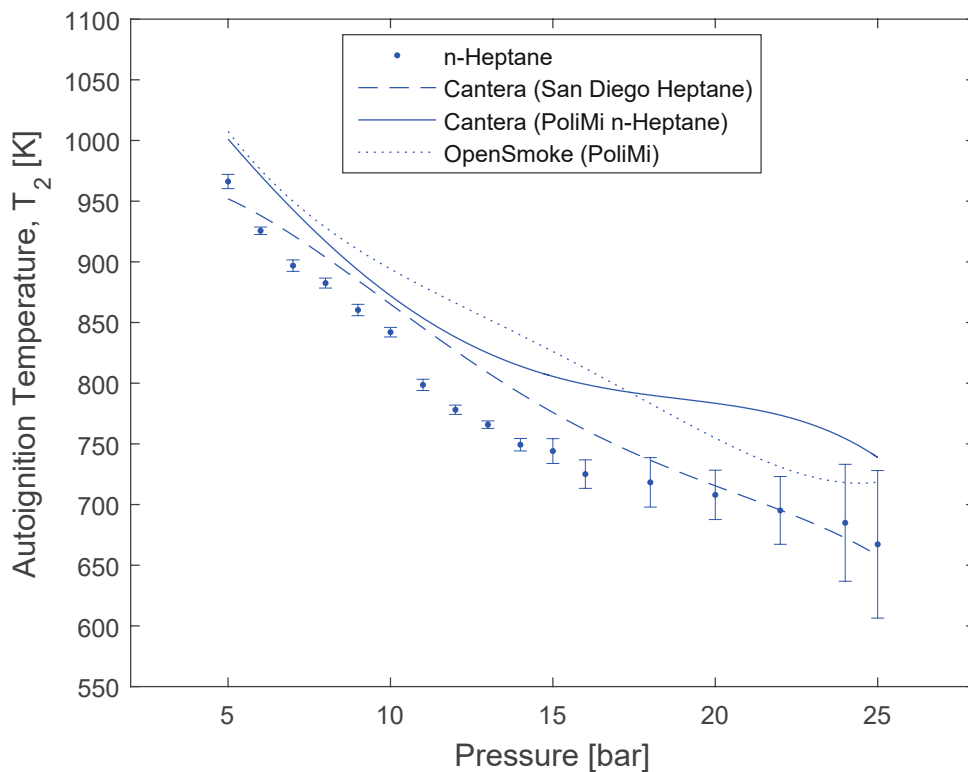


Figure 5.29: Experimental data obtained through measurements plotted with standard errors and computational results for n-heptane at a strain rate of 150 1/s and an oxygen mass fraction of 0.15. (Appendix, Tables D.16 and D.17)

Due to the elevated pressures, a multitude of severe difficulties arise during experimentation which is evidently noticeable in the standard errors of the measurements. Not only the limitation of the potential time for operation of the HPCEF per experiment, increased maintenance, and necessary downtime due to the large batches of required nitrogen, but also the increased sensitivity of the system at elevated pressures to minor changes and variations, make experimentation a time consuming and highly volatile task. For instance, uncontrollable fluctuations in the cooling or water supply systems or minor expansions in equipment due to an increase in temperature inside the chamber can lead to slight misalignment of equipment parts which in turn require a full reset of the HPCEF or potentially render entire sets of measurements useless. The gathered data has to be carefully checked for plausibility and sets of experiments have to be repeated several times, and preferably even compared against experimental data with slightly modified boundary conditions, to reach an adequate level of certainty. The significantly larger standard errors on the upper end of the pressure range are discussed in Sections 4.3 and 5.2.1, and cannot be overcome in the current configuration of the HPCEF under the given boundary conditions.

The elevated pressures also pose a challenge for the numerical calculations. Certain boundary conditions lead to the inability of the numerical software to generate solutions, and even after adaptations to achieve convergence, discontinuities and abrupt jumps can be found in the results over the investigated pressure range. Noticeably, similar inconsistencies and phenomena can be observed in the measured autoignition temperatures, however, it is unclear if these arise due to the underlying chemistry and transport phenomena, unobserved variations in process and environmental parameters, or from minor errors in the setup and experimental procedures. Closer investigation would require tremendous effort and an uneconomical number of experiments under varying conditions which are not part of this thesis.

Even though the process of gathering results at elevated pressures comes with significant challenges, eventually, the computations agree very well with the measured autoignition temperatures. The differences between the measured and calculated data points are below 100 K over the entire pressure range which, considering the mode of temperature measurement, boundary conditions, and setup, can be expected and is absolutely acceptable. Also the different modes of computational calculations agree very well with one another, regardless of the software or mechanism used. Considering the plausible predictions of the computations at atmospheric pressure, and the similarity of results when comparing Cantera and OpenSmoke, it is safe to assume that Cantera in conjunction with the UCSDComLab-Module offers an effective, fast, and free option when predictions from numerical computations of counterflow problems are required.

Experimental and Computational Results for n-Decane

Compared to the n-heptane results, similar statements can be made for the generated data of n-decane at elevated pressures. Figure 5.30 shows the gathered results for n-decane at a strain rate of 150 1/s and an oxygen mass fraction of 0.15 over a pressure range of 5 to 25 bar. The computations do not cover the entire pressure range due to arising issues in the proximity of the critical pressure of n-decane.

As depicted in Figure 5.30, the deviation between measured autoignition temperatures and the computations is even lower than the difference of 100 K for n-heptane, resulting in a very good agreement between the data sets. Also the two modes of numerical calculations yield similar results. Compared to n-heptane, n-decane measurements show a slightly higher standard error. This can be attributed to the difference in physical parameters and resulting behaviour of the two species, but also to the higher absolute number of overall experiments with n-heptane.

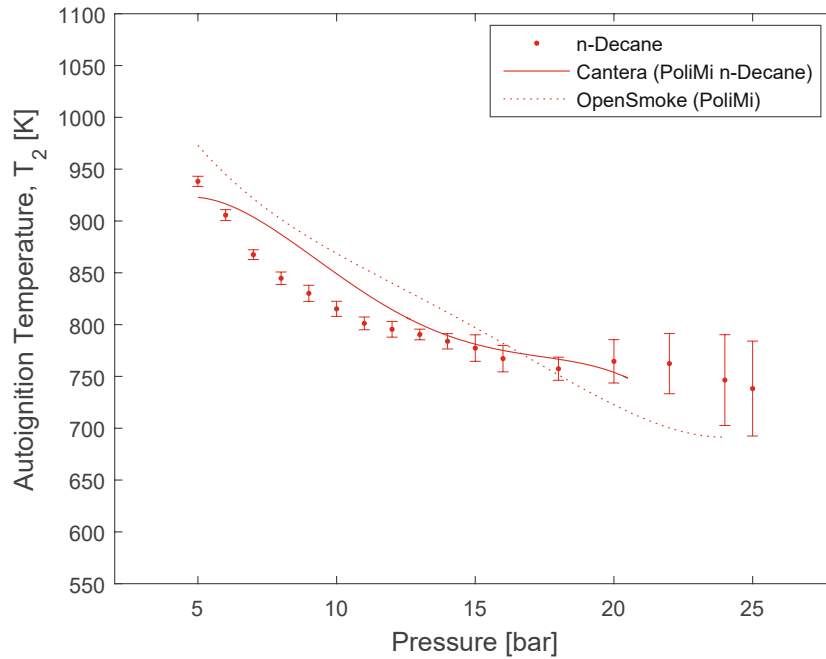


Figure 5.30: Experimental data obtained through measurements plotted with standard errors and computational results for n-decane at a strain rate of 150 1/s and an oxygen mass fraction of 0.15. (Appendix, Tables D.20 and D.21)

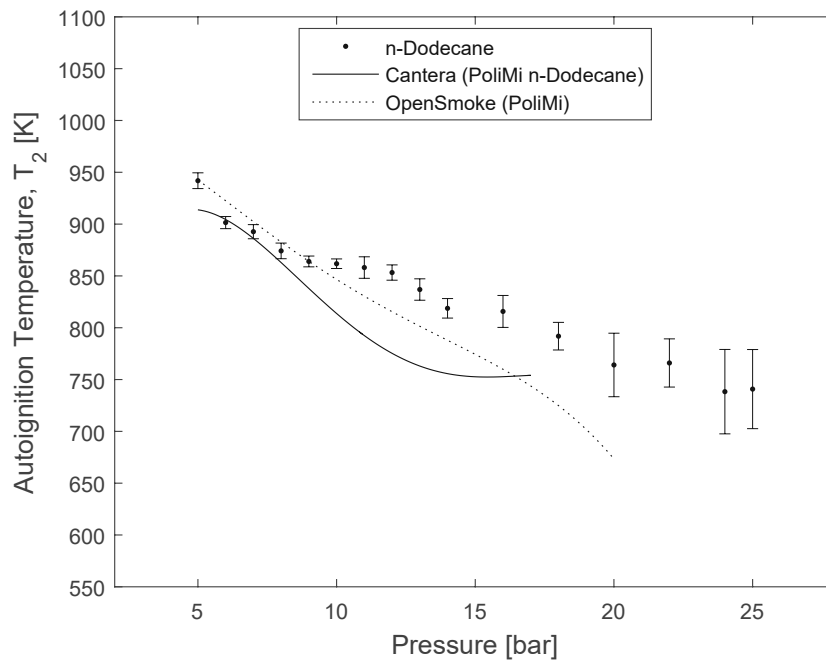


Figure 5.31: Experimental data obtained through measurements plotted with standard errors and computational results for n-dodecane at a strain rate of 150 1/s and an oxygen mass fraction of 0.15. (Appendix, Tables D.24 and D.25)

Experimental and Computational Results for n-Dodecane

In Figure 5.31, the results for n-dodecane at elevated pressures are given. Again, the strain rate was 150 1/s and the oxygen mass fraction 0.15. Measurements were taken in a pressure range of 5 to 25 bar at the HPCEF, and computations were carried out with the aid of Cantera in conjunction with the UCSComLab-Module, and OpenSmoke respectively. Similar to the numerical calculations involving n-decane, no plausible predictions could be generated approaching n-dodecane's critical pressure, and are therefore not included in the graphs. Being the species with the highest density and viscosity of the three tested PRFs, working with and handling n-dodecane was noticeably different, in terms of sensitivity to parameter and setup changes, compared to the other alkanes. The added challenges lead to the disregarding of numerous experimental data sets due to their exhibition of questionable plausibility during evaluation. The slightly higher standard errors of the measurements are owed to that circumstance. Nevertheless, computational and measured data deviation is around and below 100 K and thereby comparable to the other tested PRFs. The seemingly increased difference and change in trend between the numerical calculations of Cantera and OpenSmoke in the range between 10 and 15 bar are mainly rooted in the forth order polynomial approximation approach of the curve fitting and the fewer individual computational results from Cantera the respective fit was based on.

Comparison of the Experimental and Computational Results

Looking at the measurement and computational results of the individual species gives the impression of a satisfying level of agreement between the data sets. However, the direct comparison of the results from the experiments with each PRF at elevated pressures reveals certain discrepancies which cannot be attributed to systematic or measurement errors, and require further investigation to elucidate their origins.

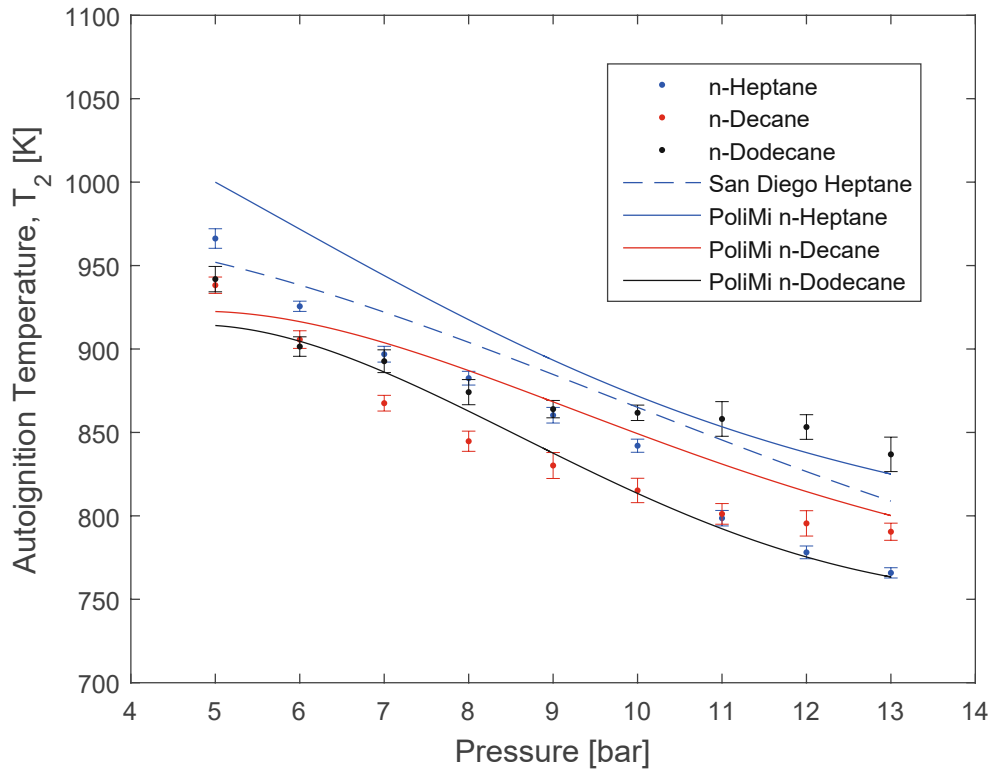


Figure 5.32: Experimental and computational results for n-heptane, n-decane, and n-dodecane at a strain rate of 150 1/s and an oxygen mass fraction of 0.15 up to 13 bar. (Appendix, Tables D.16, D.20, and D.24)

Figure 5.32 summarizes the previously shown experimental and computational results for n-heptane, n-decane, and n-dodecane in a pressure range of 5 to 13 bar. The computations all show the expected trend that the autoignition temperature decreases with increasing pressure and molecular weight of the species over the entire range. The measured data on the other hand exhibit a phenomenon that, for the purposes of this thesis, will be called the “crossover” from here on out. Around 7 bar, the measurements start to deviate from the expected trend by n-heptane measurements yielding lower autoignition temperatures than for n-dodecane and eventually, at around 11 bar, even lower than for n-decane. Temperatures gathered with n-decane as a fuel exhibit the same unexpected behaviour in relation to n-dodecane, but at even lower pressures than n-heptane. The deviation can be noticed to increase with the experimental pressure, but cannot be attributed to the previously

mentioned limitations of the flush stream which become relevant at pressures around 13 bar. When the setting of the inert flush stream at elevated pressures is inadequate for the experimental boundary conditions, measurements start to noticeably deviate as a whole, but the crossover, even if shifted, still occurs. As shown in Figure 5.33, the crossover remains present at pressures above 13 bar, even though standard errors start to significantly increase, leaving certainty and plausibility of the measurements at the predominant boundary conditions questionable.

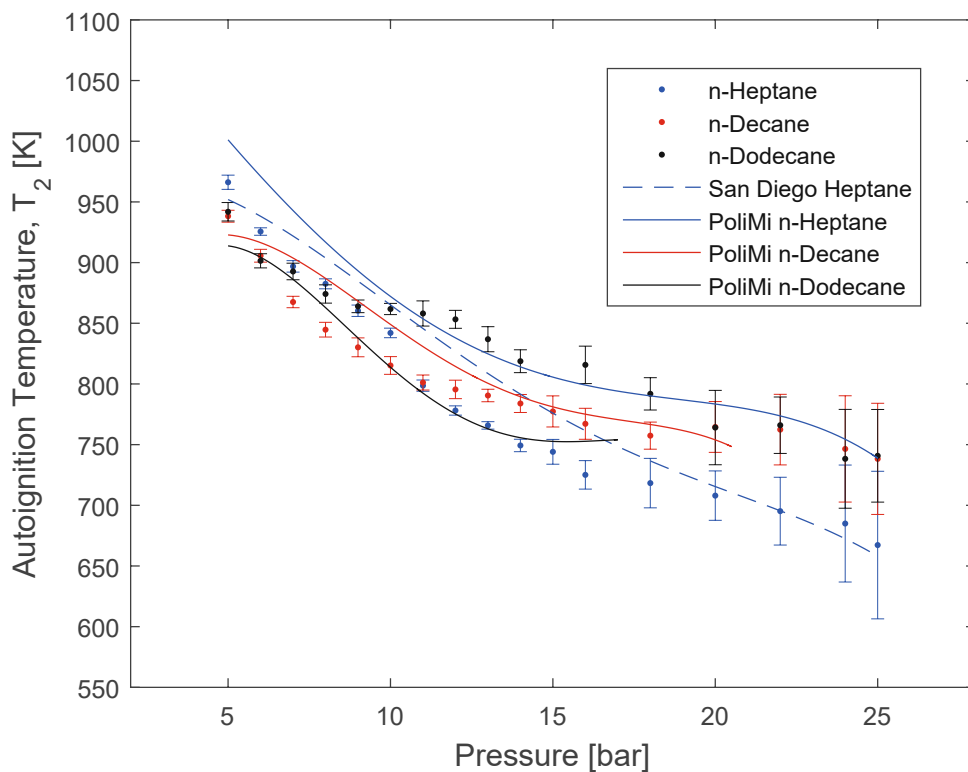


Figure 5.33: Experimental and computational results for n-heptane, n-decane, and n-dodecane at a strain rate of 150 1/s and an oxygen mass fraction of 0.15 up to 25 bar. (Appendix, Tables D.16, D.17, D.20, D.21, D.24, and D.25)

5.3 Liquid Pool and the Crossover

Since the occurrence of the crossover and its origin cannot be traced back to systematic or measurement errors during the experiments at the HPCEF, further investigation and an in-depth analysis of the basic liquid pool setup and its modeling are necessary to identify the causes of the crossover phenomenon at elevated pressures. For that purpose, components of the counterflow burner in its liquid pool configuration for experiments at atmospheric pressure were refurbished, and a new experimental workbench was set up and dedicated to that task. The new setup including the counterflow burner in its liquid pool configuration can be seen in Figures 5.34 and 5.35, and is described in detail in Section 3.2 in Figures 3.8 and 3.9. An inspection camera system for the operator to monitor the liquid level in the cup from the workstation was added to mirror the circumstances at the HPCEF.

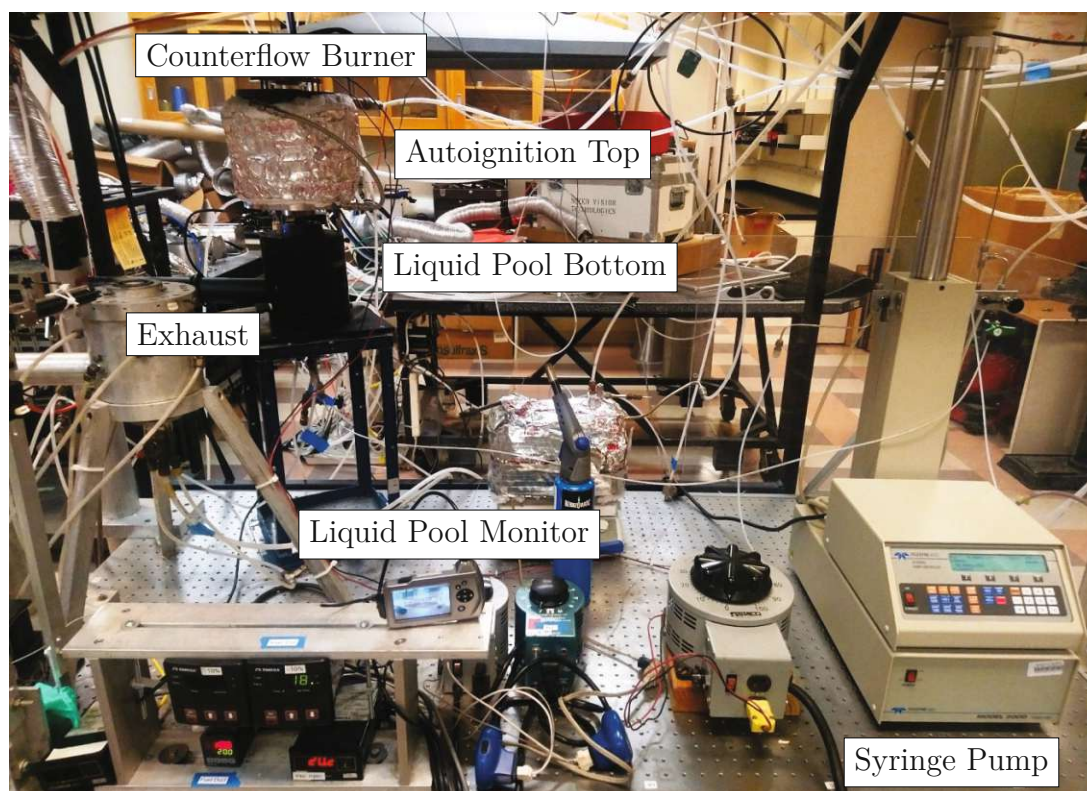


Figure 5.34: Experimental setup employing the counterflow burner in its liquid pool configuration for determining autoignition temperatures of condensed fuels.

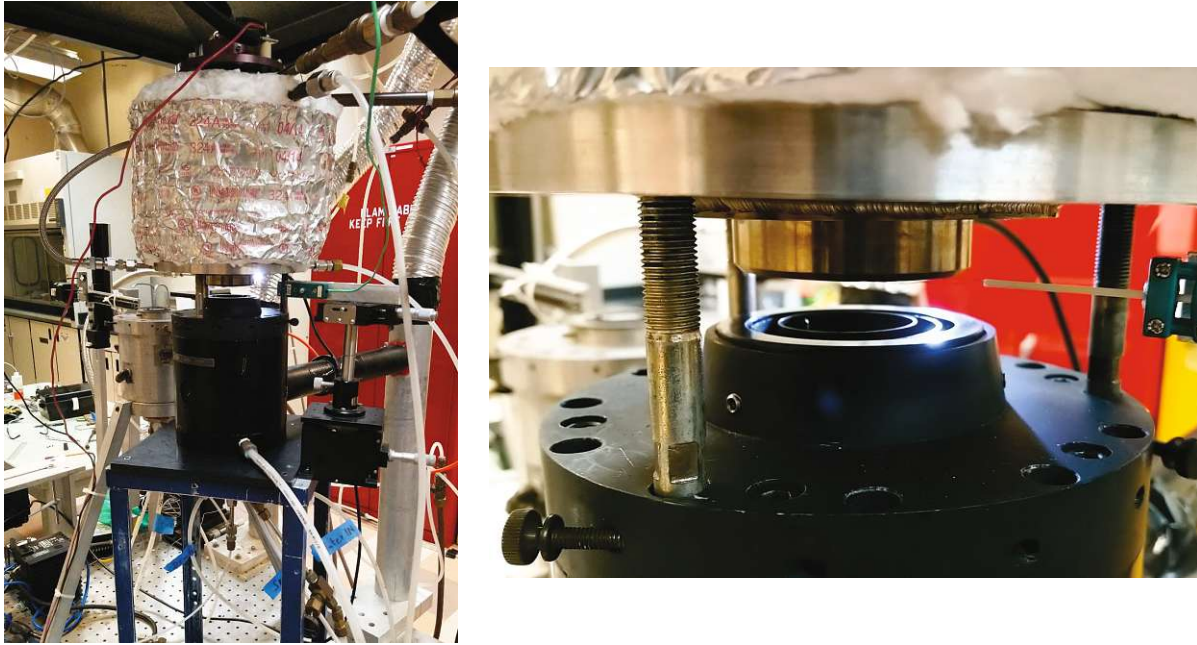


Figure 5.35: Counterflow burner in liquid pool configuration with autoignition top (left) and the reaction zone of the assembly showing the cup for condensed fuels and the needle to facilitate the monitoring of the liquid pool level (right).

Measurements at the new atmospheric liquid pool setup were compared to results from previous investigations carried out in UC San Diego's Combustion Laboratory [30,101]. After positive confirmation of the results matching, it was verified if there is any notable difference when using air from the building supply system or an inline mixture of oxygen and nitrogen instead of the premixed medical air as implemented at the HPCEF. Since no significant differences were detected, other than occasional instabilities due to the shop air supply system, the content from separate oxygen and nitrogen cylinders was mixed inline to form the oxidizer stream for the experiments at atmospheric pressure.

5.3.1 Fuel Level Prior to Ignition

The first parameter to be tested for its influence on autoignition temperatures and potential for causing the crossover phenomenon observed at the HPCEF was the level of the fuel in the cup prior to ignition. Under representative boundary conditions, the fuel level showed

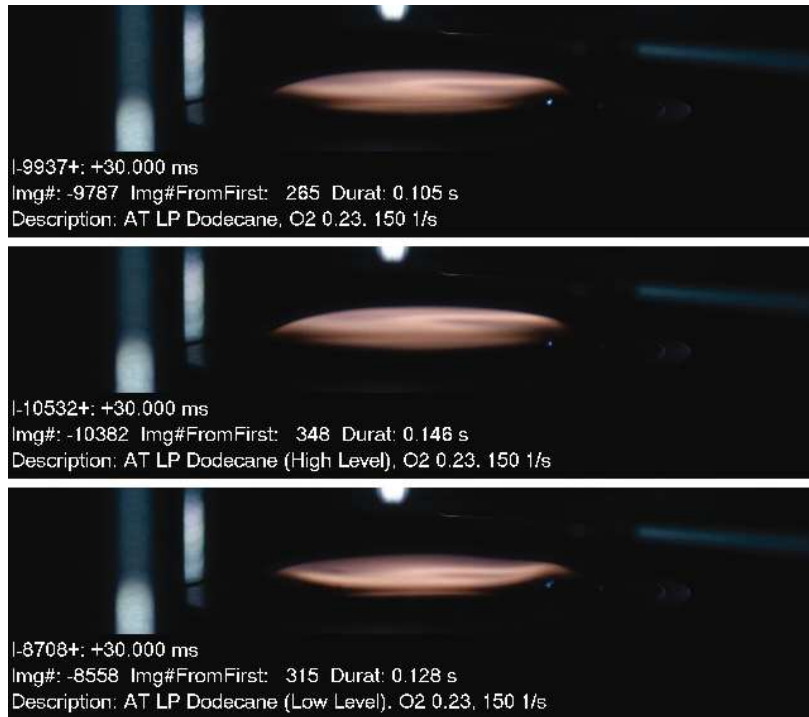


Figure 5.36: Flames after autoignition above the liquid pool surface of n-dodecane at regular/full (top), high/overflowing (middle), and low (bottom) cup levels.

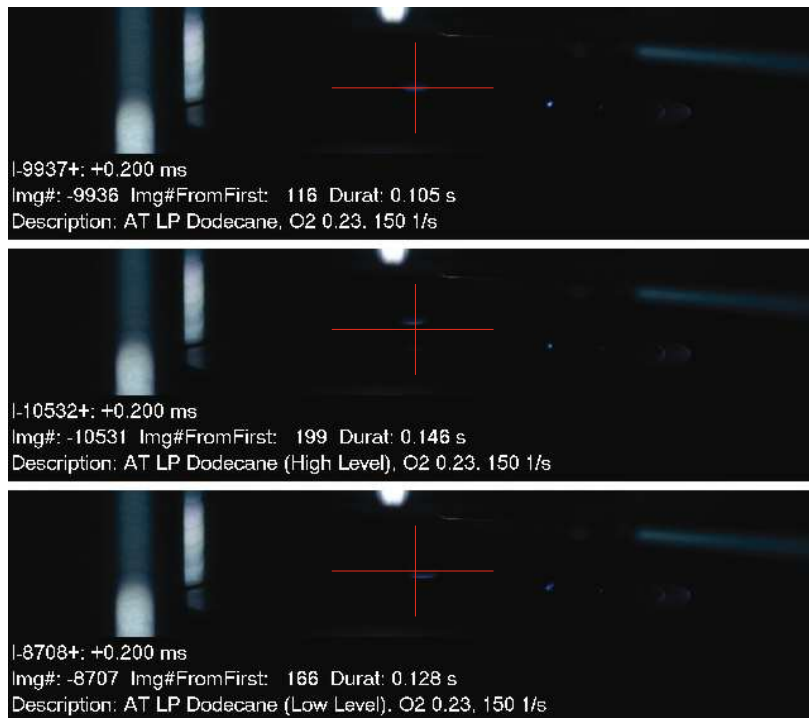


Figure 5.37: Autoignition events of n-dodecane at regular/full (top), high/overflowing (middle), and low (bottom) cup levels leading to the respective flames shown in Figure 5.36.

very little influence on the flame structure and only had an insignificant effect on measured autoignition temperatures. Figures 5.36 and 5.37 are screenshots of high-speed recordings from experiments with n-dodecane showing flames and ignition events respectively with various levels of fuel in the cup. Similar results were generated with the other PRFs and at higher strain rates. As it can be seen, the vertical flame position is moving along with the fuel level in the cup, but results in similar structures. The horizontal position of the initial ignition event on the other hand slightly but noticeably shifts when the fuel level is low which suggests that fuel overflowing from the cup is more desirable than having too little fuel in the cup prior to ignition. The needle in the cup might play a role in cases of low fuel level as well.

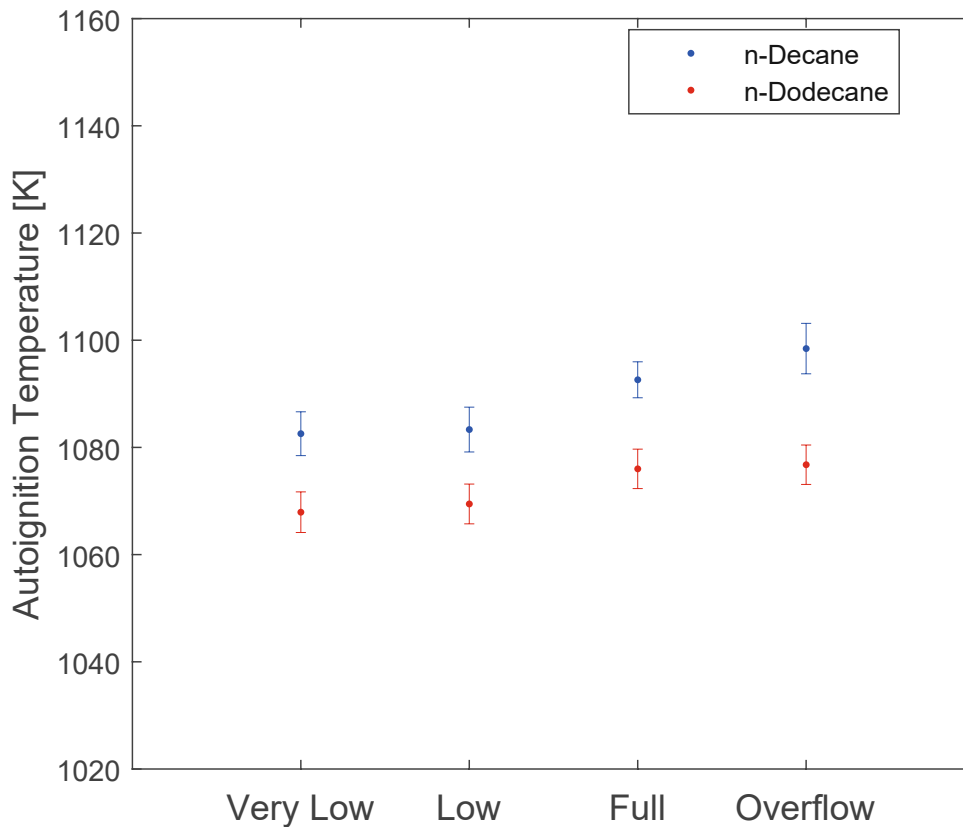


Figure 5.38: Measured autoignition temperatures including standard error bars for n-decane and n-dodecane at various liquid levels in the fuel cup immediately prior to ignition.

In Figure 5.38 the measured autoignition temperatures for various levels of n-decane and n-dodecane at otherwise identical boundary conditions are presented. The state labeled as “Full” is desired during liquid pool experiments and is achieved when no fuel is overflowing from the cup, the liquid level forms a plain surface with the brim of the cup, and the needle is barely visible. Compared to atmospheric pressures, maintaining a perfectly full liquid level state while no fuel is overflowing, is not possible at elevated pressures because of the significantly increased forces exerted on the liquid surface by the oxidizer. The result is a concave shaped fuel surface where a compromise has to be made to avoid rapid depletion of the fuel cup. It was also tested if any deviation can be noticed in case the cup runs almost empty, a state labeled as “Very Low”. As expected and similar to the situation in the gaseous configuration, only the evaporated fuel exiting the cup, now acting as a gaseous duct with the upstream configuration having no influence on the outcome, is relevant to the reaction. Nevertheless, depletion of the cup has to be avoided as to prevent overheating and thereby changing the temperature of the liquid fuel in the system which is supposed to be kept at constant room temperature.

As seen in the measurements, the deviation of the autoignition temperatures resulting from various levels of fuel prior to ignition is not significant, although the fuel used has some influence when it is overflowing from the cup. The fuel dependency can be explained by differences in physical properties which lead to different heights of the liquid surface relative to the cup during experimentation. When fuel is overflowing and the push from the oxidizer is relatively low, the rise in surface detracts from the separation distance which can have an impact on experimental results because of its direct relation to the strain rate. It is important to point out that at the atmospheric setup, the fuel surface when the level is too high, forms a convex surface, a shape, however, which cannot be achieved and maintained at the HPCEF at elevated pressures. To simulate that circumstance at atmospheric pressures the strain rate has to be significantly increased.

5.3.2 Elevated Strain Rates

To investigate the behaviour of the liquid pool at atmospheric pressures and increased strain rates, previous results gathered at UC San Diego's Combustion Laboratory were reviewed and used as the basis to verify reproducibility and also proper operation of the new setup [30,101]. The results presented in Figure 5.39 were produced under similar conditions as in [101], but on a different counterflow setup. The fuels were n-heptane and n-decane with an oxygen mass fraction of 0.23 in the oxidizer while autoignition temperatures were measured for various strain rates. A sequence composed of images taken from a high-speed recording of an autoignition event captured during an experiment with n-heptane can be viewed in Appendix C.

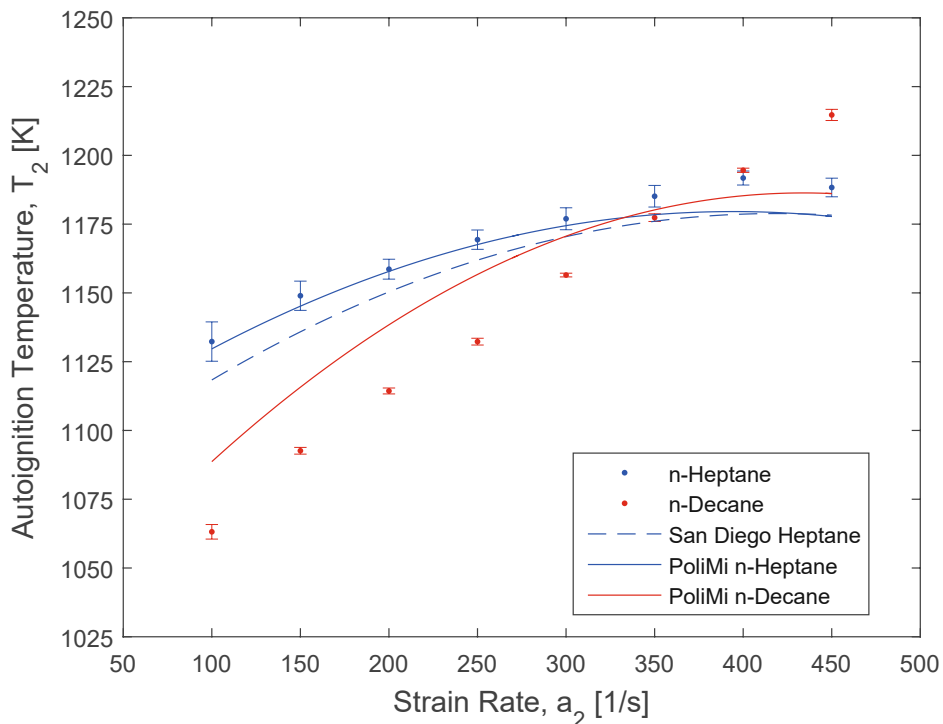


Figure 5.39: Autoignition temperatures obtained through measurements plotted with standard errors and computational results generated with Cantera using the UCSDComLab-Module for condensed n-heptane and n-decane at atmospheric pressure and an oxygen mass fraction of 0.23 in the oxidizer. (Appendix, Tables D.26 and D.27)

The computations in Figure 5.39 were based on reduced and specialized versions of the PoliMi Mechanism, and the San Diego Heptane Mechanism. As it can be seen in the diagram, San Diego and PoliMi yield very similar numerical results for n-heptane and also show a high level of agreement with the measured temperatures. The computations for n-decane do not match the experimental results as closely over the entire investigated range as for n-heptane, but are still at an acceptable level. However, the most important aspect of the results in Figure 5.39, namely a crossover of the autoignition temperature curves of the two PRFs with increasing strain rate, is reflected in both, the experimental as well as the computational data.

The fact that at elevated strain rates, when the forces exerted on the liquid fuel by the oxidizer are significantly increased compared to when boundary conditions are mild, a crossover in the data is observed similar to the experimental results at elevated pressures, suggests that it might simply originate from an unaccounted transport phenomenon instead of being directly related to any interaction between high and low temperature chemistry which gets more pronounced with increasing pressure. If that in fact is the case, it should be possible to computationally simulate the crossover at elevated pressures, reflect it in the numerical data, and identify the unaccounted physical transport phenomenon through variations in the implementation of the underlying liquid pool configuration model without the need for changes in the chemical kinetic mechanisms.

5.3.3 Simulation of the Crossover

Based on the observations from the experiments at atmospheric pressure where the height of the liquid pool surface relative to the fuel cup showed a fuel dependent influence on the measurements, at first, it was tested if the introduction of pressure dependency of the separation distance can generate the crossover in the numerical results. The separation

distance was constantly adapted according to the boundary conditions during the simulations through a purely empirical algorithm for the purpose of testing. The implementation certainly changed the absolute values of the autoignition temperatures for all PRFs, but still no crossover was seen in the numerical results.

However, during extensive computational testing it was observed that at increased pressures and strain rates, and especially with lower separation distances, the solver exhibited more and more convergence issues. At first, it seemed plausible and was attributed to computational interference at elevated pressures of high and low temperature chemistry implemented in the mechanism files, but from a closer look at the simulated flame structures and particularly the flame positions, it was noticed that the domain where the flame is formed, is too narrow for the solver to properly operate. To overcome the convergence issues, a new empirical pressure dependent algorithm was implemented in the UCSDComLab-Module for Cantera which increased the flow and resulting momentum of the evaporated fuel from the cup while maintaining a constant separation distance. Thereby, the flame position is artificially heightened to move the stagnation plane away from the cup and the liquid fuel surface, giving the solver a wider domain to calculate the parameters of the flame.

The original formulation and model of the liquid pool configuration assume a perfectly still and even surface of the liquid fuel, exerting no significant momentum on the flowing oxidizer [101]. The experimental algorithm and model obviously violate that condition, but eventually might better reflect the imperfect conditions of the real physical experiment and the actual situation in the reaction zone where evaporation and the amount of fuel might be of significance after all. Figure 5.40 is showing computational results from Cantera with the UCSDComLab-Module and the newly implemented experimental liquid pool model, labeled as “dynamic LP”, which adapts the fuel evaporation rate and resulting flame position according to the boundary conditions to avoid convergence issues. The simulations with the classic model are included as well and are labeled “static LP”. As seen in the diagram,

the crossover can be simulated with the experimental liquid pool model. It also mitigates convergence issues and increases computation speed under certain boundary conditions where the classic model struggles to find solutions within a reasonable number of iterations.

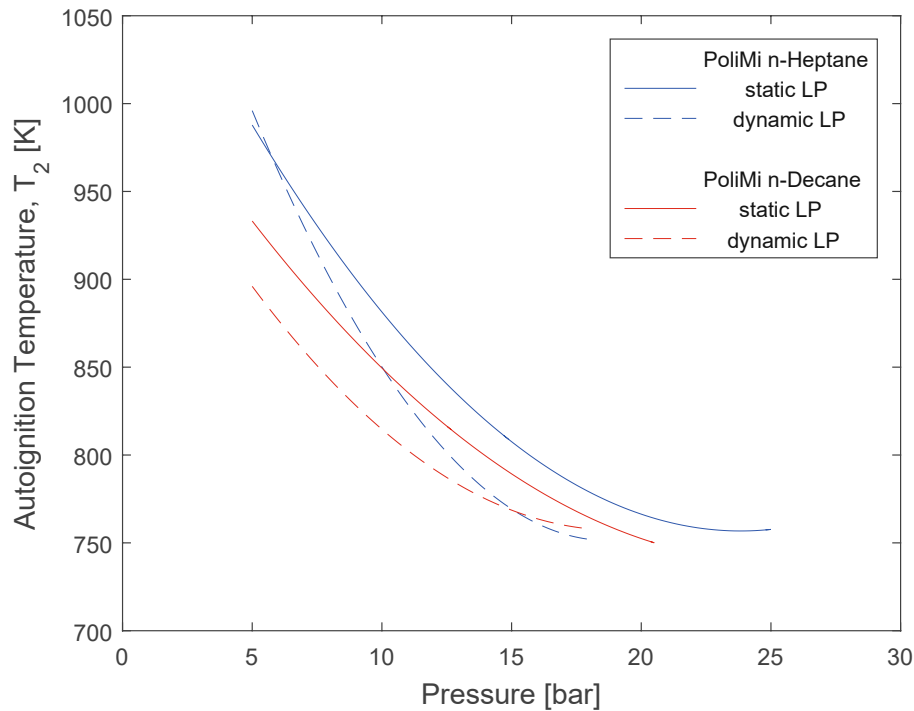


Figure 5.40: Computational results from Cantera with the UCSDComLab-Module implementing an experimental and purely empirical liquid pool model (dynamic LP) compared to simulations based on the classic model (static LP).

To take the investigations one step further, n-heptane and n-decane were tested at elevated pressures under varying strain rates. The measurement results are given in Figure 5.41 and show that the crossover of n-heptane and n-decane is moving to lower pressures with decreasing strain rates. Notice that the lines in the diagram simply connect the measured data points, and are only drawn to clearly show the crossovers at various strain rates and to make them more visible. The computations under similar conditions are shown in Figure 5.42 and exhibit the same trend, namely that the crossover is occurring at lower pressures the lower the strain rate gets. It has to be pointed out once more that the experimental liquid pool model used for the computations presented in Figure 5.42

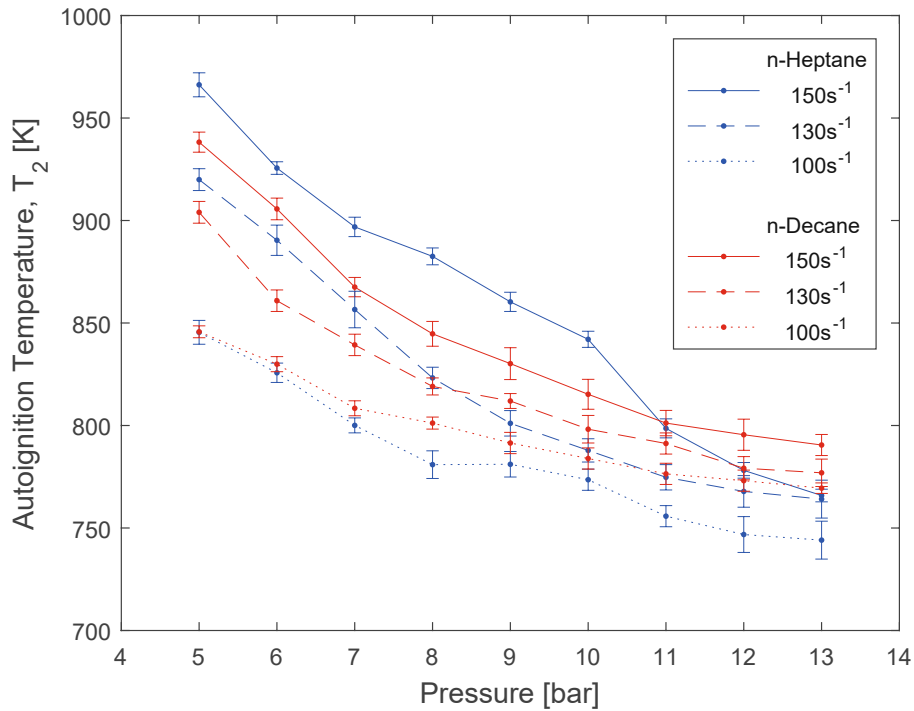


Figure 5.41: Experimentally measured autoignition temperatures for condensed n-heptane and n-decane at elevated pressures up to 13 bar and various strain rates. The oxygen mass fraction was 0.15. (Appendix, Tables D.16, D.18, D.19, D.20, D.22, and D.23)

implements a purely empirical and improvised algorithm which was developed for the sole purpose of testing. The new model gives hints in the direction where the crossover might be coming from, but in-depth investigations are required to identify the exact mechanisms causing the phenomenon, or to fine tune the empirical parameters of the algorithm and model.

The fact that the crossover is reflected in the numerical data when the experimental implementation of the liquid pool model is used, offers two different explanations why the phenomenon is observed in the measured results, but not in the computations with the classic model. Either the influence of the liquid pool evaporation is far greater than expected under harsher boundary conditions, or the numerical solver is simply incapable of generating proper solutions and handling the thin mixing layer and domain around the flame sheet

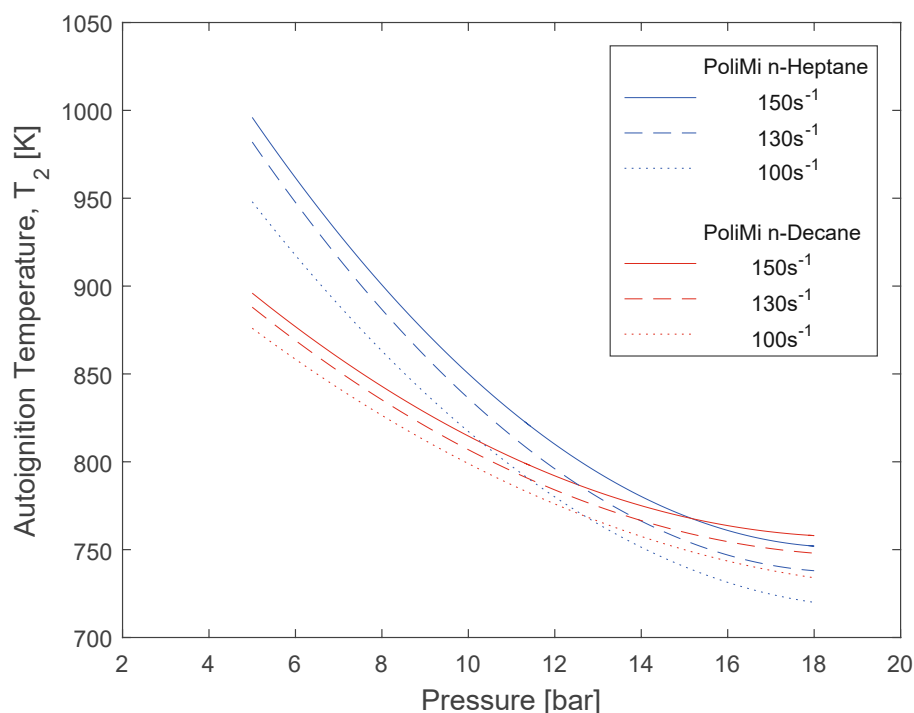


Figure 5.42: Computational predictions for autoignition temperatures of condensed n-heptane and n-decane at elevated pressures up to 18 bar, an oxygen mass fraction of 0.15, and various strain rates generated with Cantera, the UCSDComLab-Module with the experimental liquid pool model implementation, and reduced versions of the PoliMi Mechanism.

because the gradients of the calculated parameters are too steep when the flame is too close to the liquid pool surface, leading to incorrect predictions when the classic model is used even though the chemical kinetic mechanisms are accurate. Either way, since the potential to make further adaptations to the physical device to closer match the classic model is very limited and resource-consuming without the guaranty of a positive outcome, it is recommended to adapt the model of the liquid pool configuration in order to closer match the measured results under the given boundary conditions. If the experimental parameters are to be varied, however, a change of inert gas in the oxidizer stream might offer an alternative that allows for maintaining the other boundary conditions while simultaneously lowering the forces exerted on the liquid pool surface, thereby widening the mixing layer and flame sheet, and also shifting the position of the flame further away from the liquid pool surface.

5.3.4 Helium as an Inert

By changing the inert gas in the oxidizer stream from nitrogen with a molecular weight of 28 g/mol to helium which is a single atom species with only 4 g/mol of molecular weight, the density of the stream and resulting momentum imposed on the liquid pool surface at any given strain rate or pressure can be reduced to a fraction of its value in comparison to air. Considering that a mass fraction of $Y_{O_2/N_2} = 0.23$ of oxygen in nitrogen is corresponding to a mole fraction of $X_{O_2} = 0.207$ of oxygen in the oxidizer stream, a mixture with helium would require a mass fraction of $Y_{O_2/He} = 0.676$ to match the boundary conditions of experiments with air as an oxidizer. Several experiments with varying boundary conditions at atmospheric pressure with helium as an inert were conducted, and the results were compared to flame structures and also autoignition temperatures of measurements with nitrogen in the oxidizer stream. Two n-decane flames, one with nitrogen and one with helium as an inert, at atmospheric pressure are given in Figure 5.43, while measured autoignition temperatures at a strain rate of 450 1/s and an oxygen mole fraction of 0.21 are shown in Figure 5.44.

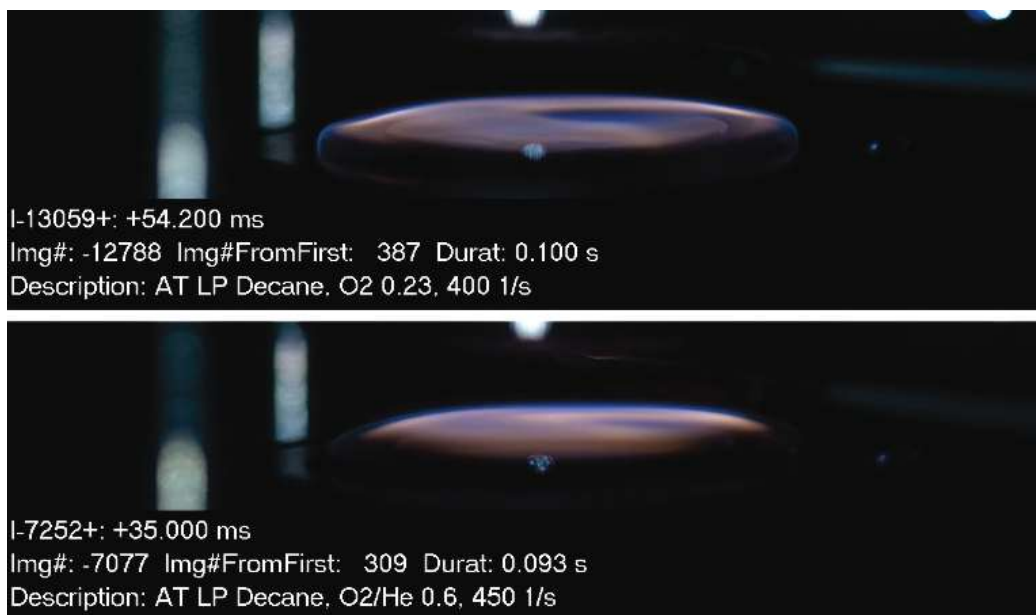


Figure 5.43: Flames of n-decane after autoignition with nitrogen (top) and helium (bottom) as an inert in the oxidizer stream at slightly different boundary conditions.

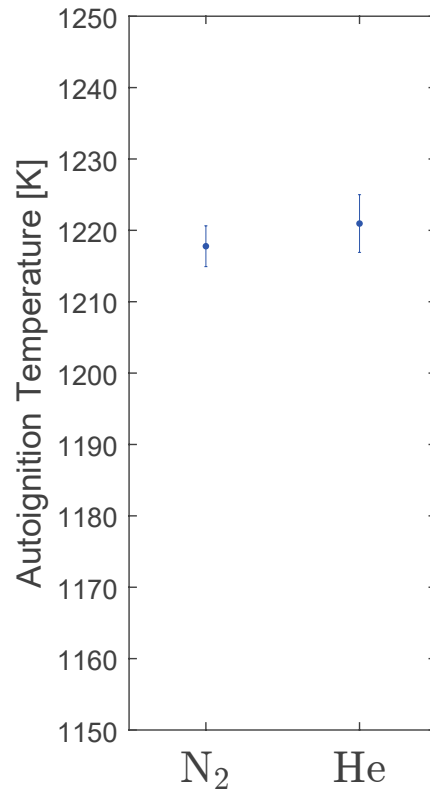


Figure 5.44: Autoignition temperature measurements including standard errors of condensed n-decane at atmospheric pressure with respectively nitrogen and helium as an inert in the oxidizer. The strain rate was 450 1/s and the oxygen mole fraction 0.21.

According to the autoignition temperature measurements at atmospheric pressure, the results under otherwise identical boundary conditions are similar whether nitrogen or helium is used as an inert when the oxygen mole fractions are matched. Furthermore, the similar color of the flames observed during the measurements is a good indicator that the fuel to oxidizer ratio is matched as well in both configurations even though flame structures can differ significantly. The images in Figure 5.43 also reveal that, even though the strain rate was slightly higher during one of the experiments with helium, the flame position is noticeably higher above the fuel surface, and less spread out not extending the reaction into the suction gap and exhaust than when nitrogen was used. That also suggests that overall, a better flame stability can be maintained at higher strain rates when helium is used.

Additional experiments showed that with helium as an inert, the strain rate can be significantly increased before resulting in flame structures similar to the ones achieved with nitrogen at relatively low strain rates. Two flames of n-decane under atmospheric conditions at 450 1/s and 1400 1/s are shown in Figure 5.45. Even though the difference in strain rate is 950 1/s, both flames are equally stable and ignite centrally when observed with the high-speed camera. As it can be seen in the images in Figures 5.43 and 5.45, at a strain rate of 1400 1/s, the flame starts to look similar to the structure at 400 1/s when nitrogen is used. However, in comparison, after 450 1/s nitrogen flames become increasingly unstable and center ignition is less likely to occur, while helium flames prove to be absolutely stable and ignite centrally even at strain rates beyond 1400 1/s.

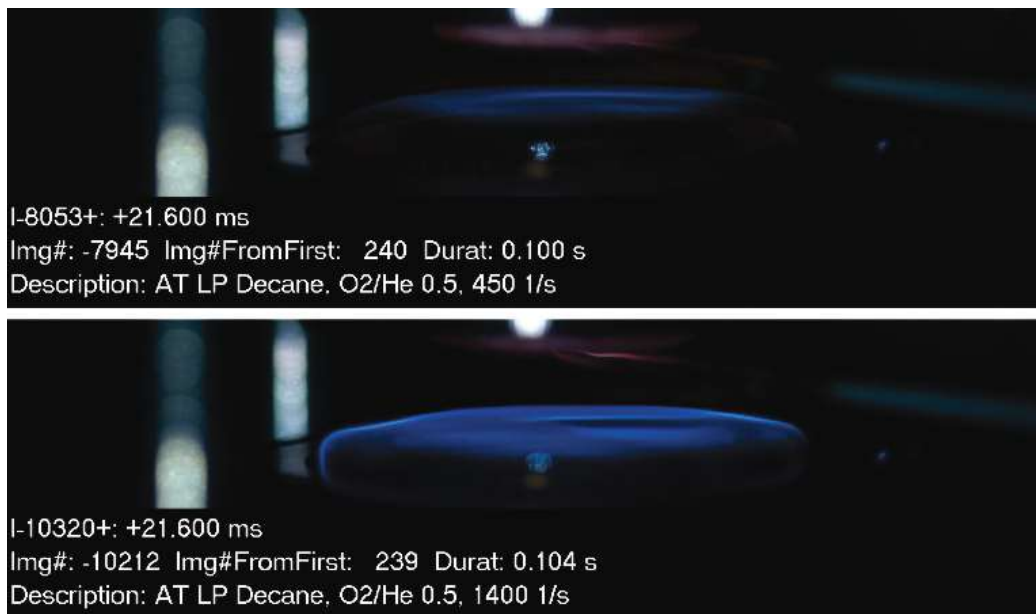


Figure 5.45: Flames of n-decane after autoignition with helium as an inert in the oxidizer stream at strain rates of 450 1/s (top) and 1400 1/s (bottom).

6 Conclusion and Future Work

After considerable refurbishment efforts and expansion of the capabilities of both setups at UC San Diego’s Combustion Laboratory, the atmospheric counterflow workbench as well as the High Pressure Combustion Experimental Facility (HPCEF), extinction and autoignition properties of a number of alternative and surrogate fuel components were investigated. The tested fuels under various conditions and configurations were dimethyl ether (DME), propane, and the primary reference fuel (PRF) and surrogate components n-heptane, n-decane, and n-dodecane. The complete set of evaluated measurement data, including the correlating standard errors of measurement, is summarized for reference in Appendix D. The exact boundary conditions for each set can be found in the respective chapter referenced in Appendix D by the subsection title.

To quickly and efficiently generate computations and predictions for the investigation of this thesis, a new Python module named “UCSDComLab” for the software toolkit Cantera was created. Cantera can numerically solve chemical kinetic, thermodynamic, and transport processes, and also offers some basic models for the counterflowing configuration. Those models were significantly modified and expanded to fit the requirements of this thesis and to virtually represent the experiments on the real physical devices in UC San Diego’s Combustion Laboratory. Aside from the new models, several functions were implemented in the UCSDComLab-Module to simplify the simulation of conducted experiments and to streamline the evaluation of measured and computational data. During the entire development phase, the module was repeatedly successfully compared and tested against other software toolkits, utilizing various mechanisms for the purpose of evaluation. Eventually, Cantera in conjunction with the UCSDComLab-Module, when used adequately, proved to be a highly efficient and practical tool to generate predictions and contributed vital data for the investigations and development of this thesis.

While the HPCEF is now technically capable of experimentation up to 60 bar, it is still not recommended to operate at pressures beyond 13 bar in the current burner configuration in combination with the gas flow control system installed. Due to the specifications of certain equipment pieces in place and geometrical restrictions of the burner, the main device is very inflexible in terms of boundary conditions and can only be operated in a fairly narrow range, especially when elevated pressures are involved. If the burner is operated outside that boundary condition range, results become increasingly unreliable, unreproducible, and implausible. Widening the range for meaningful results would require unfeasible replacement of parts and major adaptations to the setup every time pressure, strain rate, or oxygen mass fraction requirements for an experiment are to be slightly changed. Further modifications required to increase flexibility and, more importantly, safety would include replacing the threaded connections on the bottom plate of the chamber with welded mount fittings, upgrading all currently o-ring sealed connections with proper high pressure packing and sealing methods, installing a double acting pump to feed the water sprays of the burner to minimize oscillation, and most importantly, a proper scale-up analysis of the system to determine adequate parameters of the flow control system, exhaust dimensions, and gaseous oxidizer duct to liquid pool surface ratio of the counterflow burner to regain control of the flow field inside the reaction zone at elevated pressures.

The loss of control over the flow field at elevated pressures, clearly noticeable through the resulting unsteady flames and preceding visible density differences inside the reaction zone, is the biggest issue for gathering meaningful measurements at the HPCEF that properly correspond with the assumed models. As found during the investigation for this thesis, the cause for the disturbances is the exerted force at elevated pressure resulting from the sheer amount of gas streaming into the reaction zone. Due to the results, it is highly recommended to explore the option of using helium as an inert in the oxidizer stream at the HPCEF. Considering the findings that similar phenomena occur at elevated pressures

and atmospheric pressure in combination with high strain rates, utilizing helium has the potential to tremendously increase the stability of flames at the HPCEF. Not only are the stability issues a major factor for safe and proper operation at the facility, but the instabilities also visually show that the underlying flow field in the reaction zone is not as perfect as described by the models used for the computations, whereby the potential for errors and phenomena that are not accounted for in the simulations is introduced.

Appendix A Code Listings

Listing A.1: Calculations from the counterflow setup control software's main VI to compute all relevant fluid flow parameters implemented as a function in MATLAB - calcFlows.m

```
1 function [flowdata, inputdata, V2, V1, a1, rho2, rho1, W2, W1, X0x, XF, flowVol0x, flowVol0xIn,
    ↳ flowVolF, flowVolFIn, flowVol0xCur, flowVolFCur, flowSLM0x, flowSLM0xIn, flowSLMF,
    ↳ flowSLMFIn, flowSLM0xCur, flowSLMFCur, TB, flowVolFlush, flowSLMHeat] = calcFlows(config
    ↳ , top, ox, f, a2, Y02, YF, T2, T1, P, cur)
2 %% Calculate Counterflow Burner Flow Parameters (UC San Diego, Combustion Laboratory)
3 % by Martin Hunyadi-Gall <mhunyadigall@ucsd.edu>
4
5 % -) set/check MFC Configuration and Calibration
6 % -) set/check Top and Configuration Data
7 % -) set/check Surroundings Temperature
8
9 % Examples:
10 % [flowdata, inputdata, V2, V1, a1, rho2, rho1, W2, W1, X0x, XF, flowVol0x, flowVol0xIn, flowVolF,
    ↳ flowVolFIn, flowVol0xCur, flowVolFCur, flowSLM0x, flowSLM0xIn, flowSLMF, flowSLMFIn,
    ↳ flowSLM0xCur, flowSLMFCur, TB, flowVolFlush, flowSLMHeat]=calcFlows('ATG', 'AI', 'OXY',
    ↳ 'nC7H16', 300, 0.233, 0.6, 700, 530, 2, 0.2);
11 % [flowdata, inputdata, V2, V1, a1, rho2, rho1, W2, W1, X0x, XF, flowVol0x, flowVol0xIn, flowVolF,
    ↳ flowVolFIn, flowVol0xCur, flowVolFCur, flowSLM0x, flowSLM0xIn, flowSLMF, flowSLMFIn,
    ↳ flowSLM0xCur, flowSLMFCur, TB, flowVolFlush, flowSLMHeat]=calcFlows('HPL', 'AI', 'CAIR',
    ↳ 'nC7H16', 150, 0.15, -1, 700, -1, 13, 0.28);
12 % [flowdata, inputdata]=calcFlows('ATG', 'AI', 'OXY', 'nC7H16', 300, 0.233, 0.6, 700, 530, 2, 0.2);
13 % [flowdata, inputdata]=calcFlows('HPL', 'AI', 'CAIR', 'nC7H16', 150, 0.15, -1, 700, -1, 13, 0.28);
14
15 % Indices:
16 % Ox ... Oxidizer
17 % F ... Fuel
18 % In ... Inert
19 % 2 ... Oxidizer Stream
20 % 1 ... Fuel Stream
21 % Cur ... Curtain
22
23 % Variables (declaration and initiation):
24 % a2 = 0; % [1/s] Oxidizer Stream strain rate
25 % a1 = 0; % [1/s] Fuel Stream strain rate
26 % Y02 = 0; % [-] Oxygen mass fraction
27 % YAIR = 0; % [-] Air mass fraction
28 % Y0x = 0; % [-] Oxidizer mass fraction
29 % Y0xIn = 0; % [-] Oxidizer Inert mass fraction
30 % YF = 0; % [-] Fuel mass fraction
31 % YFIn = 0; % [-] Fuel Inert mass fraction
32 % T2 = 0; % [K] Oxidizer Stream temperature
33 % T1 = 0; % [K] Fuel Stream temperature
34 % V2 = 0; % [m/s] Oxidizer Stream injection velocity
35 % V1 = 0; % [m/s] Fuel Stream injection velocity
36 % rho2 = 0; % [kg/m^3] Oxidizer Stream density
37 % rho1 = 0; % [kg/m^3] Fuel Stream density
38 % X0x = 0; % [-] Oxidizer mole fraction
39 % X0xIn = 0; % [-] Oxidizer Inert mole fraction
40 % XF = 0; % [-] Fuel mole fraction
41 % XFIn = 0; % [-] Fuel Inert mole fraction
42 % WF = 0; % [g/mol] molecular weight of Fuel
43 % W0x = 0; % [g/mol] molecular weight of Oxidizer
44 % W1 = 0; % [g/mol] molecular weight of Fuel Stream
```

```

45 % W2 = 0;           % [g/mol] molecular weight of Oxidizer Stream
46 % flowVol = 0;     % [L/min] Volumetric Flow
47 % flowSLM = 0;     % [SL/min] Volumetric Flow at MFC Standard Temperature/Pressure
48
49
50 format bank;
51
52 inputdata = table(cellstr(config),cellstr(top),cellstr(ox),cellstr(f),a2,YO2,YF,T2,T1,P,
    ↪ cur);
53 inputdata.Properties.VariableNames(1:4) = {'config','top','ox','f'};
54 inputdata.Properties.Description = ...
55     'Input Parameters to Calculate relevant Flow Parameters for Counter Flow Burner';
56 inputdata.Properties.VariableUnits(:) = ...
57     {'-' '-' '-' '-' '1/s' '1' '1' 'K' 'K' 'bar' '1'};
58 inputdata.Properties.VariableDescriptions(:) = {...
59     'Configuration (ATG/ATL/HPL)' ...
60     'Experiment Type/Top (AI/EX)' ...
61     'Oxidizer (CAIR/SAIR/OXY)' ...
62     'Fuel (as in '>> Fuel.printFuelsList')' ...
63     'Oxidizer Stream strain rate' ...
64     'Oxygen mass fraction' ...
65     'Fuel mass fraction' ...
66     'Oxidizer Stream temperature' ...
67     'Fuel Stream temperature' ...
68     'Pressure' ...
69     'Curtain fraction'...
70     };
71
72 % select Experiment Typ/Top
73 if strcmpi(top,'ai')           % 'AI' for Autoignition
74     L = 12/1000;               % [mm]->[m] Separation Distance
75     DOx = 23.3/1000;          % [mm]->[m] Oxidizer Duct diameter
76     AOxCur = 882.5912/1000000; % [mm^2]->[m^2] Oxidizer Curtain area
77 elseif strcmpi(top,'ex')      % 'EX' for Extinction
78     L = 10/1000;              % [mm]->[m] Separation Distance
79     DOx = 23.45/1000;         % [mm]->[m] Oxidizer Duct diameter
80     AOxCur = 910.49/1000000;  % [mm^2]->[m^2] Oxidizer Curtain area
81 else
82     fprintf(2,'Choose between Autoignition (AI) or Extinction (EX) Experiment!\n\n');
83     return;
84 end
85
86 % set MFC Configuration
87 if strcmpi(config,'atg') || strcmpi(config,'atl')
88     % factory calibrated maximum flow rates of MFCs
89     mfcSetup = [30 50 100 100 20 10 50 5];
90     % actual maximum flow rates of MFCs after calibration in the lab
91     mfcCalib = [28.10 50.10 98.94 99.06 18.90 10.19 52.41 5.15];
92     % port setup [Ox OxIn OxCur F FIn FCur]
93     ports = [2 5 0 1 3 4];
94 else
95     % factory calibrated maximum flow rates of MFCs
96     mfcSetup = [500 500 50 200 150 300 100 30];
97     % actual maximum flow rates of MFCs after calibration in the lab
98     mfcCalib = [503.50 528.50 69.80 217.01 150.00 332.74 103.97 27.05];
99     % port setup [Ox OxIn OxCur F FIn FCur]
100    ports = [3 6 1 -1 -1 2];
101 end
102
103 % select Configuration

```

```

104 if strcmpi(config,'atg')           % 'ATG' for Gaseous or Vaporized Fuel at Atmospheric
    ↳ Pressure
105     config = 2;                    % [-] Strain Rate factor
106     DF = 23.1/1000;                % [mm]->[m] Fuel Duct diameter
107     AF = DF^2 * pi/4;              % [m^2] Fuel Duct Area
108     AgFCur = 650.3097/1000000;    % [mm^2]->[m^2] Fuel Curtain area
109 elseif strcmpi(config,'atl')      % 'ATL' for Pool of Liquid Fuel at Atmospheric Pressure
110     config = 1;                    % [-] Strain Rate factor
111 elseif strcmpi(config,'hpl')      % 'HPL' for Pool of Liquid Fuel at High Pressure
112     config = 1;                    % [-] Strain Rate factor
113     DOx = 22.5/1000;               % [mm]->[m] Oxidizer Duct diameter
114     AOxCur = 1050/1000000;       % [mm^2]->[m^2] Oxidizer Curtain area
115 else
116     fprintf(2,['Choose between Gaseous/Vaporized Fuel (ATG), Pool of '...
117         'Liquid Fuel (ATL) or High Pressure (HPL) Configuration!\n\n']);
118     return;
119 end
120
121 AOx = DOx^2 * pi/4;                % [m^2] Oxidizer Duct Area
122 calib = mfcSetup./mfcCalib;       % [-] MFC Calibration Factors
123
124 % declaration and initiation of constants
125 R = 8.3144598; % [J/(mol K)] Universal Gas Constant
126 Tsur = 298.15; % [K] Surroundings temperature
127 P = P*10^5; % [bar]->[Pa] pressure
128 TSTP = 273.15; % [K] Standard Temperature for MFC Calibration
129 PSTP = 101325; % [Pa] Standard Pressure for MFC Calibration
130 YO2AIR = 0.233; % [-] mass fraction of Oxygen in Air
131 WO2 = 31.998; % [g/mol] molecular weight of Oxygen
132 WN2 = 28.013; % [g/mol] molecular weight of Nitrogen
133 %WHe = 4.003; % [g/mol] molecular weight of Helium
134 WCAIR = 28.97; % [g/mol] molecular weight of Medical Air
135 WSAIR = WCAIR; % [g/mol] molecular weight of Shop Air
136 WIn = WN2; % [g/mol] molecular weight of Inert
137
138 % select Oxidizer
139 if strcmpi(ox,'cair')              % 'CAIR' for Compressed Air/Medical Air
140     YAIR = YO2/YO2AIR;
141     YOx = YAIR;
142     WOx = WCAIR;
143 elseif strcmpi(ox,'sair')          % 'SAIR' for Shop Air
144     YAIR = YO2/YO2AIR;
145     YOx = YAIR;
146     WOx = WSAIR;
147 elseif strcmpi(ox,'oxy')          % 'OXY' for Oxygen
148     YOx = YO2;
149     WOx = WO2;
150 else
151     fprintf(2,['Choose between Compressed Air/Medical Air (CAIR), Shop '...
152         'Air (SAIR) or Oxygen (OXY) in the Oxidizer Stream!\n\n']);
153     return;
154 end
155
156 % select Fuel (separate class 'Fuel' used to store and retrieve relevant Fuel Data)
157 try
158     if eq(config,2)
159         [fuel,WF,TB,rhoF] = Fuel.getFuel(f,T1);
160     else
161         [fuel,WF,TB,rhoF] = Fuel.getFuel(f,Tsur);
162     end
163 catch

```

```

164     return
165 end
166
167 if eq(config,1) && ~fuel.liquid
168     fprintf(2,['Fuel will be gaseous at Surroundings Temperature. '...
169         'Liquid Pool Configuration cannot be used.\n\n']);
170     return;
171 elseif eq(config,2) && fuel.liquid
172     fprintf(2,['Fuel will be liquid at given Fuel Temperature. '...
173         'Gaseous/Vaporized Configuration cannot be used.\n\n']);
174     return;
175 end
176
177
178 % Oxidizer Stream
179 V2 = a2 * L / (2 * config);
180
181 YOxIn = 1 - YOx;
182
183 XOx = YOx/WOx * (sum([YOx/WOx YOxIn/WIn]))^(-1);
184 XOxIn = 1 - XOx;
185
186 W2 = sum([XOx*WOx XOxIn*WIn]); % mixture of ideal gases
187
188 rho2 = P * W2 / (R * T2) /1000; % ideal gas law
189
190 flowVolOx = V2 * 60 * AOx * 1000 * XOx;
191 flowVolOxIn = V2 * 60 * AOx * 1000 * XOxIn;
192 flowVolOxCur = V2 * 60 * AOxCur * 1000 * cur;
193
194 flowSLMOx = flowVolOx * calib(ports(1)+1) * TSTP/T2 * P/PSTP;
195 flowSLMOxIn = flowVolOxIn * calib(ports(2)+1) * TSTP/T2 * P/PSTP;
196 flowSLMOxCur = flowVolOxCur * calib(ports(3)+1) * TSTP*3/(T2+2*TSur) * P/PSTP;
197
198
199 % Fuel Stream
200 % Gaseous or Vaporized Configuration
201 if isequal(config,2)
202     YFIn = 1 - YF;
203
204     XF = YF/WF * (sum([YF/WF YFIn/WIn]))^(-1);
205     XFIn = 1 - XF;
206
207     W1 = sum([XF*WF XFIn*WIn]); % mixture of ideal gases
208
209     rho1 = P * W1 / (R * T1) /1000; % ideal gas law
210
211     V1 = sqrt(rho2 * V2^2 / rho1); % momentum balance to center flame
212
213     a1 = (2 * config) * V1 / L;
214
215     flowVolF = V1 * 60 * AF * 1000 * XF; % Vaporized: ideal gas law ->[g/min]->[mL/min]
216     flowVolFIn = V1 * 60 * AF * 1000 * XFIn;
217     flowVolFCur = V1 * 60 * AgFCur * 1000 * cur;
218
219     flowSLMF = flowVolF * calib(ports(4)+1) * TSTP/T1 * P/PSTP;
220     flowSLMFIn = flowVolFIn * calib(ports(5)+1) * TSTP/T1 * P/PSTP;
221     flowSLMFCur = flowVolFCur * calib(ports(6)+1) * TSTP/(T1*0.9+TSur*0.1) * P/PSTP;
222
223 % Liquid Pool Configuration
224 else

```

```

225     XF = 1;
226     W1 = WF;
227     rho1 = rhoF;
228     V1 = 0;
229     a1 = 0;
230     flowVolF = 0;
231     flowVolFIn = 0;
232     flowVolFCur = 0;
233     flowSLMF = flowVolF*1;
234     flowSLMFIn = flowVolFIn*1;
235     flowSLMFCur = flowVolFCur*1;
236 end
237
238 flowVolFlush = flowVolOx + flowVolOxIn + flowVolOxCur + flowVolFCur;
239 flowSLMHeat = flowSLMOx + flowSLMOxIn;
240
241
242 % generate Table with Flow Data
243 flowdata = table(V2,V1,a1,rho2,rho1,W2,W1,XOx,XF,flowVolOx,flowVolOxIn,flowVolF,flowVolFIn
    ↪ ,flowVolOxCur,flowVolFCur,flowSLMOx,flowSLMOxIn,flowSLMF,flowSLMFIn,flowSLMOxCur,
    ↪ flowSLMFCur,TB,flowVolFlush,flowSLMHeat);
244 flowdata.Properties.Description = ...
245     'Flow Parameters for Counter Flow Burner';
246 flowdata.Properties.VariableUnits(:) = {...
247     'm/s' 'm/s' '1/s' 'kg/m^3' 'kg/m^3' 'g/mol' 'g/mol' '1' '1' ...
248     'L/min' 'L/min' 'L/min' 'L/min' 'L/min' 'L/min' 'L/min' ...
249     'SL/min' 'SL/min' 'SL/min' 'SL/min' 'SL/min' 'SL/min' 'SL/min' ...
250     'degC' 'L/min' 'SL/min'};
251 flowdata.Properties.VariableDescriptions(:) = {
252     'Oxidizer Stream injection velocity' ...
253     'Fuel Stream injection velocity' ...
254     'Fuel Stream strain rate' ...
255     'Oxidizer Stream density' ...
256     'Fuel Stream density' ...
257     'Oxidizer Stream molecular weight' ...
258     'Fuel Stream molecular weight' ...
259     'Oxidizer mole fraction' ...
260     'Fuel mole fraction' ...
261     'Oxidizer Volumetric Flow' ...
262     'Oxidizer Inert Volumetric Flow' ...
263     'Fuel Volumetric Flow' ...
264     'Fuel Inert Volumetric Flow' ...
265     'Oxidizer Stream Curtain Volumetric Flow' ...
266     'Fuel Stream Curtain Volumetric Flow' ...
267     'Oxidizer Volumetric Flow at MFC Standard Temperature/Pressure' ...
268     'Oxidizer Inert Volumetric Flow at MFC Standard Temperature/Pressure' ...
269     'Fuel Volumetric Flow at MFC Standard Temperature/Pressure' ...
270     'Fuel Inert Volumetric Flow at MFC Standard Temperature/Pressure' ...
271     'Oxidizer Stream Curtain Volumetric Flow at MFC Standard Temperature/Pressure' ...
272     'Fuel Stream Curtain Volumetric Flow at MFC Standard Temperature/Pressure' ...
273     'boiling point of Fuel' ...
274     'Total Volumetric Flow of Streams for matching Flush' ...
275     'Total Volumetric Flow at MFC Standard Temperature/Pressure of Oxidizer Stream over
    ↪ Heating Element'};
276 end

```

Listing A.2: Working example of a Python script to simulate an autoignition experiment utilizing the module “UCSDComLab” - ucsdcomlab.exp.py

```

1 import sys
2 sys.path.append('../')
3 import numpy as np
4 import ucsdcomlab as sd
5
6 #####
7 # Input Parameters
8
9 config = 'ATG' # Experiment Configuration ('ATG'/'ATL'/'HPL')
10 L = 12 # Separation Distance [mm]
11
12 P = 1 # Pressure [bar]
13 T0x = 1210 # Oxidizer Stream Inlet Temperature [K]
14 TF = 298 # Fuel Stream Inlet Temperature [K]
15 Y02 = 0.23 # Oxygen Mass Fractions [-]
16 Fuel = 'C3H8' # Fuel
17 YF = 0.21 # Fuel Mass Fractions [-]
18 a2 = 400 # Oxidizer Strain Rate [1/s]
19
20 mech = 'SD.cti' # Mechanism File
21 initGrids = np.array([]) # Initial Grid
22
23
24 param = [config,P,T0x,TF,Y02,Fuel,YF,a2,mech,L,initGrids]
25 #param = [config,P,T0x,TF,Y02,Fuel,YF,a2,mech,L]
26 #param = [config,P,T0x,TF,Y02,Fuel,YF,a2]
27
28
29 #####
30 # Run
31
32 Exp = sd.Experiment(*param)
33 #Exp.setExpTyp(L)
34 Exp.run(loglevel=0)

```

Listing A.3: Working example of a Python script to simulate an autoignition experiment utilizing the module “UCSDComLab” by means of different methods - ucsdcomlab.expai.py

```

1 import sys
2 sys.path.append('../')
3 import numpy as np
4 import ucsdcomlab as sd
5
6 #####
7 # Input Parameters
8 #
9 # Exp.sim():
10 # Iteration starts at 'Flame: True' until 'Flame: False' is found (AI: neg/-, EX: pos/+)
11 #
12 # Numeric parameter to be iterated along Y-Axis must be initiated as True and yParam must
13 #   ↳ be set
14 # Numeric parameter to be varied along X-Axis must be initiated as False and xParam must
15 #   ↳ be set

```

```

14
15 config = 'ATG' # Experiment Configuration ('ATG'/'ATL'/'HPL')
16
17 P = 1.013 # Pressure [bar]
18 TOx = True # Oxidizer Stream Inlet Temperature [K]
19 TF = 294 # Fuel Stream Inlet Temperature [K]
20 YO2 = False # Oxygen Mass Fractions [-]
21 Fuel = 'C3H8' # Fuel
22 YF = 0.21 # Fuel Mass Fractions [-]
23 a2 = 400 # Oxidizer Strain Rate [1/s]
24
25 mech = 'SD.cti' # Mechanism File
26 yPrec = 2 # Precision: Interval for Iteration of yParam
27
28 # Initial Values of Parameter for Iteration (initiated as True):
29 yParam = np.array([1202, 1218])
30 # Values of Parameter to be varied along X-Axis (initiated as False):
31 xParam = np.array([0.23, 0.15])
32
33 initGrids = np.array([]) # No/Default Initial Grid
34 #initGrids = np.array([0.0, 0.2, 0.4, 0.6, 0.8, 1.0]) # Original Cantera Initial
    ↪ Grid
35 #initGrids = np.array([i for i in np.arange(0,1.1,0.2)]) # Modified Cantera Initial
    ↪ Grid
36 # Various Initial Grids for each Parameter in xParam
37 #initGrids = np.array([ [0.0, 0.2, 0.4, 0.5, 0.6, 0.8, 1.0]\
38 # , [i for i in np.arange(0,1.1,0.2)]\
39 # ], dtype=object)
40
41
42 param = [config,P,TOx,TF,YO2,Fuel,YF,a2,yParam,xParam,mech,initGrids,yPrec]
43 #param = [config,P,TOx,TF,YO2,Fuel,YF,a2,yParam,xParam]
44
45
46 #####
47 # Run - Method 1 - ucsdcomlab.Experiment
48
49 Exp = sd.Experiment(*param)
50 Res = Exp.sim(mode=3,loglevel=1)
51 #Fit = Exp.fitSim(loglevel=1)
52 #print(Fit[0])
53 sys.exit('DELETE THIS LINE TO RUN ucsdcomlab.solve() DIRECTLY')
54
55
56 #####
57 # Run - Method 2 - ucsdcomlab.solve(), ucsdcomlab.fitFile()
58
59 config = 2 # Setup Configuration Factor: 2 ... Gaseous/Vaporized, 1 ...
    ↪ Liquid Pool
60 L = 12 # Separation Distance [mm]
61 initGrid = np.array([]) # Initial Grid
62 TOx = yParam[0]
63 YO2 = xParam[0]
64 result = sd.solve(config,L,P,TOx,TF,YO2,Fuel,YF,a2,mech,initGrid,mode=1,loglevel=0,
    ↪ diaglevel=1)
65
66 #Fit = sd.fitFile('AI Experiment',loglevel=1)

```

Listing A.4: Working example of a Python script to simulate an autoignition experiment in liquid pool configuration utilizing the module “UCSDComLab” - ucsdcomlab.explp.py

```
1 import sys
2 sys.path.append('../')
3 import numpy as np
4 import ucsdcomlab as sd
5
6 #####
7 # Input Parameters
8
9 config = 'HPL' # Experiment Configuration ('ATG'/'ATL'/'HPL')
10
11 P = False # Pressure [bar]
12 TOx = True # Oxidizer Stream Inlet Temperature [K]
13 TF = 298 # Fuel Stream Inlet Temperature [K]
14 YO2 = 0.15 # Oxygen Mass Fractions [-]
15 Fuel = 'C7H16' # Fuel
16 a2 = 150 # Oxidizer Strain Rate [1/s]
17
18 mech = 'SDHEPT.cti' # Mechanism File
19 yPrec = 2 # Precision: Interval for Iteration of yParam
20
21 # Initial Values of Parameter for Iteration (initiated as True):
22 yParam = np.array([920, 872, 808, 762])
23 # Values of Parameter to be varied along X-Axis (initiated as False):
24 xParam = np.array([7, 10, 13, 16])
25
26 # Initial Grid
27 initGrid = np.array([])
28
29
30 param = [config, P, TOx, TF, YO2, Fuel, None, a2, yParam, xParam, mech, initGrid, yPrec]
31
32
33 #####
34 # Run
35
36 Exp = sd.Experiment(*param)
37 Res = Exp.sim(mode=3, loglevel=1)
38 Fit = Exp.fitSim(loglevel=1, yLim=np.array([500, 1300]))
```

Appendix B Apparatus



Figure B.1: High Pressure Combustion Experimental Facility - Workstation.



Figure B.2: High Pressure Combustion Experimental Facility - Apparatus.

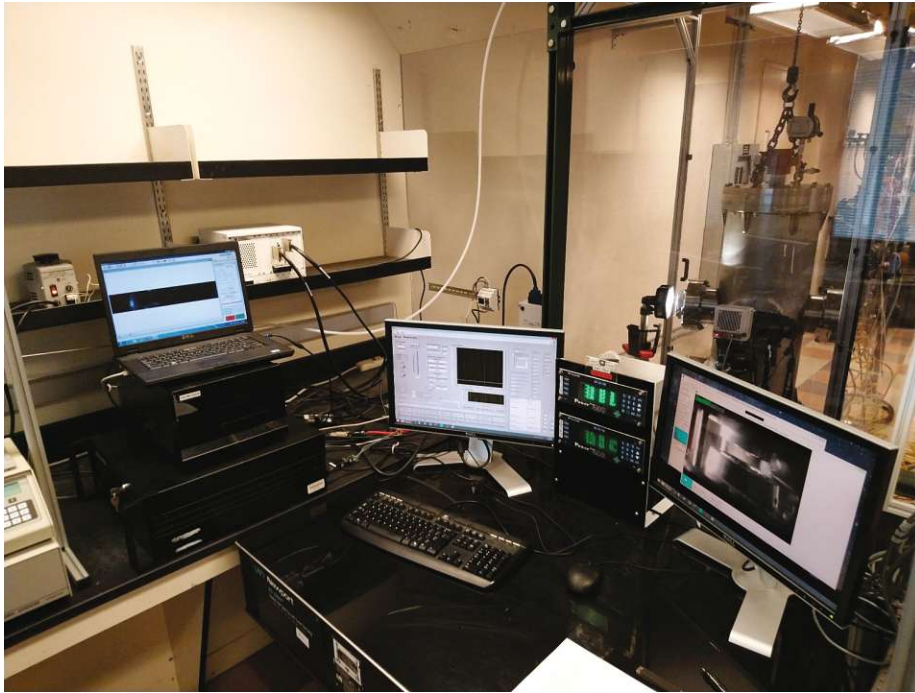


Figure B.3: High Pressure Combustion Experimental Facility - Workstation during experimentation with high-speed camera recording.

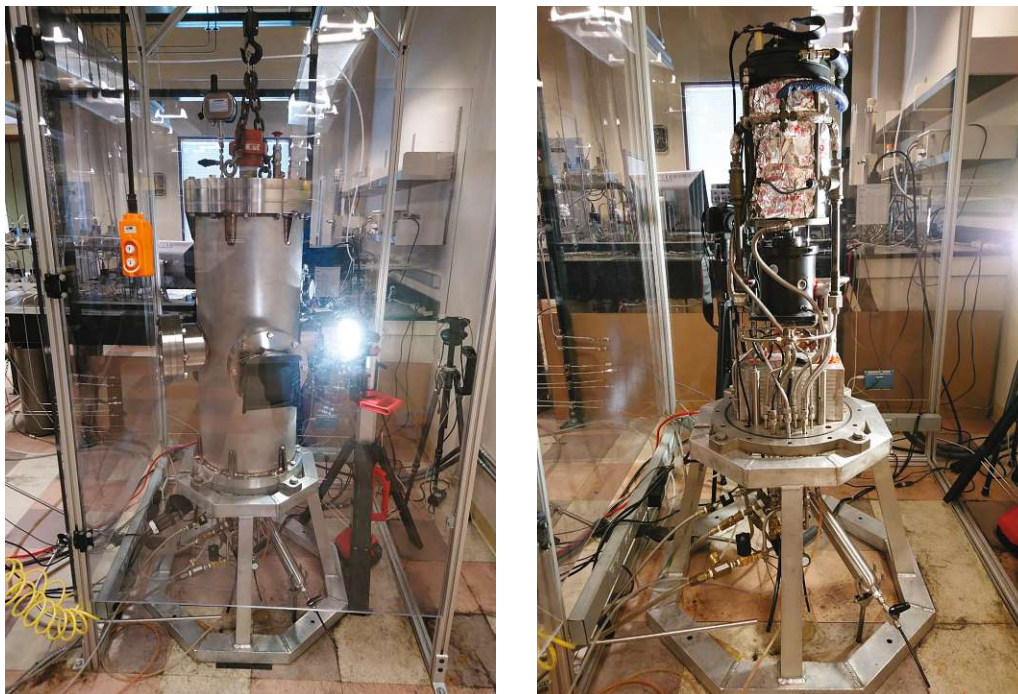


Figure B.4: High Pressure Combustion Experimental Facility - Chamber closed for experimentation (left) and opened for maintenance (right).

Listing B.1: Comparison of high pressure 2-way solenoid valves for automatically draining the residual liquid components from the HPCEF - SeparatorDrainValves.m

```

1 %% Comparison of High Pressure 2-Way Solenoid Valves for HPCEF
2
3 flowRateSprays = 0.3; % water sprays flow rate [U.S. gal/min]
4
5
6 %%
7 % Get the Flow Rate for Liquid Water [U.S. gal/min] through a Valve by
8 % providing the Flow Factor Cv [-] and the Pressure Drop deltaP [psi].
9 flowRateWaterGalPMin = @(Cv,deltaP) Cv * sqrt(deltaP);
10
11
12 %% 700 psi Valve: 7121KBN2JR00NOC111P3
13 % low pressure valve
14
15 V_700_At_43psi = flowRateWaterGalPMin(0.17,43); % 3bar
16 V_700_At_290psi = flowRateWaterGalPMin(0.17,290); % 20bar
17 V_700_At_870psi = flowRateWaterGalPMin(0.17,870); % 60bar
18
19 if(V_700_At_43psi > flowRateSprays && V_700_At_290psi > flowRateSprays && V_700_At_870psi
    ↪ >flowRateSprays)
20     disp('700 psi Valve (7121KBN2JR00NOC111P3) will work.')
21 else
22     disp('700 psi Valve (7121KBN2JR00NOC111P3) will NOT work.')
23 end
24
25
26 %% 3000 psi Valve: 71216SN2BL00NOC111P3
27 % high pressure valve candidate
28
29 V_3000_At_43psi = flowRateWaterGalPMin(0.021,43); % 3bar
30 V_3000_At_290psi = flowRateWaterGalPMin(0.021,290); % 20bar
31 V_3000_At_870psi = flowRateWaterGalPMin(0.021,870); % 60bar
32
33 if(V_3000_At_43psi > flowRateSprays && V_3000_At_290psi > flowRateSprays &&
    ↪ V_3000_At_870psi > flowRateSprays)
34     disp('3000 psi Valve (71216SN2BL00NOC111P3) will work.')
35 else
36     disp('3000 psi Valve (71216SN2BL00NOC111P3) will NOT work.')
37 end
38
39
40 %% 1100 psi Valve: 7121KBN2GR00NOC111P3
41 % high pressure valve
42
43 V_1100_At_43psi = flowRateWaterGalPMin(0.11,43); % 3bar
44 V_1100_At_290psi = flowRateWaterGalPMin(0.11,290); % 20bar
45 V_1100_At_870psi = flowRateWaterGalPMin(0.11,870); % 60bar
46
47 if(V_1100_At_43psi > flowRateSprays && V_1100_At_290psi > flowRateSprays &&
    ↪ V_1100_At_870psi > flowRateSprays)
48     disp('1100 psi Valve (7121KBN2GR00NOC111P3) will work.')
49 else
50     disp('1100 psi Valve (7121KBN2GR00NOC111P3) will NOT work.')
51 end
52
53
54 %save SeparatorDrainValves.mat -regexp \d;

```



Figure B.5: High Pressure Combustion Experimental Facility - View of the bottom plate during pressure testing, with droplets of water forming on fittings showing leakage.



Figure B.6: High Pressure Combustion Experimental Facility - Residual water on o-ring sealed surface after pressure testing with water.

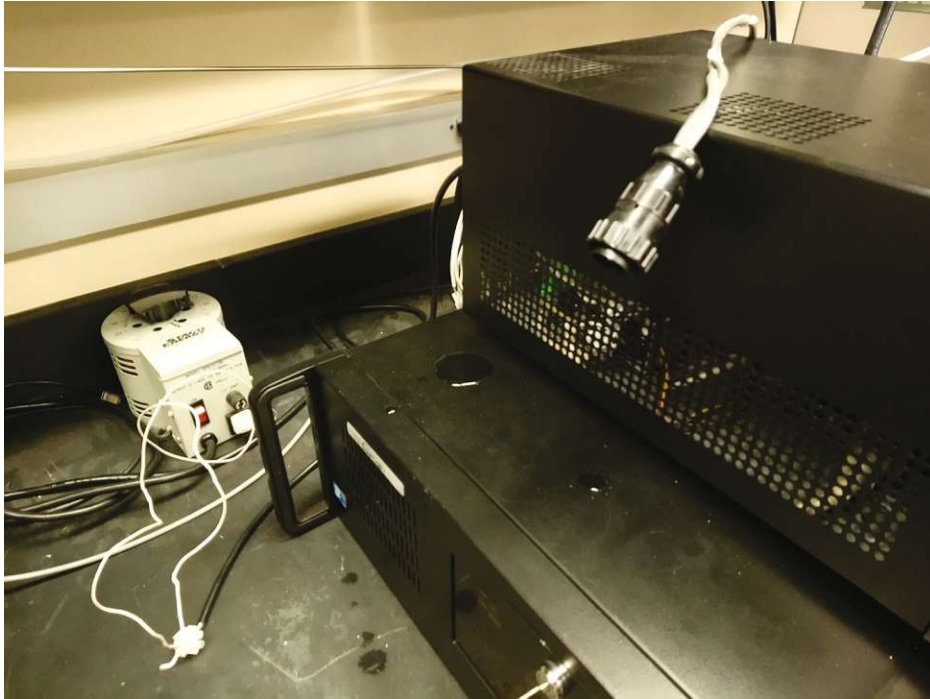


Figure B.7: High Pressure Combustion Experimental Facility - Water from the chamber pushed into workstation units through connected wiring during pressure testing.

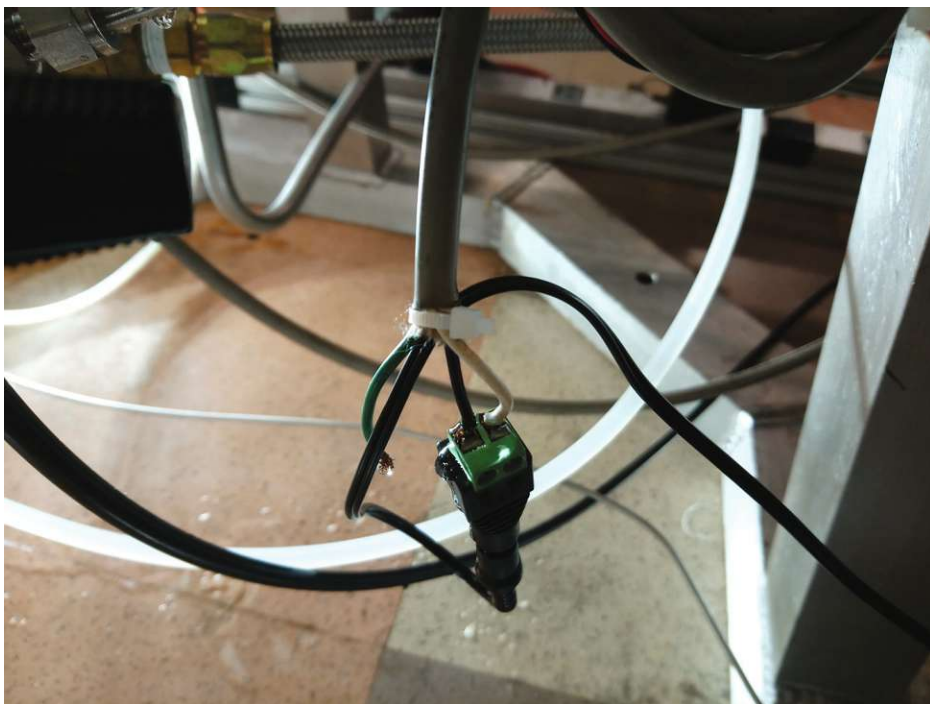


Figure B.8: High Pressure Combustion Experimental Facility - Water leaking from electrical wiring during pressure testing due to inadequate fittings on the bottom plate.

Listing B.2: Calculations for estimating the minimum nitrogen demand and comparison of the approximated time for experimentation on the HPCEF using gaseous and liquid nitrogen supply systems in Mathcad - N2 Supply.xmcd



N₂ Supply for Combustion Lab

Requirements: $\text{flowVolStd} := 7000 \frac{\text{L}}{\text{min}}$ for $\text{runTime} := 2\text{hr}$ **Standard Conditions:** $\text{tempStd} := 0\text{ }^\circ\text{C}$
 Standard L per min (SLM) $\text{presStd} := 760\text{torr}$
 $\text{presStd} = 1\cdot\text{atm}$
 $\text{flowVolStd} = 14832 \cdot \frac{\text{ft}^3}{\text{hr}}$

Properties: $\rho_{\text{GN2},0.760} := 1.2504 \frac{\text{kg}}{\text{m}^3}$ **Boiling Point of N₂: -195.8°C**
 $\rho_{\text{LN2},\text{neg}195.8,760} := 808.5 \frac{\text{kg}}{\text{m}^3}$

Demand: $V_{\text{StdN2}} := \text{flowVolStd} \cdot \text{runTime} = 840000\text{ L}$

$$V_{\text{StdN2}} = 840 \cdot \text{m}^3$$

$$V_{\text{StdN2}} = 29664 \cdot \text{ft}^3$$

GN₂: $m_{\text{GN2}} := V_{\text{StdN2}} \cdot \rho_{\text{GN2},0.760} = 1050\text{ kg}$

LN₂: $V_{\text{LN2}} := \frac{m_{\text{GN2}}}{\rho_{\text{LN2},\text{neg}195.8,760}} = 1299\text{ L}$

$$V_{\text{LN2}} = 45.9 \cdot \text{ft}^3$$

Expansion: $\text{expL2G} := \frac{V_{\text{StdN2}}}{V_{\text{LN2}}} = 647$

$$\text{GN}_2: \quad n_{\text{cyl}} := 25 \quad \text{vol}_{\text{cyl}} := 228 \text{ft}^3 \quad f_{\text{cyl}} := \frac{3}{4} \quad \text{flow}_{13\text{bar}} := 700 \frac{\text{L}}{\text{min}}$$

$$\text{flow}_{25\text{bar}} := 1500 \frac{\text{L}}{\text{min}}$$

$$\text{runtime}_{13\text{bar}.G} := \frac{\text{vol}_{\text{cyl}} \cdot n_{\text{cyl}} \cdot f_{\text{cyl}}}{\text{flow}_{13\text{bar}}} = 2.882 \text{ hr}$$

$$\text{runtime}_{25\text{bar}.G} := \frac{\text{vol}_{\text{cyl}} \cdot n_{\text{cyl}} \cdot f_{\text{cyl}}}{\text{flow}_{25\text{bar}}} = 1.345 \text{ hr}$$

$$\text{LN}_2: \quad \text{vol}_{\text{tank}} := 1500 \text{L} \quad \text{vol}_{\text{GN}_2} := \text{vol}_{\text{tank}} \cdot \text{expL}_2\text{G} = 9.699 \times 10^5 \text{L}$$

$$\text{runtime}_{25\text{bar}.L} := \frac{\text{vol}_{\text{GN}_2}}{\text{flow}_{25\text{bar}}} = 10.777 \text{ hr}$$

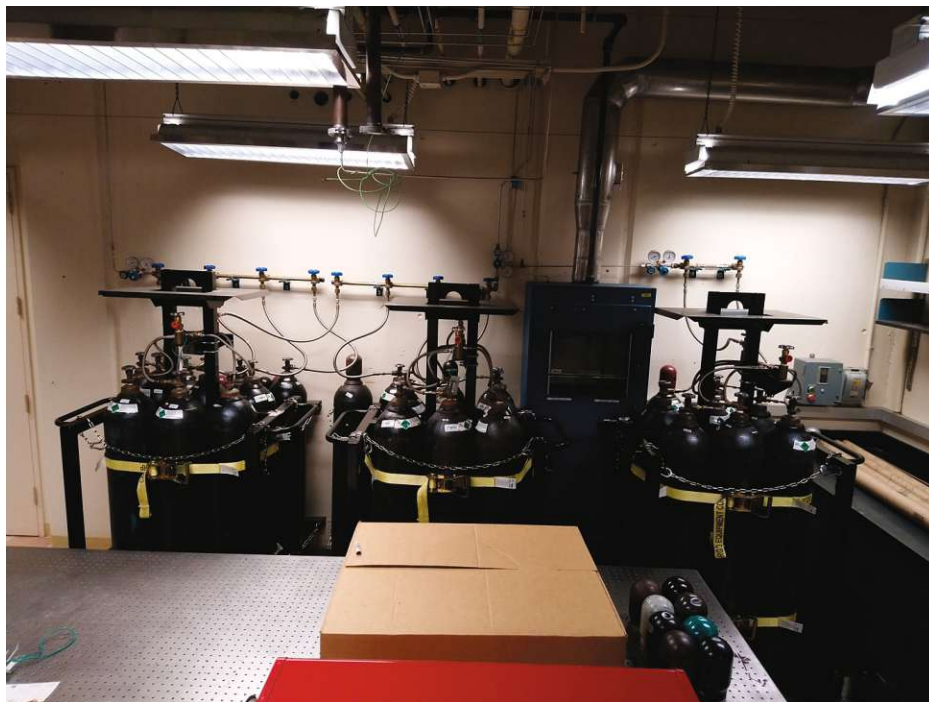


Figure B.9: Nitrogen Supply System - Cylinder carts carrying a manifold of pressurized gas cylinders providing gaseous nitrogen for experiments and pressurization to the HPCEF.



Figure B.10: Nitrogen Supply System - Cylinder carts carrying a manifold of pressurized gas cylinders providing various gases to the HPCEF.



Figure B.11: Nitrogen Supply System - Portable tank on stand (right), vaporizer and control station assembly (center), and high pressure cylinder pack (left).



Figure B.12: Nitrogen Supply System - Back view of the system showing the cryogenic pump together with its actuating motor (left) and moving the tank for refilling (right).

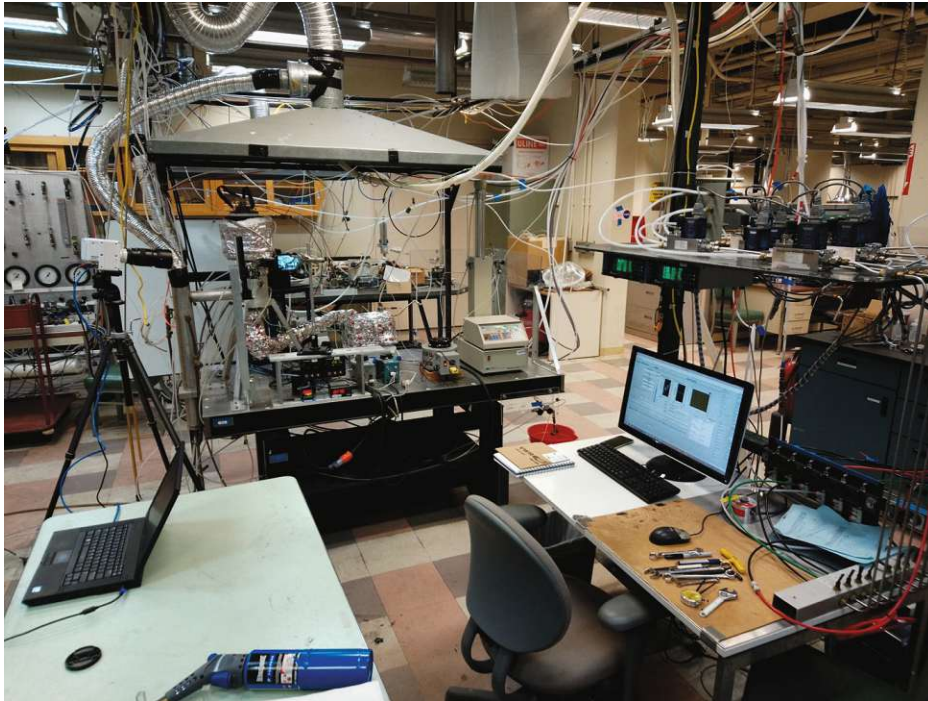


Figure B.13: Atmospheric Counterflow Setup.

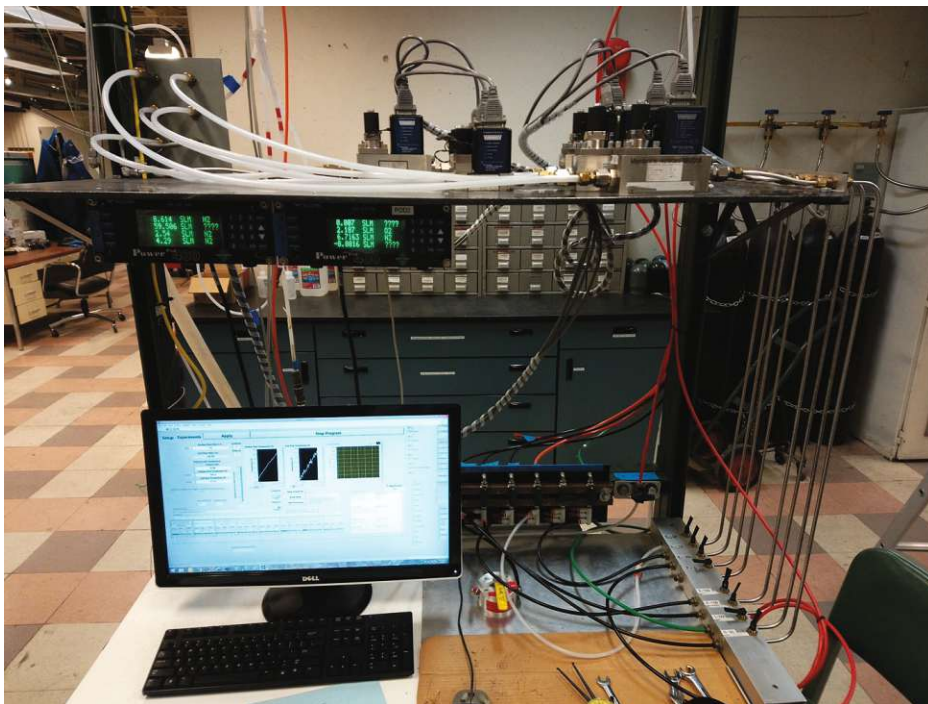


Figure B.14: Atmospheric Counterflow Setup - Workstation and gas flow control.

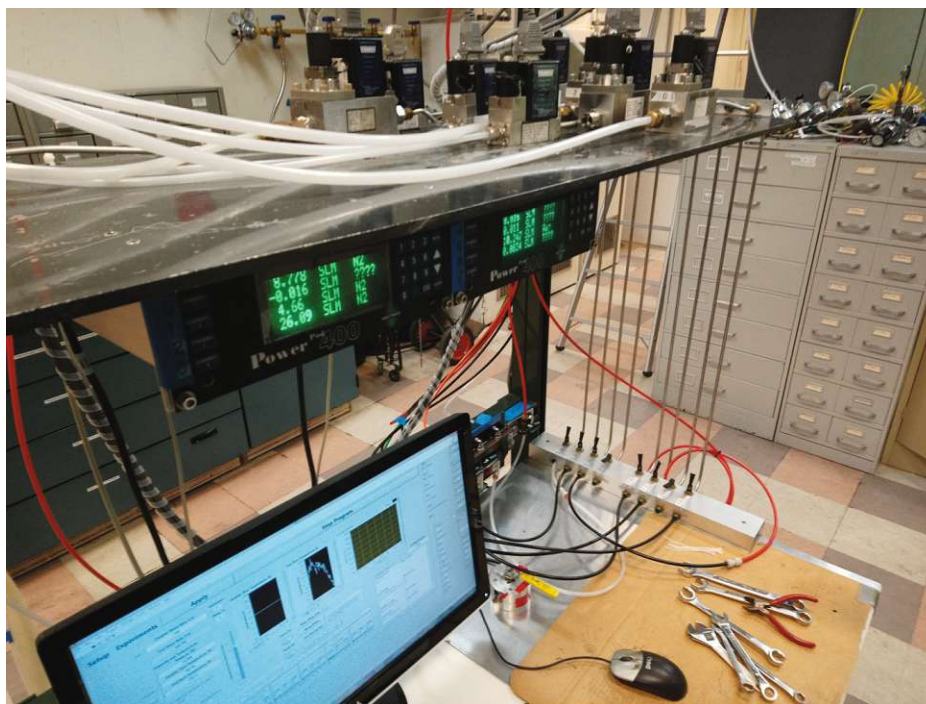


Figure B.15: Atmospheric Counterflow Setup - Mass flow controllers, MFC controller units, and gas flow control switch and plug boards.

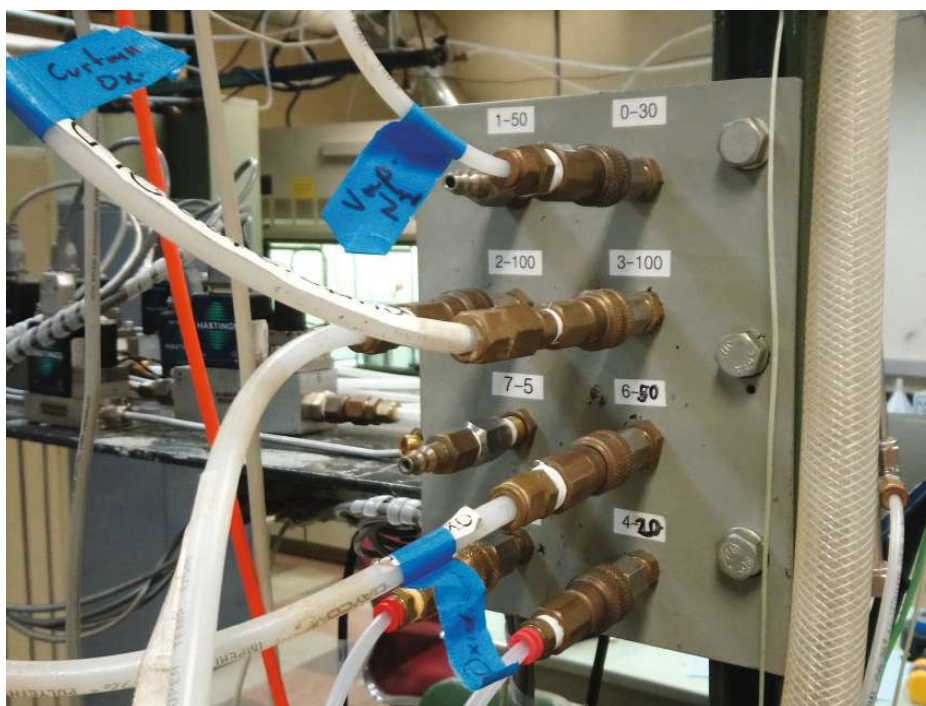


Figure B.16: Atmospheric Counterflow Setup - Gas flow control quick connect board.

Appendix C Experiments



Figure C.1: View of the fuel duct during an ongoing autoignition experiment with inserted thermocouple and the oxidizer stream at around 1100 K.



Figure C.2: View of the oxidizer duct during an ongoing autoignition experiment with inserted thermocouple and the oxidizer stream at around 1100 K.

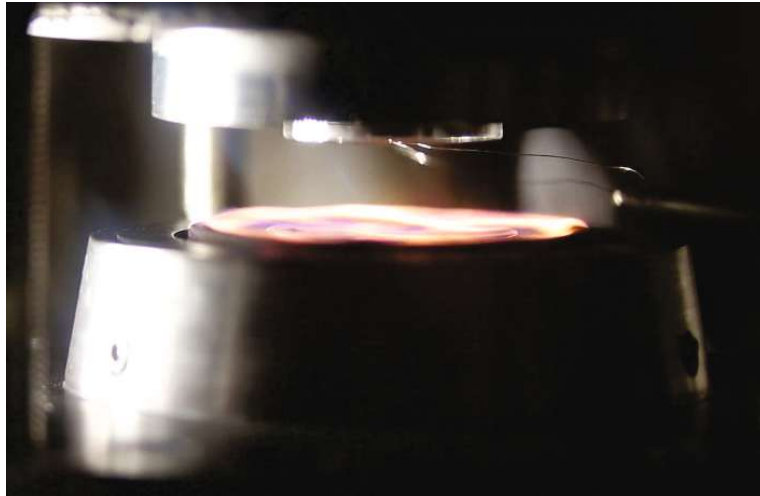


Figure C.3: Established n-heptane flame after the autoignition event at 5 bar.

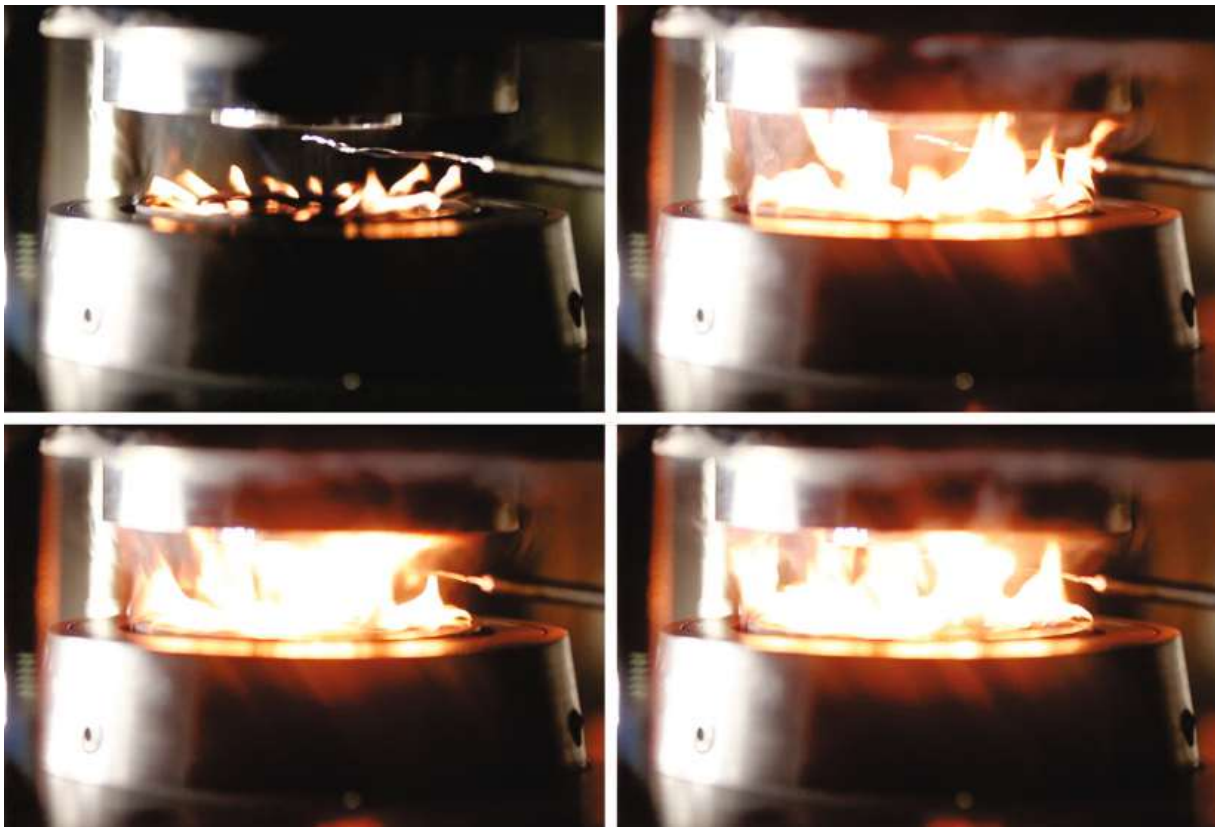


Figure C.4: N-heptane flame at 22 bar before (upper left) and after autoignition showing the preceding curtain ignition typically occurring at elevated pressures.

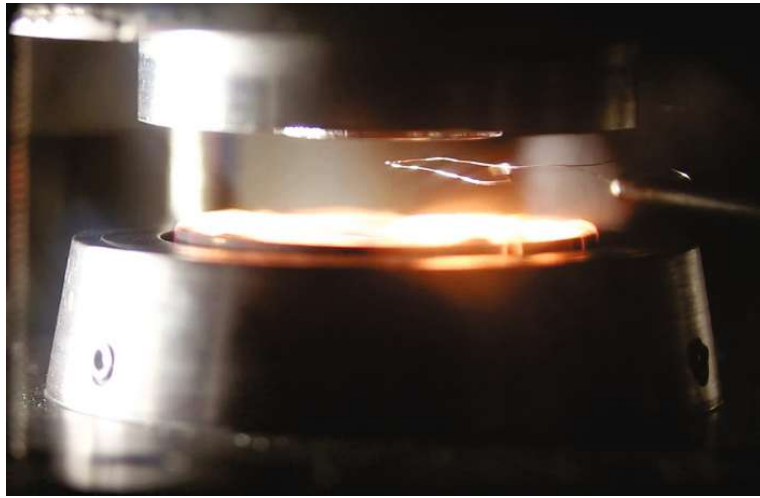


Figure C.5: Established n-heptane flame after the autoignition event at 13 bar.

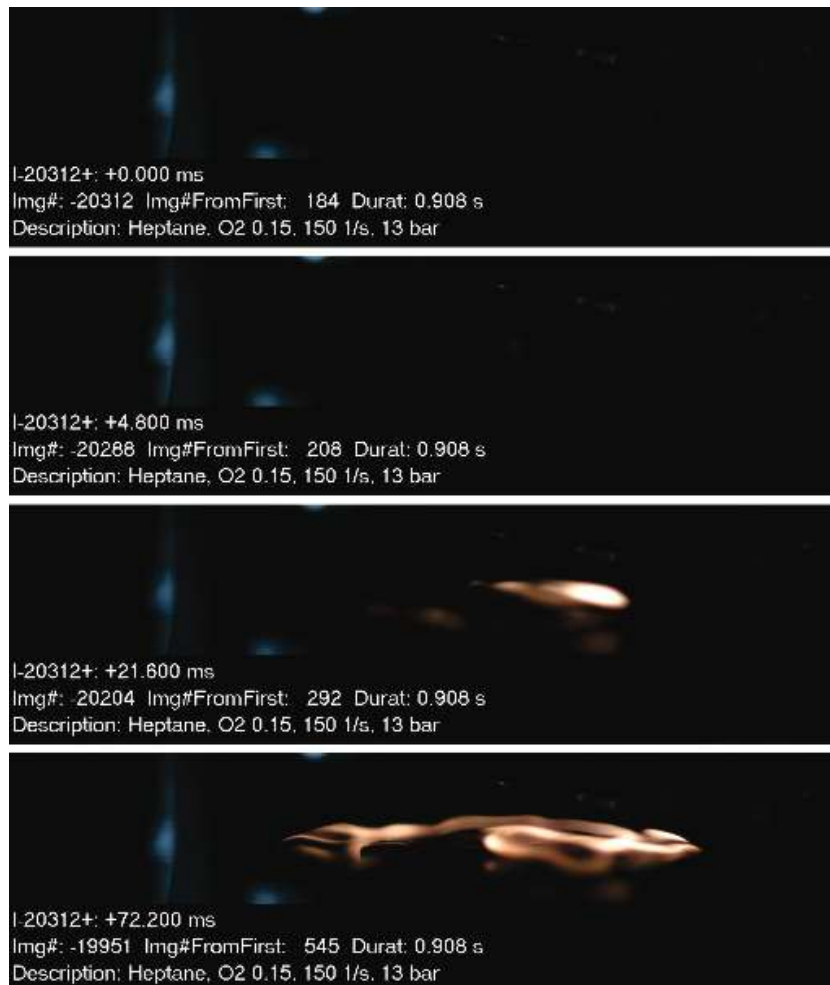


Figure C.6: Screenshots of a high-speed recording at 13 bar showing the autoignition event which led to the flame depicted in Figure C.5.

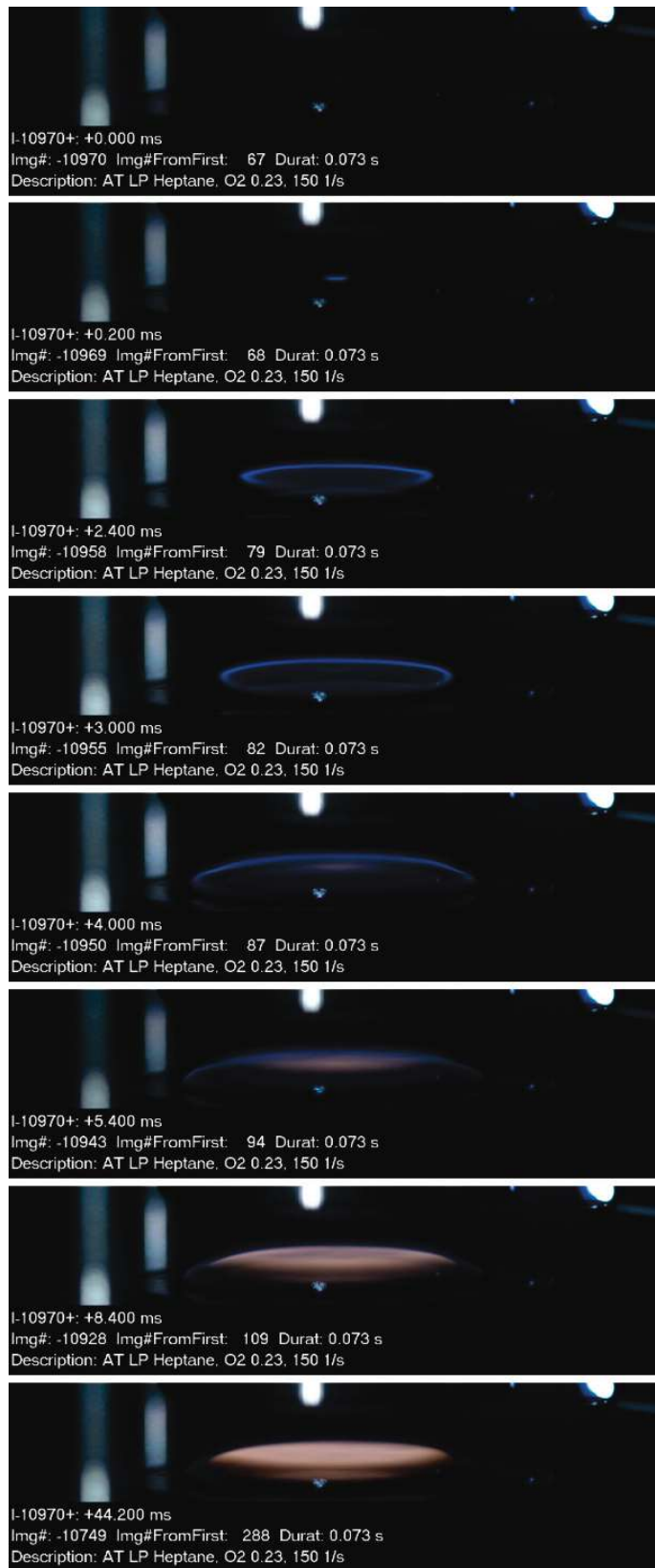


Figure C.7: Autoignition event of condensed n-heptane at atmospheric pressure.

Appendix D Experimental Data

Experimental and Computational Investigation on Critical Conditions of Extinction of Laminar, Non-Premixed Dimethyl Ether Flames

Z_{st} [-]	0.134	0.16	0.19	0.22	0.314	0.4	0.5	0.6	0.7	0.8
a_2 [1/s]	570	539	531	521	514	503	532	547	593	828
SE [1/s]	7.4	4.3	5.5	4.7	4.1	3.9	4.4	2.7	5.6	16.9

Table D.1: Mean values and standard errors (SE) plotted in Figures 5.2 and 5.3

Experimental and Computational Investigation of Extinction and Autoignition of Propane and n-Heptane in Non-Premixed Flows

Propane

Y_{O_2} [-]	0.195	0.2	0.205	0.21	0.215	0.22	0.225	0.23	0.233
a_2 [1/s]	235	263	319	368	412	468	489	538	606
SE [1/s]	2.1	1.5	2.9	1.7	1.7	2.2	1.5	1.8	0.9

Table D.2: Mean values and standard errors (SE) plotted in Figure 5.9

Y_F [-]	0.3	0.35	0.4	0.45	0.5	0.55	0.6
T_2 [K]	1197	1194	1193	1191	1188	1185	1183
SE [K]	2.1	2.8	2.7	3.4	2.6	2.0	3.3

Table D.3: Mean values and standard errors (SE) plotted in Figure 5.10

Y_{O_2} [-]	0.07	0.11	0.15	0.19	0.23
T_2 [K]	1243	1237	1223	1219	1206
SE [K]	4.9	5.3	3.5	2.8	2.1

Table D.4: Mean values and standard errors (SE) plotted in Figure 5.11 ($Y_F = 0.21$)

Y_{O_2} [-]	0.07	0.11	0.15	0.19	0.23
T_2 [K]	1223	1214	1202	1197	1193
SE [K]	3.1	3.0	2.3	3.4	2.7

Table D.5: Mean values and standard errors (SE) plotted in Figure 5.12 ($Y_F = 0.4$)

Y_{O_2} [-]	0.07	0.11	0.15	0.19	0.23
T_2 [K]	1213	1195	1189	1185	1183
SE [K]	2.7	3.4	3.1	2.8	3.3

Table D.6: Mean values and standard errors (SE) plotted in Figure 5.13 ($Y_F = 0.6$)**n-Heptane**

Y_F [-]	0.25	0.3	0.35	0.4	0.45	0.5
a_2 [1/s]	261	354	402	460	513	578
SE [1/s]	1.6	1.0	1.8	0.7	1.0	2.1

Table D.7: Mean values and standard errors (SE) plotted in Figures 5.19 and 5.23

Y_F [-]	0.25	0.3	0.35	0.4	0.45	0.5
T_2 [K]	1219	1215	1211	1208	1204	1200
SE [K]	1.6	1.4	1.2	1.2	1.6	1.6

Table D.8: Mean values and standard errors (SE) plotted in Figures 5.20 and 5.24

Y_{O_2} [-]	0.07	0.09	0.11	0.13	0.15	0.17	0.19	0.21	0.23
T_2 [K]	1241	1234	1230	1225	1220	1215	1214	1211	1208
SE [K]	1.6	1.4	1.2	1.4	1.3	1.3	1.7	1.5	1.2

Table D.9: Mean values and standard errors (SE) plotted in Figures 5.21 and 5.25

Experimental and Computational Investigation of Extinction and Autoignition of Prevaporized Primary Reference Fuels in Non-Premixed Flows

n-Decane

Y_F [-]	0.25	0.3	0.35	0.4	0.45	0.5
a_2 [1/s]	212	262	301	343	386	428
SE [1/s]	1.1	1.1	0.8	1.0	0.9	1.4

Table D.10: Mean values and standard errors (SE) plotted in Figure 5.23

Y_F [-]	0.25	0.3	0.35	0.4	0.45	0.5
T_2 [K]	1235	1228	1225	1221	1218	1214
SE [K]	1.4	1.4	2.1	1.4	1.7	2.0

Table D.11: Mean values and standard errors (SE) plotted in Figure 5.24

Y_{O_2} [-]	0.07	0.09	0.11	0.13	0.15	0.17	0.19	0.21	0.23
T_2 [K]	1249	1241	1235	1232	1230	1227	1223	1222	1221
SE [K]	1.7	2.4	1.6	1.6	2.1	1.8	1.8	1.8	1.4

Table D.12: Mean values and standard errors (SE) plotted in Figure 5.25

n-Dodecane

Y_F [-]	0.25	0.3	0.35	0.4	0.45	0.5
a_2 [1/s]	137	216	266	290	318	362
SE [1/s]	1.6	2.0	1.3	1.0	0.8	0.9

Table D.13: Mean values and standard errors (SE) plotted in Figure 5.23

Y_F [-]	0.25	0.3	0.35	0.4	0.45	0.5
T_2 [K]	1250	1244	1239	1234	1231	1224
SE [K]	1.8	2.2	1.7	1.8	1.4	1.4

Table D.14: Mean values and standard errors (SE) plotted in Figure 5.24

Y_{O_2} [-]	0.07	0.09	0.11	0.13	0.15	0.17	0.19	0.21	0.23
T_2 [K]	1261	1256	1249	1246	1243	1241	1241	1238	1234
SE [K]	1.4	1.4	1.4	1.6	1.8	1.4	1.8	1.6	1.8

Table D.15: Mean values and standard errors (SE) plotted in Figure 5.25

Experimental and Computational Investigation of Autoignition of Condensed Primary Reference Fuels in Non-Premixed Flows

n-Heptane at Elevated Pressures

P [bar]	5	6	7	8	9	10	11	12	13
T_2 [K]	966	926	897	883	860	842	799	778	766
SE [K]	5.9	3.1	4.7	4.1	4.7	3.9	4.6	3.8	3.1

Table D.16: Mean values and standard errors (SE) plotted in Figures 5.29, 5.32, 5.33, and 5.41 ($a_2 = 150$ 1/s)

P [bar]	14	15	16	18	20	22	24	25
T_2 [K]	749	744	725	718	708	695	685	667
SE [K]	5.1	10.2	11.7	20.4	20.3	27.9	48.2	60.8

Table D.17: Mean values and standard errors (SE) plotted in Figures 5.29 and 5.33 ($a_2 = 150$ 1/s, $P > 13$ bar)

P [bar]	5	6	7	8	9	10	11	12	13
T_2 [K]	920	890	857	823	801	788	775	768	764
SE [K]	5.3	7.4	8.9	5.2	6.2	5.7	6.2	7.7	9.2

Table D.18: Mean values and standard errors (SE) plotted in Figure 5.41 ($a_2 = 130$ 1/s)

P [bar]	5	6	7	8	9	10	11	12	13
T_2 [K]	845	826	800	781	781	774	756	747	744
SE [K]	5.8	4.7	3.7	6.7	6.2	5.2	5.2	8.7	9.2

Table D.19: Mean values and standard errors (SE) plotted in Figure 5.41 ($a_2 = 100$ 1/s)**n-Decane at Elevated Pressures**

P [bar]	5	6	7	8	9	10	11	12	13
T_2 [K]	938	906	868	845	830	815	801	795	790
SE [K]	4.9	5.3	4.7	6.1	7.8	7.3	6.2	7.6	5.1

Table D.20: Mean values and standard errors (SE) plotted in Figures 5.30, 5.32, 5.33, and 5.41 ($a_2 = 150$ 1/s)

P [bar]	14	15	16	18	20	22	24	25
T_2 [K]	784	777	767	757	765	762	746	738
SE [K]	7.4	12.8	12.8	11.2	20.9	29.1	43.8	45.8

Table D.21: Mean values and standard errors (SE) plotted in Figures 5.30 and 5.33 ($a_2 = 150$ 1/s, $P > 13$ bar)

P [bar]	5	6	7	8	9	10	11	12	13
T_2 [K]	904	861	839	819	812	798	791	779	777
SE [K]	5.3	5.3	5.2	4.2	3.6	6.7	5.2	5.7	6.7

Table D.22: Mean values and standard errors (SE) plotted in Figure 5.41 ($a_2 = 130$ 1/s)

P [bar]	5	6	7	8	9	10	11	12	13
T_2 [K]	846	830	808	801	791	784	776	773	769
SE [K]	2.9	3.7	3.7	2.9	5.2	5.2	5.2	5.2	2.6

Table D.23: Mean values and standard errors (SE) plotted in Figure 5.41 ($a_2 = 100$ 1/s)

n-Dodecane at Elevated Pressures

P [bar]	5	6	7	8	9	10	11	12	13
T_2 [K]	942	901	893	874	864	862	858	853	837
SE [K]	7.6	5.8	6.8	7.5	5.2	4.6	10.4	7.4	10.3

Table D.24: Mean values and standard errors (SE) plotted in Figures 5.31, 5.32, and 5.33 ($a_2 = 150$ 1/s)

P [bar]	14	16	18	20	22	24	25
T_2 [K]	819	816	792	764	766	738	741
SE [K]	9.4	15.4	13.3	30.6	23.3	40.7	38.2

Table D.25: Mean values and standard errors (SE) plotted in Figures 5.31 and 5.33 ($a_2 = 150$ 1/s, $P > 13$ bar)

Liquid Pool and the Crossover**n-Heptane at Atmospheric Pressure**

a_2 [1/s]	100	150	200	250	300	350	400	450
T_2 [K]	1132	1149	1159	1169	1177	1185	1192	1188
SE [K]	7.2	5.3	3.6	3.5	4.0	3.9	2.5	3.4

Table D.26: Mean values and standard errors (SE) plotted in Figure 5.39

n-Decane at Atmospheric Pressure

a_2 [1/s]	100	150	200	250	300	350	400	450
T_2 [K]	1063	1093	1114	1132	1156	1177	1195	1215
SE [K]	2.6	1.2	1.1	1.2	0.7	1.4	0.8	2.0

Table D.27: Mean values and standard errors (SE) plotted in Figure 5.39

Bibliography

- [1] BEECKMANN, J. ; CAI, L. ; BERENS, A. ; PETERS, N. ; PITSCH, H.: *An analytical approximation for low- and high-temperature autoignition for dimethyl ether–air mixtures*. In: Proceedings of the Combustion Institute 35 (2015), no. 1: 275–281. <http://dx.doi.org/10.1016/j.proci.2014.05.116>
- [2] BELL, Ian H. ; WRONSKI, Jorrit ; QUOILIN, Sylvain ; LEMORT, Vincent: *Pure and Pseudo-pure Fluid Thermophysical Property Evaluation and the Open-Source Thermophysical Property Library CoolProp*. In: Industrial & Engineering Chemistry Research 53 (2014), no. 6: 2498–2508. <http://dx.doi.org/10.1021/ie4033999>
- [3] BIELEVELD, Tom ; FRASSOLDATI, Alessio ; CUOCI, Alberto ; FARAVELLI, Tiziano ; RANZI, Eliseo ; NIEMANN, Ulrich ; SESHADRI, Kalyanasundaram: *Experimental and kinetic modeling study of combustion of gasoline, its surrogates and components in laminar non-premixed flows*. In: Proceedings of the Combustion Institute 32 (2009), no. 1: 493–500. <http://dx.doi.org/10.1016/j.proci.2008.06.214>
- [4] CAMPBELL, Matthew F. ; WANG, Shengkai ; DAVIDSON, David F. ; HANSON, Ronald K.: *Shock tube study of normal heptane first-stage ignition near 3.5 atm*. In: Combustion and Flame 198 (2018), no. 6: 376–392. <http://dx.doi.org/10.1016/j.combustflame.2018.08.008>
- [5] CANTERA: *version 2.3.0 documentation : One-Dimensional Flames*. <http://www.cantera.org/docs/sphinx/html/flames.html>, accessed: 12.05.2017
- [6] CHEMWATCH: *GoldFFX : Complete Chemical Management Solution*. <https://www.chemwatch.net/page/products/chemicals-management/gold-ffx>
- [7] CIEZKI, H. K. ; ADOMEIT, G.: *Shock-tube investigation of self-ignition of n-heptane-air mixtures under engine relevant conditions*. In: Combustion and Flame 93 (1993), no. 4: 421–433. [http://dx.doi.org/10.1016/0010-2180\(93\)90142-P](http://dx.doi.org/10.1016/0010-2180(93)90142-P)
- [8] COLLIS, D. C. ; WILLIAMS, M. J.: *Two-dimensional convection from heated wires at low Reynolds numbers*. In: Journal of Fluid Mechanics 6 (1959), no. 3: 357–384. <http://dx.doi.org/10.1017/S0022112059000696>

- [9] COMBUSTION RESEARCH GROUP, DEPARTMENT OF MECHANICAL & AEROSPACE ENGINEERING, UC SAN DIEGO: *San Diego Mechanism : Chemical-Kinetic Mechanisms for Combustion Applications*. <http://combustion.ucsd.edu>, accessed: 07.02.2019
- [10] COOLPROP: *version 6.2.1 (Python 3.x wrapper)*. <http://www.coolprop.org>
- [11] CRECK MODELING GROUP, DEPARTMENT OF CHEMISTRY, MATERIALS, AND CHEMICAL ENGINEERING, POLITECNICO DI MILANO: *PoliMi Kinetic Mechanisms*. <http://creckmodeling.chem.polimi.it/menu-kinetics>, accessed: 17.06.2019
- [12] CURRAN, Henry J.: *Developing detailed chemical kinetic mechanisms for fuel combustion*. In: *Proceedings of the Combustion Institute* 37 (2019), no. 1: 57–81. <http://dx.doi.org/10.1016/j.proci.2018.06.054>
- [13] DAGAUT, P. ; RISTORI, A. ; FRASSOLDATI, A. ; FARAVELLI, T. ; DAYMA, G. ; RANZI, E.: *Experimental and semi-detailed kinetic modeling study of decalin oxidation and pyrolysis over a wide range of conditions*. In: *Proceedings of the Combustion Institute* 34 (2013), no. 1: 289–296. <http://dx.doi.org/10.1016/j.proci.2012.05.099>
- [14] DAGAUT, Philippe ; RISTORI, Alain ; FRASSOLDATI, Alessio ; FARAVELLI, Tiziano ; DAYMA, Guillaume ; RANZI, Eliseo: *Experimental Study of Tetralin Oxidation and Kinetic Modeling of Its Pyrolysis and Oxidation*. In: *Energy & Fuels* 27 (2013), no. 3: 1576–1585. <http://dx.doi.org/10.1021/ef4001456>
- [15] DENG, Sili ; HAN, Dong ; LAW, Chung K.: *Ignition and extinction of strained nonpremixed cool flames at elevated pressures*. In: *Combustion and Flame* 176 (2017), no. 4: 143–150. <http://dx.doi.org/10.1016/j.combustflame.2016.10.015>
- [16] DENG, Sili ; ZHAO, Peng ; ZHU, Delin ; LAW, Chung K.: *NTC-affected ignition and low-temperature flames in nonpremixed DME/air counterflow*. In: *Combustion and Flame* 161 (2014), no. 8: 1993–1997. <http://dx.doi.org/10.1016/j.combustflame.2014.01.020>
- [17] DJOKIC, Marko R. ; VAN GEEM, Kevin M. ; CAVALLOTTI, Carlo ; FRASSOLDATI, Alessio ; RANZI, Eliseo ; MARIN, Guy B.: *An experimental and kinetic modeling study of cyclopentadiene pyrolysis : First growth of polycyclic aromatic hydrocarbons*. In: *Combustion and Flame* 161 (2014), no. 11: 2739–2751. <http://dx.doi.org/10.1016/j.combustflame.2014.04.013>
- [18] EATON: *Control Relay easy-512-AC-RC : Manual* / Eaton Industries. May 2010

- [19] FENDELL, Francis E.: *Ignition and extinction in combustion of initially unmixed reactants*. In: *Journal of Fluid Mechanics* 21 (1965), no. 2: 281–303. <http://dx.doi.org/10.1017/S0022112065000186>
- [20] FRASSOLDATI, Alessio ; CUOCI, Alberto ; FARAVELLI, Tiziano ; NIEMANN, Ulrich ; RANZI, Eliseo ; SEISER, Reinhard ; SESHADRI, Kalyanasundaram: *An experimental and kinetic modeling study of n-propanol and iso-propanol combustion*. In: *Combustion and Flame* 157 (2010), no. 1: 2–16. <http://dx.doi.org/10.1016/j.combustflame.2009.09.002>
- [21] GARDINER, William C. J. (ed.): *Combustion Chemistry*. New York : Springer-Verlag, 1984. – ISBN 978–1–4684–0188–2
- [22] GEHMLICH, Ryan K. ; KUO, Austin ; SESHADRI, Kalyanasundaram: *Experimental investigations of the influence of pressure on critical extinction conditions of laminar nonpremixed flames burning condensed hydrocarbon fuels, jet fuels, and surrogates*. In: *Proceedings of the Combustion Institute* 35 (2015), no. 1: 937–943. <http://dx.doi.org/10.1016/j.proci.2014.05.111>
- [23] GEHMLICH, Ryan K.: *Experimental Studies on Nonpremixed Combustion at Atmospheric and Elevated Pressures*. La Jolla, University of California, San Diego, Department of Mechanical & Aerospace Engineering, 2015. – dissertation
- [24] GLASSMAN, Irvin ; YETTER, Richard A. ; GLUMAC, Nick G.: *Combustion*. Fifth Edition. Waltham and San Diego and London and Oxford : Academic Press, 2015. – ISBN 978–0–12–407913–7
- [25] GOODWIN, David G. ; MOFFAT, Harry K. ; SPETH, Raymond L.: *Cantera : An Object-oriented Software Toolkit for Chemical Kinetics, Thermodynamics, and Transport Processes*. Version: 2.3.0, 2017. <http://dx.doi.org/10.5281/zenodo.170284>
- [26] GORDON, Sanford ; MCBRIDE, Bonnie J.: *Computer Program for Calculation of Complex Chemical Equilibrium Compositions and Applications : I. Analysis* / National Aeronautics and Space Administration. 1994 (NASA Reference Publication RP-1311)
- [27] GORDON, Sanford ; MCBRIDE, Bonnie J.: *Computer Program for Calculation of Complex Chemical Equilibrium Compositions, Rocket Performance, Incident and Reflected Shocks, and Chapman-Jouguet Detonations* / National Aeronautics and Space Administration. 1976 (NASA Special Publication 273)

- [28] GORDON, Sanford ; MCBRIDE, Bonnie J.: *Fortran IV program for calculation of thermodynamic data* / National Aeronautics and Space Administration. 1967 (NASA Technical Note D-4097)
- [29] GRANA, Roberto ; FRASSOLDATI, Alessio ; FARAVELLI, Tiziano ; NIEMANN, Ulrich ; RANZI, Eliseo ; SEISER, Reinhard ; CATTOLICA, Robert ; SESHADRI, Kalyanasundaram: *An experimental and kinetic modeling study of combustion of isomers of butanol*. In: *Combustion and Flame* 157 (2010), no. 11: 2137–2154. <http://dx.doi.org/10.1016/j.combustflame.2010.05.009>
- [30] GRANA, Roberto ; SESHADRI, Kalyanasundaram ; CUOCI, Alberto ; NIEMANN, Ulrich ; FARAVELLI, Tiziano ; RANZI, Eliseo: *Kinetic modelling of extinction and autoignition of condensed hydrocarbon fuels in non-premixed flows with comparison to experiment*. In: *Combustion and Flame* 159 (2012), no. 1: 130–141. <http://dx.doi.org/10.1016/j.combustflame.2011.06.019>
- [31] HELD, T. J. ; MARCHESE, A. J. ; DRYER, F. L.: *A Semi-Empirical Reaction Mechanism for n-Heptane Oxidation and Pyrolysis*. In: *Combustion Science and Technology* 123 (1997), no. 1-6: 107–146. <http://dx.doi.org/10.1080/00102209708935624>
- [32] HOMANN, F.: *Der Einfluß großer Zähigkeit bei der Strömung um den Zylinder und um die Kugel*. In: *Zeitschrift für Angewandte Mathematik und Mechanik* 16 (1936), no. 3: 153–164. <http://dx.doi.org/10.1002/zamm.19360160304>
- [33] HONNET, S. ; SESHADRI, K. ; NIEMANN, U. ; PETERS, N.: *A surrogate fuel for kerosene*. In: *Proceedings of the Combustion Institute* 32 (2009), no. 1: 485–492. <http://dx.doi.org/10.1016/j.proci.2008.06.218>
- [34] HUMER, S. ; FRASSOLDATI, A. ; GRANATA, S. ; FARAVELLI, T. ; RANZI, E. ; SEISER, R. ; SESHADRI, K.: *Experimental and kinetic modeling study of combustion of JP-8, its surrogates and reference components in laminar nonpremixed flows*. In: *Proceedings of the Combustion Institute* 31 (2007), no. 1: 393–400. <http://dx.doi.org/10.1016/j.proci.2006.08.008>
- [35] HUMER, S. ; SEISER, R. ; SESHADRI, K.: *NON-PREMIXED AND PREMIXED EXTINCTION AND AUTOIGNITION OF C₂H₄, C₂H₆, C₃H₆, AND C₃H₈*. In: *Proceedings of the Combustion Institute* 29 (2002): 1597–1604
- [36] HUNTER, J. D.: *Matplotlib : A 2D graphics environment*. In: *Computing In Science & Engineering* 9 (2007), no. 3: 90–95

- [37] HUNYADI-GALL, Martin ; MAIRINGER, Gerald ; KHARE, Rohit S. ; NARAYANASWAMY, Krithika ; RAGHAVAN, Vasudevan ; SESHADRI, Kalyanasundaram: *The Influence of Stoichiometric Mixture Fraction on Extinction of Laminar, Nonpremixed DME Flame*. In: *Proceedings of the 10th U. S. National Combustion Meeting*, 2017
- [38] HUNYADI-GALL, Martin ; NARAYANASWAMY, Krithika ; HOCKNER, Emanuel ; INNERKOFER, Mathias ; BADIALI, Lucia ; SESHADRI, Kalyanasundaram ; WILLIAMS, Forman: *Experimental and computational investigation of extinction and autoignition of propane and n-heptane in nonpremixed flows*. In: *Proceedings of the Combustion Institute* 38 (2021), no. 2: 2257–2263. <http://dx.doi.org/10.1016/j.proci.2020.06.027>
- [39] I²R: *Starbar Silicon Carbide Heating Element, Type SER : Info & Specifications Sheet* / I Squared R Element Co., Inc. Sep. 2007
- [40] INNERKOFER, Mathias ; HUNYADI-GALL, Martin ; PIZZETTI, Fabio ; TURELLO, Massimiliano ; CUOCI, Alberto ; FRASSOLDATI, Alessio ; PUCHER, Ernst ; SESHADRI, Kalyanasundaram: *Experimental and Computational Investigation of Autoignition of High Molecular Weight Alkanes in Nonpremixed Flows*. In: *2018 Spring Technical Meeting of the Western States Section of the Combustion Institute*, 2018
- [41] JONES, Eric ; OLIPHANT, Travis ; PETERSON, Pearu ; ET AL.: *SciPy : Open Source Scientific Tools for Python*. 2001. <http://www.scipy.org/>
- [42] KATTA, Viswanath R. ; AGGARWAL, Suresh K. ; ROQUEMORE, William M.: *Evaluation of chemical-kinetics models for n-heptane combustion using a multidimensional CFD code*. In: *Fuel* 93 (2012), no. 4: 339–350. <http://dx.doi.org/10.1016/j.fuel.2011.10.035>
- [43] KEE, Robert J. ; COLTRIN, Michael E. ; GLARBORG, Peter ; ZHU, Huayang: *Chemically Reacting Flow : Theory, Modeling, and Simulation*. Second Edition. Hoboken, NJ : John Wiley & Sons, 2017. – ISBN 978–1–119–18628–1
- [44] LABVIEW: *version 13.0.0.4047 (2013, 32-bit)* / National Instruments Corporation. Austin, TX, Jul. 2013
- [45] LACKNER, Maximilian ; PALOTAS, Arpad B. ; WINTER, Franz: *Combustion : From Basics to Applications*. Weinheim : Wiley-VCH, 2013. – ISBN 978–3–527–66721–5

- [46] LI, S. C. ; VARATHARAJAN, B. ; WILLIAMS, F. A.: *Chemistry of JP-10 Ignition*. In: AIAA Journal 39 (2001), no. 12: 2351–2356. <http://dx.doi.org/10.2514/2.1241>
- [47] LIÑÁN, A. ; WILLIAMS, F. A.: *Oxford Engineering Science Series*. Vol. 34: *Fundamental aspects of combustion*. New York : Oxford University Press, 1993. – ISBN 0–1950–7626–5
- [48] LIÑÁN, Amable: *The asymptotic structure of counterflow diffusion flames for large activation energies*. In: Acta Astronautica 1 (1974), no. 7-8: 1007–1039. [http://dx.doi.org/10.1016/0094-5765\(74\)90066-6](http://dx.doi.org/10.1016/0094-5765(74)90066-6)
- [49] LIU, Wei ; KOCH, Jeremy A. ; LAW, Chung K.: *Nonpremixed ignition of C7–C16 normal alkanes in stagnating liquid pool*. In: Combustion and Flame 158 (2011), no. 11: 2145–2148. <http://dx.doi.org/10.1016/j.combustflame.2011.03.013>
- [50] MAIRHOFER, Philipp ; MAIRINGER, Gerald ; SESHADRI, Kalyanasundaram ; BAI, Xue-Song ; SEISER, Reinhard ; PUCHER, Ernst: *Rate-ratio asymptotic analysis of the influence of stoichiometric mixture fraction on structure and extinction of laminar, nonpremixed methane flames with comparison to experiments*. In: Proceedings of the Combustion Institute 36 (2017), no. 1: 1495–1503. <http://dx.doi.org/10.1016/j.proci.2016.05.027>
- [51] MAIRINGER, Gerald: *Experimental Studies on Combustion of Jet, Automotive and Alternative Fuels*. Wien, Technische Universität Wien, Fakultät für Maschinenwesen und Betriebswissenschaften, 2018. – dissertation
- [52] MAIRINGER, Gerald ; FRASSOLDATI, Alessio ; CUOCI, Alberto ; PELUCCHI, Matteo ; PUCHER, Ernst ; SESHADRI, Kalyanasundaram: *Experimental and computational investigation of autoignition of jet fuels and surrogates in nonpremixed flows at elevated pressures*. In: Proceedings of the Combustion Institute 37 (2019), no. 2: 1605–1614. <http://dx.doi.org/10.1016/j.proci.2018.06.224>
- [53] MAIRINGER, Gerald ; FRASSOLDATI, Alessio ; GEHMLICH, Ryan ; NIEMANN, Ulrich ; STAGNI, Alessandro ; RANZI, Eliseo ; SESHADRI, Kalyanasundaram: *Autoignition of condensed hydrocarbon fuels in non-premixed flows at elevated pressures*. In: Combustion Theory and Modelling 20 (2016), no. 6: 995–1009. <http://dx.doi.org/10.1080/13647830.2016.1232437>

- [54] MAIRINGER, Gerald ; KHARE, Rohit S. ; NARAYANASWAMY, Krithika ; HUNYADIGALL, Martin ; RAGHAVAN, Vasudevan ; SESHADRI, Kalyanasundaram: *Experimental and computational investigation of the influence of stoichiometric mixture fraction on structure and extinction of laminar, nonpremixed dimethyl ether flames*. In: *Combustion Theory and Modelling* 23 (2019), no. 2: 376–386. <http://dx.doi.org/10.1080/13647830.2018.1551577>
- [55] MATLAB: *version 8.6.0.267246 (R2015b, 64-bit)* / The MathWorks, Inc. Natick, Massachusetts, Aug. 2015
- [56] MCBRIDE, Bonnie J. ; GORDON, Sanford: *Computer Program for Calculation of Complex Chemical Equilibrium Compositions and Applications : II. User's Manual and Program Description* / National Aeronautics and Space Administration. 1996 (NASA Reference Publication RP-1311-P2)
- [57] MCBRIDE, Bonnie J. ; GORDON, Sanford ; RENO, Martin A.: *Coefficients for Calculating Thermodynamic and Transport Properties of Individual Species* / National Aeronautics and Space Administration. 1993 (NASA Technical Memorandum 4513)
- [58] MEASUREMENT COMPUTING: *ULx for NI LabVIEW : Info & Specifications Sheet* / Measurement Computing Corporation. Apr. 2017
- [59] MEASUREMENT COMPUTING: *USB-TEMP and USB-TC Series : Info & Specifications Sheet* / Measurement Computing Corporation. Jun. 2017
- [60] MERCHANT, Shamel S. ; GOLDSMITH, C. F. ; VANDEPUTTE, Aäron G. ; BURKE, Michael P. ; KLIPPENSTEIN, Stephen J. ; GREEN, William H.: *Understanding low-temperature first-stage ignition delay: Propane*. In: *Combustion and Flame* 162 (2015), no. 10: 3658–3673. <http://dx.doi.org/10.1016/j.combustflame.2015.07.005>
- [61] NATIONAL INSTRUMENTS: *PXI-1033 5-slot 3U PXI and CompactPCI Chassis : Manual* / National Instruments Corporation. May 2012
- [62] NIEMANN, U. ; SESHADRI, K. ; WILLIAMS, F. A.: *Effect of pressure on structure and extinction of near-limit hydrogen counterflow diffusion flames*. In: *Proceedings of the Combustion Institute* 34 (2013), no. 1: 881–886. <http://dx.doi.org/10.1016/j.proci.2012.06.145>
- [63] NIEMANN, Ulrich: *Experimental and Computational Studies of the Combustion of Classical and Alternative Fuels*. La Jolla, University of California, San Diego, Department of Mechanical & Aerospace Engineering, 2013. – dissertation

- [64] NIEMANN, Ulrich ; SEISER, Reinhard ; SESHADRI, Kalyanasundaram: *Ignition and extinction of low molecular weight esters in nonpremixed flows*. In: *Combustion Theory and Modelling* 14 (2010), no. 6: 875–891. <http://dx.doi.org/10.1080/13647830.2010.517275>
- [65] NIEMANN, Ulrich ; SESHADRI, Kalyanasundaram ; WILLIAMS, Forman A.: *Accuracies of laminar counterflow flame experiments*. In: *Combustion and Flame* 162 (2015), no. 4: 1540–1549. <http://dx.doi.org/10.1016/j.combustflame.2014.11.021>
- [66] NIEMANN, Ulrich ; SESHADRI, Kalyanasundaram ; WILLIAMS, Forman A.: *Effect of addition of a non-equidiffusional reactant to an equidiffusional diffusion flame*. In: *Combustion Theory and Modelling* 17 (2013), no. 3: 563–576. <http://dx.doi.org/10.1080/13647830.2013.791724>
- [67] NIEMANN, Ulrich ; SESHADRI, Kalyanasundaram ; WILLIAMS, Forman A.: *Methane, ethane, and ethylene laminar counterflow diffusion flames at elevated pressures: Experimental and computational investigations up to 2.0MPa*. In: *Combustion and Flame* 161 (2014), no. 1: 138–146. <http://dx.doi.org/10.1016/j.combustflame.2013.07.019>
- [68] NIST: *Chemistry WebBook*. <https://webbook.nist.gov/chemistry/>
- [69] NIST-JANAF: *Thermochemical Tables*. <https://janaf.nist.gov/>
- [70] OLIPHANT, Travis E.: *A guide to NumPy* / Trelgol Publishing. USA, 2006
- [71] OMEGA: *Fine Gage Bare Wire Thermocouple Elements, J, K, T, E, N, R & S*. https://www.omega.com/pptst/IRCO_CHAL_P13R_P10R.html, accessed: 21.09.2017
- [72] OMEGA: *Thermocouple Accuracy and Color Code charts* / OMEGA Engineering. Feb. 2017
- [73] OMEGA: *Ultrasonic Point Level Switch LVSW-701 : User's Guide* / OMEGA Engineering. Aug. 2012
- [74] OSECO: *STD Rupture Disc for Union Assembly : Installation Instructions* / Oseco. Jan. 2011
- [75] PARKER: *2-Way Solenoid Valve 7121KBN2GR00N0C111P3 : Installation, Operating & Maintenance Instructions* / Parker Hannifin. Nov. 1998

- [76] PELUCCHI, Matteo ; BISSOLI, Mattia ; CAVALLOTTI, Carlo ; CUOCI, Alberto ; FARAVELLI, Tiziano ; FRASSOLDATI, Alessio ; RANZI, Eliseo ; STAGNI, Alessandro: *Improved Kinetic Model of the Low-Temperature Oxidation of n-Heptane*. In: Energy & Fuels 28 (2014), no. 11: 7178–7193. <http://dx.doi.org/10.1021/ef501483f>
- [77] PETERS, Norbert: *Combustion Theory*. CEFRC Summer School, Princeton, 2010. – lecture materials
- [78] PETERS, Norbert (ed.) ; ROGG, Bernd (ed.): *Reduced Kinetic Mechanisms for Applications in Combustion Systems*. Berlin and Heidelberg : Springer-Verlag, 1993. – ISBN 3–540–56372–5
- [79] PHANTOM: *VEO 410L High-Speed Camera : Manual* / Vision Research. Jan. 2018
- [80] PRAXAIR: *Portable High Performance Microbulk Storage System PERMA-CYL 1500 ZX VHP : Info & Specifications Sheet* / Praxair Technology. 2015
- [81] PRINCE, Juan C. ; WILLIAMS, Forman A.: *Revised short mechanism for the low-temperature ignition of n-heptane for a wider pressure range*. In: Fuel 150 (2015): 730–731. <http://dx.doi.org/10.1016/j.fuel.2015.02.029>
- [82] PRINCE, Juan C. ; WILLIAMS, Forman A.: *Short chemical-kinetic mechanisms for low-temperature ignition of propane and ethane*. In: Combustion and Flame 159 (2012), no. 7: 2336–2344. <http://dx.doi.org/10.1016/j.combustflame.2012.02.012>
- [83] PRINCE, Juan C. ; WILLIAMS, Forman A.: *A short reaction mechanism for the combustion of dimethyl-ether*. In: Combustion and Flame 162 (2015), no. 10: 3589–3595. <http://dx.doi.org/10.1016/j.combustflame.2015.06.016>
- [84] PRINCE, Juan C. ; WILLIAMS, Forman A. ; OVANDO, Guillermo E.: *A short mechanism for the low-temperature ignition of n-heptane at high pressures*. In: Fuel 149 (2015): 138–142. <http://dx.doi.org/10.1016/j.fuel.2014.08.063>
- [85] RANZI, E. ; FRASSOLDATI, A. ; FARAVELLI, T. ; CUOCI, A.: *Lumped Kinetic Modeling of the Oxidation of Isocetane (2,2,4,4,6,8,8-Heptamethylnonane) in a Jet-Stirred Reactor (JSR)*. In: Energy & Fuels 23 (2009), no. 10: 5287–5289. <http://dx.doi.org/10.1021/ef900815j>

- [86] RANZI, E. ; FRASSOLDATI, A. ; GRANA, R. ; CUOCI, A. ; FARAVELLI, T. ; KELLEY, A. P. ; LAW, C. K.: *Hierarchical and comparative kinetic modeling of laminar flame speeds of hydrocarbon and oxygenated fuels*. In: Progress in Energy and Combustion Science 38 (2012), no. 4: 468–501. <http://dx.doi.org/10.1016/j.pecs.2012.03.004>
- [87] RANZI, Eliseo ; FARAVELLI, Tiziano ; GAFFURI, Paolo ; SOGARO, Angelo: *Low-Temperature Combustion : Automatic Generation of Primary Oxidation Reactions and Lumping Procedures*. In: Combustion and Flame 102 (1995), no. 1-2: 179–192
- [88] RANZI, Eliseo ; FRASSOLDATI, Alessio ; GRANATA, Silvia ; FARAVELLI, Tiziano: *Wide-Range Kinetic Modeling Study of the Pyrolysis, Partial Oxidation, and Combustion of Heavy n-Alkanes*. In: Industrial & Engineering Chemistry Research 44 (2005), no. 14: 5170–5183. <http://dx.doi.org/10.1021/ie049318g>
- [89] RANZI, Eliseo ; FRASSOLDATI, Alessio ; STAGNI, Alessandro ; PELUCCHI, Matteo ; CUOCI, Alberto ; FARAVELLI, Tiziano: *Reduced Kinetic Schemes of Complex Reaction Systems : Fossil and Biomass-Derived Transportation Fuels*. In: International Journal of Chemical Kinetics 46 (2014), no. 9: 512–542. <http://dx.doi.org/10.1002/kin.20867>
- [90] RITTER: *Drum-Type Gas Meters : Manual / Dr.-Ing. RITTER Apparatebau*. Jul. 2010
- [91] RITTER: *TG 5 Drum-Type Gas Meter : Data & Specifications Sheet / Dr.-Ing. RITTER Apparatebau*. Feb. 2011
- [92] RITTER: *TG 50 Drum-Type Gas Meter : Data & Specifications Sheet / Dr.-Ing. RITTER Apparatebau*. Feb. 2011
- [93] SAGGESE, Chiara ; FRASSOLDATI, Alessio ; CUOCI, Alberto ; FARAVELLI, Tiziano ; RANZI, Eliseo: *A wide range kinetic modeling study of pyrolysis and oxidation of benzene*. In: Combustion and Flame 160 (2013), no. 7: 1168–1190. <http://dx.doi.org/10.1016/j.combustflame.2013.02.013>
- [94] SARATHY, S. M. ; NIEMANN, Ulrich ; YEUNG, Coleman ; GEHMLICH, Ryan ; WESTBROOK, Charles K. ; PLOMER, Max ; LUO, Zhaoyu ; MEHL, Marco ; PITZ, William J. ; SESHADRI, Kalyanasundaram ; THOMSON, Murray J. ; LU, Tianfeng: *A counterflow diffusion flame study of branched octane isomers*. In: Proceedings of the Combustion Institute 34 (2013), no. 1: 1015–1023. <http://dx.doi.org/10.1016/j.proci.2012.05.106>

- [95] SCHLICHTING, Hermann ; GERSTEN, Klaus: *Boundary-Layer Theory*. Ninth Edition. Berlin and Heidelberg : Springer, 2017. – ISBN 978–3–662–52919–5
- [96] SEISER, R. ; NIEMANN, U. ; SESHADRI, K.: *Experimental study of combustion of n-decane and JP-10 in non-premixed flows*. In: Proceedings of the Combustion Institute 33 (2011), no. 1: 1045–1052. <http://dx.doi.org/10.1016/j.proci.2010.06.078>
- [97] SEISER, R. ; PITSCH, H. ; SESHADRI, K. ; PITZ, W. J. ; CURRAN, H. J.: *EXTINCTION AND AUTOIGNITION OF n-HEPTANE IN COUNTERFLOW CONFIGURATION*. In: Proceedings of the Combustion Institute 28 (2000), no. 2: 2029–2037. [http://dx.doi.org/10.1016/S0082-0784\(00\)80610-4](http://dx.doi.org/10.1016/S0082-0784(00)80610-4)
- [98] SEISER, R. ; SESHADRI, K. ; PISKERNIK, E. ; LIÑÁN A.: *Ignition in the viscous layer between counterflowing streams: asymptotic theory with comparison to experiments*. In: Combustion and Flame 122 (2000), no. 3: 339–349. [http://dx.doi.org/10.1016/S0010-2180\(00\)00139-5](http://dx.doi.org/10.1016/S0010-2180(00)00139-5)
- [99] SEISER, Reinhard: *Nonpremixed Combustion of Liquid Hydrocarbon Fuels*. Graz, Technische Universität Graz, Fakultät für Maschinenbau, July 2000. – dissertation
- [100] SESHADRI, K.: *Multistep asymptotic analyses of flame structures*. In: *Proceedings of the Twenty-Sixth Symposium (International) on Combustion*, Elsevier Inc., 1996, 831–846
- [101] SESHADRI, K. ; HUMER, S. ; SEISER, R.: *Activation-energy asymptotic theory of autoignition of condensed hydrocarbon fuels in non-premixed flows with comparison to experiment*. In: Combustion Theory and Modelling 12 (2008), no. 5: 831–855. <http://dx.doi.org/10.1080/13647830802054207>
- [102] SESHADRI, K. ; PETERS, N. ; PACZKO, G.: *Rate-ratio asymptotic analysis of autoignition of n-heptane in laminar nonpremixed flows*. In: Combustion and Flame 146 (2006), no. 1-2: 131–141. <http://dx.doi.org/10.1016/j.combustflame.2006.04.005>
- [103] SESHADRI, K. ; TREVINO, C.: *The Influence of the Lewis Numbers of the Reactants on the Asymptotic Structure of Counterflow and Stagnant Diffusion Flames*. In: Combustion Science and Technology 64 (1989), no. 4-6: 243–261. <http://dx.doi.org/10.1080/00102208908924033>

- [104] SESHADRI, K. ; WILLIAMS, F. A.: *Laminar flow between parallel plates with injection of a reactant at high reynolds number*. In: International Journal of Heat and Mass Transfer 21 (1978), no. 2: 251–253. [http://dx.doi.org/10.1016/0017-9310\(78\)90230-2](http://dx.doi.org/10.1016/0017-9310(78)90230-2)
- [105] SESHADRI, Kalyanasundaram ; BAI, Xue-Song: *Rate-Ratio Asymptotic Analysis of the Influence of Addition of Hydrogen on the Structure and Mechanisms of Extinction of Nonpremixed Methane Flames*. In: Combustion Science and Technology 187 (2014), no. 1-2: 3–26. <http://dx.doi.org/10.1080/00102202.2014.971948>
- [106] SESHADRI, Kalyanasundaram ; BAI, Xue-Song ; WILLIAMS, Forman: *Rate-ratio asymptotic analysis of the structure and mechanisms of extinction of nonpremixed CH₄/N₂-O₂/N₂O/N₂ flames*. In: Proceedings of the Combustion Institute 35 (2015), no. 1: 945–953. <http://dx.doi.org/10.1016/j.proci.2014.05.002>
- [107] SESHADRI, Kalyanasundaram ; FRASSOLDATI, Alessio ; CUOCI, Alberto ; FARAVELLI, Tiziano ; NIEMANN, Ulrich ; WEYDERT, Patrick ; RANZI, Eliseo: *Experimental and kinetic modeling study of combustion of JP-8, its surrogates and components in laminar premixed flows*. In: Combustion Theory and Modelling 15 (2011), no. 4: 569–583. <http://dx.doi.org/10.1080/13647830.2011.552635>
- [108] SESHADRI, Kalyanasundaram ; LU, Tianfeng ; HERBINET, Olivier ; HUMER, Stefan ; NIEMANN, Ulrich ; PITZ, William J. ; SEISER, Reinhard ; LAW, Chung K.: *Experimental and kinetic modeling study of extinction and ignition of methyl decanoate in laminar non-premixed flows*. In: Proceedings of the Combustion Institute 32 (2009), no. 1: 1067–1074. <http://dx.doi.org/10.1016/j.proci.2008.06.215>
- [109] SHADDIX, Christopher R.: *Correcting Thermocouple Measurements for Radiation Loss : A Critical Review*. In: JENSEN, M. K. (ed.) ; DI MARZO, M. (ed.): *Proceedings of the 33rd national heat transfer conference NHTC'99*. New York, NY : American Society of Mechanical Engineers, 1999
- [110] SMOOKE, M. D. ; CRUMP, J. ; SESHADRI, K. ; GIOVANGIGLI, V.: *Comparison between experimental measurements and numerical calculations of the structure of counterflow, diluted, methane-air, premixed flames*. In: *Proceedings of the Twenty-Third Symposium (International) on Combustion*, Elsevier Inc., 1990, 463–470

- [111] STAGNI, A. ; FRASSOLDATI, A. ; CUOCI, A. ; FARAVELLI, T. ; RANZI, E.: *Skeletal mechanism reduction through species-targeted sensitivity analysis*. In: *Combustion and Flame* 163 (2016): 382–393. <http://dx.doi.org/10.1016/j.combustflame.2015.10.013>
- [112] STAGNI, Alessandro ; CUOCI, Alberto ; FRASSOLDATI, Alessio ; FARAVELLI, Tiziano ; RANZI, Eliseo: *Lumping and Reduction of Detailed Kinetic Schemes : an Effective Coupling*. In: *Industrial & Engineering Chemistry Research* 53 (2014), no. 22: 9004–9016. <http://dx.doi.org/10.1021/ie403272f>
- [113] SWAGELOK: *Double-Ended Sample Cylinder, 500 ml 316L-HDF4-500 : Specifications Sheet* / Swagelok. Jan. 2017
- [114] SWAGELOK: *High Pressure Proportional Relief Valve SS-R4M8F8-MO : Specifications Sheet* / Swagelok. Dec. 2016
- [115] SWAGELOK: *Purple Spring Kit for R4 Series Proportional Relief Valve, 750 to 1500 psig (51.7 to 103 bar) 177-13K-R4-C : Specifications Sheet* / Swagelok. Dec. 2016
- [116] TELEDYNE HASTINGS INSTRUMENTS: *Gas Conversion Factors*. <http://www.teledyne-hi.com/resourcecenter/Documents/>, accessed: 10.12.2018
- [117] TELEDYNE HASTINGS INSTRUMENTS: *HFC-302 Flow Controller : Manual* / Teledyne Technologies. Mar. 2015
- [118] TELEDYNE HASTINGS INSTRUMENTS: *HFC-303/307 Flow Controllers : Manual* / Teledyne Technologies. Mar. 2015
- [119] TELEDYNE HASTINGS INSTRUMENTS: *PowerPod-400 Power Supply/Totalizer : Manual* / Teledyne Technologies. Dec. 2012
- [120] TELEDYNE ISCO: *1000D Syringe Pump : Specifications Sheet* / Teledyne Technologies. Jul. 2018
- [121] TELEDYNE ISCO: *500D Syringe Pump : Specifications Sheet* / Teledyne Technologies. Jul. 2018
- [122] TELEDYNE ISCO: *D-Series Pumps : Manual* / Teledyne Technologies. Jul. 2018
- [123] TESCOM: *Electronic Regulator ER3000 : Manual* / Emerson Process Management Regulator Technologies. Feb. 2013

- [124] TESCOM: *Electronic Regulator ER5000 : Manual* / Emerson Process Management Regulator Technologies. Oct. 2015
- [125] TESCOM: *Membrane Back Pressure Regulator : Manual* / Emerson Process Management Regulator Technologies. Jun. 2015
- [126] VAN DER WALT, STÉFAN ; COLBERT, S. C. ; VAROQUAUX, Gaël: *The NumPy Array : A Structure for Efficient Numerical Computation*. In: *Computing In Science & Engineering* 13 (2011): 22–30. <http://dx.doi.org/10.1109/MCSE.2011.37>
- [127] WANG, Hai: *Combustion Chemistry*. CEFRC Summer School, Princeton, 2015. – lecture materials
- [128] WANG, Zhandong ; ZHANG, Xiaoyuan ; XING, Lili ; ZHANG, Lidong ; HERRMANN, Friederike ; MOSHAMMER, Kai ; QI, Fei ; KOHSE-HÖINGHAUS, Katharina: *Experimental and kinetic modeling study of the low- and intermediate-temperature oxidation of dimethyl ether*. In: *Combustion and Flame* 162 (2015), no. 4: 1113–1125. <http://dx.doi.org/10.1016/j.combustflame.2014.10.003>
- [129] WELDCOA: *LCA06-APB LowPro Cylinder Cart : Specifications Sheet* / Welding Company of America. 2011
- [130] WESTBROOK, Charles K. ; PITZ, William J. ; HERBINET, Olivier ; CURRAN, Henry J. ; SILKE, Emma J.: *A comprehensive detailed chemical kinetic reaction mechanism for combustion of n-alkane hydrocarbons from n-octane to n-hexadecane*. In: *Combustion and Flame* 156 (2009), no. 1: 181–199. <http://dx.doi.org/10.1016/j.combustflame.2008.07.014>
- [131] WILLIAMS, Forman A.: *Combustion Theory : The Fundamental Theory of Chemically Reacting Flow Systems*. Second Edition. Menlo Park, CA : The Benjamin/Cummings Publishing Company Inc., 1985 (Combustion Science and Engineering Series). – ISBN 0–8053–9801–5
- [132] ZELEZNIK, Frank J. ; GORDON, Sanford: *An Analytical Investigation of Three General Methods of Calculating Chemical-Equilibrium Compositions* / National Aeronautics and Space Administration. 1960 (NASA Technical Note D-473)